UNIVERSITÀ
DEGLI STUDI
DI TRIESTE

UNIVERSITÀ DEGLI STUDI DI TRIESTE

XXXVII CICLO DEL DOTTORATO DI RICERCA IN

FISICA

Decoherence and Stochastic Schrödinger Equations: Applications to Quantum Computing and Wave Function Collapse Models

Settore scientifico-disciplinare: **FIS/02 FISICA TEORICA E MODELLI MATEMATICI**

DOTTORANDO / A
Giovanni Di Bartolomeo

COORDINATORE
PROF. Francesco Longo

SUPERVISORE DI TESI
PROF. Angelo Bassi

ANNO ACCADEMICO 2023/2024

Contents

Introduction

Decoherence is the process through which quantum systems lose coherence and become classical-like due to interactions with their environment. Stochastic Schrödinger Equations (SSEs) offer a powerful framework for describing the dynamics of open quantum systems subjected to decoherence effects. These equations, derived from the Schrödinger equation and incorporating stochastic terms to account for environmental noise, provide valuable insights into the behavior of quantum systems in realistic settings.

The primary results of this thesis demonstrate how SSEs can be effectively utilized in a novel manner to both simulate the dynamics of open quantum systems on quantum computers and model the behavior of noisy quantum devices. Specifically, we present an efficient quantum algorithm leveraging Quantum Stochastic Differential Equations (QSDEs) for simulating Markovian open quantum systems dynamics, called Gorini-Kossakowski-Lindblad-Sudarshan (GKLS). The algorithm employs random unitary gates on a set of n system qubits and, remarkably, only one ancillary qubit representing the environment. This ancilla overhead remains constant regardless of the size of the system. It follows that, for the typical case of m-locality of the Lindblad operators, our approach achieves an exponential reduction in the number of ancilla qubits in terms of m, and up to a polynomial reduction in ancilla overhead for large n compared to other methods. Although stochasticity is introduced, necessitating multiple circuit realizations, the sampling overhead remains independent of system size. Additionally, we demonstrate that, under fixed accuracy conditions, our algorithm reduces the number of the required Trotter steps, decreasing the circuit depth. These advancements are particularly significant for near-term quantum computers, where minimizing both circuit width and depth is crucial due to inherent noise.

While our algorithm is fundamentally designed for noise-free quantum computers, current technological limitations mean that we cannot avoid their intrinsic noisy behavior due to unwanted interactions with the surrounding environment. Consequently, we investigate the impact of noise on quantum simulations, specifically focusing on closed dynamics for simplicity. We introduce an equivariant quantum circuit that preserves total spin and translational symmetry to accurately describe the singlet and triplet excited states in the J1-J2 Heisenberg model on a chain, which are crucial for characterizing its phase transition point. Using standard classical simulation methods, we evaluate the impact of noise on the variational state, showing that mitigation techniques such as Zero Noise Extrapolation (ZNE) are necessary to reliably restore its physical properties.

However, standard methods for classically simulating noisy quantum circuits implement noisy operations before and after each ideal quantum gate, effectively decoupling the action of the gate from the noise. While this approximation is valid when quantum gates operate almost instantaneously relative to the noise, it has limitations, as quantum gates and noise can potentially influence each other during the gate execution. To address this problem, we propose an alternative simulation method, the Noisy Gates approach, based on principles similar to the previous quantum algorithm we introduced for simulating GKLS dynamics and grounded in Stochastic Differential Equations (SDEs). This approach enables the efficient incorporation of noise effects into the evolution of quantum gates, resulting in more accurate classical simulations compared to standard methods. We successfully apply the Noisy Gates approach to simulate superconducting devices and dual-rail encoding photonic platforms.

The second part of the thesis is devoted to construct and study the simplest universal dissipative GKLS master equation for many-body systems with the purpose of a new dissipative extension of existing non-relativistic theories of fundamental spontaneous wave function collapse. The model is written in terms of second-quantized mass density and current. Assuming linear friction in the current, we find that the dissipative structure is strictly constrained. Then, we establish experimental bounds on free parameters of the

so-constructed linear-friction dissipative Diósi-Penrose (dDP) and Continuous Spontaneous localisation (dCSL) models by exploiting experiments in the field of levitated optomechanics. Specifically, we analyze the dynamics of the center of mass of a rigid body composed of N particles and after having suitably linearised the dynamics, we derive (again by exploiting the QSDE formalism) the modified Langevin equations describing the dynamics of the mechanical oscillator. Our results in the dDP case exclude collapse temperatures below $10^{-13}\,\mathrm{K}$ and $6 \times 10^{-12}\,\mathrm{K}$ respectively for values of the localisation length smaller than $10^{-6}\,\mathrm{m}$ and $10^{-8}\,\mathrm{m}$. In the dCSL case the entire parameter space is excluded for values of the temperature lower than $6 \times 10^{-9}\,\mathrm{K}$.

The thesis is organized as follows. In Chapter 1 we briefly introduce the topics of decoherence and stochastic Schrödinger Equations and connect them to the frameworks of quantum computing and spontaneous wave function collapse models. Then Chapters 2, 3, 4 and 5 are dedicated to applications in the domain of quantum computing. In particular in Chapter 2 we present an efficient quantum algorithm for simulating the GKLS dynamics, in Chapter 3 we study the impact of inherent noise on a variational quantum eigensolver (VQE), in Chapter 4 we introduce a novel classical simulation approach of noisy quantum devices and in Chapter 5 we adapt and extend the latter approach in order to simulate noisy photonic quantum devices. Finally, Chapters 6 and 7 are devoted to applications to wave function collapse models where in Chapter 6 we introduce a linear-friction dissipative mechanism and in Chapter 7 we establish bounds on the free parameters of the models from experimental data.

The research presented in this thesis has resulted in the following publications:

1. G. Di Bartolomeo, M. Vischi, T. Feri, A. Bassi and S. Donadi. Efficient quantum algorithm to simulate open systems through a single environmental qubit. Phys. Rev. Research, accepted 23 October 2024, arXiv:2311.10009 [quant-ph]

2. G. Crognaletti, G. Di Bartolomeo, M. Vischi and L. L. Viteritti. Equivariant Variational Quantum Eigensolver to detect

Phase Transitions through Energy Level Crossings. Quantum Sci. Technol. 10 (2025) 01504.

3. G. Di Bartolomeo, M. Vischi, F. Cesa, R. Wixinger, M. Grossi, S. Donadi and A. Bassi. Noisy gates for simulating quantum computers. Phys. Rev. Research 5, 043210 (2023).

4. M. Vischi, G. Di Bartolomeo, M. Proietti, S. Koudia, F. Cerocchi, M. Dispenza and A. Bassi. Simulating photonic devices with noisy optical elements. Phys. Rev. Research 6, 033337 (2024).

5. G. Di Bartolomeo, M. Carlesso, K. Piscicchia, C. Curceanu, M. Derakhshani, and L. Diósi. Linear-friction many-body equation for dissipative spontaneous wave-function collapse. Phys. Rev. A 108, 012202 (2023).

6. G. Di Bartolomeo and M. Carlesso. Experimental bounds on linear-friction dissipative collapse models from levitated optomechanics. New J. Phys. 26 (2024) 043006.

Chapter 1

Decoherence and Stochastic Schrödinger Equations (SSEs)

In the following chapter, we introduce the basic tools employed throughout the reminder of the thesis. We show how the phenomenon of decoherence — specifically, the loss of quantum coherence — arises within the theory of open quantum systems and how it can be effectively described using appropriate Stochastic Schrödinger Equations (SSEs). Subsequently, we explore the topics of decoherence and SSEs within the frameworks of quantum computing and spontaneous wave function collapse models.

1.1 The theory of open quantum systems

Quantum mechanics tells us that the evolution of a quantum system is unitary, ruled by the Schrödinger Equation for the state vector of the system, or alternatively, by the von Neumann equation when considering the system's density matrix. However, when a system interacts with its surrounding environment and the environmental degrees of freedom are averaged out, the system's evolution becomes non-unitary. In such a scenario the evolution is better described by a more general equation for the system's density matrix called Gorini-Kossakowski-Lindblad-Sudarshan (GKLS) master equation [1,2]. A direct consequence of such a non-unitary evolution is decoherence, namely the decay over time of the off-diagonal entries of the system's density matrix in a certain basis. In other words, the system transitions from a pure state to a mixed state, thereby losing coherence and exhibiting classical behavior [3].

1.1.1 The Kraus representation of quantum maps

Given a general quantum system, the total density matrix $\hat{\rho}_{tot}$ of the system plus its environment evolves with a unitary quantum map

$$\mathcal{U}\hat{\rho}_{tot} = \hat{U}\hat{\rho}_{tot}\hat{U}^{\dagger}, \tag{1.1}$$

where $\hat{U}$ is the unitary evolution operator. Without loss of generality we assume that the initial state of the environment is pure $\hat{\rho}_E = |e_0\rangle\langle e_0|$, where $|e_j\rangle\langle e_j|$ is an orthonormal basis for the Hilbert space of the environment. By assuming for simplicity a separable input density matrix $\hat{\rho}_{tot} = \hat{\rho} \otimes \hat{\rho}_E$, then the reduced state of the system evolves as

$$\mathcal{E}\hat{\rho} = \mathrm{Tr}_E\big(\mathcal{U}\hat{\rho}_{tot}\big) = \sum_j \langle e_j|\, \hat{U}\big(\hat{\rho} \otimes |e_0\rangle\langle e_0|\big)\hat{U}^{\dagger}\, |e_j\rangle\,, \tag{1.2}$$

where $\mathrm{Tr}_E(\cdot)$ is the trace over the environment's degrees of freedom. By defining the so-called Kraus operators $\hat{K}_j = \langle e_j|\, \hat{U}\, |e_0\rangle$ we obtain the following Kraus map [4, 5]

$$\mathcal{E}\hat{\rho} = \sum_j \hat{K}_j \hat{\rho} \hat{K}_j^{\dagger}, \tag{1.3}$$

where $\sum_j \hat{K}_j^{\dagger}\hat{K}_j = \hat{\mathbb{I}}$. It is simple to show that Eq. (1.3) satisfies the following properties that are fundamental in order to have a valid output density matrix $\hat{\rho}' = \mathcal{E}\hat{\rho}$:

- Linearity: $\mathcal{E}(\alpha\hat{\rho}_1 + \beta\hat{\rho}_2) = \alpha\mathcal{E}\hat{\rho}_1 + \beta\mathcal{E}\hat{\rho}_2$ where $0 \leq \alpha \leq 1$ and $\beta = 1 - \alpha$.
- Hermiticity-preserving: $\mathcal{E}^{\dagger}\hat{\rho} = \mathcal{E}\hat{\rho}$
- Trace-preserving: $\mathrm{Tr}(\mathcal{E}\hat{\rho}) = 1$
- Positivity: Given a Hilbert space $\mathcal{H}$ then $\langle\phi|\, \mathcal{E}\hat{\rho}\, |\phi\rangle \geq 0$ for each $|\phi\rangle \in \mathcal{H}$.
- Complete positivity: Given a bipartite Hilbert space $\mathcal{H} = \mathcal{H}_1 \otimes \mathcal{H}_2$ then the map $\mathcal{E}_1\hat{\rho} \otimes \mathbb{I}_2$ is positive for each choice of $\mathcal{H}_2$.

1.1.2 The GKLS master equation

In the same spirit as the Kraus representation, we may ask what form a dynamical equation should take, under certain approximations, to ensure a valid system's density matrix. The Kraus representation of the system's density matrix written with explicit time dependence reads

$$\hat{\rho}(t) = \mathcal{E}_t\hat{\rho}(0) = \sum_j \hat{K}_j(t)\hat{\rho}(0)\hat{K}_j^\dagger(t). \tag{1.4}$$

When the characteristic timescales over which the environmental correlation functions decay are much shorter than the characteristic timescale of the system's evolution, it becomes reasonable to disregard memory effects in the reduced system dynamics. This is known as the Markovian approximation and formally implies that the map $\mathcal{E}_t$ belongs to a family of completely positive maps for $t \geq 0$, referred to as a quantum dynamical semigroup [1,2] with the following properties:

- $\mathcal{E}_t$ is strongly continuous (uniformly continuous in the infinite-dimensional case).
- $\mathcal{E}_t\mathcal{E}_s = \mathcal{E}_{t+s}$ for each $t, s \geq 0$.

Thus by applying group theory we can write

$$\mathcal{E}_t = e^{\mathcal{L}t}, \tag{1.5}$$

where $\mathcal{L} = \frac{\partial}{\partial t}\mathcal{E}_t|_{t=0}$ is the semigroup generator called Lindbladian. Then from Eq. (1.5) follows

$$\frac{\mathrm{d}}{\mathrm{d}t}\hat{\rho}(t) = \mathcal{L}\hat{\rho}(t). \tag{1.6}$$

In order to find the expression for the Lindbladian we start from Eq. (1.4) for an infinitesimal time evolution $t \to t + \mathrm{d}t$ and express the Kraus operators as [5]

$$\begin{aligned} \hat{K}_0(\mathrm{d}t) &= \hat{\mathbb{I}} + \frac{1}{\hbar}(-i\hat{H} + \hat{C})\mathrm{d}t, \\ \hat{K}_j(\mathrm{d}t) &= \sqrt{\gamma_j \mathrm{d}t}\ \hat{L}_j \quad j > 0, \end{aligned} \tag{1.7}$$

where $\hat{H}$ is the system's Hamiltonian, $\hat{C}$ is a Hermitian operator to be determined, γ_j are positive real constants and $\hat{L}_j$ are generic

operators called Lindblad operators. By imposing the completeness relation $\sum_j \hat{K}_j^\dagger(\mathrm{d}t)\hat{K}_j(\mathrm{d}t) = \hat{\mathbb{I}}$ we find

$$\hat{C} = -\frac{\hbar}{2}\sum_{j>0}\gamma_j \hat{L}_j^\dagger \hat{L}, \tag{1.8}$$

then the expression for the density matrix at time $t+\mathrm{d}t$ reads

$$\hat{\rho}(t+\mathrm{d}t) = \hat{\rho}(t) - \frac{i}{\hbar}[\hat{H},\hat{\rho}(t)]\mathrm{d}t + \sum_{j>0}\gamma_j\Big(\hat{L}_j\hat{\rho}(t)\hat{L}_j^\dagger - \frac{1}{2}\{\hat{L}_j^\dagger\hat{L}_j,\hat{\rho}(t)\}\Big)\mathrm{d}t + o\big((\mathrm{d}t)^2\big). \tag{1.9}$$

We notice that in general $\hat{\rho}(t+\mathrm{d}t)$ can depend not only on $\hat{\rho}(t)$ but also on $\hat{\rho}(\tau)$ for each $\tau \leq t$, because the environment retains a memory of the information for a while, and can transfer it back to system. However, if we assume the Markov approximation, then information can just flow from the system to the environment neglecting information back flow, then $\hat{\rho}(t+\mathrm{d}t) = \hat{\rho}(t)+\mathrm{d}\hat{\rho}(t)+o\big((\mathrm{d}t)^2\big)$. Thus the Lindbladian reads

$$\mathcal{L}\hat{\rho}(t) = -\frac{i}{\hbar}[\hat{H},\hat{\rho}(t)] + \sum_j \gamma_j\Big(\hat{L}_j\hat{\rho}(t)\hat{L}_j^\dagger - \frac{1}{2}\{\hat{L}_j^\dagger\hat{L}_j,\hat{\rho}(t)\}\Big). \tag{1.10}$$

Eq. (1.6) with the Lindbladian in Eq. (1.10) is the GKLS master equation for the density matrix of the system.

We mention that alternatively Eq. (1.10) can be found directly from a microscopic point of view starting from the von Neumann equation of the total system-environment dynamics, moving to the interaction picture and then tracing over the environmental degrees of freedom [3,5]. The physical assumptions underlying this derivation are the weak coupling between the system and the environment (Born approximation) and the Markov approximation discussed above.

Let us now focus on Eq. (1.10). The first term corresponds to the standard Hamiltonian term appearing in the von Neumann equation, while the second term is responsible for non-unitary evolution and in particular for decoherence. Indeed, if we neglect for simplicity the Hamiltonian term in Eq. (1.10), we take just one Lindblad operator $\hat{L}^\dagger = \hat{L}$ and we define $|l_m\rangle$ and l_m respectively as eigenvectors and eigenvalues of $\hat{L}$, then the master equation expressed in

the $|l_m\rangle$ basis becomes

$$\frac{\mathrm{d}}{\mathrm{d}t}\langle l_{m'}|\,\hat{\rho}(t)\,|l_m\rangle = -\frac{\gamma}{2}(l_{m'}-l_m)^2\,\langle l_{m'}|\,\hat{\rho}(t)\,|l_m\rangle\,. \tag{1.11}$$

By solving the latter equation one finds the decay over time of the off-diagonal elements of the density matrix in the $|l_m\rangle$ basis

$$\langle l_{m'}|\,\hat{\rho}(t)\,|l_m\rangle = e^{-\frac{\gamma}{2}(l_{m'}-l_m)^2 t}\,\langle l_{m'}|\,\hat{\rho}(0)\,|l_m\rangle\,. \tag{1.12}$$

To conclude this section we notice that given an arbitrary operator $\hat{O}$ then $\mathrm{Tr}\Big(\hat{O}\hat{\rho}(t)\Big) = \mathrm{Tr}\Big(\hat{O}e^{\mathcal{L}t}\hat{\rho}(0)\Big) = \mathrm{Tr}\Big(e^{\mathcal{L}^\dagger t}\hat{O}\hat{\rho}(0)\Big) = \mathrm{Tr}\Big(\hat{O}(t)\hat{\rho}(0)\Big)$ where $\hat{O}(t) = e^{\mathcal{L}^\dagger t}\hat{O}$, thus the master equation in the Heisenberg picture reads

$$\begin{aligned} \frac{\mathrm{d}}{\mathrm{d}t}\hat{O}(t) &= \mathcal{L}^\dagger\hat{O}(t), \\ \mathcal{L}^\dagger\hat{\rho}(t) &= \frac{i}{\hbar}[\hat{O}(t),\hat{H}] + \sum_j \gamma_j\Big(\hat{L}_j^\dagger\hat{O}(t)\hat{L}_j - \frac{1}{2}\{\hat{L}_j^\dagger\hat{L}_j,\hat{O}(t)\}\Big), \end{aligned} \tag{1.13}$$

where $\mathcal{L}^\dagger$ is the adjoint of the Lindbladian.

1.2 Stochastic Schrödinger equations (SSEs)

As shown in the previous section, the theory of open quantum systems operates at the level of the density matrix, providing a statistical description of the evolution of a quantum state. However, if one is interested in the open dynamics of the system state vector, a stochastic modification of the Schrödinger equation is required to remain consistent with the statistical description [6–9]. There is not a unique way to build SSE, indeed several approaches are able to reproduce the same master equation at the density matrix level. Consequently, different SSE represent different ways to unravel the same master equation, for this reason they are also called unravellings of the master equation. The solutions of a SSE yield random trajectories that describe the dynamics of the state vector. By averaging over these trajectories, the statistical description of the system is recovered. The introduction of stochasticity into the Schrödinger equation involves adding an appropriate noise term. Noise terms with different statistical properties generates different unravellings.

1.2.1 SSE with classical Gaussian noise

Typically, the construction of Markovian SSE is based on the theory of stochastic differential equations (SDE) expressed in the Itô formalism [10–12]. We start from the following SDE for the state vector of the system

$$\mathrm{d}|\psi(t)\rangle = \left[-\frac{i}{\hbar}\hat{H}\mathrm{d}t + \sum_j\Big(\sqrt{\gamma_j}\,\hat{L}_j\mathrm{d}W_j(t) + \hat{A}_j\mathrm{d}t\Big)\right]|\psi(t)\rangle \tag{1.14}$$

where $\hat{H}$ is the system's Hamiltonian, $\hat{L}_j$ are Lindblad operators, $\hat{A}_j$ are unknown operators to be determined and $W_j(t)$ are classical standard Wiener processes with the following statistical properties

$$\mathbb{E}\big[\mathrm{d}W_j(t)\big] = 0, \quad \mathbb{E}\big[\mathrm{d}W_j(t)\mathrm{d}W_k(t)\big] = \delta_{jk}\mathrm{d}t. \tag{1.15}$$

In order to fix the operators $\hat{A}_j$ we derive the master equation from Eq. (1.14)

$$\begin{aligned}\frac{\mathrm{d}}{\mathrm{d}t}\hat{\rho}(t) &= \frac{1}{\mathrm{d}t}\mathbb{E}\Big[\mathrm{d}|\psi(t)\rangle\,\langle\psi(t)| + |\psi(t)\rangle\mathrm{d}\langle\psi(t)| + \mathrm{d}|\psi(t)\rangle\mathrm{d}\langle\psi(t)|\Big]\\ &= -\frac{i}{\hbar}[\hat{H},\hat{\rho}(t)] + \sum_j\Big(\gamma_j\hat{L}_j\hat{\rho}(t)\hat{L}_j^\dagger + \hat{A}_j\hat{\rho}(t) + \hat{\rho}(t)\hat{A}_j^\dagger\Big)\end{aligned} \tag{1.16}$$

and find

$$\hat{A}_j = -\frac{\gamma_j}{2}\hat{L}_j^\dagger\hat{L}_j. \tag{1.17}$$

The reason for retaining the term $\mathrm{d}|\psi(t)\rangle\mathrm{d}\langle\psi(t)|$ in Eq.(1.16) is the fact that for second order terms $(\mathrm{d}W_j(t))^2$ we have $\mathbb{E}\big[(\mathrm{d}W_j(t))^2\big] = \mathrm{d}t$. We notice that by setting

$$\hat{L}_j \to i\hat{L}_j, \tag{1.18}$$

we get the same master equation but in the case of Hermitian Lindblad operators $\hat{L}_j^\dagger = \hat{L}_j$ the SSE becomes unitary (this can be easily checked by moving from the Itô to the Stratonovich SDE formalism [9, 11]). Thus, by using Eq. (1.18) we get the following SSE

$$\mathrm{d}|\psi(t)\rangle = \left[-\frac{i}{\hbar}\hat{H}\mathrm{d}t + \sum_j\Big(i\sqrt{\gamma_j}\,\hat{L}_j\mathrm{d}W_j(t) - \frac{\gamma_j}{2}\hat{L}_j^\dagger\hat{L}_j\mathrm{d}t\Big)\right]|\psi(t)\rangle\,. \tag{1.19}$$

Eq. (1.19) is linear and in general (for $\hat{L}_j^\dagger \neq \hat{L}_j$) does not preserve the norm of the state vector. Moreover, by normalizing Eq. (1.14) ($|\varphi(t)\rangle = |\psi(t)\rangle / || \, |\psi(t)\rangle \, ||$) and by properly fixing the statistical properties of the Wiener increments $\mathrm{d}W_j(t)$ [8,9], one can also derive a non-linear and norm preserving SSE

$$\begin{aligned} \mathrm{d}|\varphi(t)\rangle = \Bigg[-\frac{i}{\hbar}\hat{H}\mathrm{d}t + \sum_j \Bigg(\sqrt{\gamma_j} \left(\hat{L}_j - \frac{1}{2} \left\langle \hat{L}_j + \hat{L}_j^\dagger \right\rangle_t \right) \mathrm{d}W_j(t) \\ - \frac{\gamma_j}{2} \left(\hat{L}_j^\dagger \hat{L}_j - \left\langle \hat{L}_j + \hat{L}_j^\dagger \right\rangle_t \hat{L}_j + \frac{1}{4} \left\langle \hat{L}_j + \hat{L}_j^\dagger \right\rangle_t^2 \right) \mathrm{d}t \Bigg) \Bigg] |\varphi(t)\rangle \, , \end{aligned} \tag{1.20}$$

where $\left\langle \hat{L}_j \right\rangle_t = \langle \varphi(t)| \, \hat{L}_j \, |\varphi(t)\rangle$.
We notice that Eqs. (1.14), (1.19) and (1.20) are three different unravellings of the master equation with Gaussian noise.

1.2.2 SSE with classical Poissonian noise

SSE can be built also by employing classical Poissonian random variables instead of Gaussian ones. While the latter are continuous variables, Poissonian variables are discrete variables as they count the number of so-called quantum jumps [5,6]. The derivation of the SSEs is similar to the previous above and can be found in [6, 13], here we show only the results. The linear and in general non-norm preserving SSE reads

$$\mathrm{d}|\psi(t)\rangle = \left[-\frac{i}{\hbar}\hat{H}\mathrm{d}t + \sum_j \left(\left(\hat{L}_j - \hat{\mathbb{I}} \right) \mathrm{dN}_j(t) + \frac{\gamma_j}{2} \left(\hat{\mathbb{I}} - \hat{L}_j^\dagger \hat{L}_j \right) \mathrm{d}t \right) \right] |\psi(t)\rangle \, , \tag{1.21}$$

where $\mathrm{N}_j(t)$ are Poissonian random variables such that

$$\mathbb{E}\left[\mathrm{dN}_j(t) \right] = \gamma_j \mathrm{d}t, \quad \mathbb{E}\left[\mathrm{dN}_j(t) \mathrm{dN}_k(t) \right] = \delta_{jk} \gamma_j \mathrm{d}t. \tag{1.22}$$

The related non-linear and norm preserving SSE reads

$$\begin{aligned} \mathrm{d}|\varphi(t)\rangle = \Bigg[-\frac{i}{\hbar}\hat{H}\mathrm{d}t + \sum_j \Bigg(\left(\frac{\hat{L}_j}{\sqrt{\left\langle \hat{L}_j^\dagger \hat{L}_j \right\rangle_t}} - \hat{\mathbb{I}} \right) \mathrm{d}\tilde{\mathrm{N}}_j(t) \\ - \frac{\gamma_j}{2} \left(\hat{L}_j^\dagger \hat{L}_j - \left\langle \hat{L}_j^\dagger \hat{L}_j \right\rangle_t \right) \mathrm{d}t \Bigg) \Bigg] |\varphi(t)\rangle \, , \end{aligned} \tag{1.23}$$

where now the statistical properties of $\tilde{\mathrm{N}}_j(t)$ read

$$\mathbb{E}\big[\mathrm{d}\tilde{\mathrm{N}}_j(t)\big] = \gamma_j \left\langle \hat{L}_j^\dagger \hat{L}_j \right\rangle_t \mathrm{d}t, \quad \mathbb{E}\big[\mathrm{d}\tilde{\mathrm{N}}_j(t)\mathrm{d}\tilde{\mathrm{N}}_k(t)\big] = \delta_{jk}\gamma_j \left\langle \hat{L}_j^\dagger \hat{L}_j \right\rangle_t \mathrm{d}t. \tag{1.24}$$

We mention that in the limit of an infinite numbers of jumps in a time interval that goes to zero the Poissonian random variables tend to Gaussian continuous random variables. In such a limit Eq. (1.20) can be derived from (1.23) [6, 13].

1.2.3 SSE with quantum noise

Another unravelling of the master equation we take in to account is based on the so-called quantum noise formalism [6, 13–15]. We consider the following Hamiltonian $\hat{H} = \hat{H}_{\mathrm{S}} + \hat{H}_{\mathrm{E}} + \hat{H}_{\mathrm{SE}}$ where $\hat{H}_{\mathrm{S}}$ is the system Hamiltonian while $\hat{H}_{\mathrm{E}}$ and $\hat{H}_{\mathrm{SE}}$ are, respectively, the environment Hamiltonian and the system-environment interaction Hamiltonian, that read

$$\hat{H}_{\mathrm{E}} = \hbar \sum_j \int \mathrm{d}\omega \omega \hat{b}_j^\dagger(t,\omega)\hat{b}_j(t,\omega), \tag{1.25}$$

$$\hat{H}_{\mathrm{SE}} = i\hbar \sum_j \int \mathrm{d}\omega \chi_j(\omega)\Big(\hat{b}_j^\dagger(t,\omega)\hat{L}_j - \hat{L}_j^\dagger \hat{b}_j(t,\omega)\Big), \tag{1.26}$$

where $\hat{b}_j(t,\omega)$ is the annihilation operator of the j-th thermal bath at time t, ω is the frequency of the mode and $\hat{L}_j$ is an arbitrary system operator. By using the Hamiltonian $\hat{H}$ one can solve the Heisenberg equation for $\hat{b}_j(t,\omega)$ and substitute the solution in the Heisenberg equation for an arbitrary operator $\hat{O}$. In the Markov approximation, namely when $\chi_j(\omega) = \sqrt{\gamma_j/(2\pi)}$, the Heisenberg equation for the operator $\hat{O}$ reads [14]:

$$\begin{aligned} \frac{\mathrm{d}}{\mathrm{d}t}\hat{O}(t) = \frac{i}{\hbar}[\hat{H}_{\mathrm{S}}, \hat{O}(t)] + \sum_j \gamma_j \Big(\hat{L}_j^\dagger \hat{O}(t)\hat{L}_j - \frac{1}{2}\{\hat{L}_j^\dagger \hat{L}_j, \hat{O}(t)\}\Big) \\ + \sum_j \sqrt{\gamma_j}\Big(\hat{b}_{\mathrm{in},j}^\dagger(t)[\hat{O}(t), \hat{L}_j] + \hat{b}_{\mathrm{in},j}(t)[\hat{L}_j^\dagger, \hat{O}(t)]\Big), \end{aligned} \tag{1.27}$$

where $\hat{b}_{\mathrm{in},j}(t) = \frac{1}{\sqrt{2\pi}} \int \mathrm{d}\omega e^{-i\omega(t-t_0)}\hat{b}_j(t_0,\omega)$. We notice that the first two terms of Eq. (1.27) are the same of the GKLS master equation in the Heisenberg picture in Eq. (1.13).

Now we consider the ground state $|0_\omega\rangle_{\rm E}$ of the thermal baths and define $\hat{\rho}_{\rm in} = |0_\omega\rangle_{\rm E}\langle 0_\omega|_{\rm E}$. In this way by defining $\mathbb{E}_{\rm Q}[\,\cdot\,] \equiv {\rm Tr}_{\rm E}(\hat{\rho}_{\rm in}\,\cdot\,)$ the following relation holds $\mathbb{E}_{\rm Q}[\hat{b}_j(\omega)\hat{b}_k^\dagger(\omega')] = {\rm Tr}_{\rm E}(\hat{\rho}_{\rm in}\hat{b}_j(\omega)\hat{b}_k^\dagger(\omega')) = \delta_{jk}\delta(\omega-\omega')$ and the mean values of the other combinations of two thermal baths operators are zero. We notice that if we define ${\rm d}\hat{B}_j(t) = \hat{b}_{{\rm in},j}(t){\rm d}t$, then by using this latter operator the only non zero mean value is

$$\mathbb{E}_{\rm Q}\Big[{\rm d}\hat{B}_j(t){\rm d}\hat{B}_k^\dagger(t)\Big] = \delta_{jk}{\rm d}t. \tag{1.28}$$

Thus in force of Eq. (1.28) the operator $\hat{B}_j(t)$ can be interpreted as the quantum generalization of a Wiener process [11, 12] and from Eq. (1.27) one can build the following quantum stochastic differential equation (QSDE) for the state vector $|\Psi(t)\rangle$ of the system plus environment

$$\begin{aligned}{\rm d}|\Psi(t)\rangle =&\Big[-\frac{i}{\hbar}\hat{H}_{\rm S}{\rm d}t + \sum_j \sqrt{\gamma_j}\left(\hat{L}_j\,{\rm d}\hat{B}_j^\dagger(t) - \hat{L}_j^\dagger\,{\rm d}\hat{B}_j(t)\right)\\ &-\sum_j\frac{\gamma_j}{2}\hat{L}_j^\dagger\hat{L}_j dt\Big]\,|\Psi(t)\rangle\,.\end{aligned} \tag{1.29}$$

Finally from Eq. (1.29), by assuming a factorized initial state $|\Psi(0)\rangle = |\psi(0)\rangle_S\,|0_\omega\rangle_E$, we can compute the master equation for the density matrix. For simplicity we consider a single Lindblad operator $\hat{L}$ with coefficient γ, the generalization to more Lindblad operators being straightforward. Starting from $\hat{\rho}_S = {\rm Tr}_{\rm E}(|\Psi\rangle\langle\Psi|)$ (where here $|\Psi\rangle \equiv |\Psi(t)\rangle$) we differentiate on both sides to get

$${\rm d}\hat{\rho}_S = {\rm Tr}_{\rm E}\big({\rm d}|\Psi\rangle\langle\Psi| + |\Psi\rangle{\rm d}\langle\Psi| + {\rm d}|\Psi\rangle{\rm d}\langle\Psi|\big). \tag{1.30}$$

Similarly to the case of classical noise, we retain the term ${\rm d}|\Psi\rangle{\rm d}\langle\Psi|$ in Eq.(1.30) because it contains terms of the form ${\rm d}\hat{B}_j(t){\rm d}\hat{B}_j^\dagger(t)$ for which we have $\mathbb{E}_Q\big[{\rm d}\hat{B}_j(t){\rm d}\hat{B}_j^\dagger(t)\big] = {\rm d}t$.

By using the expression for ${\rm d}|\Psi\rangle$, its conjugate for ${\rm d}\langle\Psi|$, and neglect-

ing terms of order $o(\mathrm{d}t^2)$ one gets

$$\begin{aligned}
\mathrm{d}\hat{\rho}_S = &-\frac{i}{\hbar}[\hat{H}_\mathrm{S}, \hat{\rho}_S]\mathrm{d}t - \frac{\gamma}{2}\{\hat{L}^\dagger\hat{L}, \hat{\rho}_S\}\mathrm{d}t + \sqrt{\gamma}\hat{L}\,\mathrm{Tr}_\mathrm{E}\big(\mathrm{d}\hat{B}^\dagger\,|\Psi\rangle\,\langle\Psi|\big) \\
&- \sqrt{\gamma}\hat{L}^\dagger\,\mathrm{Tr}_\mathrm{E}\big(\mathrm{d}\hat{B}\,|\Psi\rangle\,\langle\Psi|\big) + \sqrt{\gamma}\,\mathrm{Tr}_\mathrm{E}\big(|\Psi\rangle\,\langle\Psi|\mathrm{d}\hat{B}\big)\hat{L}^\dagger \\
&- \sqrt{\gamma}\,\mathrm{Tr}_\mathrm{E}\big(|\Psi\rangle\,\langle\Psi|\mathrm{d}\hat{B}^\dagger\big)\hat{L} + \gamma\hat{L}\,\mathrm{Tr}_\mathrm{E}\big(\mathrm{d}\hat{B}^\dagger\,|\Psi\rangle\,\langle\Psi|\mathrm{d}\hat{B}\big)\hat{L}^\dagger \\
&- \gamma\hat{L}\,\mathrm{Tr}_\mathrm{E}\big(\mathrm{d}\hat{B}^\dagger\,|\Psi\rangle\,\langle\Psi|\mathrm{d}\hat{B}^\dagger\big)\hat{L} - \gamma\hat{L}^\dagger\,\mathrm{Tr}_\mathrm{E}\big(\mathrm{d}\hat{B}\,|\Psi\rangle\,\langle\Psi|\mathrm{d}\hat{B}\big)\hat{L}^\dagger \\
&+ \gamma\hat{L}^\dagger\,\mathrm{Tr}_\mathrm{E}\big(\mathrm{d}\hat{B}\,|\Psi\rangle\,\langle\Psi|\mathrm{d}\hat{B}^\dagger\big)\hat{L} = \\
&= -\frac{i}{\hbar}[\hat{H}_\mathrm{S}, \hat{\rho}_S]\mathrm{d}t - \frac{\gamma}{2}\{\hat{L}^\dagger\hat{L}, \hat{\rho}_S\}\mathrm{d}t + \gamma\hat{L}\hat{\rho}_S\hat{L}^\dagger\mathrm{d}t
\end{aligned} \tag{1.31}$$

where we used the fact that $\mathrm{d}\hat{B}\,|\Psi\rangle = \mathrm{d}\hat{B}\hat{N}(t)\,|\Psi(0)\rangle = \\ = \hat{N}(t)\,|\psi(0)\rangle_S\mathrm{d}\hat{B}\,|0_\omega\rangle_E = 0$ at all times [15] (here $\hat{N}(t)\,|\Psi(0)\rangle$ is the solution of Eq.(1.29)) together with the ciclicity of the trace, which implies that the only term surviving is the second term in the second line, leading to the master equation in the GKLS form. We mention that this derivation is valid for a generic state $|\Psi\rangle$ of the system-environment as far as this state is evolved from an initial state which is factorized with the bath in the ground state i.e. $|\psi(0)\rangle_S\,|0_\omega\rangle_E$.

1.3 Decoherence in the framework of quantum computing

Quantum computing holds the potential to revolutionize computation, offering unmatched computational power to address complex problems across a wide range of high-impact fields. These include molecular and material simulations, optimization problems of interest to industries ranging from logistics to finance, and advancements in artificial intelligence, particularly in areas of machine learning and data analysis. In quantum computing, decoherence plays a key role in two main contexts: i) the quantum simulation of the GKLS dynamics and in general of open quantum systems; ii) the modeling and the classical simulation of the inherent noisy behaviour of quantum computers. In this Section we briefly explore the state of the art of i) and ii).

1.3.1 Quantum simulation of the GKLS dynamics

The primary and most immediate application envisioned for quantum computers is the simulation of quantum systems [16], particularly isolated systems that do not interact with an environment. This task has been extensively explored over the past three decades, resulting in the proposal of numerous quantum algorithms [17–22]. Furthermore, significant progress has been made in terms of the practical application of these algorithms on quantum devices: Presently, there exist several examples of successful quantum simulations, despite the inherent noise acting on these devices [23–25]. In light of this, the idea that quantum computers could be utilized to simulate open quantum systems has gained increasing interest in recent years. Endeavors in this direction primarily fall into two strands of research. The first one is based on the concept that, since quantum devices themselves are open systems subject to noise, one can harness the inherent noise of the computer to simulate open systems. Recent promising results have emerged in this domain, holding the potential for fruitful outcomes [26–28]. However, this approach is limited in that it can only simulate open systems described by the same master equation that characterizes the device, and building an adequate noise model of the device itself poses a significant challenge [29–33]. The second line of research is based on the notion that also for open systems efficient quantum algorithms are devised, without relying on the natural noise of the computer [34–39]. The work we present in Chapter 2 falls within the latter research line.

1.3.2 Noisy quantum computers: Standard approach

As powerful as they promise to be, quantum computers are still far from being ideal: since, as for any quantum system, they can hardly be isolated from the surrounding environment, they are prone to errors, which limit their capabilities. This stage of development is referred to as noisy intermediate-scale quantum (NISQ) era [40,41]. It is clear that NISQ computers require a good understanding of how noises affect quantum circuits and, in order to do so, a proper modeling of the noises is needed. This can be unlocked by understanding

the major sources of noise affecting the qubits, and writing better algorithms for simulating a given noise model on a classical computer. To date, the standard approach to simulate noisy digital gate-based quantum computers is based on adding appropriate quantum operations before and after each ideal gate [5, 42, 43]: schematically, and working with the density matrix formalism, if an ideal (unitary) gate $\hat{U}$ is supposed to be executed, the noises affecting it are modeled by adding appropriate Kraus maps (see Section 1.1.1) $\mathcal{E}_1$ ($\mathcal{E}_2$) mimicking the noise, before (after) the gate and independent from the latter:

$$\rho \;\text{—}\boxed{\mathcal{E}_1}\text{—}\boxed{\mathcal{U}}\text{—}\boxed{\mathcal{E}_2}\text{—}\; \rho' \;. \tag{1.32}$$

Such a modeling completely decouples the action of the controlled operation generating the unitary map $\mathcal{U}\hat{\rho} = \hat{U}\hat{\rho}\hat{U}^\dagger$ from that of the environment. This approximation works well if $\hat{U}$ acts almost instantaneously with respect to the noise, i.e. if the gate time t_g required to implement the gate is much smaller than the characteristic time scales of the system-environment interaction. For instance, in IBM's superconducting devices [44] $t_g \sim 10^{-8}s$, while typical environmental effects such as relaxation and phase damping have characteristic times of order $T_1, T_2 \sim 10^{-4}s$.
Here we report the main Kraus maps that are used in the standard approach and the main algorithms employed in classical simulations of noisy quantum computers based on state vector evolution. Then in Chapters 4 and 5 we present a new and alternative simulation approach.

State preparation and measurement (SPAM)

This kind of error is usually described as a bit-flip channel that acts on a single qubit [43]. Hence, its Kraus representation reads:

$$\mathcal{E}\hat{\rho} = (1-p)\hat{\rho} + p\hat{X}\hat{\rho}\hat{X}, \tag{1.33}$$

where $\hat{\rho}$ is the density matrix of a single qubit, $\hat{X}$ is the x-Pauli matrix and p is the probability of having a flip of the states of the computational basis.

Depolarization

Depolarization drives the qubit towards the maximally mixed state [43] and models incoherent gate infidelities. Its Kraus representation for a single qubit reads:

$$\mathcal{E}\hat{\rho} = \left(1 - \frac{3}{4}p\right)\hat{\rho} + \frac{p}{4}\hat{X}\hat{\rho}\hat{X} + \frac{p}{4}\hat{Y}\hat{\rho}\hat{Y} + \frac{p}{4}\hat{Z}\hat{\rho}\hat{Z}, \tag{1.34}$$

where $\hat{\rho}$ is the density matrix of a single qubit, $\hat{X}, \hat{Y}, \hat{Z}$ are the Pauli matrices and $p/4$ is the equal probability of having a bit flip, a phase flip or a bit and phase flip of the states of the computational basis. The generalization for an arbitrary number of qubits n is

$$\mathcal{E}\hat{\rho} = \left(1 - \frac{d^2-1}{d}p\right)\hat{\rho} + \frac{p}{d^2}\sum_{j\neq 0}^{d^2}\hat{\mathcal{P}}_j\hat{\rho}\hat{\mathcal{P}}_j = (1-p)\hat{\rho} + \frac{p}{d}\hat{\mathbb{I}}^{\otimes n}, \tag{1.35}$$

where $d = 2^n$ and $\hat{\mathcal{P}}_j$ are tensor products of Pauli matrices, called Pauli strings. Eqs. (1.34) and (1.35) describe a sort of symmetric depolarizing process due to the fact that the error probabilities associated to each Pauli string are the same. The most general case for n qubits is

$$\mathcal{E}\hat{\rho} = \sum_{j=0}^{d^2} p_j\hat{\mathcal{P}}_j\hat{\rho}\hat{\mathcal{P}}_j, \tag{1.36}$$

and it is called asymmetric depolarizing channel.

Amplitude and phase damping (Relaxation)

The amplitude-damping channel describes the decay $|1\rangle \to |0\rangle$ due to the interaction with the environment; on the other hand, phase-damping represents the process in which phase-coherences decay over time. Here we briefly call relaxation the combination of both effects. The Kraus representation is given by [42, 43]

$$\mathcal{E}\hat{\rho} = \hat{K}\hat{\rho}\hat{K} + p_1\hat{\sigma}^+\hat{\rho}\hat{\sigma}^- + p_z\hat{P}_1\hat{\rho}\hat{P}_1, \tag{1.37}$$

where we define

$$\hat{K} = \begin{pmatrix} 1 & 0 \\ 0 & \sqrt{1-p_1-p_z} \end{pmatrix}; \tag{1.38}$$

as usual, $\hat{\sigma}^+ = |0\rangle\langle 1|$, $\hat{\sigma}^- = |1\rangle\langle 0|$ and $\hat{P}_1 = |1\rangle\langle 1|$. Moreover, $p_1 = 1 - e^{-t/T_1}$ is the probability of amplitude damping, T_1 being

the relaxation time (the time it takes for the qubit to decay in the ground state), and $p_z = (1 - p_1)p_{pd}$, where $p_{pd} = 1 - e^{-t/T_{pd}}$ and $T_{pd} = T_1T_2/(2T_1 - T_2)$, T_2 being the decoherence time. We mention that the time scales T_1 and T_2 are related by $T_2 \leq 2T_1$.

Unravelling of Kraus maps

In general a Kraus map can be unraveled as a stochastic map on the state vector by imposing that, at a given time and given Kraus operators $\hat{K}_j$, the state $|\psi\rangle$ changes randomly as follows:

$$|\psi'\rangle = \frac{1}{\sqrt{p_j}} \hat{K}_j |\psi\rangle , \tag{1.39}$$

with probability:

$$p_j = | \langle\psi| \hat{K}_j^\dagger \hat{K}_j |\psi\rangle |^2. \tag{1.40}$$

The associate pseudo code is reported in Alg. 1.

Algorithm 1 KRAUS MAPS SIMULATION

Input: Initial state $|\psi_0\rangle$, a noiseless circuit $\mathrm{C} = \{\hat{U}^{(1)}, ..., \hat{U}^{(n_g)}\}$ composed by n_g gates $\hat{U}^{(i)}$ and number of samples N_s

for $0 \leq k \leq N_s$ **do**
  while $1 \leq i \leq n_g$ **do**
    compute $|\psi_k\rangle^{(i)} = \hat{U}^{(i)} |\psi_k\rangle^{(i-1)}$
    compute $p_j = | \langle\psi_k|^{(i)} \hat{K}_j^\dagger \hat{K}_j |\psi_k\rangle^{(i)} |^2$
    sample $\hat{K}_j$ operator from $\{p_j\}$
    update the state to $|\psi_k\rangle^{(i)} = \frac{1}{\sqrt{p_j}} \hat{K}_j |\psi_k\rangle^{(i)}$
  end
  compute $\hat{\rho}_k = |\psi_k\rangle^{(n_g)} \langle\psi_k|^{(n_g)}$
end

Output: $\hat{\rho}_f = \frac{1}{N_s} \sum_{k=1}^{N_s} \hat{\rho}_k$

The time complexity of Alg.1 is primarily determined by the matrix vector multiplication step, exhibiting a complexity of $\mathcal{O}(2^{2n})$, where n is the number of qubits. The space complexity is dominated by the storage of the state vector and it scales as $\mathcal{O}(2^n)$. It has to be noted that when the Kraus operators are not unitary, as for relaxation, one needs to store the intermediate state vectors, which are necessary in order to compute the probabilites in Eq.(1.40).

This operation has the same time and space complexity as those of the the previous step. This can be avoided for mixed unitary error channels: probabilities are known and independent of the current state.

Monte Carlo wave function method

Another state vector simulation method is based on the application of the quantum jumps SSE of Section 1.2.2, in particular Eq. (1.23). The algorithm is based on the Monte Carlo wave function method [45]. To simulate the noisy quantum computer evolution over the time period $[t_0, t_g]$, which corresponds to the duration required for a gate operation, we start with the system in the pure state $|\psi(t_0)\rangle$. A time step $\mathrm{d}t$ is selected such that it is smaller than the relevant time scales for the system's evolution within $[t_0, t_g]$. Given Lindblad operators $\hat{L}_j$ we define

$$\mathrm{d}p_j = \gamma_j \left\langle \hat{L}_j^\dagger \hat{L}_j \right\rangle_{t_0} \mathrm{d}t = \gamma_j \langle\psi(t_0)| \hat{L}_j^\dagger \hat{L}_j |\psi(t_0)\rangle \mathrm{d}t \,, \tag{1.41}$$

and

$$\hat{H}_{\text{eff}} = \hat{H} - i\hbar \sum_j \frac{\gamma_j}{2} \hat{L}_j^\dagger \hat{L}_j \,. \tag{1.42}$$

At each time step $\mathrm{d}t$, a random number ϵ is drawn from a uniform distribution over the interval $[0, 1]$. If $\epsilon < \sum_j \mathrm{d}p_j$, the system undergoes a jump to one of the states

$$|\psi_j\rangle = \frac{1}{||\hat{L}_j |\psi(t_0)\rangle\,||} \hat{L}_j |\psi(t_0)\rangle \;, \tag{1.43}$$

where $||\hat{L}_j |\psi(t_0)\rangle\,|| = \sqrt{\left\langle \hat{L}_j^\dagger \hat{L}_j \right\rangle_{t_0}}$. Specifically, it transitions to $|\psi_1\rangle$ if $0 < \epsilon < \mathrm{d}p_1$, to $|\psi_2\rangle$ if $\mathrm{d}p_1 < \epsilon < \mathrm{d}p_1 + \mathrm{d}p_2$, and so forth. Conversely, if $\epsilon > \sum_j \mathrm{d}p_j$, the system evolves to the state

$$|\psi_0\rangle = \frac{1}{\sqrt{1 - \sum_j \mathrm{d}p_j}} (\hat{\mathbb{I}} - \frac{i}{\hbar} \hat{H}_{\text{eff}} \mathrm{d}t) |\psi(t_0)\rangle \tag{1.44}$$

via the effective evolution operator. This process is repeated at every time step $\mathrm{d}t$, generating a quantum trajectory for the system evolution. The associated pseudo code is reported in Alg. 2.

Algorithm 2 QUANTUM JUMPS SIMULATION

Input: Initial state $|\psi_0\rangle$, a noiseless circuit $\mathrm{C} = \{\hat{U}^{(1)}, ..., \hat{U}^{(n_g)}\}$ composed by n_g gates $\hat{U}^{(i)}$, time step $\mathrm{d}t$ and number of samples N_s

for $0 \leq k \leq N_s$ **do**

  while $1 \leq i \leq n_g$ **do**

    while $dt \leq j \;\; dt \leq t_g$ **do**

      compute $\mathrm{d}p_l^{(i,j)} = \gamma_l^{(i)} \langle\psi_k((j-1)\mathrm{d}t)|^{(i)} \hat{L}_l^{(i)\dagger} \hat{L}_l^{(i)} |\psi_k((j-1)\mathrm{d}t)\rangle^{(i)} \mathrm{d}t$;

      sample a random number $0 < \epsilon < 1$;

      if $0 < \epsilon < dp_1^{(i,j)}$ **then**

        update the state to $|\psi_k(j\mathrm{d}t)\rangle^{(i)} = \frac{1}{||\hat{L}_1^{(i)}|\psi_k((j-1)\mathrm{d}t)\rangle^{(i)}||} \hat{L}_1^{(i)} |\psi_k((j-1)\mathrm{d}t)\rangle^{(i)}$

      else if $dp_1^{(i,j)} < \epsilon < dp_1^{(i,j)} + dp_2^{(i,j)}$ **then**

        update the state to $|\psi_k(j\mathrm{d}t)\rangle^{(i)} = \frac{1}{||\hat{L}_2^{(i)}|\psi_k((j-1)\mathrm{d}t)\rangle^{(i)}||} \hat{L}_2^{(i)} |\psi_k((j-1)\mathrm{d}t)\rangle^{(i)}$

      $\vdots$

      else

        update the state to $|\psi_k(j\mathrm{d}t)\rangle^{(i)} = \frac{1}{\sqrt{1-\sum_l \mathrm{d}p_l^{(i,j)}}} (\hat{\mathbb{I}} - \frac{i}{\hbar} \hat{H}_{\mathrm{eff}}^{(i)} \mathrm{d}t) |\psi_k((j-1)\mathrm{d}t)\rangle^{(i)}$

      end

    end

  end

  compute $\hat{\rho}_k = |\psi_k\rangle^{(n_g)} \langle\psi_k|^{(n_g)}$

end

Output: $\hat{\rho}_f = \frac{1}{N_s} \sum_{k=1}^{N_s} \hat{\rho}_k$

The time and space complexities of Alg. 2 are the same as those for Alg. 1, respectively $\mathcal{O}(2^{2n})$, where n is the number of qubits, and $\mathcal{O}(2^n)$. Similarly to the unraveling of Kraus maps, the state of the system must be stored in order to compute the probabilities in Eq. (1.41) and the normalization factors in Eq. (1.44) and Eq. (1.43).

1.4 Decoherence in the framework of spontaneous wave function collapse models

Models of spontaneous wavefunction collapse [8, 46, 47] represent a well established paradigm in the realm of quantum foundations, and constitute a strong figure of merit for the study of the macroscopic limits of quantum mechanics. Indeed, their investigation

finds motivation in the lack of observed quantum superpositions at the macroscopic scale: while quantum mechanics has proven highly successful in describing microscopic phenomena, it has yet to explain why macroscopic objects do not exhibit quantum superpositions although the theory predicts them. The key idea of collapse models is that quantum mechanics must be modified to explain the quantum-to-classical transition at macroscopic scales. The two most studied collapse models are the Diósi-Penrose (DP) model [48, 49] and the Continuous Spontaneous Localisation (CSL) model [50, 51].

1.4.1 Spontaneous collapse models

Spontaneous collapse models add suitably constructed phenomenological terms to the standard Schrödinger equation yielding a non-linear SSE. Their action can be seen as that of a noise field that leads to the collapse of the wavefunction. Depending on the specific collapse model, the origin of such a field can be either unknown or related to the gravitational field. These models introduce additional free parameters that control the collapse mechanism, and their validity is subject to experimental verification.
In the context of this thesis we work directly at the density matrix level. For a treatment of spontaneous collapse models at the level of SSE for the state vector we refer to [8, 46].
We start from the following master equation in the GKLS form

$$\frac{\mathrm{d}}{\mathrm{d}t}\hat{\rho} = -\frac{i}{\hbar}[\hat{H}, \hat{\rho}] + \mathcal{D}\hat{\rho}, \tag{1.45}$$

where $\hat{H}$ is the many-body Hamiltonian and $\mathcal{D}$ is a new term introducing the action of spontaneous collapse. For the latter, we consider a simple form corresponding to the spontaneous measurement of the second-quantised mass density $\hat{\mu}(\mathbf{x}) = m\hat{\psi}^\dagger(\mathbf{x})\hat{\psi}(\mathbf{x})$ with $\hat{\psi}(\mathbf{x})$ being the (fermionic) annihilation field-operator. Explicitly, it reads

$$\begin{aligned}\mathcal{D}\hat{\rho} &= -\frac{1}{2\hbar^2}\int\int \mathrm{d}^3x\mathrm{d}^3y D(\mathbf{x}-\mathbf{y})[\hat{\mu}(\mathbf{x}),[\hat{\mu}(\mathbf{y}),\hat{\rho}]] \\ &= \frac{1}{\hbar^2}\int \frac{\mathrm{d}^3k}{(2\pi)^3} D_{\mathbf{k}}\Big(\hat{\mu}_{\mathbf{k}}\hat{\rho}\hat{\mu}^\dagger_{\mathbf{k}} - \tfrac{1}{2}\{\hat{\mu}^\dagger_{\mathbf{k}}\hat{\mu}_{\mathbf{k}},\hat{\rho}\}\Big),\end{aligned} \tag{1.46}$$

where we introduced the Fourier transform of the kernel $D_{\mathbf{k}}$ showed in Eq. (1.47) and of mass density $\hat{\mu}_{\mathbf{k}} = m \int \frac{\mathrm{d}^3 q}{(2\pi)^3} \hat{a}^\dagger_{\mathbf{q}} \hat{a}_{\mathbf{q}+\mathbf{k}}$ with $\hat{a}_{\mathbf{q}}$ being the Fourier transform of $\hat{\psi}(\mathbf{x})$. Depending on the explicit space (or momentum) dependence of the kernel, one might want to introduce a short-length regularization, typically in the form of a Gaussian smearing of the field $\hat{\mu}(\mathbf{x})$. In the Fourier representation, a Gaussian smearing of scale σ takes a simple form for both the models (DP and CSL) we will consider:

$$D_{\mathbf{k}} = \exp\left(-\sigma^2 k^2\right) \times \begin{cases} 4\pi\hbar G/k^2 & \text{(DP)} \\ \hbar^2 \gamma & \text{(CSL)} \end{cases} \tag{1.47}$$

where $k = |\mathbf{k}|$. In the DP model, the decoherence rate is set by the Newton constant G and the kernel contains a $1/k^2$ factor in addition to the smearing prefactor. Using an alternative notation, $R_0 = \sigma$ is the spatial cutoff in the DP model and it is the only free parameter of the model. Current experimental bounds set the typical smearing at subatomic length-scales $\sigma \geq 5 \times 10^{-11}\,\mathrm{m}$ [52], although larger values can be also considered [53, 54]. On the other hand, the CSL model can be described in terms of two free parameters being $\lambda = \gamma m_0^2/(\sqrt{4\pi} r_{\mathrm{C}})^3$ and $r_{\mathrm{C}} = \sigma$, which are respectively the collapse rate and localization length of the model (m_0 is a reference mass chosen as that of a nucleon). Conversely to the DP model, the typically considered values of the spatial smearing are around $\sigma \simeq 10^{-7}\,\mathrm{m}$, well in the mesoscopic regime. A mapping between the two models can be introduced, and it is based on the simple relationship $D_{\mathrm{CSL}} = -\mathrm{const} \times \partial D_{\mathrm{DP}}/\partial(\sigma^2)$ between the two kernels. Consequently, the decoherence term of the CSL model can be obtained from the DP one through

$$\mathcal{D}_{\mathrm{CSL}} = -\frac{\hbar\gamma}{4\pi G} \frac{\partial \mathcal{D}_{\mathrm{DP}}}{\partial(\sigma^2)}. \tag{1.48}$$

The inverse integral relation can be also simply derived.

1.4.2 The heating problem

The smaller the cutoff σ, the larger the strength of the collapse effect and the spontaneous heating as well [55]. The latter implies a continuous increase of the kinetic energy for each particle. We elucidate this mechanism on a single point-like, free particle of mass

m and canonical variables $\hat{\mathbf{x}}$ and $\hat{\mathbf{p}}$. The corresponding heating power P, i.e. the time-derivative of the kinetic energy $\hat{H} = (\hat{\mathbf{p}}^2/2m)$, is obtained from the master equation (1.45):

$$P = \frac{\mathrm{d}}{\mathrm{d}t}\left\langle \hat{H} \right\rangle_t = \left\langle \mathcal{D}^\dagger \hat{H} \right\rangle_t = \frac{1}{2m}\left\langle \mathcal{D}^\dagger \hat{\mathbf{p}}^2 \right\rangle_t , \tag{1.49}$$

where $\mathcal{D}^\dagger$ is given by

$$\mathcal{D}^\dagger \hat{O} = \frac{1}{\hbar^2}\int \frac{\mathrm{d}^3 k}{(2\pi)^3} D_{\mathbf{k}} \left(\hat{\mu}_{\mathbf{k}}^\dagger \hat{O} \hat{\mu}_{\mathbf{k}} - \tfrac{1}{2}\{\hat{\mu}_{\mathbf{k}}^\dagger \hat{\mu}_{\mathbf{k}}, \hat{O}\} \right). \tag{1.50}$$

For the case under study, the mass density and its Fourier transform read

$$\hat{\mu}(\mathbf{x}) = m\delta(\mathbf{x} - \hat{\mathbf{x}}), \qquad \hat{\mu}_{\mathbf{k}} = m e^{i\mathbf{k}\hat{\mathbf{x}}}. \tag{1.51}$$

We insert $\hat{\mu}_{\mathbf{k}}$ in Eq. (1.50) and obtain the expression of the heating power

$$P = \frac{m}{2}\int \frac{\mathrm{d}^3 k}{(2\pi)^3} D_{\mathbf{k}} k^2. \tag{1.52}$$

where we used the identity

$$e^{-i\mathbf{k}\hat{\mathbf{x}}} f(\hat{\mathbf{p}}) e^{i\mathbf{k}\hat{\mathbf{x}}} = f(\hat{\mathbf{p}} + \hbar\mathbf{k}), \tag{1.53}$$

and the spherical symmetry of $D_{\mathbf{k}}$. We calculate the integral in Eq. (1.52) from Eq. (1.47) for both models:

$$P = -\frac{m}{2} D''(\mathbf{x})|_{\mathbf{x}=0} = \frac{1}{\sqrt{(2\pi)^3}} \begin{cases} 4\pi\hbar G/\sigma^3 & \text{(DP)} \\ 3\hbar^2\gamma/\sigma^5 & \text{(CSL)} \end{cases} \tag{1.54}$$

Hence, we get the following heating powers:

$$P^{\mathrm{DP}} = \frac{\hbar G m}{4\sqrt{\pi}\sigma^3}, \qquad P^{\mathrm{CSL}} = \frac{3m\hbar^2\gamma}{32\pi^{3/2}\sigma^5}, \tag{1.55}$$

which are related to each other in conformity with the mapping of Eq. (1.48).

To get an insight into the underlying effective mechanism, we consider the dynamics of the momentum $\hat{\mathbf{p}}$ in details, i.e. the dynamics of arbitrary functions $f(\hat{\mathbf{p}})$ of momentum. It could be shown that the Heisenberg equation of motion of $f(\hat{\mathbf{p}})$ is closed, this important feature has its parallel in the equivalent dynamics (1.45) of the state

$\hat{\rho}$. Insofar, since we are not interested in the dynamics of the coordinate $\hat{\mathbf{x}}$ but of $\hat{\mathbf{p}}$, we can start with the specific form $\hat{\rho} = \rho(\hat{\mathbf{p}})$ of the state[1], then consider its evolution under the Fourier representation of the dissipator in Eq. (1.46). The specific form $\rho(\hat{\mathbf{p}})$, diagonal in momentum basis, is preserved:

$$\frac{\mathrm{d}\rho(\hat{\mathbf{p}})}{\mathrm{d}t} = \frac{m^2}{\hbar^2}\int \frac{\mathrm{d}^3k}{(2\pi)^3} D_{\mathbf{k}}\Big(\rho(\hat{\mathbf{p}} - \hbar\mathbf{k}) - \rho(\hat{\mathbf{p}})\Big). \tag{1.56}$$

The result is a semi-classical single particle kinetic equation. The effect of dissipator $\mathcal{D}$ is equivalent to the random jumps $\hat{\mathbf{p}} \to \hat{\mathbf{p}} + \hbar\mathbf{k}$ in momentum at the isotropic probability rate

$$\frac{m^2}{\hbar^2}\frac{\mathrm{d}^3k}{(2\pi)^3} D_{\mathbf{k}}. \tag{1.57}$$

Since the kernel $D_{\mathbf{k}}$ contains the regularizing factor $\exp(-\sigma^2 k^2)$, the elementary momentum and energy transfers are in a bounded range. We introduce the characteristic bound of the elementary energy transfer, which reads

$$E_\sigma = \frac{\hbar^2}{4m\sigma^2}. \tag{1.58}$$

The quantity E_σ is important when, in Chapter 6, we balance the spontaneous heating by a new dissipative mechanism to reach a balance equation:

$$\frac{\mathrm{d}}{\mathrm{d}t}\left\langle \hat{H} \right\rangle_t = P - \Gamma \left\langle \hat{H} \right\rangle_t, \tag{1.59}$$

with a dissipation rate $\Gamma > 0$. In such a way, a finite asymptotic (equilibrium) energy $\left\langle \hat{H} \right\rangle_\infty = P/\Gamma$ is reached for $\mathrm{d}\left\langle \hat{H} \right\rangle_t / \mathrm{d}t = 0$, and the corresponding effective temperature T is defined by the equipartition theorem $\left\langle \hat{H} \right\rangle_\infty = \frac{3}{2} k_{\mathrm{B}} T$, where k_{B} is the Boltzmann constant.

The formalism presented in this section is used in Chapters 6 and 7 in order to respectively build and test a new dissipative extension of collapse models.

[1]From a mathematical standpoint, $\hat{\rho} = \rho(\hat{\mathbf{p}})$ cannot be considered a proper density matrix, because by expressing it in terms of the momentum eigenstates, it becomes proportional to a Dirac delta function. To address this issue with precision, the system should be confined to a finite volume, and an appropriate cut-off should be applied to the momentum values.

Chapter 2

A quantum algorithm to simulate open systems dynamics through the quantum noise formalism

Here we present an efficient algorithm for simulating open quantum systems dynamics described by the GKLS master equation (1.6) on quantum computers [56], addressing key challenges in the field of quantum simulation of the GKLS dynamics (see Section 1.3.1).

First, we show that it is always possible to drive the open system dynamics via a repetition of unitary gates applied to a set of n system qubits and crucially only a single ancillary bath qubit, representing the environment. As such, the ancilla overhead is always equal to 1, meaning that it does not scale with the number n of qubits neither, in the case of m-locality of the Lindblad operators, with m. For a comparison, among state of the art implementations, some methods [34–39] use a number of ancillary qubits that scales polynomially with large n; our method provides a polynomial improvement, for large n, with respect to them. For other methods [57] the number of ancillary qubits scales exponentially with m; in this case we provide an exponential improvement. The price to pay is stochasticity, i.e. multiple realizations of the quantum circuit, which however is preferable because the sampling overhead does not scale with the number of qubits.

Second, given a fixed accuracy, for small system-environment coupling constants, the approximations that we use allows to implement a number of Trotter steps which is smaller than those required other approaches [36, 37, 58], implying a reduction of the circuit depth.

2.1 Approximate solution of the QSDE

Our approach is based on the quantum noise formalism [13–15], that we introduced in Section 1.2.3. The QSDE in Eq. (1.29) acting on the full system-environment space is linear meaning that knowing the state at time t, the state at time $t + \Delta t$ is given by

$$|\Psi(t + \Delta t)\rangle = \hat{N}(\Delta t)\,|\Psi(t)\rangle\,, \tag{2.1}$$

where $\hat{N}(\Delta t)$ is a matrix which is also unitary, thus implementable on a quantum computer. As we show in Appendix A.1, the unitary evolution $\hat{N}(\Delta t)$ in Eq.(2.1) can be obtained by resorting to perturbative techniques [11], as Eq. (1.29) in general is not solvable in a closed form. This leads to the following approximate expression

$$\begin{aligned} \hat{N}(\Delta t) &= \hat{U}(\Delta t)\mathrm{T}\Big[e^{\sum_k \sqrt{\gamma_k}\hat{S}_k(\Delta t)}\Big] \\ &\simeq \hat{U}(\Delta t)\prod_k e^{\sqrt{\gamma_k}\hat{S}_k(\Delta t)}, \end{aligned} \tag{2.2}$$

where $\hat{U}(\Delta t)$ is the closed system evolution operator, $\mathrm{T}[\cdot]$ is the time ordering operator and the stochastic terms $\hat{S}_k(t)$ are defined as

$$\hat{S}_k(\Delta t) = \int_t^{t+\Delta t}\Big(\hat{L}_k(s)d\hat{B}_k^\dagger(s) - \hat{L}_k^\dagger(s)d\hat{B}_k(s)\Big), \tag{2.3}$$

and $\hat{L}_k(s) = \hat{U}^\dagger(s-t)\hat{L}_k\hat{U}(s-t)$ are the Lindblad operators in interaction picture.

Under this approximation by computing $\hat{\rho}_S(t+\Delta t) = \mathrm{Tr}_E\left(\hat{N}(\Delta t)\right.$ $\left.|\Psi(t)\rangle\,\langle\Psi(t)|\,\hat{N}^\dagger(\Delta t)\right)$ one recovers the following final density matrix of the system (see [56] for a derivation)

$$\hat{\rho}_S(t+\Delta t) \simeq \hat{U}(\Delta t)\left(\hat{\rho}_S(t) + \int_t^{t+\Delta t}\mathrm{d}s\mathcal{D}(s)\hat{\rho}_S(t)\right)\hat{U}^\dagger(\Delta t) \tag{2.4}$$

where $\mathcal{D}(s)\hat{\rho}_S(t) = \sum_k \gamma_k\Big(\hat{L}_k(s)\hat{\rho}_S(t)\hat{L}_k^\dagger(s) - \frac{1}{2}\big\{\hat{L}_k^\dagger(s)\hat{L}_k(s), \hat{\rho}_S(t)\big\}\Big)$.

2.1.1 Upper bound on the approximation error

The approximate expression in Eq. (2.4) leads to an approximation error due to the perturbative expansion

$$\begin{aligned}\varepsilon_p = \Big\| &\hat{U}(\Delta t)\mathrm{T}\big[e^{\int_t^{t+\Delta t}\mathrm{d}s\mathcal{D}(s)}\big]\hat{U}^\dagger(\Delta t) \\ &- \hat{U}(\Delta t)\Big(\hat{\mathbb{I}} + \int_t^{t+\Delta t}\mathrm{d}s\mathcal{D}(s)\Big)\hat{U}^\dagger(\Delta t)\Big\|_{1\to 1}\end{aligned} \tag{2.5}$$

where we use the $1 \to 1$ superoperator norm [34, 57] and $\mathrm{T}[\,\cdot\,]$ is the time ordering operator. ε_p is quantified in Appendix A.2 by assuming a m-locality condition, namely by considering the decomposition of $\mathcal{D}(s)$ into $\mathcal{D}(s) = \sum_j^K \mathcal{D}_j(s)$ where each $\mathcal{D}_j(s)$ acts non trivially on a subset of $m < n$ qubits. Then each $\mathcal{D}_j(s)$ has a maximum of $2^{2m} - 1$ Lindblad operators. For simplicity we assume that all parameters γ_k have the same order of magnitude $\gamma_k = \gamma$. Thus, the approximation error is bounded by

$$\varepsilon_p \leq 2e\Big(K(2^{2m}-1)\max_k \big\|\hat{L}_{k,j}\big\|_\infty^2 \gamma\Delta t\Big)^2, \tag{2.6}$$

where e is the Euler number and $K(2^{2m}-1)$ is the total number of Lindblad operators which scales polynomially with the number of the system qubits n: $K \sim \mathcal{O}(n^m)$ (see Appendix A.2).

2.2 Finite representation of the bath operators

If we wish to simulate the evolution given by Eq. (2.1) on quantum computers, a problem arises in terms of how to represent the terms $\mathrm{d}\hat{B}_k(t)$ and $\mathrm{d}\hat{B}_k^\dagger(t)$, which are operators acting on an infinite dimensional Hilbert space. To overcome this difficulty we proceed as follows: we assume that at every given time Δt the system interacts only with a small portion of the bath, and being the bath of infinite dimension, the portion with which the system is interacting changes at each time step. Effectively we couple the system with a single ancillary qubit, representing a part of the bath, evolve the full state for Δt and then reset the bath qubit to the ground state. This last step can be seen as changing the part of the bath connected to the system (see Fig. 2.2.1).

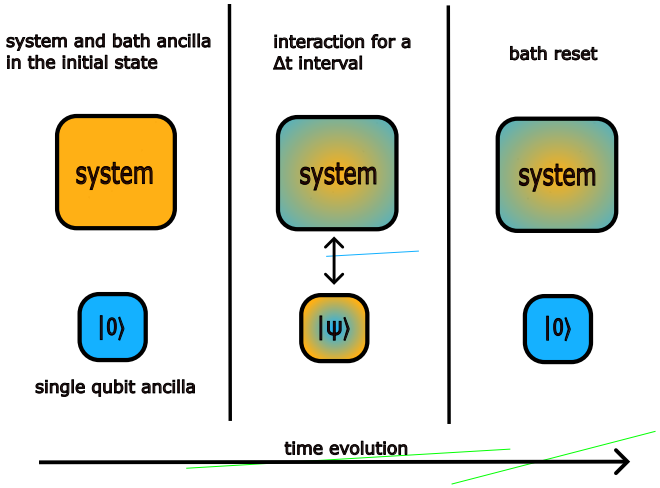

Figure 2.2.1: Schematic picture of the three main steps of the protocol: preparation of the system and bath qubit in the initial state; system-bath interaction for a time Δt; reset of the bath qubit. In order to obtain the total evolution at a given time T, the last two steps have to be repeated $N_{steps} = T/\Delta t$ times.

This idea corresponds to selecting the following finite representation for the bath operators

$$\mathrm{d}\hat{B}_k(t) \to \hat{\sigma}_E^- \mathrm{d}W_k(t), \quad \mathrm{d}\hat{B}_k^\dagger(t) \to \hat{\sigma}_E^+ \mathrm{d}W_k(t), \tag{2.7}$$

where $\hat{\sigma}_E^- = |0\rangle_E \langle 1|_E$, $\hat{\sigma}_E^+ = |1\rangle_E \langle 0|_E$ and $\mathrm{d}W_k(t)$ are classical Wiener processes. By using the latter definitions and applying the following prescriptions

1. Substitute $\mathbb{E}_{\mathrm{Q}}[\,\cdot\,]$ with $\mathbb{E}_{\mathrm{C}}[\mathrm{Tr}_{\mathrm{E}}(\hat{\rho}_{\mathrm{in}}\,\cdot\,)]$, where $\mathbb{E}_C[\,\cdot\,]$ is the average over classical stochastic processes and $\hat{\rho}_{\mathrm{in}} = |0\rangle_E\langle 0|_E$ is the ground state of the bath qubit,

2. At each time step Δt the state is factorized as $|\Psi\rangle = |\psi\rangle_S |0\rangle_{\mathrm{E}}$,

3. The density matrix of the system has to be computed as $\hat{\rho}_S = \mathbb{E}_C[\mathrm{Tr}_{\mathrm{E}}(|\Psi\rangle \langle\Psi|)]$,

one reproduces Eq. (1.28) and the GKLS master equation in Eqs. (1.6) and (1.10). This proves that for a generic $\hat{H}_S$ and generic Lindbald operators a single bath qubit is enough to reproduce the open dynamics. The complete derivation of the master equation is in Appendix A.3. Prescription 2 follows directly from the fact that in the finite dimensional representation the bath qubit must be reset after each time step to preserve Markovianity; the first

and the third prescriptions are required to average over classical stochastic processes, thus to obtain the right result.
By assuming the finite representation (2.7) of the bath operators the stochastic terms in Eq. (2.3) become

$$\hat{S}_k(\Delta t) = \int_t^{t+\Delta t} \Big(\hat{L}_k(s)\hat{\sigma}_E^+ - \hat{L}_k^\dagger(s)\hat{\sigma}_E^- \Big) \mathrm{d}W_k(s). \tag{2.8}$$

For convenience we define $\hat{J}_k(s) \equiv \hat{L}_k(s)\hat{\sigma}_E^+ - \hat{L}_k^\dagger(s)\hat{\sigma}_E^-$. The real $[\hat{S}_k(\Delta t)]_{ij}^R$ and imaginary part $[\hat{S}_k(\Delta t)]_{ij}^I$ of the entries of the operators $\hat{S}_k(\Delta t)$ in Eq. (2.8) are Itô integrals of deterministic functions $[\hat{S}_k(\Delta t)]_{ij}^\lambda = \int_t^{t+\Delta t} \mathrm{d}W_k(s) [\hat{J}_k(s)]_{ij}^\lambda$ for $\lambda = R, I$, that represent Gaussian stochastic processes with means zero $\mathbb{E}\big[[\hat{S}_k(\Delta t)]_{ij}^\lambda\big] = 0$, variances $\mathbb{V}\big[[\hat{S}_k(\Delta t)]_{ij}^\lambda\big] = \int_t^{t+\Delta t} \mathrm{d}s ([\hat{J}_k(s)]_{ij}^\lambda)^2$ and covariances $\mathbb{E}\big[[\hat{S}_k(\Delta t)]_{ij}^\lambda [\hat{S}_k(\Delta t)]_{i'j'}^{\lambda'}\big] = \int_t^{t+\Delta t} \mathrm{d}s [\hat{J}_k(s)]_{ij}^\lambda [\hat{J}_k(s)]_{i'j'}^{\lambda'}$. In a quantum simulation once all the variances and covariances are computed, the stochastic processes can be sampled to get a single realization of the evolution $\hat{N}(\Delta t)$. Finally by averaging over all the realizations of the final state $\hat{\rho}_S(t+\Delta t) = \mathbb{E}_C[\mathrm{Tr}_E\left(\hat{N}(\Delta t)\,|\Psi(t)\rangle\,\langle\Psi(t)|\,\hat{N}^\dagger(\Delta t)\right)]$, in accordance with the prescriptions, one obtains the same final density matrix in Eq. (2.4).

2.3 Algorithm implementation

In Alg. 3 we now describe the algorithmic implementation of the approach. We notice that when $\hat{H}_S = \sum_{\alpha=1}^K \hat{H}_\alpha$, with $[\hat{H}_\alpha, \hat{H}_\beta] \neq 0$, then at point 2 of Alg. 3 one can apply the first order Trotter-Suzuki product formula $\hat{U}(s-t) \simeq \prod_{\alpha=1}^K e^{-\frac{i}{\hbar}\hat{H}_\alpha(s-t)}$ [59]. Since for relevant applications each $\hat{H}_\alpha$ is m-local, then by plugging the latter expression in Eq. (2.2), all the resulting terms have a locality that depends on m but not on n. Indeed, the Lindblad operators in general are strings of operators with the structure $\hat{L}_k = \hat{l}_k^{(\alpha)} ... \hat{l}_k^{(\beta)}$ where α, β are integer numbers, $\hat{l}_k^{(q)}$ with $q \in [1, ..., \alpha, ..., \beta, ..., n]$ are generic single-qubit operators applied to the q-th qubit. In the case of m-locality of the GKLS equation, the number of $\hat{l}_k^{(q)}$ in $\hat{L}_k$ is $m < n$. Thus, by using $\hat{U}(\Delta t) \simeq \prod_\alpha e^{-\frac{i}{\hbar}\hat{H}_\alpha \Delta t}$, each operator $\hat{L}_k(s) = \hat{U}^\dagger(s-t)\hat{L}_k\hat{U}(s-t)$ in Eq. (2.2) has a fixed locality, since $\hat{L}_k$ acts on a set $\mathbb{A}$ of m qubits, then all the terms in $\hat{U}$ that act on a

Algorithm 3

Input: A GKLS equation with system Hamiltonian $\hat{H}_S$ and a set of m-local Lindblad operators; a number $\mathcal{N}_r$ of samples to be performed.

Protocol:

1. Trotterize the unitary evolution of the closed system $\hat{U}(T) = e^{-\frac{i}{\hbar}\hat{H}_S T}$ in Δt time steps as $\hat{U}(T) = \prod_j^{N_{\text{step}}} \hat{U}(\Delta t)$ where $T = N_{\text{step}}\Delta t$.

2. Compute $\hat{N}(\Delta t)$ corresponding to $\hat{U}(\Delta t)$ by using Eq. (2.2) in the finite representation of Sec. 2.2;

3. Apply $\prod_j^{N_{\text{step}}} \hat{N}(\Delta t)$ making sure to reset the ancilla qubit after the application of each $\hat{N}(\Delta t)$.

4. Repeat the resulting quantum circuit of point 3 by sampling $\mathcal{N}_r$ times the stochastic processes inside each $\hat{N}(\Delta t)$.

Output: Final probabilities computed by taking the average over all $\mathcal{N}_r$ circuit realizations.

set of qubits disjoint from $\mathbb{A}$, do not contribute in the expression for $\hat{L}_k(s)$. As a result, if we assume for simplicity that the Hamiltonians $\hat{H}_\alpha$ have the same locality m of the Lindblad operators $\hat{L}_k$, then the locality of $\hat{L}_k(s)$ depends only on m and not on n (in general if the locality of $\hat{H}_\alpha$ is $l \neq m$ then the locality of $\hat{L}_k(s)$ depends on m and l).

Given the analysis of the perturbative approximation of Sec. 2.1, in Appendix A.4 we prove that each $\hat{N}(\Delta t)$ contributes with an error $\varepsilon \leq \varepsilon_T + \varepsilon_p$, where ε_p is defined in Eq. (2.5) and ε_T is the error due to the first order Trotter-Suzuki product formula, upper bounded by

$$\varepsilon_T \leq \left(K J \max_{\alpha,j} \left\| \hat{h}_{\alpha,j} \right\|_\infty \omega \Delta t \right)^2, \tag{2.9}$$

where ω is the strength of the Hamiltonian $\hat{H}_S$, assuming for simplicity that the frequencies of each $\hat{H}_\alpha$ have the same order of magnitude and $\hat{H}_\alpha = \omega \sum_{j=1}^{J}, \hat{h}_{\alpha,j}$ where J is a constant whose value depends on the system Hamiltonian under study and $\hat{h}_{\alpha,j}$ are generic m-local operators. Thus the global approximation error for the total time T is $\varepsilon_{global} = N_{step}\, \varepsilon$ which by using Eqs. (2.6) and (2.9) is upper

bounded by

$$\varepsilon_{global} \leq \frac{T^2K^2}{N_{step}}\left(J^2\omega^2 \max_{\alpha,j}\left\|\hat{h}_{\alpha,j}\right\|_\infty^2 + (2^{2m}-1)^2\gamma^2 \max_{k,j}\left\|\hat{L}_{k,j}\right\|_\infty^4\right). \tag{2.10}$$

This bound is polynomial in the system qubits number n as $K \sim \mathcal{O}(n^m)$.
Additionally, we show in [56] that the algorithm works also for higher order of the Trotter-Suzuki product formula, improving the upper bound on ε_T in Eq. (2.9).

2.4 Resources estimation

In the following section we estimate the resources needed to implement the algorithm.

2.4.1 Number of gates and of trotter steps

In order to simulate the dynamics up to time T making an error not greater than ε_{global}, our algorithm needs

$$\begin{aligned} \mathrm{N}_G &\propto \left\lceil \left(KJ + K(2^{2m}-1) + 1\right)\frac{T^2K^2(\gamma^2+\omega^2)}{\varepsilon_{global}} \right\rceil \\ &\sim \mathcal{O}\left(\left\lceil \frac{n^{4m}T^2(\gamma^2+\omega^2)}{\varepsilon_{global}} \right\rceil\right) \end{aligned} \tag{2.11}$$

total number of gates. In Eq. (2.11) KJ is the number of gates to implement $\hat{U}(\Delta t)$, that is polynomial in n for m-local Hamiltonians. The term $K(2^{2m}-1)$ counts the number of gates needed to implement the product in Eq. (2.2), where K scales polynomially with n. The term $+1$ counts the reset of the ancillary qubit. Thus, $\mathrm{N}_G = \mathrm{poly}(n, \gamma T, \omega T, 1/\varepsilon_{global})$ and therefore our algorithm is efficiently simulatable on a quantum computer [57].
The advantage of our protocol is that it is based on a perturbative expansion of the environment coupling constants. We provide an approximate solution of the GKLS equation (Eq. (2.4)) which is more accurate (closer to the exact formal solution of the GKLS equation in interaction picture $\hat{\rho}_S(t+\Delta t) = \hat{U}(\Delta t)\mathrm{T}\left[e^{\int_t^{t+\Delta t} \mathrm{d}s\mathcal{D}(s)}\right]\hat{\rho}_S(t)\hat{U}^\dagger(\Delta t)$)

in the interval Δt than just

$$\hat{\rho}_S(t+\Delta t) = \hat{\rho}_S(t) + \Big(-\frac{i}{\hbar}[\hat{H}_S, \hat{\rho}_S(t)] + \mathcal{D}\hat{\rho}_S(t)\Big)\Delta t, \tag{2.12}$$

that is used in the majority of approaches. Thus, given a fixed target accuracy ε_{global}, when the perturbative expansion holds ($\gamma << \omega$) our approximation reduces the number of total time steps required to reach the final time T with respect to Eq. (2.12). This is also confirmed by the panel (a) in Fig. 2.5.2. For these reasons, given a fixed accuracy, our approximation (see Eqs. (2.2) and (2.4)) allows to implement a number of trotter steps which is smaller than those required in other approaches [36,37,58], implying a reduction of the circuit depth.
We mention that when the characteristic times of the environmental noise and of the system Hamiltonian evolution become comparable, i.e. $\gamma \sim \omega$, the perturbative approach is not justified anymore. In this regime, Eq. (2.4) reduces to Eq. (2.12) and the stochastic exponents in $\hat{N}(\Delta t) \simeq \hat{U}(\Delta t)\prod_k e^{\sqrt{\gamma_k}\hat{S}_k(\Delta t)}$ become $\sqrt{\gamma}_k \hat{J}_k W_k(\Delta t)$, where $\hat{J}_k \equiv \hat{L}_k\hat{\sigma}_E^+ - \hat{L}_k^\dagger\hat{\sigma}_E^-$. As $W_k(\Delta t)$ have variances Δt, our algorithm resembles a stochastic implementation of the algorithm proposed in [36,37] with the significant difference that in our case the system-environment interaction is mediated by a single ancillary qubit regardless of the total number of the system Lindblad operators.

2.4.2 Ancilla overhead

In general our ancilla overhead is constant and is always equal to one, thus of order $\mathcal{O}(1)$, as shown above, while many of the state of the art implementations [34–39] have an ancilla overhead proportional to the number of Lindblad operators thus in general of order $\mathcal{O}(2^{2n}-1)$ where n is the number of system qubits or, assuming a m-locality condition, of order $\mathcal{O}(n^m)$, or if the implementation is based on the vectorization of the density matrix, of order $\mathcal{O}(n)$. Other methods, such as the one presented in [57], are able to use the same set of 2^{2m} ancillary qubits for every m-local term in the Lindbladian, i.e. an asymptotic overhead of order $\mathcal{O}(1)$. However these methods need a number of ancillary qubits that is exponential

in the m-locality, while our algorithm always need a single ancilla regardless of both n and m. Already in the most simple case of m = 2, the algorithms in [57] need 16 ancillas versus 1 ancilla of our method. This is a relevant achievement especially in the NISQ era.

2.4.3 Sampling error

Finally, our approach needs to evaluate multiple circuits due to the sampling of the stochastic processes and this leads to a sampling error on the evaluation of expectation values of an m-local observable $\hat{O}$ given by $\eta \sim \mathcal{O}(1/\sqrt{\mathcal{N}_r})$ with $\mathcal{N}_r$ the total number of samples of the classical stochastic processes. Thus η does not scale with the size of the system. We give further details on η in Appendix A.5.

2.5 Proof of concept

We now provide a proof of concept of the effectiveness of the approach. We consider a toy model dynamics of a single spin under external magnetic field with system Hamiltonian $H_S = \frac{\hbar\Omega}{2}\hat{X}$ with $\Omega = \pi/6\,\mathrm{MHz}$ and Lindblad operators $\hat{L}_1 = \hat{\sigma}^+$, $\hat{L}_2 = \hat{\sigma}^-$ and $\hat{L}_3 = \hat{Z}$ driven by the same parameter $\gamma = 0.1\,\mathrm{kHz}$. The isolated dynamics of the system can be implemented by a single-qubit x-rotation $\hat{R}_x(\theta)$ in time steps Δt where $\theta = \Omega\Delta t$. First we compute the trace distances [42] $\mathcal{T}^{(QN)} = \mathcal{T}(\hat{\chi}(T), \hat{\rho}^{(QN)}(T))$ and $\mathcal{T}^{(SA)} = \mathcal{T}(\hat{\chi}(T), \hat{\rho}^{(SA)}(T))$ where $\hat{\chi}(T)$ is the analytic solution of the GKLS equation, $\hat{\rho}^{(QN)}(T)$ is obtained with our approximation in Eq.(2.4) that from now on we call quantum noise (QN) approximation, $\hat{\rho}^{(SA)}(T)$ is obtained with the approximation $\hat{\rho}_S(t+\Delta t) = \hat{\rho}_S(t) + \big(-\frac{i}{\hbar}[\hat{H}_S, \hat{\rho}_S(t)] + \mathcal{D}\hat{\rho}_S(t)\big)\Delta t$, that from now on we call standard approximation (SA). We fix the total evolution time $T = 30\,\mu\mathrm{s}$ for different values of Δt. In Fig.2.5.2(a) we plot the results. The red and blue curves are respectively the trends of $\mathcal{T}^{(SA)}$ and $\mathcal{T}^{(QN)}$ for different values of $\gamma\Delta t$. The theoretical upper bound for QN computed in Appendix A.2 is reported as a blue dashed line and the theoretical upper bound for SA as a red dashed line, computed by using the formula in [36]. Notably, for $\gamma\Delta t \sim 10^{-4}$, $\mathcal{T}^{(QN)} \sim 10^{-7}$ while $\mathcal{T}^{(SA)} \sim 10^{-1}$. To reach the same precision of QN the SA needs

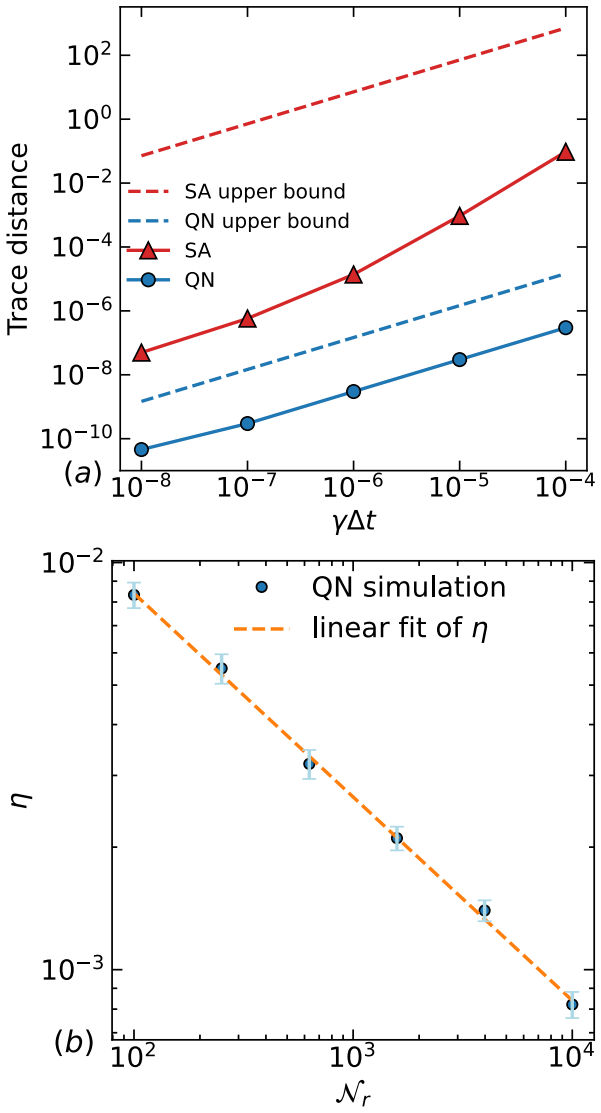

Figure 2.5.2: Evolution of a single spin under external magnetic field and in contact with a thermal bath with coupling constant $\gamma = 0.1\,\text{kHz}$, for a total time $T = 30\,\mu\text{s}$. Panel (a) displays in blue the trace distance $\mathcal{T}^{(QN)}(T)$ between the exact solution of the GKLS equation and the quantum noise (QN) approximation in Eq. (2.4) as a function of $\gamma\Delta t$ and in red the trace distance $\mathcal{T}^{(SA)}(T)$ between the exact solution of the GKLS equation and the standard approximation (SA). As one can see, to reach the same precision of QN, the SA needs $N_{step}^{(SA)} \sim 10^5$ against $N_{step}^{(QN)} \sim 10^1$, implying that the resulting depth for SA is four orders magnitude larger than for QN. The blue dashed line reports the theoretical upper bound for QN computed in Appendix A.2, while the red dashed line is the theoretical upper bound for SA, computed by using the formula in [36]. The blue dots in panel (b) are the values of $\eta = |\langle\hat{Z}\rangle - \langle\hat{Z}\rangle_{\mathcal{N}_r}|$ for the observable $\hat{Z}$ where $\langle\hat{Z}\rangle$ is the true expected value and $\langle\hat{Z}\rangle_{\mathcal{N}_r}$ is the estimate with $\mathcal{N}_r$ total number of realizations obtained by simulating Alg. 3 with fixed $\Delta t = 10^{-6}$ s, $\gamma = 0.1$ kHz and for different number of realizations $\mathcal{N}_r$. Each point is the mean over 100 independent simulations, and the vertical bars show the standard deviations of the means. The orange dashed line is a fit for the sampling error, showing that $\eta \sim \mathcal{O}(1/\sqrt{\mathcal{N}_r})$.

$\gamma\Delta t \sim 10^{-8}$, meaning that Δt has to be reduced by four orders of magnitude and consequently $N_{step}^{(SA)} \sim 10^5$ against $N_{step}^{(QN)} \sim 10^1$.
The blue dots in Fig. 2.5.2 (b) are the values of $\eta = |\langle \hat{Z} \rangle - \langle \hat{Z} \rangle_{\mathcal{N}_r}|$ for the observable $\hat{Z}$ obtained by simulating Alg. 3 with fixed $\Delta t = 10^{-6}$ s, $\gamma = 0.1$ kHz and for different number of realizations $\mathcal{N}_r$. Each point is the mean over 100 independent simulations, vertical bars are the standard deviations of the means. The orange dashed line is a linear fit in log-log scale of the data, giving angular coefficient $\simeq -1/2$, showing that the behaviour of the sampling error is $\eta \sim \mathcal{O}(1/\sqrt{\mathcal{N}_r})$. By taking larger $\mathcal{N}_r$ one can reach a precision consistent with the one of the rightmost point of the blue curve in Fig. 2.5.2 (a), that corresponds to the same choice of parameters Δt and γ. This requires a huge number of samples, but it is a consequence of the simple toy model of a single system qubit interacting with an environment, for which the approximation error is very small. When considering systems with high number of qubits, since the approximation error scales with $\sim n^{2m}$, a limited number of realizations $\mathcal{N}_r$ is required to reach the accuracy of the approximation error.
Finally we simulated classically Alg. 3 applied to the problem of the energy transfer dynamics in molecular systems. In particular we considered the following Hamiltonian for a linear chain of two molecules

$$\hat{H}_S = -\sum_{k=0}^{1} \frac{E_k}{2} \hat{Z}_k + \frac{J_{0,1}}{2} \Big(\hat{X}_0 \hat{X}_1 + \hat{Y}_0 \hat{Y}_1 \Big), \tag{2.13}$$

where each molecule has only two energy levels encoded in the qubits computational states. All the chosen parameters are dimensionless. The values of the energy gaps are $E_0 \simeq 773.5$, $E_1 \simeq 770.3$. The interactions coupling reads $J_{0,1} = 3.2$. The dissipator of the GKLS equation we used is

$$\mathcal{D}\hat{\rho}_S = \sum_{k=0}^{15} \gamma_k \Big(\hat{\mathcal{P}}_k \hat{\rho}_S \hat{\mathcal{P}}_k - \hat{\rho}_S \Big), \tag{2.14}$$

where $\hat{\mathcal{P}}_k$ are two-qubits Pauli strings and the values of γ_k are listed in [56]. The initial state of the two qubits is $|10\rangle$. We chose $\Delta t = 5 \times 10^{-2}$ with $N_{step} = 40$, and a number of shots $\mathcal{N}_r = 100$. In Fig. 2.5.3 we show the evolution of the diagonal entries of the density

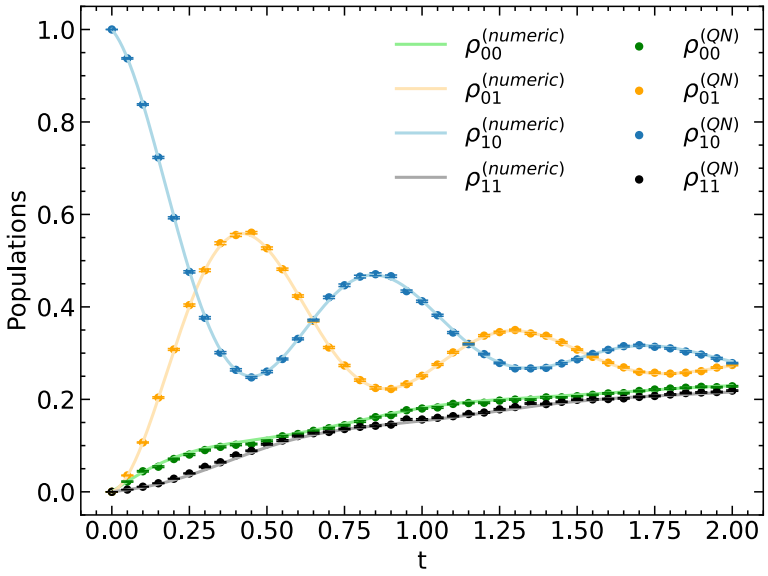

Figure 2.5.3: Evolution of the diagonal entries of the density matrix describing the energy transfer between two molecules represented by two qubits. The results of our algorithm are shown in dots, while those obtained by numerically solving the GKLS equation are shown with solid lines. The initial state of the two qubits is $|10\rangle$. All the chosen parameters are dimensionless. The values of the energy gaps are $E_0 \simeq 773.5$, $E_1 \simeq 770.3$. The interactions coupling reads $J_{0,1} = 3.2$. We chose $\Delta t = 5 \times 10^{-2}$ with $N_{step} = 40$, and a number of shots $\mathcal{N}_r = 100$. The values of γ_k are listed in [56].

matrix. Solid lines are numeric solutions while dots are obtained with our algorithm. The good agreement between the two confirm the validity of the method.

2.6 Conclusions

We have presented an algorithm based on the quantum noise formalism tailored for the efficient simulation of open quantum systems on quantum devices. Our approach allows to use a single ancilla qubit of the bath independently of the system size marking a substantial reduction in the total number of circuit qubits. Moreover our approximation, for small environment coupling constants, permits to reduce the total number of steps while maintaining the desired accuracy. For bigger values of the environment coupling constants, our approach still works and converges to the standard first order solution in Δt. Moreover, in principle, the accuracy can be improved by expanding the approximation to higher orders, see Appendix A.1.

As future work we expect to apply the algorithm on real quantum computers paired with error mitigation techniques to reduce the impact of the inherent noise of the devices. We will also explore the possibility of introducing non-Markovian effects by relaxing the prescription of resetting the bath qubit after each gate in the time step.

Chapter 3

The impact of inherent noise on quantum algorithms: A case study

The algorithm presented in the previous chapter is an example of a quantum algorithm that should run on a quantum hardware. However, as quantum hardware is highly susceptible to the interaction with the environment, understanding the effects of noise in quantum circuits becomes crucial [41]. For this reason, in the following chapter we study the impact of inherent noise on quantum algorithms through numerical simulations of noisy quantum circuits. In particular we focus on a Variational Quantum Eigensolver (VQE) [60] to detect phase transitions through the energy level crossing technique [61].

Exploring phase transitions is crucial for understanding the fundamental behavior of matter [62]. These transitions are usually identified by analyzing order parameters that describe specific phase changes. However, accurate estimates of transition points require large systems approaching the thermodynamic limit, which typically is highly computationally expensive. An alternative approach involves utilizing level spectroscopy [63–65]. In this framework, the ground state phase transition is detected by the energy level crossings of low-lying excited states. Indeed, if the quantum numbers of the ground state do not change across the phase transition, but those of the low-energy excited states do change, then a correspondence between excited energy level crossings and the phase transitions is expected [66–69]. For several one-dimensional models this mapping is well established. Moreover, it seems to be a promising approach also for two-dimensional spin systems [70–72]. The ben-

efit of this method lies in its insensitivity to system size, enabling highly accurate predictions of the phase transition point even with small clusters.

Here we introduce a variational Ansatz adequate for the implementation on quantum devices to detect the transition by exploiting level spectroscopy. In particular, we focus on the J_1-J_2 Heisenberg model on a chain, where level crossing has been successfully applied with classical methods. The Hamiltonian of the model reads

$$\hat{H}_{J_1\text{-}J_2} = J_1 \sum_{r=1}^{N} \hat{\boldsymbol{S}}_r \cdot \hat{\boldsymbol{S}}_{r+1} + J_2 \sum_{r=1}^{N} \hat{\boldsymbol{S}}_r \cdot \hat{\boldsymbol{S}}_{r+2} \ , \tag{3.1}$$

where $\hat{\boldsymbol{S}}_r = (\hat{S}^x_r, \hat{S}^y_r, \hat{S}^z_r)$ is the spin 1/2 operator at site r and $J_1, J_2 \geq 0$ are the antiferromagnetic couplings between nearest and next-nearest neighbors sites, respectively. For $J_2 = 0$ the model in Eq. (3.1) reduces to the one-dimensional Heisenberg model and the ground-state properties can be computed using the Bethe Ansatz [73]. However, when $J_2 > 0$ there are no exact solutions. Still, its phase diagram is well established by numerical and analytical calculations [74, 75]. On one hand, the detection of the phase transition transition is especially complicated by the direct computation of an order parameter. Indeed, large size effects are present and a huge number of sites is necessary to give a meaningful estimation of the phase transition point [74–77]. On the other hand, by employing level spectroscopy, a small number of sites ($N \sim 30$) is sufficient to achieve a very accurate estimation [63].

The eigenstates of the Hamiltonian in Eq. (3.1) can be classified according to the total spin S^2 and the momentum k, respectively the quantum numbers of $\hat{\boldsymbol{S}}^{\boldsymbol{2}}$, where $\hat{\boldsymbol{S}} = \sum_{r=1}^{N} \hat{\boldsymbol{S}}_r$, and of the one-site translation operator $\hat{\mathcal{T}}$ (assuming periodic boundary conditions). The transition point can be detected as the energy level crossing between the first singlet ($S^2 = 0$) and triplet ($S^2 = 1$) excited states with momentum π with respect to the ground state. We point out that defining spin symmetric states is difficult with classical methods such as Tensor Network and Neural Network Quantum States [78–81]. These approaches typically restrict computations to the S^z symmetry sectors [72, 77, 82–88]. The effectiveness of preparing translational- and spin-equivariant quantum circuits, combined with the level spectroscopy technique on small clusters, makes the

problem suitable for quantum computers, even in the near-term.

In this scenario, we devise an equivariant variational quantum circuit [89–92] preserving both total spin and translational symmetry, optimized through the Variational Quantum Eigensolver (VQE) [60]. The latter is a hybrid quantum-classical algorithm based on the variational principle. Importantly, the variational principle can be extended beyond approximating ground state properties to describe low-lying excited states as well. For instance, this can be achieved by constructing suitable variational states where specific symmetry sectors can be specified [72, 76, 83, 93, 94]. In this work, we explore this possibility focusing on the variational approximation of the excited states of the J_1-J_2 Heisenberg model in Eq. (3.1). However, our approach can be suitably extended to handle other Hamiltonians, and it results particularly valuable to treat those that conserve total spin.

The sensitivity of our algorithm to noise is evaluated through numerical simulations of noisy quantum circuits. Despite the explicit breaking of variational state symmetries in the presence of noise [95], we demonstrate that by integrating standard error mitigation techniques, such as Zero Noise Extrapolation (ZNE) [96], we can successfully restore the desired physical properties.

3.1 Variational Ansatz

Given a Hamiltonian $\hat{H}$, the VQE offers a method to approximate its eigenstates by exploiting the variational principle, which involves minimizing the variational energy $E_\theta = \langle \Psi_\theta | \hat{H} | \Psi_\theta \rangle$. Here, $|\Psi_\theta\rangle$ constitutes a variational state depending on θ, a vector of parameters. In the VQE framework, the Ansatz is represented as a quantum circuit identified by a unitary transformation $\hat{U}_\theta$ acting on an initial state $|\phi\rangle$, such that $|\Psi_\theta\rangle = \hat{U}_\theta |\phi\rangle$. In this study, we utilize a quantum circuit based on the Hamiltonian Variational Ansatz (HVA) [60,97], which proved to be effective for approximating quantum many-body eigenstates [89, 98–103]. The HVA approach involves introducing a set of auxiliary Hamiltonians $\hat{H}_1, \hat{H}_2, \ldots, \hat{H}_M$ such that $\left[\hat{H}_m, \hat{H}_{m'}\right] \neq 0 \ \forall m \neq m'$. The variational state is then

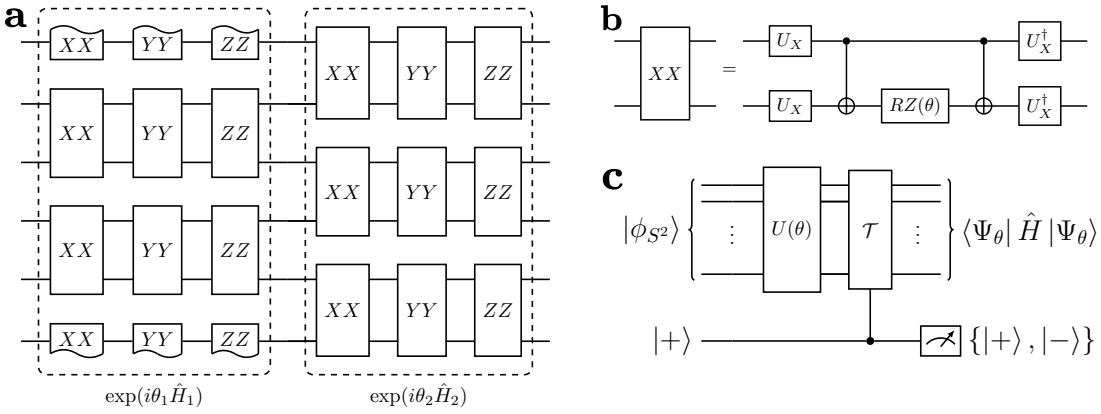

Figure 3.1.1: **a)** Implementation of a single layer of the quantum circuit defined in Eq. (3.5) of the main text. This circuit consists of 2-local rotations, such as XX, which denotes the unitary $\exp\left(i\theta \hat{S}^x_r \otimes \hat{S}^x_{r+1}\right)$ and similarly for YY and ZZ. **b)** Implementation of the 2-local rotation XX. It includes two CNOTs, a RZ rotation and diagonalizing gates U_X, defined by $\hat{U}^\dagger_X \hat{S}^x_r \hat{U}_X = \hat{S}^z_r$. The implementation is analogous for the gates YY and ZZ. **c)** Circuit used to perform symmetrization by LCU, where a controlled $\hat{\mathcal{T}}$ is added to $\hat{U}_\theta$ to symmetrize $|\Psi_\theta\rangle$.

expressed as:

$$|\psi_\theta\rangle = \prod_{l=1}^{L} e^{-i\theta^l_M \hat{H}_M} \dots e^{-i\theta^l_2 \hat{H}_2} e^{-i\theta^l_1 \hat{H}_1} |\phi\rangle \ , \tag{3.2}$$

where the initial state $|\phi\rangle$ is typically identified as a low-energy eigenstate of one of the auxiliary Hamiltonians $\hat{H}_m$ ($m > 1$). The number of variational parameters in the HVA approach is $M \cdot L$ and the accuracy of the variational state is mainly determined by the number of layers L.

In the HVA framework, the standard practice is to require that $\sum_{m=1}^{M} \hat{H}_m = \hat{H}$. However, we relax this constraint while still maintaining a connection between $\sum_{m=1}^{M} \hat{H}_m$ and $\hat{H}$. Indeed, our focus lies on the symmetry properties of the auxiliary Hamiltonians.

The simplest way to define a non-trivial variational state $|\Psi_\theta\rangle$ is to consider a set of $M = 2$ auxiliary Hamiltonians $\hat{H}_1$ and $\hat{H}_2$. As a result, the unitary operator takes the following form:

$$\hat{U}_\theta = \prod_{l=1}^{L} e^{i\theta^l_2 \hat{H}_2} e^{i\theta^l_1 \hat{H}_1} \ . \tag{3.3}$$

For the J_1-J_2 Heisenberg model in Eq. (3.1), one way to define $\hat{H}_1$ and $\hat{H}_2$ is to observe that the nearest-neighbor term $\sum_r \hat{\boldsymbol{S}}_r \cdot \hat{\boldsymbol{S}}_{r+1}$

can be decomposed into the sum of two contributions $\hat{H}_{\text{even}} = \sum_{r=1}^{N/2} \hat{\boldsymbol{S}}_{2r-1} \cdot \hat{\boldsymbol{S}}_{2r}$ and $\hat{H}_{\text{odd}} = \sum_{r=1}^{N/2} \hat{\boldsymbol{S}}_{2r} \cdot \hat{\boldsymbol{S}}_{2r+1}$. Additionally, the ground state of $\hat{H}_{\text{even}}$ is a product state of singlet pairs, and its excited states can be constructed by replacing a singlet pair with a triplet one (see Sec. 3.1.1). Therefore, we set $\hat{H}_2 = \hat{H}_{\text{even}}$, and choose the state $|\phi\rangle$ to be an appropriate eigenstate of $\hat{H}_{\text{even}}$. Subsequently, the most natural choice for the other term is $\hat{H}_1 = \hat{H}_{\text{odd}}$, since $[\hat{H}_{\text{even}}, \hat{H}_{\text{odd}}] \neq 0$ (see [61] for a discussion about an alternative choice of $\hat{H}_1$ and $\hat{H}_2$). Since the Hamiltonians $\hat{H}_1$ and $\hat{H}_2$ are defined as sums of commuting terms, the unitary operator $\hat{U}_\theta$ in Eq. (3.3) becomes

$$\hat{U}_\theta = \prod_{l=1}^{L} \prod_{r=1}^{N/2} e^{i\theta_2^l \hat{\boldsymbol{S}}_{2r-1} \cdot \hat{\boldsymbol{S}}_{2r}} \prod_{q=1}^{N/2} e^{i\theta_1^l \hat{\boldsymbol{S}}_{2q} \cdot \hat{\boldsymbol{S}}_{2q+1}} \ . \tag{3.4}$$

Furthermore, considering the definition $\hat{\boldsymbol{S}}_{2r-1} \cdot \hat{\boldsymbol{S}}_{2r} = \sum_\alpha \hat{S}^\alpha_{2r-1} \hat{S}^\alpha_{2r}$ where $\alpha = x, y, z$, it is worth noting that $[\hat{S}^\alpha_{2r-1} \hat{S}^\alpha_{2r}, \hat{S}^\beta_{2r-1} \hat{S}^\beta_{2r}] = 0$, and similarly for $\hat{\boldsymbol{S}}_{2r} \cdot \hat{\boldsymbol{S}}_{2r+1}$. Consequently, we can rewrite Eq. (3.4) without any approximation:

$$\hat{U}_\theta = \prod_{l=1}^{L} \prod_{r=1}^{N/2} \prod_{\alpha} e^{i\theta_2^l \hat{S}^\alpha_{2r-1} \hat{S}^\alpha_{2r}} \prod_{q=1}^{N/2} \prod_{\beta} e^{i\theta_1^l \hat{S}^\beta_{2q} \hat{S}^\beta_{2q+1}} \ . \tag{3.5}$$

The last step is crucial as it enables the implementation of each layer of $\hat{U}_\theta$ in constant depth relative to the number of qubits N. In fact, $\hat{U}_\theta$ in Eq. (3.5) is the composition of 2-local gates, many of which can be executed simultaneously (see Fig. 3.1.1a and Fig. 3.1.1b). Note that in Fig. 3.1.1b we show a straightforward implementation of the two local gates. Alternatively, optimized decompositions that reduce the number of required CNOT gates, as proposed in Refs. [104, 105], can also be implemented.

3.1.1 Symmetries of the variational state

An effective strategy for approximating excited states involves constructing variational states with definite quantum numbers, thereby energy minimizations are performed within specific symmetry sectors. In order to detect the phase transition point in the J_1-J_2 Heisenberg model, we need to fix both the momentum k and the total spin S^2. As a result $|\Psi_\theta\rangle$ should be invariant with respect to the

operators $\hat{\boldsymbol{S}}^{\boldsymbol{2}}$ and $\hat{\mathcal{T}}$. Given $|\Psi_\theta\rangle = \hat{U}_\theta |\phi\rangle$, if the initial state $|\phi\rangle$ lies in a definite symmetry sector and the unitary operator $\hat{U}_\theta$ preserves that symmetry (i.e., it is equivariant), then the resulting variational state $|\Psi_\theta\rangle$ can effectively estimate low-energy excitations. Regarding the total spin, each rotation $e^{i\theta \hat{\boldsymbol{S}}_j \cdot \hat{\boldsymbol{S}}_k}$ in Eq. (3.4) is equivariant under spin symmetry, namely $[\hat{\boldsymbol{S}}^{\boldsymbol{2}}, e^{i\theta \hat{\boldsymbol{S}}_j \cdot \hat{\boldsymbol{S}}_k}] = 0 \ \forall j, k$. Therefore, to restrict the optimization to a specific spin sector, it suffices to choose $|\phi\rangle$ with a definite S^2 quantum number.
The singlet state ($S^2 = 0$) is implemented as the ground state of $\hat{H}_2$

$$|\phi_0\rangle = \prod_{r=1}^{N/2} |s\rangle_{2r-1,2r} \ , \tag{3.6}$$

where $|s\rangle_{r,r'} = (|0\rangle_r |1\rangle_{r'} - |1\rangle_r |0\rangle_{r'})/\sqrt{2}$ is a singlet pair. Similarly, the triplet state ($S^2 = 1$) can be constructed as the first excited state of $\hat{H}_2$ by replacing in Eq. (3.6) a singlet pair with a triplet one $|t\rangle_{r,r'} = (|0\rangle_r |1\rangle_{r'} + |1\rangle_r |0\rangle_{r'})/\sqrt{2}$. Thus we can select as initial state either of the following $N/2$ degenerate states

$$\left|\tilde{\phi}_1^j\right\rangle = |t\rangle_{2j-1,2j} \prod_{r=1, r\neq j}^{N/2} |s\rangle_{2r-1,2r} \ , \tag{3.7}$$

where $j = 1, \ldots, N/2$. Concerning translational invariance, while the Hamiltonian $\hat{H}_{J_1\text{-}J_2}$ in Eq. (3.1) preserves one-site translations, the unitary operator $\hat{U}_\theta$ does not. However, the Hamiltonians $\hat{H}_1$ and $\hat{H}_2$ are equivariant under translations of two lattice sites, meaning $[\hat{H}_1, \hat{\mathcal{T}}^2] = [\hat{H}_2, \hat{\mathcal{T}}^2] = 0$. Consequently, by sharing the variational parameters across different qubits [see Eq. (3.5)], we easily achieve $[\hat{U}_\theta, \hat{\mathcal{T}}^2] = 0$. The latter condition leads us to consider a simple way to restore the one-site symmetry, which is necessary to fix the momentum k in the variational state. This involves defining initial states $|\phi\rangle$ that possess translational invariance over two lattice sites. Notably, the state $|\phi_0\rangle$ in Eq. (3.6) already exhibits this symmetry, while the states $\left|\tilde{\phi}_1^j\right\rangle$ in Eq. (3.7) lack it. However, we can prepare a superposition of $\left|\tilde{\phi}_1^j\right\rangle$ states as

$$|\phi_1\rangle = \frac{1}{\sqrt{N/2}} \sum_{j=1}^{N/2} \left|\tilde{\phi}_1^j\right\rangle \ , \tag{3.8}$$

implying $\hat{\mathcal{T}}^2 |\phi_1\rangle = |\phi_1\rangle$ (for a detailed discussion on the quantum circuit implementation of $|\phi_0\rangle$ and $|\phi_1\rangle$ refer to Appendix B.1. At this point, full translational invariance can be recovered using Linear Combination of Unitaries (LCU) [106], as described below.

3.1.2 Symmetrization by Linear Combination of Unitaries (LCU)

Given a variational state $|\Psi_\theta\rangle$ satisfying $\hat{\mathcal{T}}^2 |\Psi_\theta\rangle = |\Psi_\theta\rangle$, we define the following linear combination to represent normalized, translationally invariant states:

$$\left|\Psi_\theta^{\pm}\right\rangle = \frac{|\Psi_\theta\rangle \pm \hat{\mathcal{T}} |\Psi_\theta\rangle}{|| \, |\Psi_\theta\rangle \pm \hat{\mathcal{T}} |\Psi_\theta\rangle \, ||} \, , \tag{3.9}$$

Here, $\left|\Psi_\theta^{+}\right\rangle$ and $\left|\Psi_\theta^{-}\right\rangle$ correspond to states with momentum $k = 0$ and $k = \pi$, respectively. In the following discussion, we show how to implement the symmetrized state in Eq. (3.9) as a quantum circuit, making use of the Linear Combination of Unitaries (LCU) technique [106].

The latter method allows the preparation of normalized states in the form $|\Phi\rangle \propto \hat{\Gamma} |\Phi_0\rangle$, given a normalized initial state $|\Phi_0\rangle$ and a general linear combination of unitaries $\hat{\Gamma} = \sum_{a=0}^{A-1} c_a \hat{U}_a$. Since $\hat{\Gamma}$ is non unitary, the procedure succeeds only with a certain probability, which is related to the normalization constant of $\hat{\Gamma} |\Phi_0\rangle$. To achieve this goal, it is necessary to unitarize $\hat{\Gamma}$, a process that involves introducing $\lceil \log_2(A) \rceil$ ancillary qubits, followed by a projection.

Focusing on the translational symmetry, given a state invariant under A-site translations, namely $\hat{\mathcal{T}}^A |\Phi_0\rangle = |\Phi_0\rangle$, symmetrizing it necessitates $\hat{\Gamma} = \sum_{a=0}^{A-1} e^{ika} \hat{\mathcal{T}}^a$, where $k = 2\pi n/A$ with $n = 0, \ldots, A-1$ (see [61] for further details). This procedure requires a logarithmic number of ancillary qubits $\lceil \log_2(A) \rceil$ and $O(A \cdot N)$ quantum operations independently of the state $|\Phi_0\rangle$. Moreover, as this procedure succeeds only with a fixed probability, it may involve a sampling overhead. Nevertheless, it can be shown (see [61]) that the average probability of success across various initializations of the variational parameters is approximately $1/A$, with corrections of order $O(2^{A-N})$. This suggests that, at the beginning of the optimization, the sampling overhead is expected to scale linearly with A (assuming $N \gg A$).

In our case, we implement Eq. (3.9) by choosing $A = 2$, $|\Phi_0\rangle = \hat{U}_\theta |\phi\rangle$ and $\hat{\Gamma} = \hat{\mathbb{I}} + \hat{\mathcal{T}}$. Consequently, only one ancilla is required, regardless of the system size N. The corresponding circuit is schematically illustrated in Fig. 3.1.1c. First, we prepare the ancilla in the $|+\rangle$ state. Then, we apply a controlled version of $\hat{\mathcal{T}}$. Finally, the projection is performed by measuring the ancilla in the $\{|+\rangle, |-\rangle\}$ basis. Depending on the measurement outcome, the computational register is prepared in either $\left|\Psi_\theta^+\right\rangle$ or $\left|\Psi_\theta^-\right\rangle$ states. Thus, by post-selecting the appropriate measurement results from the ancillary qubit, both momenta ($k = 0$ or $k = \pi$) can be obtained using just one circuit[1]. Additionally, we mention that other symmetrization approaches, based on classical post-processing, are possible but may require a higher number of circuit evaluations [89].
While effective in the ideal case, a posteriori symmetrization procedures (like those discussed in this Section) are are notably sensitive to errors arising from noise [107,108]. Hence, in the following we investigate the impact of small perturbations on the quantum circuit (see Sec. 3.2 and Sec. 3.4).

3.2 Noise and mitigation

As mentioned in Section 1.3.2, quantum devices are susceptible to noise, leading to errors during quantum computation. These errors arise from interactions of qubits with the environment [5,109]. Here we present the noise model that we used to simulate our VQE in the presence of ineherent noise. It is based on the standard approach described in Section 1.3.2.

3.2.1 Noise model

Accurately modeling incoherent errors is challenging [29–31]. Here, we define a simple noise model that captures only 1-local errors, allowing to examine how small perturbations affect the symmetries of the variational state. This noise model is implemented as quantum channels $\mathcal{E}_\tau$, in the Kraus form of Section 1.1.1, which generally

[1] In [61] we discuss both the computational cost of LCU to restore translational symmetry on a two-site translationally invariant state and to enforce a generic discrete symmetry.

depend on the gate time τ. The most common models include depolarization $\mathcal{E}_\tau^D$ and relaxation $\mathcal{E}_\tau^R$, which are applied after each gate in the quantum circuit (see Section 1.3.2) [42, 43]. Both maps induce single-qubit decoherence. However, the fixed points of the two maps differ, thus introducing competing effects. On the one hand, single-qubit depolarization tends to bring the state towards $\hat{\mathbb{I}}/2$, namely the maximally mixed one. On the other hand, thermal relaxation tends to bring the state to $|0\rangle\langle 0|$. Here, we choose to combine the two as $\mathcal{E}_\tau = \mathcal{E}_\tau^D \circ \mathcal{E}_\tau^R$. Furthermore, we neglect cross talks and correlated noises [110] implying that the total channel associated to m-qubit gates is $\mathcal{E}_\tau^{\otimes m}$, i.e., the tensor product of the single-qubit one. In Appendix B.2 we show a schematic depiction of the nosie model.
Together with errors arising from the gate execution, readout errors are also present during the measurement procedure at the end of computation [111]. However, we neglect this error source, since highly effective techniques such as T-REX [112], capable of mitigating these errors, are already accessible on current quantum devices [44]. Moreover, since such quantum devices can only implement a specific set of universal gates (see Appendix B.2), to conduct numerical simulations that are more faithful to the real hardware, we transpiled our algorithm accordingly.

3.2.2 Zero Noise Extrapolation (ZNE)

In the noise model outlined previously, the quantum channels $\mathcal{E}_\tau$ depend on the gate time τ and the error probabilities, associated to each channel, increases with τ (see Appendix B.2). This parameter can be theoretically adjusted to control the noise level, a manipulation that can also be realized experimentally through various techniques [96, 113, 114]. This allows to perform Zero Noise Extrapolation (ZNE) [96], an error mitigation strategy suitable for expectation value estimations. In this approach, the expectation value is computed with increasing noise levels (i.e., the gate time τ), in order to extrapolate the ideal result in the zero-noise limit (i.e., $\tau \to 0$). Generally, the introduction of noise explicitly breaks the symmetries of the Ansatz [95], implying possibly wrong estimations of the low-lying excited energies. To counteract this ef-

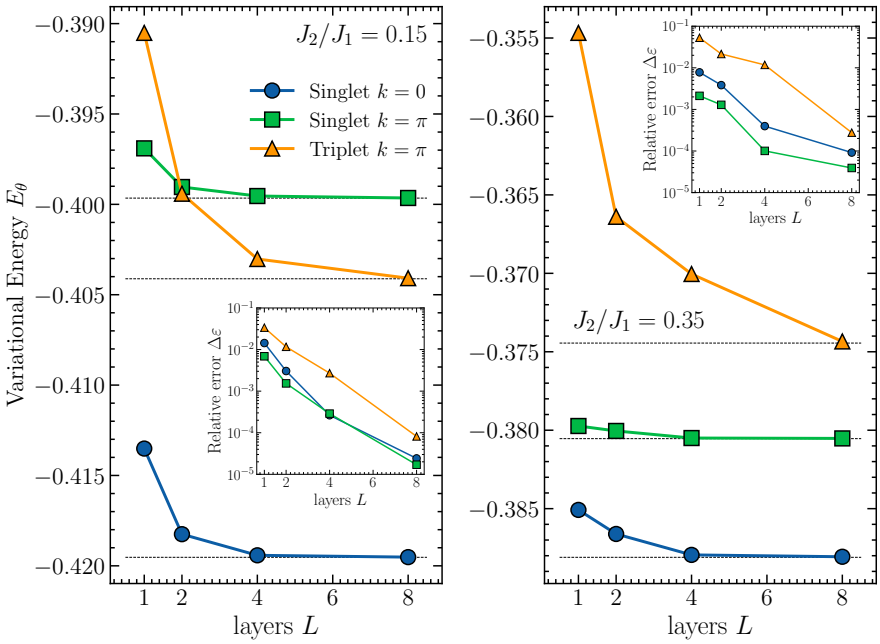

Figure 3.2.2: The variational energy for a cluster of $N = 16$ sites as a function of the number of layer $L = 1, \ldots, N/2$ for $J_2/J_1 = 0.15$ (left panel) and $J_2/J_1 = 0.35$ (right panel). The exact energies are also reported as dotted lines in both panels. The corresponding relative error $\Delta\varepsilon = |E_\theta - E_{\text{ex}}|/E_{\text{ex}}$ with respect to the exact energies is reported as insets as a function of L.

fect we modify the VQE cost function with a penalty term which favours variational states lying in the correct symmetry sector. By exploiting the optimizer to mitigate the noise-induced effects on the symmetries of the Ansatz, in combination with ZNE, we accurately recover the zero-noise limit.

3.3 Noiseless Numerical Results

In the following we examine the results obtained in the noiseless scenario by performing numerical state-vector simulations (PennyLane's `lightning.qubit` backend [115]). Specifically, we investigate how the accuracy of the variational state can be systematically enhanced by increasing the number of layers L in the circuit across the different symmetry sectors.

We focus on a cluster of $N = 16$ qubits for two frustration ratios: $J_2/J_1 = 0.15$ (gapless phase) and $J_2/J_1 = 0.35$ (gapped phase). In Fig. 3.2.2 we show the dependence of the variational energies with respect to the number of layers L of the circuit. The optimizations

are carried out fixing the quantum numbers of total spin S^2 (singlet or triplet) and momentum ($k = 0, \pi$). For both frustration ratios, the ground state is a singlet ($S^2 = 0$) with $k = 0$. The first excited state before the phase transition ($J_2/J_1 = 0.15$, left panel) is a triplet state ($S^2 = 1$) with momentum $k = \pi$. Then, after the transition ($J_2/J_1 = 0.35$, right panel), it becomes a singlet state ($S^2 = 0$) with momentum $k = \pi$. The situation is reversed for the second excited state.

For both frustration ratios, the relative error of the states compared to the exact ones [64, 116] is of order $\Delta\varepsilon \approx 0.01\%$ for a number of layers $L = N/2$ [102] (see insets in Fig. 3.2.2). We observe that the convergence of the triplet state is slower compared to the singlet case (see Fig. 3.2.2). However, by reaching $L = N/2$, the accuracy is of the same order of magnitude for both cases. The accurate results obtained before and after the transition suggest that the variational state accurately captures the transition point through the crossing of excited states.

3.4 Noisy Numerical Results

The introduction of noise in the circuit modifies the performance of the Ansatz. In this section we investigate the impact of the noise model (see Sec. 3.2) on the symmetries of the variational state. We show that it is possible to mitigate errors through ZNE combined with the introduction of a suitable penalty term in the cost function. Here, we focus on a system of $N = 4$ sites using a circuit with $L = 1$ layer. Indeed, for such a small cluster one layer is sufficient to get accurate estimations in the noiseless limit. Using as reference current IBM superconducting devices [44], the single-qubit gate time is $t_g \approx 3.5 \times 10^{-8}$ s. For this reason, variational optimizations are performed setting $\tau = t_g$ (see Sec. B.2). Regarding mitigation, we dub *ZNE region* the gate-time interval attainable to perform ZNE on current quantum hardware (i.e. from $\tau = t_g$ up to $\tau \approx 3t_g$). All numerical simulations are performed by employing a density matrix simulator (PennyLane's `default.mixed` backend [115]).

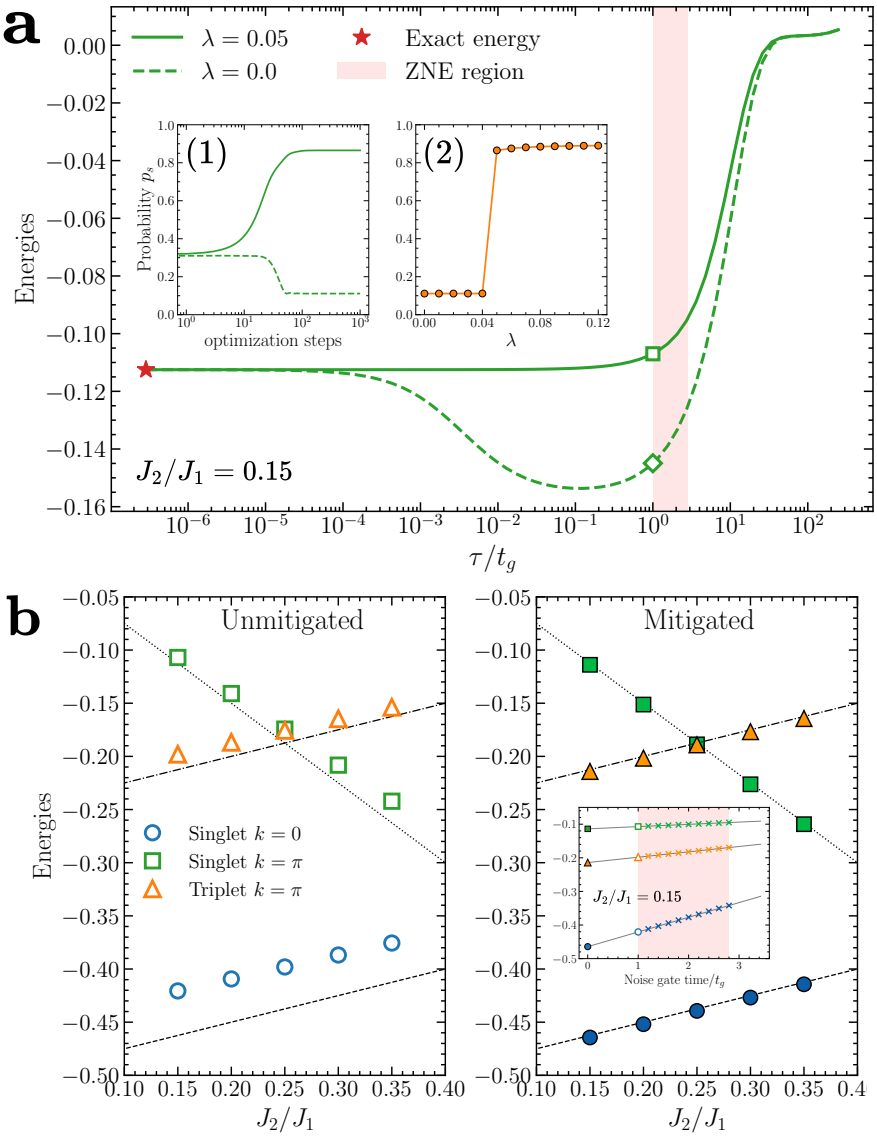

Figure 3.3.3: **a)** Variational energies for $S^2 = 0$ and $k = \pi$ on a $N = 4$ site cluster at $J_1/J_2 = 0.15$, plotted as a function of τ/t_g, with $\lambda = 0.0$ (dashed green curve) and $\lambda = 0.05$ (solid green curve). The empty green square (diamond) indicates the energy at $\tau/t_g = 1$ for $\lambda = 0.05$ ($\lambda = 0.0$). The shaded red region marks the *ZNE region* spanning $\tau/t_g \in [1, 3]$. The exact energy value is also shown for comparison (red star). The inset (1) displays the evolution of the probability p_s over optimization steps for the gate time $\tau = t_g$, with $\lambda = 0.0$ (dashed green curve) and $\lambda = 0.05$ (solid green curve). The inset (2) shows the values of the probability p_s, at the end of the optimization, as a function of λ. **b)** Variational energies for the different symmetry sectors in the interval $J_2/J_1 \in [0.15, 0.35]$. Unmitigated results are obtained at $\tau = t_g$ (left panel), while the mitigated energies obtained via ZNE are shown in the right panel. The inset shows ZNE extrapolations performed within the *ZNE region* ($\tau/t_g \in [1, 3]$) for $J_1/J_2 = 0.15$.

3.4.1 Breaking of Equivariance due to Noise

In Fig. 3.3.3a we show the results at $J_2/J_1 = 0.15$ for the singlet excited state ($S^2 = 0$) at $k = \pi$. We start describing what happens when changing continuously the gate time τ in the variational circuit. First, we optimize the variational state at $\tau = t_g$ (empty green diamond). Then, fixing the optimal parameters, the noise level is changed shifting τ in the interval $\tau/t_g \in [10^{-7}, 10^2]$ (dashed green curve). We point out that for small values of the gate time ($\tau/t_g \sim 10^{-7}$) the variational result approaches the exact energy (red star).

However, in the *ZNE region* (shaded interval) the variational energy is lower with respect to the exact one in the selected symmetry sector[2]. As a result, due to the non-monotonic behaviour of the noisy energy curve, performing the ZNE in the *ZNE region* gets a off-target result, committing an error of 45% with respect to the exact energy. This suggests that the variational state has no definite momentum, implying a breaking in the equivariance of the circuit due to the presence of noise [95].

To better understand this behaviour, we measure, during the energy optimization at $\tau = t_g$, the probability $p_s(\theta) = (1+e^{ik} \langle \Psi_\theta | \hat{\mathcal{T}} | \Psi_\theta \rangle)/2$ (see [61] for a derivation), which quantifies the success in performing the LCU symmetrization (green dashed curve in the inset (1) of Fig. 3.3.3a). This probability decreases during the optimization and at the end is quite low ($p_s \approx 15\%$). We point out that in a noiseless scenario, the definition of a state with a definite momentum is achieved irrespective of the value of p_s. However, when noise is present, the probability of success p_s in executing the LCU symmetrization becomes relevant to the effective generation of translationally invariant states. In general for both scenarios, low values of p_s imply that the one-site translations are primarly restored by LCU, indicating that components in the wrong symmetry sectors are relevant before the LCU application. Conversely, when p_s is high, most of the symmetrization is effectively performed by optimizing the parameters within the variational circuit $\hat{U}_\theta$, relegating

[2]We remark that the variational energy is consistently higher than the ground state energy. However, if the symmetries of the variational state are not preserved, its energy may be lower than that of the excited state we are approximating.

a minor role to LCU. Since the latter is the most susceptible component to noise in the quantum circuit [107, 108], its contribution to equivariance loss is expected to be predominant. Consequently, we identify the decay of p_s during training as the main indicator of noise-induced equivariance breaking within the circuit.

3.4.2 Noise mitigation and symmetry restoration

In this section, we devise a strategy to mitigate the effect of noise on the symmetries of the Ansatz. As discussed in the previous section, in order to reduce the role of the LCU in the construction of a translationally invariant state we aim at increasing the probability p_s. This can be achieved by adding a penalty term in the loss function

$$P(\lambda, \theta) = \lambda \left[1 - p_{\mathrm{s}}(\theta)\right]^2 \ . \tag{3.10}$$

Here, λ is an hyperparameter which controls the intensity of the penalty term. Performing energy minimizations at different values of λ, fixing the gate time $\tau = t_g$, allows to determine its optimal value. In the inset (2) of Fig. 3.3.3a we show a sharp transition at $\lambda = 0.05$ from a regime of low ($p_{\mathrm{s}} \approx 15\%$) to high ($p_{\mathrm{s}} \approx 90\%$) probability measured at the end of the training. In addition, in the inset (1) we show how the behaviour of the probability p_{s}, during the energy optimization, is modified by introducing a penalty term (solid green curve). As a result, by setting $\lambda = 0.05$, the energy of the optimized state (empty green square in Fig. 3.3.3a) results in a reliable approximation of the energy of the singlet excited state at $k = \pi$ (with a relative error $\Delta\varepsilon \approx 5\%$).
At this stage, maintaining the optimal variational parameters obtained at $\tau = t_g$, the noise level is changed shifting τ in the interval $\tau/t_g \in [10^{-7}, 10^{2}]$ (green solid curve in Fig. 3.3.3a). Here, a monotonic behaviour emerges, facilitating the implementation of Zero Noise Extrapolation within the *ZNE region* (see below).

3.4.3 Mitigated energy level crossing

Finally, in Fig. 3.3.3b we estimate the variational energies, at gate time $\tau = t_g$, for the different symmetry sectors varying the values

of the frustration ratio in the interval $J_2/J_1 \in [0.15, 0.35]$[3]. As shown in the left panel, the variational energies are shifted with respect to the exact ones (marked by dashed lines) due to noise. The mitigated results with ZNE technique performed in the *ZNE region* are depicted in the right panel.
In the inset, for $J_2/J_1 = 0.15$, the empty points represent the noisy energies (also depicted on the left panel), while the crosses denote the expectation values obtained with increasing gate time. The filled points indicate the extrapolated values in the zero-noise limit (also displayed in the right panel) after fitting the data by linear regression.
We point out that even in the unmitigated scenario (left panel), the crossing point is adequately captured, despite slight energy shifts. However, through mitigation, we not only identify the energy level crossing accurately but also approximate the exact energies with an $\Delta\varepsilon \approx 1\%$ error (right panel).

3.5 Conclusions

We have introduced an Ansatz inspired by HVA to investigate the excited states of an interacting spin system on a lattice. Specifically, we have discussed the possibility to carry out optimizations in specific symmetry sectors by fixing the quantum numbers in the variational state. Although this approach was applied to identify energy level crossings on small clusters in the one-dimensional J_1-J_2 Heisenberg model, it can be properly generalized to study other models. We emphasize the advantage of this approach in providing a simple method to construct total spin invariant states, compared to classical approaches such as Tensor Networks or Neural Network Quantum States.
It is worth noting that, by employing level spectroscopy, the quantum phase transition point is estimated at $J_2/J_1 = 0.25$ on a cluster of $N = 4$ sites (see Fig. 3.3.3b) with an error of 3.6% compared to the thermodynamic limit result $(J_2/J_1)_c = 0.24117(6)$. Given the negligible size effects of this technique, the application of the same approach to systems with long-range interactions or two-dimensional

[3]In particular, an appropriate value of λ is chosen for each simulation.

systems, where the presence of phase transitions is still under debate, is the focus of future investigations.
Furthermore, we discussed how noise, which explicitly breaks state symmetries, can be mitigated by standard techniques such as ZNE, with the addition of an appropriate penalty term which helps in finding symmetric solutions. From this perspective, the implementation of this Ansatz on current quantum devices represents the next step in verifying whether the mitigation techniques employed in simulations are still effective. Moreover, this implementation will involve assessing also the impact of finite samples on the estimation of the expectation values [117].

Chapter 4

The Noisy Gates approach

The standard approach to classically simulate noisy quantum computers is presented in Section 1.3.2 and is used in Chapter 3. This approach works well if the unitary gate acts almost "instantaneously" with respect to the noise dynamics, however it still has some limitations. By separating the action of the gate from that of the noise, it does not represent a faithful description of what happens inside a computer, where the controlled action on the qubit(s) generating the gate and the environment act simultaneously and potentially affect each other. Therefore it is expected not to be fully accurate in describing a NISQ computer, especially when the number of gates and qubits is relatively large, which is actually the regime where simulations are more interesting.
In this chapter we propose an alternative approach [30], where the noise is *integrated* into the logical gates, in the sense that the resulting noisy gate is computed by solving for the dynamics generating it, with additional terms describing the noise added to it:

$$\rho \;\text{—}\boxed{\mathcal{N}}\text{—}\; \rho' \;, \tag{4.1}$$

where in general $\mathcal{N} \neq \mathcal{E}_2 \circ \mathcal{U} \circ \mathcal{E}_1$, and under standard assumptions (e.g., Markovianity) it gives an analytic expression for the solution of the GKLS equation obtained with perturbative methods. Now $\mathcal{N}$ captures, within the limits of validity of the GKLS equation, the entire physics occurring during the execution of each gate; not only it offers a more accurate description of the system and therefore a better protocol for circuit simulations, but also it helps to understand the different noises acting on the computer, especially in view of possible mitigation strategies. As we show in the following this

new approach does not have any computational disadvantage with respect to (1.32).
As a note, Markovianity, which is the main physical assumption behind the GKLS equation, and it is a very convenient working hypothesis, can be released in favour of more general noises [5, 9, 118–121]; we will not touch on this possibility here.
Both approaches (1.32) and (4.1) have a drawback if they are implemented at the density matrix level: the simulation will be slowed down quadratically as a function of the number of qubits. This drawback can be resolved for (1.32) by replacing the superoperations $\mathcal{E}_{1,2}$ acting on the density matrix with suitable stochastic operations acting on the state vector [122, 123]; in this way, the noisy algorithm becomes random and each single run of the simulation can be seen as a single run of the algorithm on the noisy quantum computer. The same strategy can be adopted for (4.1); one writes

$$|\psi\rangle \;\text{—}\boxed{N_{\boldsymbol{\xi}}}\text{—}\; |\psi'_{\boldsymbol{\xi}}\rangle \;, \tag{4.2}$$

where $N_{\boldsymbol{\xi}}$ is a stochastic gate, solution of a stochastic Schrödinger equation, incorporating both the controlled action generating the (otherwise ideal) gate $\hat{U}$ and the noise. Here $\boldsymbol{\xi}$ denotes a set of stochastic gaussian variables, and stresses the fact that $N_{\boldsymbol{\xi}}$, and hence $|\psi'_{\boldsymbol{\xi}}\rangle$, are random; we will omit to indicate $\boldsymbol{\xi}$ in the rest of the thesis. Physical quantities are obtained by averaging over the noise. The general procedure therefore is the following. Given a noiseless algorithm, the corresponding noisy one is obtained by replacing each ideal gate with a noisy gate. The resulting noisy algorithm, which is stochastic, is repeated for different realizations of the random variables, as if they were different runs on a physical quantum computer. This produces a statistics of outcomes, to be compared with those of a real computer, or to be used to predict the behavior of a future NISQ device.
As such, as already mentioned, a first application of our approach is to predict the behaviour of NISQ devices, their potentialities and limitations. But its use goes beyond the NISQ-era horizon: by offering a more accurate modeling of the noise, it allows to better understand the physics underlying the functioning of a quantum computer and to enforce appropriate error mitigation schemes [96,

124, 125].
The rest of the chapter details this program. Here we present the noisy gates method by designing it on the IBM superconducting computers [44] although the approach is general and can be used to describe any NISQ quantum platform, once the native gate set and the proper noise model are defined. Indeed, in the next Chapter 5 we extend the approach to photonic devices.

4.1 Review of the noise model in the GKLS formalism

The noises which are more relevant in the functioning of superconducting devices have already been characterized in literature [42, 43, 109]; in this section we briefly present them. With good approximation they are described by the GKLS dynamics (Eqs. (1.6), (1.10)) that now for convenience we rewrite as:

$$\frac{\mathrm{d}\hat{\rho}_s}{\mathrm{d}t} = -\frac{i}{\hbar}\big[\hat{H}_s, \hat{\rho}_s\big] + \mathfrak{D}(\hat{\rho}_s); \tag{4.3}$$

here, $\hat{H}_s$ is the Hamiltonian of the system which implements the ideal gate, and $\mathfrak{D}$ is a term describing the effect of the environment. Here for simplicity we neglect possible further Hamiltonian terms due to interactions with the environment [5]. For convenience, we will describe the evolution with a time schedule $s \in [0, 1]$, defined as $s = t/t_g$, where t_g is the duration of a gate.
Apart from state preparation and measurement (SPAM) errors, which happen at the very beginning and very end, during the execution of an algorithm there are two main sources of noise, namely, depolarization and relaxation [29, 109]. The first, which can be ascribed to the imperfections of the device, tends to bring the state towards the totally mixed one, $\hat{\mathbb{I}}/\sqrt{d}$, where $d = 2^n$ and n is the number of qubits; for the single qubit, this can be modeled by the following term [42, 43],

$$\mathfrak{D}_{\mathrm{D}}(\hat{\rho}) = \gamma_{\mathrm{D}} \sum_{k=1}^{3} \big[\hat{\sigma}^k \hat{\rho} \hat{\sigma}^k - \hat{\rho}\big], \tag{4.4}$$

where $\hat{\sigma}^1 = \hat{X}, \hat{\sigma}^2 = \hat{Y}, \hat{\sigma}^3 = \hat{Z}$ are the standard Pauli matrices and $\gamma_{\mathrm{D}} \geq 0$ is the rate at which depolarization occurs.

The second type of noise is due to the interaction of the physical qubits with the surrounding environment; in particular, due the thermalization towards an equilibrium with the environment, energy exchanges occur. In the scenario of interest, this induces the decay of a qubit towards the ground state $|0\rangle$, an effect which is also known as amplitude damping [42,43]. This damping is characterized by a relaxation time T_1, which identifies the scales at which the initial state decays towards $|0\rangle$; it causes also a damping of the off-diagonal elements of the density matrix in terms of dephasing, which (if only amplitude damping is acting) has a characteristic time $2T_1$. However, at the same time also a contribution of pure dephasing must be taken in account, resulting in an effective dephasing rate $1/T_2 \geq 1/2T_1$. When also $T_1 \geq T_2$ holds (and this is the case of interest to us), the combined action of these two effects, that we refer to as relaxation (as in Section 1.3.2), can be described by the following GKLS term,

$$\mathfrak{D}_{\text{R}}(\hat{\rho}) = \gamma_1\big[\hat{\sigma}^+\hat{\rho}\hat{\sigma}^- - \frac{1}{2}\big\{\hat{P}_1, \hat{\rho}\big\}\big] + \gamma_z\big[\hat{Z}\hat{\rho}\hat{Z} - \hat{\rho}\big], \tag{4.5}$$

where we use the convention $\hat{\sigma}^\pm = (\hat{X} \pm i\hat{Y})/2$ and $\hat{P}_1 = |1\rangle\langle 1|$ is the projector onto $|1\rangle$; the coefficients are related to the characteristic times as $\gamma_1 = t_g T_1^{-1}$ and $\gamma_z = t_g(2T_1 - T_2)/4T_1T_2$.
We consider both sources of noise together, meaning that the GKLS term is $\mathfrak{D} = \mathfrak{D}_{\text{D}} + \mathfrak{D}_{\text{R}}$, which can be diagonalized in the canonical GKLS form by standard procedures. Eventually one obtains the term

$$\mathfrak{D}(\hat{\rho}) = \epsilon^2 \sum_{k=1}^{3} \big[\hat{L}_k\hat{\rho}\hat{L}_k^\dagger - \frac{1}{2}\big\{\hat{L}_k^\dagger\hat{L}_k, \hat{\rho}\big\}\big], \tag{4.6}$$

where the non normalized Lindblad operators are

$$\hat{L}_1 = \sqrt{\frac{\lambda_1}{\lambda}}\hat{\sigma}^-, \quad \text{L}_2 = \sqrt{\frac{\lambda_2}{\lambda}}\hat{\sigma}^+, \quad \hat{L}_3 = \sqrt{\frac{\lambda_3}{\lambda}}\hat{Z}; \tag{4.7}$$

here, we set $\lambda_1 = 2\gamma_{\text{D}}$, $\lambda_2 = 2\gamma_{\text{D}} + \gamma_1$, $\lambda_3 = \gamma_{\text{D}} + \gamma_z$ and $\lambda = \lambda_1 + \lambda_2 + \lambda_3$, and we defined the parameter $\epsilon = \sqrt{\lambda}$. In the case of IBM's superconducting devices the typical order of magnitude of the decoherence times is $\sim 10^{-4}$ s; by contrast, the typical order of magnitude of the time to execute a gate is $t_g \sim 10^{-8}$ s, which is small compared to $T_{1,2}$; in particular, one has $\gamma_{\text{D}}, \gamma_1, \gamma_z \ll 1$, which

leads to $\epsilon = \sqrt{\lambda} \ll 1$. This justifies the perturbative expansion we implement in the next section of in the chapter.
While terms of the form (4.6) describe the dissipation occurring at the single qubit level, one straightforward generalization to the multi-qubit case (the one we will consider in this work) is obtained via

$$\mathfrak{D}(\hat{\rho}) = \sum_{k=1}^{n} \mathfrak{D}^{(k)}(\hat{\rho}), \tag{4.8}$$

where the upper index (k) indicates that the GKLS term (4.6) acts on the $k-$th qubit. Such a generalization is based on the assumption that single qubit noises are dominating, therefore neglecting cross talks and correlated noises [126]; they can straightforwardly be implemented in our noisy framework, and they will be the subject of future research. We stress that through Eq. (4.8) we already account for the fact that (for instance, on IBM's devices) multiple-qubit operations are more faulty than single qubit manipulations: when entangling gates are performed, single qubit noises act together, and errors therefore amplify.
Before proceeding, one further comment is in order. Casting the behaviour of a real quantum device in a theoretical model is a hard task, and the more accurate the model, the less general it is. The purpose of this work is not that of finding the best noise model for a given quantum computer; rather, given a noise model, we are interested in the best way to simulate the device. The noise model we are considering here is therefore ultimately motivated by the fact that it is accurate enough to already give appreciable results in the simulations, but on the other hand it is also simple enough to efficiently enlighten our main points, and general enough to be readily extended to different platforms. It is understood that better results can be achieved only by specializing more the analysis on physical device to be considered.

4.2 General derivation of noisy gates

Let us consider the situation in which the computer executes a gate $\hat{U}_g$ on a set of n qubits. This is achieved by driving the system with an Hamiltonian $\hat{H}_s$ for $s \in [0, 1]$, which will induce some unitary

evolution $\hat{U}_s$, defined by $i\hbar \mathrm{d}\hat{U}_s/\mathrm{d}s = \hat{H}_s\hat{U}_s$, and such that $\hat{U}_{s=1} = \hat{U}_g$. However, if noises and imperfections are taken in account, this coherent evolution is replaced by a partially non coherent one, which under the assumptions of Markovianity (and complete positivity) is described by a master equation of the form (4.3) discussed in the previous section, with the GKLS term given, in our case, by (4.8) and (4.6), which needs to be solved in place of the Schrödinger equation. We recall here that the coefficient ϵ is small, $\epsilon \ll 1$.

In order to switch from the density matrix formalism to the state vector formalism, we use the linear SSE with classical Gaussian noise in Eq. (1.19) [6, 7, 9, 13, 127]; The latter is an unraveling of the GKLS equation in the sense that the density matrix obtained by averaging the pure states $|\psi_s\rangle \langle\psi_s|$ over the noise:

$$\hat{\rho}_s = \mathbb{E}\Big[\, |\psi_s\rangle \langle\psi_s| \,\Big], \tag{4.9}$$

is a solution of Eq. (1.19). In this sense, Eqs. (1.19) and (4.3) have the same physical content; the advantage of the stochastic unraveling is that it allows to work with Schrödinger-like equations for the state vector.

One key property of Eq. (1.19) is that it is linear, and therefore it allows to write the solution as $|\psi_{s=1}\rangle = \hat{N}_g |\psi_0\rangle$, where $\hat{N}_g$ can be interpreted as a noisy random gate acting on the system. Since Eq. (1.19) in general does not preserve the norm of the state vector, the associated gate $\hat{N}_g$ is not unitary; this is a consequence of the chosen unraveling: one could have chosen norm-preserving unravelings (see Eq. (1.20)) [8, 46], which however are not linear and therefore do not allow for a gate-like formulation. The lack of norm preservation is not a problem since at the statistical level, i.e. when the average over the noise is taken as in (4.9), one recovers the GKLS equation, which is trace preserving.

In general, Eq. (1.19) cannot be solved in a closed form [10, 11] except for few specific cases, for example when all operators commute. In Appendix C.1 we show how an approximate solution to order $\mathcal{O}(\epsilon^2)$ can be derived, which results in the following expression for the noisy version of a noiseless gate $\hat{U}_g$:

$$\hat{N}_g = \hat{U}_g e^{\hat{D}_g} e^{\hat{S}_g}, \tag{4.10}$$

where we defined the deterministic operator:

$$\hat{D}_g = -\frac{\epsilon^2}{2}\sum_k \int_0^1 \mathrm{d}s\big(\hat{L}^\dagger_{k,s}\hat{L}_{k,s} - \hat{L}^2_{k,s}\big) \tag{4.11}$$

and the stochastic one:

$$\hat{S}_g = i\epsilon\sum_k \int_0^1 \mathrm{d}W_{k,s}\hat{L}_{k,s}. \tag{4.12}$$

Note that in Eqs. (4.11) and (4.12), $\hat{L}_{k,s} = \hat{U}_s^\dagger \hat{L}_k \hat{U}_s$ are the Lindblad operators in the interaction picture, therefore the noiseless part of the dynamics $\hat{U}_s$ and the noisy one given by the Lindblad operators $\hat{L}_k$ do not factorize, as it might look from a naive understanding of Eq. (4.10).
As explained in Appendix C.1, we omitted the additional term $-(\epsilon^2/2)\sum_{k,l}\int_0^1 \mathrm{d}W_{k,s}\int_0^s \mathrm{d}W_{l,s'}\big[\hat{L}_{k,s},\hat{L}_{l,s'}\big]$ in Eq. (4.12), which in principle should contribute to order ϵ^2; this is legitimate because it is a nested Itô integral of non anticipating functions [11], and hence its stochastic average is 0. For this reason, it drops from all final averaged quantities, and therefore we can neglect it from the start. The only stochastic term entering the noisy gate $\hat{N}_g$ is $\hat{S}_g$ in Eq. (4.12), which is a function of several random variables ξ arising from the stochastic processes $W_{k,s}$. Let us call $\hat{L}_{kij,s} = \hat{L}^+_{kij,s} + i\hat{L}^-_{kij,s}$ the ij-th matrix element of the jump operator $\hat{L}_{k,s}$ in the computational basis, divided in real $(+)$ and imaginary $(-)$ part, respectively. Then, each entry of the stochastic matrix is of the form $S_{g,ij} = i\epsilon\sum_k\big[\xi^+_{kij} + i\xi^-_{kij}\big]$, where we defined the random variables

$$\xi^+_{kij} = \int_0^1 \mathrm{d}W_{k,s}\hat{L}^+_{kij,s}, \quad \xi^-_{kij} = \int_0^1 \mathrm{d}W_{k,s}\hat{L}^-_{kij,s}, \tag{4.13}$$

which, being Itô integrals of deterministic functions, are all normally distributed with zero mean, $\mathbb{E}\big[\xi^\pm_{kij}\big] = 0$, and variances $\mathbb{E}[(\xi^\pm_{kij})^2] = \int_0^1 \mathrm{d}s(\hat{L}^\pm_{kij})^2$. Moreover, one can easily check that they are correlated with each other as

$$\mathbb{E}\big[\xi^\pm_{kij}\xi^\pm_{k'i'j'}\big] = \delta_{k,k'}\int_0^1 \mathrm{d}s\hat{L}^\pm_{kij,s}\hat{L}^\pm_{ki'j',s}. \tag{4.14}$$

The random variables giving $\hat{S}_g$ its stochastic character may be defined in several other ways, and the best choice depends on the specific case of interest. In this section we presented one general

strategy for defining them, but in practice this lead to an over estimation of the actual number of random variables needed. By straightforwardly counting, one has at most $2d^2(d^2-1)$ real gaussian random variables for a noisy gate acting on $n = \log_2 d$ qubits, each random variable being correlated with at most other $2d^2 - 1$ ones. In practice, however, we immediately point out that one shall expect neither the number of random variables, nor the number of correlations between them to really follow this scaling. This is mainly due to the fact that real quantum computers usually perform single and two qubit native gates, and single qubit noises are dominating. For instance, given (4.8), one can upper bound the number of random variables by $\sim 6d^2 \log_2 d$. We notice that our derivation works for any choice of the starting GKLS master equation, meaning that any Markovian noise model can be treated. In particular, while in this chapter we specialize on the noise model described in the previous section, one can add device-motivated modifications (such as correlated noises and leakages to upper levels in the case of IBM's platform); modifications of this kind are left to future research—as also the generalization of our derivation to non Markovian situations.
More details on the difference between our perturbative approximation and the one used in the standard approach (1.32) can be found in Appendix C.2.

4.3 Comparison of the algorithms

It is instructive to compare the structure of our approach to noise simulation with that of noise simulators based on the standard approach in Section 1.3.2. We choose IBM's Qiskit [128] as term of comparison since it is the most used software development kit for quantum computing. The main algorithmic implementations based on the standard approach are in Algs. 1 and 2.
Our noisy gates simulation is based on the algorithm summarized in Alg. 4.
The time complexity of Alg. 4 is again $\mathcal{O}(2^{2n})$, determined by the matrix vector multiplication step. Analogously, the space complexity is $\mathcal{O}(2^n)$. We notice that in Alg. 4 there is no need to perform

Algorithm 4 NOISY GATES SIMULATION

Input: Initial state $|\psi_0\rangle$, a noiseless circuit $\mathrm{C} = \{\mathrm{U}^{(1)}, ..., \mathrm{U}^{(n_g)}\}$ composed by n_g gates $\mathrm{U}^{(i)}$ and number of samples N_s

for $0 \leq k \leq N_s$ **do**

map a noisy circuit $\tilde{\mathrm{C}} = \{\mathrm{N}^{(1)}, ..., \mathrm{N}^{(n_g)}\}$ on C

sample stochastic processes ξ inside noisy gates $\mathrm{N}^{(i)}$

compute $|\psi_k\rangle = \mathrm{N}^{(n_g)} \dots \mathrm{N}^{(1)} |\psi_0\rangle$

compute $\rho_k = |\psi_k\rangle \langle\psi_k|$

end

Output: $\rho_f = \frac{1}{N_s} \sum_{k=1}^{N_s} \rho_k$

the scalar product in Eqs. (1.40) and (1.41). Moreover, all optimization to reduce the time complexity that are possible for the first step of Algs. 1 and 2 are also possible for Alg. 4. Finally, all algorithms perform samples of random numbers, but this operation has a constant scaling.

We notice that, the Monte Carlo quantum jump approach in Alg. 2 provides, in the limit of a large number of realization N_s and small $\mathrm{d}t$, a solution to the full GKLS equation enabling a very accurate description. However this can be achieved only by dividing the gate time t_g into smaller time steps $\mathrm{d}t$ increasing the number of total matrix vector multiplications. This quickly becomes inefficient and therefore analytic and approximate expressions for the whole gate time are preferable, as the unravelling of the Kraus map in Alg. 1 and our noisy gates in Alg. 4. However, between these last two, the second one is the better option because although the noisy gates approach has nearly the same computational complexity as Alg. 1, it achieves a better accuracy. This feature is showed in Appendix C.2 and is confirmed by simulations in Section 4.5.

Finally, it would be interesting to compare the noisy gates algorithm (Alg. 4) with the one introduced in Chapter 2, namely Alg. 3, which we refer to here, for simplicity, as the quantum noise algorithm. Both algorithms are capable of reproducing a GKLS dynamics. In fact, by choosing the same Hamiltonian and Lindblad operators in Eq. (4.10) and Eq. (2.2), one obtains the same density matrix (see Eqs. (2.4) and. (C.15)). However, the two algorithms are based on different assumptions and are designed for different purposes. The quantum noise algorithm was developed to simulate open system

dynamics on quantum computers; it is a quantum algorithm that simulates the open dynamics of the overall system. In contrast, the noisy gates algorithm was developed to simulate the behavior of a noisy quantum computer on classical computers. As such, it cannot be implemented directly on quantum computers because in general a noisy gate is not unitary (see Eq. (4.10)). Furthermore, the noisy gates algorithm assumes that each gate in the quantum circuit can be replaced by its corresponding noisy gate, derived using its own GKLS equation.
As demonstrated in Chapter 2, the quantum noise algorithm offers specific advantages over existing approaches. These include the ability to use only one ancillary qubit and the fact that the final density matrix represents a first-order expansion in the coupling constants γ_k of the formal solution of the GKLS equation (see Eq.(2.4)), rather than merely a first-order approximation in the time step Δt (see Eq.(2.12)). On the other hand, compared to standard simulation methods the noisy gates approach has the advantage of not decoupling the action of a quantum gate from the inherent noise, resulting in more accurate classical simulations as we show in Section 4.5.

4.4 Derivation of noisy gates for superconducting qubits

In this section we derive the expressions of noisy gates focusing on superconducting quantum devices [109]. The noise model we use is the one presented in Section 4.1.

4.4.1 One-qubit noisy gates

In superconducting devices, single-qubit gates are realized by coupling a microwave drive line with the superconducting transmon qubit. The effective Hamiltonian of the drive reads [109, 129]

$$\hat{H}_t = \frac{\hbar}{2}\omega_t(\cos(\phi)\hat{X} + \sin(\phi)\hat{Y})\,, \tag{4.15}$$

where $\omega_t = -\chi V_0 s_t$ is the drive pulse, χ is a parameter depending on the capacities of the transmon qubit and the coupling capacity, V_0 is the amplitude of the drive potential, s_t is a dimensionless envelope

function of the drive pulse and ϕ is an arbitrary phase. The unitary evolution due to Eq. (4.15) is given by

$$\hat{U}(\theta,\phi) = e^{-\frac{i}{2}\theta(\cos(\phi)\hat{X}+\sin(\phi)\hat{Y})}\,, \tag{4.16}$$

where $\theta = \int_0^1 \omega_s \mathrm{d}s$ is the rotation angle on the X-Y plane. In matrix notation Eq. (4.16) reads

$$\hat{U}(\theta,\phi) = \begin{pmatrix} \cos\frac{\theta}{2} & -i\sin\frac{\theta}{2}e^{-i\phi} \\ -i\sin\frac{\theta}{2}e^{i\phi} & \cos\frac{\theta}{2} \end{pmatrix}. \tag{4.17}$$

In IBM devices, the drive Hamiltonian is calibrated to realize the native single-qubit gates $\hat{X}$ and $\hat{SX}$, which are rotations around the X-axis obtained by setting that $\theta = \pi$ or $\theta = \pi/2$ in Eq. (4.16). The additional phase ϕ allows to implement rotations around the z-axis of arbitrary angles as virtual gates, since they are mimicked by the software and are not associated to a physical action on the device [129].
By plugging Eq. (4.17) and the Lindblad operators of the noise model of Section 4.1 in Eq. (4.10), one finds the following stochastic and deterministic terms

$$\begin{aligned} \hat{D}_g^+ &= \int_0^1 \hat{P}_{s,0}\,\mathrm{d}s; \quad & \hat{S}_g^+ &= \int_0^1 \hat{\sigma}_s^+ \mathrm{d}W_{s,+}\,; \\ \hat{D}_g^- &= \int_0^1 \hat{P}_{s,1}\,\mathrm{d}s; \quad & \hat{S}_g^- &= \int_0^1 \hat{\sigma}_s^- \mathrm{d}W_{s,-}\,; \\ \hat{D}_g^z &= 0; & \hat{S}_g^z &= \int_0^1 \hat{Z}_s\,\mathrm{d}W_{s,z}\,, \end{aligned} \tag{4.18}$$

where $\hat{D}_g^\pm$ and $\hat{S}_g^\pm$ are respectively the deterministic and stochastic terms associated to the non Hermitian operators $\hat{\sigma}^\pm$; $\hat{D}_g^z$ and $\hat{S}_g^z$ are associated to the Hermitian operator $\hat{Z}$. Indeed, $\hat{P}_{s,0} = \hat{U}_s^\dagger \hat{P}_0 \hat{U}_s$, $\hat{P}_{s,1} = \hat{U}_s^\dagger \hat{P}_1 \hat{U}_s$, $\hat{\sigma}_s^\pm = \hat{U}_s^\dagger \hat{\sigma}^\pm \hat{U}_s$ and $\hat{Z}_s = \hat{U}_s^\dagger \hat{Z} \hat{U}_s$, where $\hat{U}_s = \hat{U}(\theta(s),\phi)$ with $\theta(s) = \int_0^s \omega_s \mathrm{d}s$. As an illustrative example $\hat{S}_g^z$ in Eq. (4.18) can be expressed in the matrix form as

$$\hat{S}_g^z = \begin{pmatrix} S_z^{(1)} & -i\,e^{-i\phi}\,S_z^{(2)} \\ i\,e^{i\phi}\,S_z^{(2)} & -S_z^{(1)} \end{pmatrix}, \tag{4.19}$$

where

$$S_z^{(1)} = \int_0^1 \cos\theta(s)\mathrm{d}W_{s,z}; \quad S_z^{(2)} = \int_0^1 \sin\theta(s)\mathrm{d}W_{s,z}\,. \tag{4.20}$$

These two Itô integrals have a binormal joint probability distribution, with the following momenta

$$\begin{aligned}
&\mathbb{E}[S_z^{(1)}] = \mathbb{E}[S_z^{(2)}] = 0 \\
&\mathbb{E}[(S_z^{(1)})^2] = \int_0^1 \cos^2\theta(s)\mathrm{d}s \\
&\mathbb{E}[(S_z^{(2)})^2] = \int_0^1 \sin^2\theta(s)\mathrm{d}s \\
&\mathbb{E}[S_z^{(1)}S_z^{(2)}] = \int_0^1 \cos\theta(s)\sin\theta(s)\mathrm{d}s\,.
\end{aligned} \tag{4.21}$$

Thus, the stochastic processes $\hat{S}_z^{(1)}$ and $\hat{S}_z^{(2)}$ can be sampled from a binormal distribution with the momenta in Eq. (4.21). The remaining matrices in Eq. (4.18) have similar matrix forms, which can be computed straightforwardly.

4.4.2 Two-qubit noisy gates

The native two-qubit gate in IBM devices is the cross resonant (CR) gate [109, 129, 130], whose Hamiltonian reads [109, 129, 130]

$$\hat{H}_t = \frac{\hbar}{2}\omega_t \hat{Z}\otimes(\cos(\phi)\hat{X} + \sin(\phi)\hat{Y})\,, \tag{4.22}$$

where ω_t is the drive pulse and ϕ is an arbitrary phase. The additional phase ϕ allows to implement virtual z gates similarly to single-qubit gates, see [129] for further details. The corresponding unitary evolution is given by

$$\hat{CR}(\theta,\phi) = e^{-\frac{i}{2}\theta\hat{Z}\otimes(\cos(\phi)\hat{X}+\sin(\phi)\hat{Y})} \tag{4.23}$$

where $\theta = \int_0^1 \omega_s \mathrm{d}s$. In matrix notation Eq. (4.23) reads

$$\hat{CR}(\theta,\phi) = \begin{pmatrix} \hat{U}(\theta,\phi) & 0 \\ 0 & \hat{U}(-\theta,\phi) \end{pmatrix}, \tag{4.24}$$

where $\hat{U}(\theta,\phi)$ and $\hat{U}(-\theta,\phi)$ are as in Eq. (4.17). The CNOT gate and its inverse are implemented by combining single-qubit gates and CR gates (see [109]). For two qubits we assume Eq. (4.8) thus the deterministic and stochastic terms read

$$
\begin{aligned}
\hat{D}_g^{(q_1)+} &= \int_0^1 (\hat{P}_0 \otimes \hat{\mathbb{I}})_s \, \mathrm{d}s; \quad & \hat{S}_g^{(q_1)+} &= \int_0^1 (\hat{\sigma}^+ \otimes \hat{\mathbb{I}})_s \mathrm{d}W_{s,+} \, ; \\
\hat{D}_g^{(q_1)-} &= \int_0^1 (\hat{P}_1 \otimes \hat{\mathbb{I}})_s \, \mathrm{d}s; \quad & \hat{S}_g^{(q_1)-} &= \int_0^1 (\hat{\sigma}^- \otimes \hat{\mathbb{I}})_s \mathrm{d}W_{s,-} \, ; \\
\hat{D}_g^{(q_2)+} &= \int_0^1 (\hat{\mathbb{I}} \otimes \hat{P}_0)_s \, \mathrm{d}s; \quad & \hat{S}_g^{(q_2)+} &= \int_0^1 (\hat{\mathbb{I}} \otimes \hat{\sigma}^+)_s \mathrm{d}W_{s,+} \, ; \\
\hat{D}_g^{(q_2)-} &= \int_0^1 (\hat{\mathbb{I}} \otimes \hat{P}_1)_s \, \mathrm{d}s; \quad & \hat{S}_g^{(q_2)-} &= \int_0^1 (\hat{\mathbb{I}} \otimes \hat{\sigma}^-)_s \mathrm{d}W_{s,-} \, ; \\
\hat{D}_g^{(q_1)z} &= 0; & \hat{S}_g^{(q_1)z} &= \int_0^1 (\hat{Z} \otimes \hat{\mathbb{I}})_s \, \mathrm{d}W_{s,z} \, ; \\
\hat{D}_g^{(q_1)z} &= 0; & \hat{S}_g^{(q_2)z} &= \int_0^1 (\hat{\mathbb{I}} \otimes \hat{Z})_s \, \mathrm{d}W_{s,z} \, ,
\end{aligned}
\tag{4.25}
$$

where the superscripts q_1 and q_2 stand respectively for qubit one and qubit two meaning that a non-trivial Lindblad operator is acting only on that qubit. Moreover, $(\hat{P}_0 \otimes \hat{\mathbb{I}})_s = \hat{CR}_s^\dagger (\hat{P}_0 \otimes \hat{\mathbb{I}}) \hat{CR}_s$, $(\hat{P}_1 \otimes \hat{\mathbb{I}})_s = \hat{CR}_s^\dagger (\hat{P}_1 \otimes \hat{\mathbb{I}}) \hat{CR}_s$ and so on. Here $\hat{CR}_s = \hat{CR}(\theta(s), \phi)$ with $\theta(s) = \int_0^s \omega_s \mathrm{d}s$. The statistical momenta are easy to compute similarly to the previous section.

4.5 Simulations

We now study the performances of our noisy gates method, and compare them with those of Qiskit's simulator [128]. First, in subsection 4.5.1 we test the two approaches against the solution of the GKLS equation (4.3), by studying a repeated application of IBM's native gate set. Then, in subsection 4.5.2 we compare the predictions of both methods with the behaviour of an actual quantum computer, by running the inverse QFT algorithm on the IBM's quantum processors ibmq_kolkata and ibmq_oslo. In [30] one can find the same analysis by running the GHZ algorithm on ibm_oslo. All simulations are performed by using the noise model described in section 4.1 (see also Section 1.3.2 and C.3). The implementation of the work proposed in this work is open source and available as a python package QUANTUM-GATES. It allows the user to run noisy simulations.

4.5.1 Comparison with the numerical solution of the GKLS equation

Here we compare the density matrices $\hat{\rho}^{\rm ng}$ and $\hat{\rho}^{\rm ibm}$, obtained from the noisy gates simulation and from the Qiskit simulation respectively, with the target density matrix $\hat{\sigma}$ obtained by solving numerically the GKLS equation with Mathematica [131]. We treat $\hat{\sigma}$ as the target analytic solution of the full GKLS equation. The comparison is performed with the Hellinger distances $\mathcal{H}_\sigma^{\rm ng} = \mathcal{H}(\hat{\rho}^{\rm ng}, \hat{\sigma})$, $\mathcal{H}_\sigma^{\rm ibm} = \mathcal{H}(\hat{\rho}^{\rm ibm}, \hat{\sigma})$ where the Hellinger distance is defined by

$$\mathcal{H}(\hat{\rho}, \hat{\sigma}) = \frac{1}{\sqrt{2}} \sqrt{\sum_{k=1}^{N} \left(\sqrt{\rho_{kk}} - \sqrt{\sigma_{kk}}\right)^2}, \tag{4.26}$$

with ρ_{kk} (σ_{kk}) the diagonal elements of $\hat{\rho}$ ($\hat{\sigma}$). The Hellinger distance is a classical measure of the distance between the readout probability distributions. It cannot be interpreted as a distance between quantum states since it does not take in account off diagonal elements of density matrices. The Hellinger distance directly compares the concrete outputs of a real device, which are the outcomes of Z measurements, i.e. classical bitstrings. Since in these simulations it is easy to get the full density matrices, we also compute the fidelities, which accounts for all the entries of density matrices, $\mathcal{F}_\sigma^{\rm ng} = \mathcal{F}(\hat{\rho}^{\rm ng}, \hat{\sigma})$ and $\mathcal{F}_\sigma^{\rm ibm} = \mathcal{F}(\hat{\rho}^{\rm ibm}, \hat{\sigma})$, where the fidelity is defined as

$$\mathcal{F}(\hat{\rho}, \hat{\sigma}) = \left(\mathrm{Tr}\sqrt{\hat{\sigma}^{1/2}\hat{\rho}\hat{\sigma}^{1/2}}\right)^2. \tag{4.27}$$

We notice that for the diagonal entries of density matrices, we could have used the Hellinger fidelity, related to the Hellinger distance as $\mathcal{F}_H = (1 - \mathcal{H}^2)^2$. This quantity is not a proper mathematical distance, further motivating the use of the Hellinger distance as a more reliable figure of merit.

Single qubit simulations

The X gates are obtained by setting $\theta = \pi$ and $\phi = 0$ in Eq. (4.16); we initialize the qubit in $|0\rangle$ and we use the qubit noise parameters of ibmq_manila. We evolve the state of the qubit for a time $T = \mathcal{N} t_g$, with $\mathcal{N} = 15000$. In panels (a), (b) and (c) of Fig. 4.5.1 we plot the time evolution of $\rho_{00} = \langle 0|\hat{\rho}|0\rangle$, the population of the ground

state, obtained with the three methods. In the noiseless case, ρ_{00} should oscillate between zero and one as at each t_g a complete X rotation is performed; the standard noise model modifies this behaviour: oscillations are damped due to amplitude and phase damping, while depolarization drives probabilities towards the asymptotic value $\rho_{00} \to 0.5$.

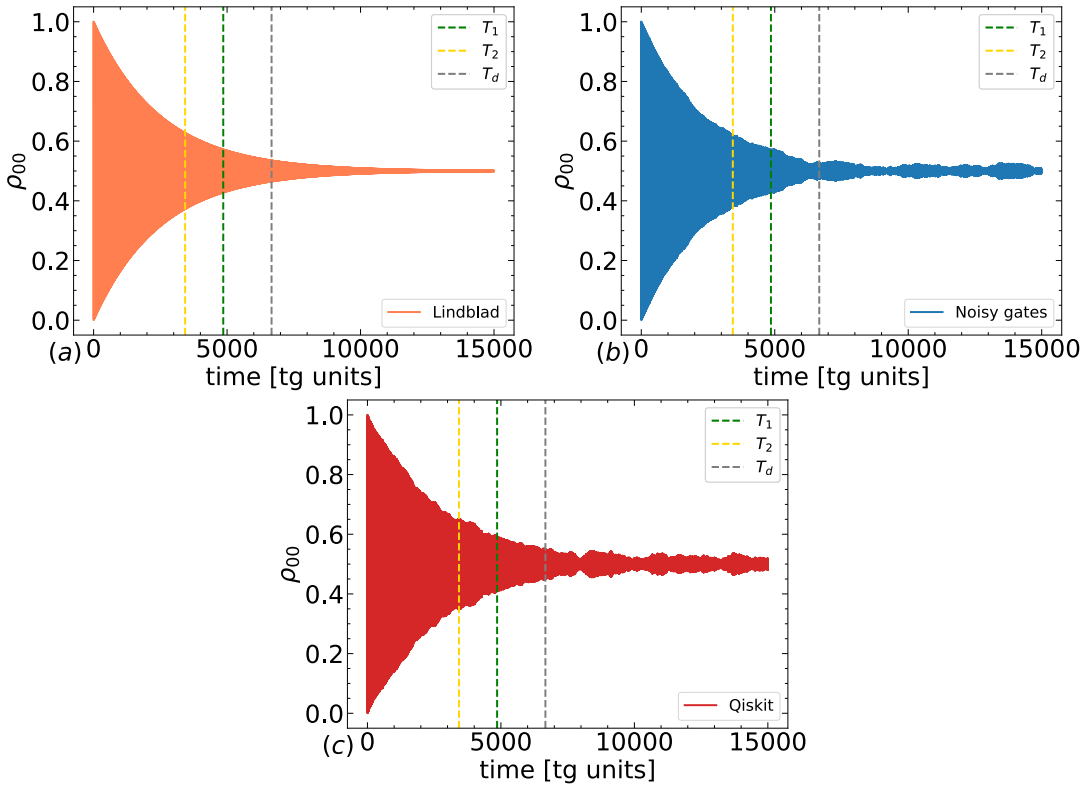

Figure 4.5.1: Repetition of X gates. Panels (a), (b), (c) show the time evolution of the $\rho_{00} = \langle 0|\hat{\rho}|0\rangle$ entry of the density matrix. The numerical solution of the GKLS equation is displayed in orange (a), that of the noisy gates simulation in blue (b), and that of the Qiskit simulation in red (c). The noisy gates and Qiskit simulations are obtained with 1000 samples, and qualitatively they reproduce the time evolution of the GKLS equation. Vertical dashed lines in the three panels represent the time scales of relaxation T_1 (green), T_2 (yellow) and depolarization T_d (grey).

Both the noisy gates simulation and that obtained using Qiskit qualitatively reproduce this behaviour. In Fig. 4.5.1 we have also highlighted with vertical dashed lines the characteristic times of amplitude damping and depolarization; for times approaching these values the state is not a usable quantum state anymore for practical applications, as the density matrix becomes completely mixed. Given this consideration, in the plots in Fig. 4.5.2 we stop at $\mathcal{N} = 2000$.

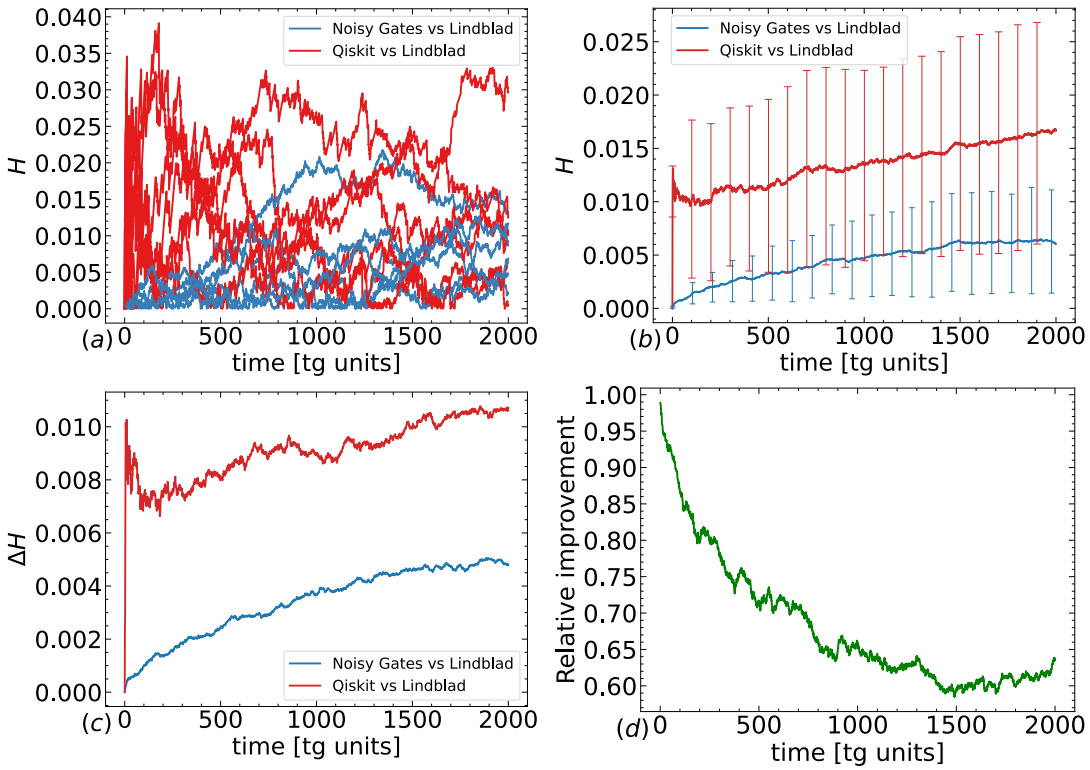

Figure 4.5.2: Repetition of X gates. Panel (a) shows the Hellinger distances $\mathcal{H}_\sigma^{\rm ng}$, in blue, and $\mathcal{H}_\sigma^{\rm ibm}$, in red, as a function of time. Different curves are obtained from 100 independent runs of the two methods (for better readability only five are shown), where each simulation is obtained by averaging over 1000 samples. Panel (b) shows the mean of the Hellinger distances $\bar{\mathcal{H}}_\sigma^{\rm ng}$, and $\bar{\mathcal{H}}_\sigma^{\rm ibm}$, obtained from the 100 independent runs, and vertical error bars show their standard deviations $\Delta\mathcal{H}_\sigma^{\rm ng}$, $\Delta\mathcal{H}_\sigma^{\rm ibm}$. Panel (c) displays $\Delta\mathcal{H}_\sigma^{\rm ng}$ and $\Delta\mathcal{H}_\sigma^{\rm ibm}$ as functions of time. Panel (d) shows the relative improvement of the distance $\bar{\mathcal{H}}_\sigma^{\rm ng}$ with respect to $\bar{\mathcal{H}}_\sigma^{\rm ibm}$, calculated as $|\bar{\mathcal{H}}_\sigma^{\rm ibm} - \bar{\mathcal{H}}_\sigma^{\rm ng}|/\bar{\mathcal{H}}_\sigma^{\rm ibm}$. The fact that noises drive the system towards the maximally mixed state is the reason why the improvement decreases in time. The noisy gates and the standard approaches lead to the same predictions when one is close to decoherence times, as the noise is dominant over the unitary evolution. In the interesting regime $[0, 2000 \cdot t_g]$ before deoherence dominates, the improvement is always above 60%.

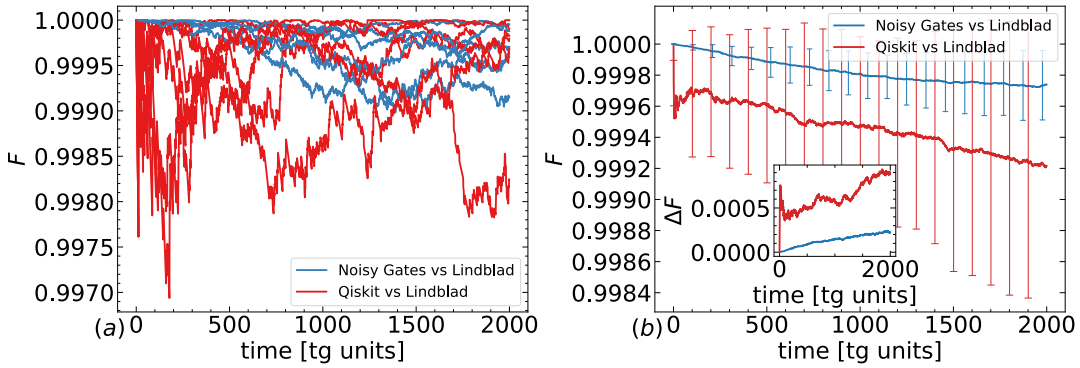

Figure 4.5.3: Fidelities $\mathcal{F}_\sigma^{\rm ng}$, in blue, and $\mathcal{F}_\sigma^{\rm ibm}$, in red, as a function of time, for a repetition of X gates. On panel (a), the fidelities obtained from 100 independent runs of the two methods are pictured (for better readability only five are shown), where each simulation is obtained by averaging over 1000 samples. On panel (b), the means $\bar{\mathcal{F}}_\sigma^{\rm ng}$, $\bar{\mathcal{F}}_\sigma^{\rm ibm}$ of the same simulations and their standard deviations $\Delta\mathcal{F}_\sigma^{\rm ng}$, $\Delta\mathcal{F}_\sigma^{\rm ibm}$ are displayed. The inset shows the standard deviations $\Delta\mathcal{F}_\sigma^{\rm ng}$, $\Delta\mathcal{F}_\sigma^{\rm ibm}$ as functions of time.

To quantify the accuracy of the methods, we have run 100 independent simulations, each with 1000 samples, with both the noisy gates simulator and the Qiskit simulator, computing for each simulation the Hellinger distance $\mathcal{H}_\sigma^{\rm ng}$, $\mathcal{H}_\sigma^{\rm ibm}$. We computed the means over the 100 independent simulations, $\bar{\mathcal{H}}_\sigma^{\rm ng}$, $\bar{\mathcal{H}}_\sigma^{\rm ibm}$ and their standard deviations $\Delta\mathcal{H}_\sigma^{\rm ng}$, $\Delta\mathcal{H}_\sigma^{\rm ibm}$. These quantities are shown in panels (a), (b) and (c) of Fig. 4.5.2. During the relevant time interval $[0, T]$ $\bar{\mathcal{H}}_\sigma^{\rm ng}$ is closer to zero than $\bar{\mathcal{H}}_\sigma^{\rm ibm}$. Results are compatible within the error bars, however the standard deviations associated to the noisy gates simulations are significantly smaller than those associated to the Qiskit simulations, as also highlighted in Fig. 4.5.2 (c). This means that the noisy gates have the additional advantage that a smaller number of samples is needed to reach a target precision. We notice that the difference between $\bar{\mathcal{H}}_\sigma^{\rm ng}$ and $\bar{\mathcal{H}}_\sigma^{\rm ibm}$ is of the order $\sim 10^{-3} - 10^{-2}$, and this corresponds to a relative improvement, calculated as $|\bar{\mathcal{H}}_\sigma^{\rm ibm} - \bar{\mathcal{H}}_\sigma^{\rm ng}|/\bar{\mathcal{H}}_\sigma^{\rm ibm}$, in the range from 90% to 60% as time increases. The relative improvement is shown in Fig. 4.5.2 (d). The fact that noises drive the system towards the maximally mixed state is the reason why the improvement decreases over time. The noisy gates and the standard approaches lead to the same predictions when approaching decoherence times. Indeed after such times the strength of the noise is dominant over the unitary evolution, or,

equivalently, the Hamiltonian contribution is negligible with respect to the Lindblad term (see Eq. (4.6)). In the interesting regime $[0, T]$ our improvement is always above 60%. We repeat the same analysis for the fidelities. Results are shown in Fig. 4.5.3 (a) and (b). Panel (a) shows the fidelities obtained from 100 independent simulations with the two methods (for better readability only five are shown). Panel (b) shows the means $\bar{\mathcal{F}}_\sigma^{\rm ng}$, $\bar{\mathcal{F}}_\sigma^{\rm ibm}$ of the same simulations and their standard deviations $\Delta\mathcal{F}_\sigma^{\rm ng}$, $\Delta\mathcal{F}_\sigma^{\rm ibm}$. Results on the fidelities are in accordance with those in Fig. 4.5.2.

Two qubits simulations

We simulate a repetition of CR gates in Eq. (4.23), choosing $\phi = 0$ and $\theta = \pi$. We initialize the system in the state $|10\rangle$ and we use the qubits noise parameters of ibmq_manila. In the three panels of Fig. 4.5.4 we show the time evolution of the entry $\rho_{22} = \langle 10|\hat{\rho}|10\rangle$; the x-axis is normalized in terms of the CR gate time t_{CR}. The two-qubit state goes asymptotically towards the completely mixed state as ρ_{22} reaches the asymptotic value 0.25. The probability ρ_{22}, which in the ideal case should flip between one and zero, is damped over time by amplitude and phase damping effects. Vertical dashed lines signal the characteristic time scales of the noises. We plot only the T_1 and T_2 values of the target qubit as representative values. Depolarization is the dominant contribution, spoiling the quantum state already after ~ 100 CR gates; for this reason, in Fig. 4.5.5 we consider a total duration corresponding to $\mathcal{N} \sim 100$. Panels (a), (b) and (c) of Fig. 4.5.5 report the Hellinger distances, showing the different results of 100 independent simulations together with their means and standard deviations.
Within the relevant time interval $[0, T]$ $\bar{\mathcal{H}}_\sigma^{\rm ng}$ is closer to zero than $\bar{\mathcal{H}}_\sigma^{\rm ibm}$. Notably, the two results are not compatible within error bars: the difference between $\bar{\mathcal{H}}_\sigma^{\rm ng}$ and $\bar{\mathcal{H}}_\sigma^{\rm ibm}$ is now of the order $\sim 10^{-1}$. This corresponds to a relative improvement in the range from 90% to 88% as time increases, shown in Fig. 4.5.5 (d). In the interesting regime $[0, T]$ our improvement is always above 88%. As noises dominate approaching decoherence times, in Fig. 4.5.5 (b) the value of $\bar{\mathcal{H}}_\sigma^{\rm ibm}$ approaches that of $\bar{\mathcal{H}}_\sigma^{\rm ng}$ for times close to 100 CR gate times. We report the results of the same analysis for the fidelities

in Fig. 4.5.6, showing accordance with the results in Fig. 4.5.5.

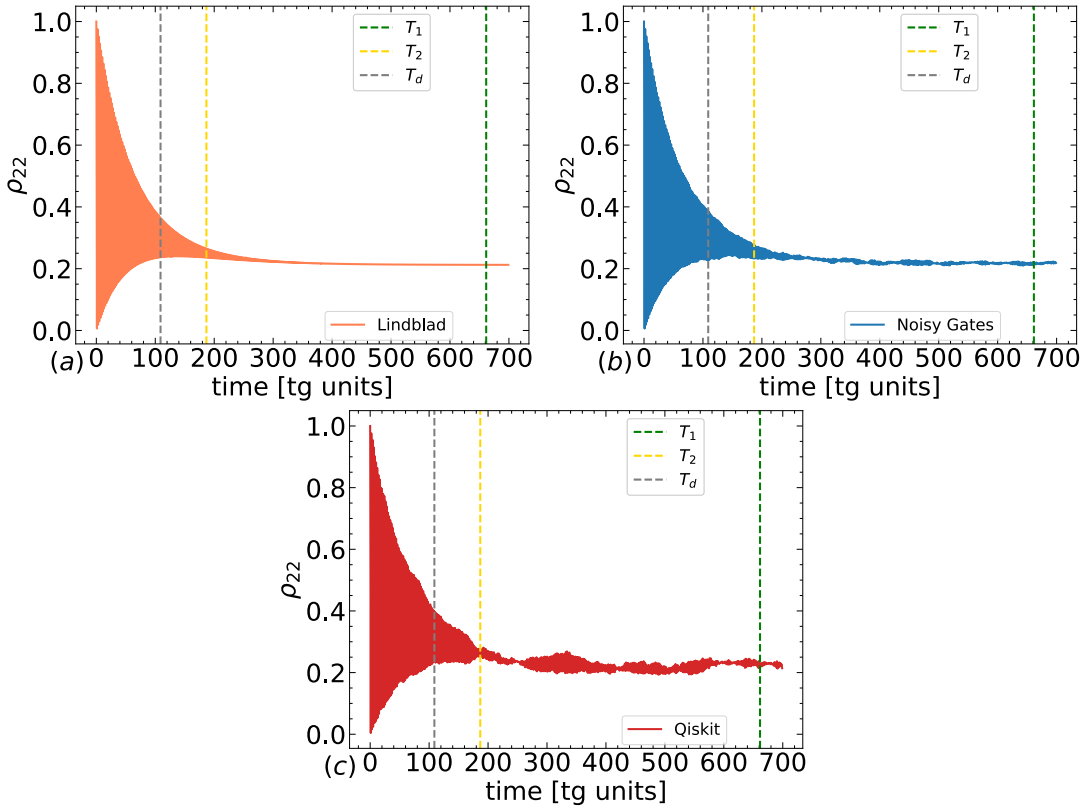

Figure 4.5.4: Repetition of CR gates. Panels (a), (b), (c) show the time evolution of the ρ_{22} entry of the density matrix for the CR gate with $\theta = \pi$ and $\phi = 0$. Colors have the same meaning as for Fig. 4.5.1. Vertical dashed lines represent the time scales of relaxation, T_1 (in green) and T_2 (in yellow) of the target qubit, and depolarization T_d (grey). The noisy gates simulations reproduce qualitatively better the time evolution obtained from the direct numerical solution of the GKLS equation.

We perform a similar analysis for a repetition of CNOT gates, for an initial state given by $|10\rangle$ and qubits noise parameters of ibmq_quito. In this simulation we implement each CNOT gate directly without expressing it as a combination of single qubit gates and CR gates, as in IBM devices. We make this choice to solve numerically the target GKLS equation more easily. Effectively, at each CNOT gate time we simulate a circuit with an increasing number of CNOT gates, where we add measurements at the end of the circuit. Thus, according to the standard noise model, we add the single-qubit bitflip channel (see C.3) to model measurements errors. This allows to extend this analysis to runs on real hardware in section 4.5.2, that of course involve measurements. For that same reason,

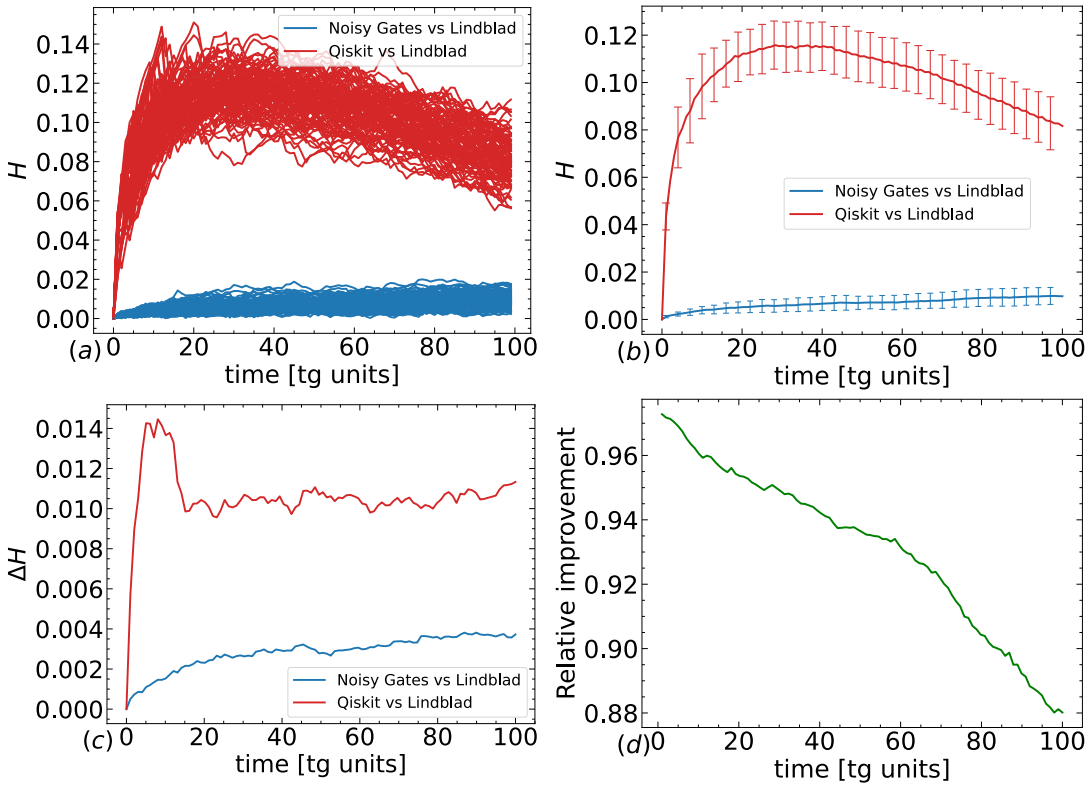

Figure 4.5.5: Repetition of CR gates. Panels (a) and (b) display the Hellinger distances $\mathcal{H}_\sigma^{\rm ng}$, in blue, and $\mathcal{H}_\sigma^{\rm ibm}$, in red, as a function of time. The plots have the same meaning as for Fig. 4.5.2. Panel (d) shows the relative improvement of the distance $\bar{\mathcal{H}}_\sigma^{\rm ng}$ with respect to $\bar{\mathcal{H}}_\sigma^{\rm ibm}$, calculated as $|\bar{\mathcal{H}}_\sigma^{\rm ibm} - \bar{\mathcal{H}}_\sigma^{\rm ng}|/\bar{\mathcal{H}}_\sigma^{\rm ibm}$. The fact that noises drive the system towards the maximally mixed state is the reason why the improvement decreases in time. The noisy gates and the standard approaches lead to the same predictions when one is close to decoherence times, as the noise is dominant over the unitary evolution. In the interesting regime $[0, 100 \cdot t_g]$ our improvement is always above 88%.

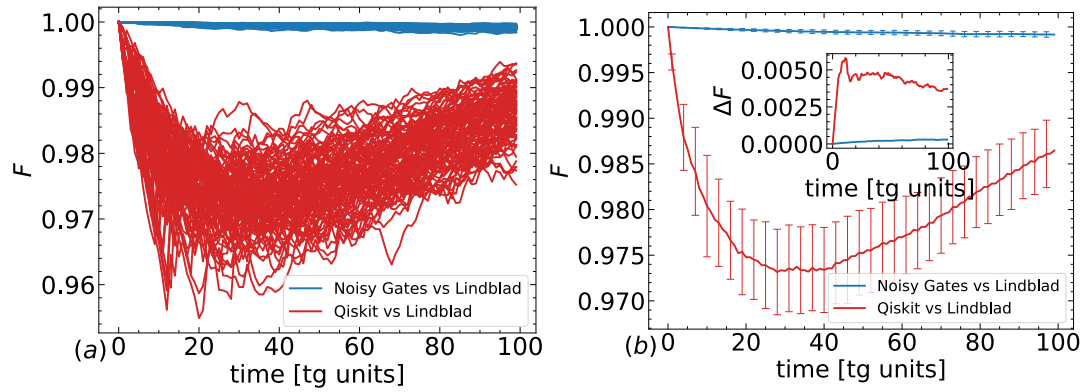

Figure 4.5.6: Fidelities $\mathcal{F}_\sigma^{\rm ng}$, in blue, and $\mathcal{F}_\sigma^{\rm ibm}$, in red, as a function of time, for a repetition of CR gates. Panels (a) and (b) have the same meaning as for Fig. 4.5.3.

we do not compute the fidelities, as the output of the quantum device is a classical probability distributions for the bitstrings.
In the three panels of Fig. 4.5.7 we show the time evolution of the $\rho_{22} = \langle 10|\hat{\rho}|10\rangle$ entry of the density matrix. The relevant time interval is given by a total duration of $\mathcal{N} \sim 100$ gates: depolarization spoils the quantum state after ~ 120 CNOT gates. Fig. 4.5.8 (a) shows the mean of the Hellinger distances $\bar{\mathcal{H}}_\sigma^{\rm ng}$ (in blue) and $\bar{\mathcal{H}}_\sigma^{\rm ibm}$ (in red) and their standard deviations $\Delta\mathcal{H}_\sigma^{\rm ng}$ and $\Delta\mathcal{H}_\sigma^{\rm ibm}$, also shown in Fig. 4.5.8 (b). In the time interval $[0, T]$ $\bar{\mathcal{H}}_\sigma^{\rm ng}$ is closer to zero than $\bar{\mathcal{H}}_\sigma^{\rm ibm}$ and their difference is of the order $\sim 10^{-2}$. This corresponds to a relative improvement in the range from 80% to 55% as time increases. This is shown in Fig. 4.5.8 (c).

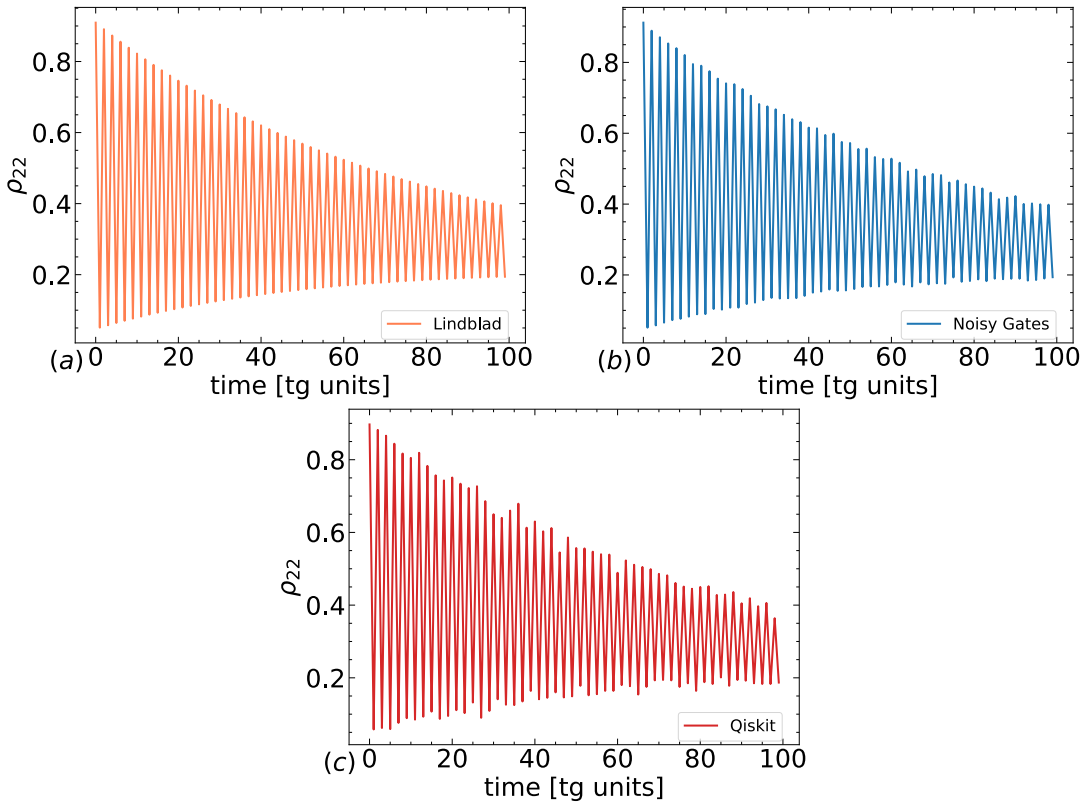

Figure 4.5.7: Repetition of CNOT gates. Panels (a), (b), (c) show the time evolution of the ρ_{22} entry of the density matrix for the CNOT gate. Colors have the same meaning as for Fig. 4.5.1. The noisy gates simulations reproduce qualitatively better the time evolution obtained from the direct numerical solution of the GKLS equation.

By looking at Figs. 4.5.5 (d) and 4.5.8 (c), we notice that the improvement in the Hellinger distance gained by using the noisy gates approach is much higher for CR gates with respect to CNOT gates.

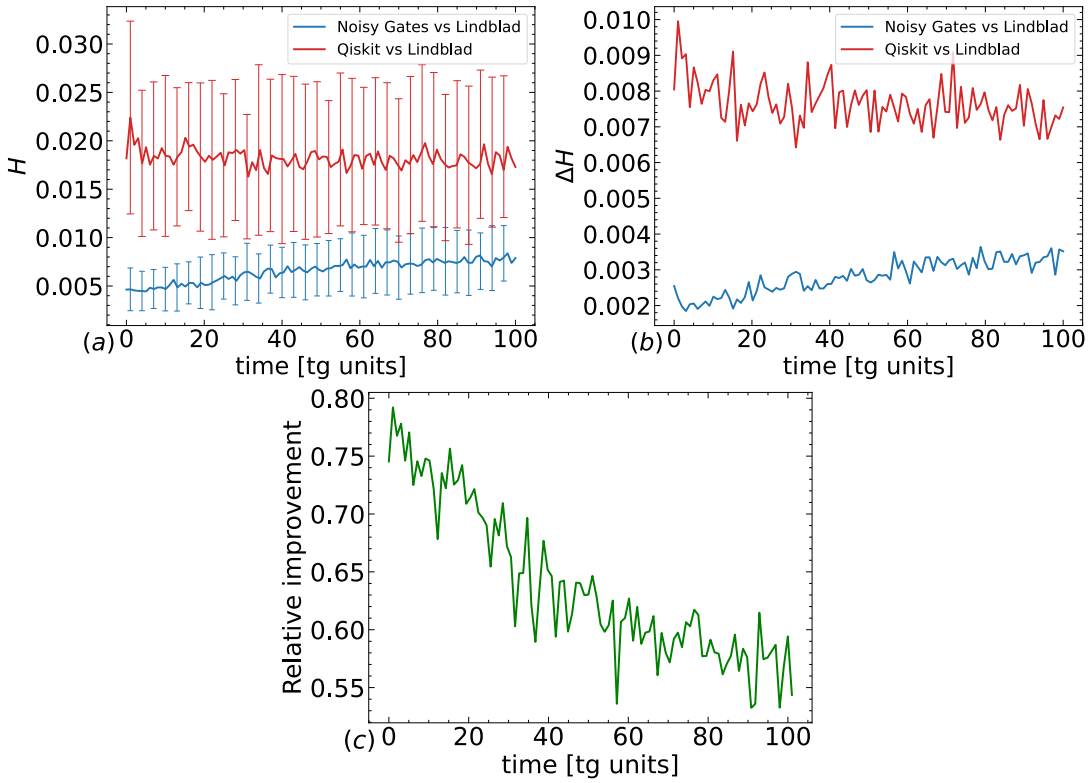

Figure 4.5.8: Repetition of CNOT gates. Panel (a) and (b) displays mean of the Hellinger distances $\bar{\mathcal{H}}_\sigma^{\rm ng}$, in blue, and $\bar{\mathcal{H}}_\sigma^{\rm ibm}$, in red, and their standard deviations as functions of time. Panel (c) shows the relative improvement. The fact that noises drive the system towards the maximally mixed state is again the reason why the improvement decreases in time: the noisy gates and the standard approaches lead to the same predictions when one is close to decoherence times, as the noise is dominant over the unitary evolution. In the interesting regime $[0, 100 \cdot t_g]$ our improvement is always above 55%.

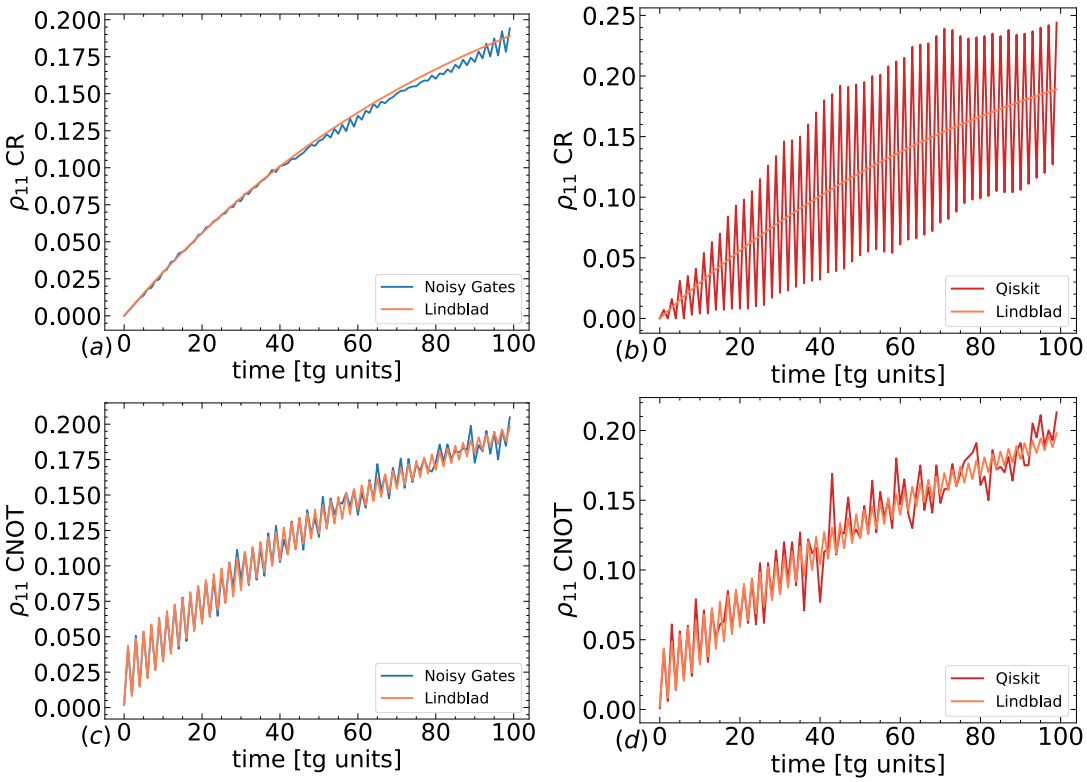

Figure 4.5.9: Repetition of CNOT gates. Panels (a), (b) show the time evolution of the ρ_{11} entry of the density matrix for the same sequence of CR gates in Fig. 4.5.5 and panels (c), (d) show the time evolution of the ρ_{11} entry of the density matrix for the sequence of CNOT gates. Colors have the same meaning as for Fig. 4.5.1. For the CR gates, the Qiskit simulation of ρ_{11} is visibly different from the Lindblad evolution, thus explaining the higher improvement of the noisy gates simulation in the Hellinger distance in Fig. 4.5.5.

We clarify this fact in Fig. 4.5.9. Panels (a), (b) show the time evolution of the ρ_{11} entry of the density matrix for the CR gates and panels (c) and (d) show the time evolution of ρ_{11} for the CNOT gates. Similarly to the convention used above, orange curves are obtained with the numerical solution of the GKLS equation, blue curves are obtained with the noisy gates simulations and red curves are obtained with Qiskit simulations. The noisy gates simulations make good predictions for both gate sequences, as the blue curves follow closely the orange curves. On the other hand, the Qiskit simulation for the CR gates is visibly different from the numerical solution of the GKLS equation. This might be due to the fact that the CR gate is a block diagonal matrix with $X(\theta)$ in the upper block and $X(-\theta)$ in the lower block while the CNOT gate is block diagonal with an identity in the upper block and $X(\theta)$ in the lower block. The identity in the CNOT might lead to a lower influence of noises on the ρ_{00} and ρ_{11} entries of the density matrix. Thus, Hellinger distances obtained with the noisy gates in different simulations are very good and similar to each other, while the Hellinger distance obtained with Qiskit is better for the CNOT with respect to the CR. Nevertheless, the noisy gates approach always significantly outperforms the standard method, as shown by the relative improvements.

4.5.2 Comparison with the behaviour of real quantum computers

We inspect the performances of the noisy gates approach when trying to reproduce the behaviour of a real quantum computer. To this purpose, we first extend the analysis of the CNOT gates sequence in section 4.5.1, and then we focus on the inverse Quantum Fourier Transform ($\text{QFT}^\dagger$) algorithm. When dealing with a real hardware, we must take into account that the standard noise model we are using (see section 4.1) might not be accurate enough in describing the device, and that different quantum devices might behave very differently from one another. We show that, despite the choice of a simple noise model and the instability of ibmq devices, our approach is still able to outperform the standard one also when compared with the real hardware.

CNOT simulations

We run the sequence of CNOT gates of section 4.5.1 on ibmq_quito, available on the cloud and comprising 7 superconducting transmon qubits to get the diagonal entries of the density matrix $\hat{\chi}$ of the physical device, to be compared with the diagonal entries of the density matrices $\hat{\rho}^{\rm ng}$, $\hat{\rho}^{\rm ibm}$ and σ obtained for the CNOT simulations in section 4.5.1. We remark again that in section 4.5.1, we implemented each CNOT gate directly without expressing it as a combination of single qubit gates and CR gates, because in this way it is easier to solve numerically the target GKLS equation. We create a list of circuits, each consisting of an increasing number of CNOT gates, and measure each circuit 1000 times to obtain the output probability distributions, thus deriving the evolution of the outcome probabilities as the number of gates increases. As noted above, each circuit involves measurements that add noise, explaining why in the simulations we added a single-qubit bitflip channel. The Hellinger distance $\mathcal{H}_\sigma^\chi = \mathcal{H}(\hat{\chi}, \hat{\sigma})$ between the Lindblad evolution and the evolution obtained with ibmq_quito is shown in Fig. 4.5.10 (a). This distance is three to tens time larger with respect to $\bar{\mathcal{H}}_\sigma^{\rm ng}$ and $\bar{\mathcal{H}}_\sigma^{\rm ibm}$ in Fig. 4.5.8 (a). While the standard approach and the noisy gates approach have a certain level of agreement with the GKLS equation, the latter is deviating from the quantum hardware by a significantly higher level. This is also the reason why it is not possible to appreciate the difference between the mean Hellinger distance $\bar{\mathcal{H}}_\chi^{\rm ng} = \bar{\mathcal{H}}(\hat{\rho}^{\rm ng}, \hat{\chi})$ between the noisy gates and ibmq_quito, and the mean Hellinger distance $\bar{\mathcal{H}}_\chi^{\rm ibm} = \bar{\mathcal{H}}(\hat{\rho}^{\rm ibm}, \hat{\chi})$ between Qiskit and ibmq_quito, as shown in Fig. 4.5.10 (b) and Fig. 4.5.10 (c). Fig. 4.5.10 (d) shows the relative improvement with respect to the device, calculated as $|\bar{\mathcal{H}}_\chi^{\rm ibm} - \bar{\mathcal{H}}_\chi^{\rm ng}|/\bar{\mathcal{H}}_\chi^{\rm ibm}$. The relative improvement is around 10%. The smaller relative improvement with respect to those shown in the previous section is only to a small extent due to the fact that we do not decompose CNOT gates. The main reason, as we explain when discussing the simulations of the QFT (see below), is that additional noises are present in ibmq devices, i.e. crosstalks, correlated noises and coherent errors [132, 133]. The simple noise model that we consider does not take such noises into account and the Lindblad solution is far from the real quantum

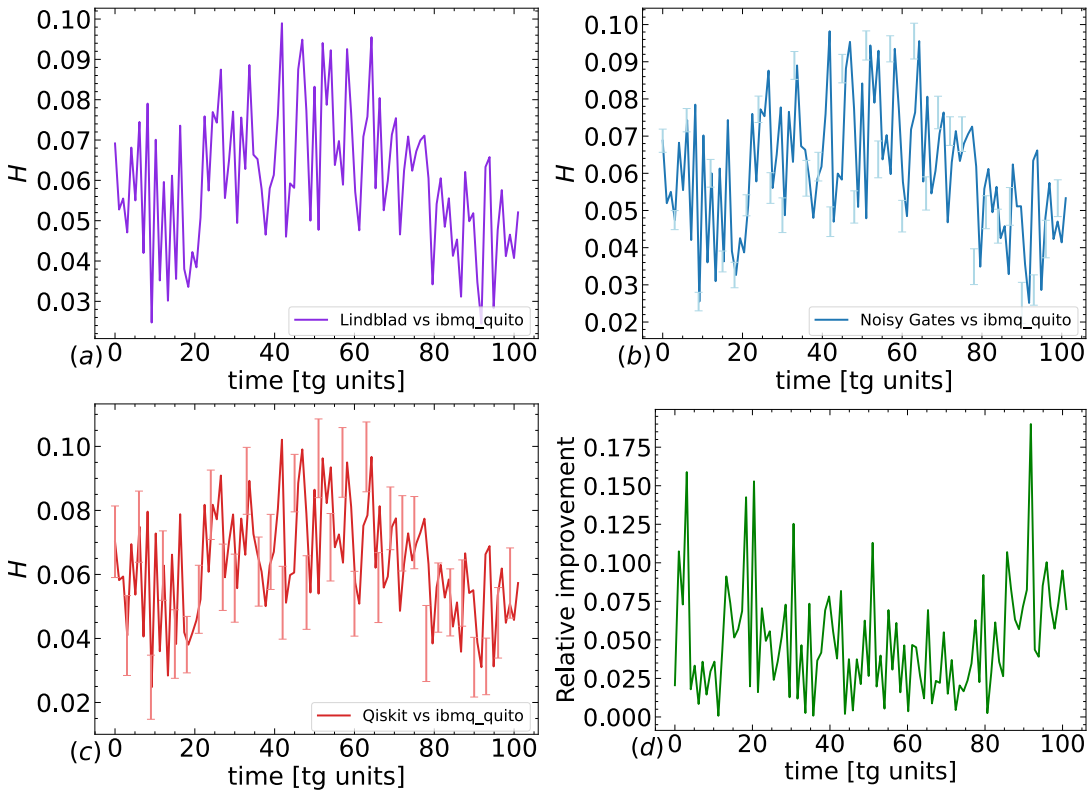

Figure 4.5.10: Repetition of CNOT gates. Panel (a) shows the Hellinger distance $\mathcal{H}_\sigma^\chi$ between the Lindblad evolution and ibmq_quito for the repetition of CNOT gates. Panel (b) shows the mean Hellinger distance $\bar{\mathcal{H}}_\chi^{\rm ng}$ and the standard deviations between the noisy gates simulation and ibmq_quito. Panel (c) shows the mean Hellinger distance $\bar{\mathcal{H}}_\chi^{\rm ibm}$ and the standard deviations between the Qiskit simulation and ibmq_quito. Panel (d) shows the relative improvement calculated as $|\bar{\mathcal{H}}_\chi^{\rm ibm} - \bar{\mathcal{H}}_\chi^{\rm ng}|/\bar{\mathcal{H}}_\chi^{\rm ibm}$. The relative improvement is around 10%. The smaller relative improvement with respect to those shown in the previous figures, is mainly due to additional noises present in ibmq devices, i.e. crosstalks, correlated noises and coherent errors.

computer.

QFT simulations

The QFT† is a subroutine of many important quantum algorithms, such as the Shor's algorithm [134, 135] or Quantum Phase Estimation. The QFT† circuit for n qubits is readily extendable to $n+1$ qubits, allowing to efficiently test the robustness of the simulation approaches as the circuit's width and depth increase. We run QFT† for $n = 2, \ldots, 5$ on ibm_oslo and for $n = 2, \ldots, 8$ on ibmq_kolkata. These devices are available on the cloud, comprising respectively 7 and 27 superconducting transmon qubits. We set as input of QFT† the state $|+\rangle^{\otimes n}$, obtained by applying a layer of Hadamard gates on each qubit initialized in $|0\rangle$. In this way the ideal output of QFT† is $|0\rangle^{\otimes n}$. Runs on real quantum computers are performed by taking 1000 shots, i.e. measurements. The QFT† circuit is transpiled into the native gate set to run on ibmq devices. Now, all CNOT gates inside the circuits are decomposed in terms of single-qubit and CR gates.

The performance of different approaches in simulating the behaviour of the quantum computer are measured with the Hellinger distances from the outcomes of the real device. This allows to avoid full state tomography to reconstruct the full density matrices, which scales exponentially with the number of qubits and becomes unfeasible for the current simulations.

We have run 100 independent simulations, each including 1000 samples, for both methods and for each n. In Fig. 4.5.11 (a) we plot the average values of $\bar{\mathcal{H}}_\chi^{\rm ng} = \bar{\mathcal{H}}(\hat{\rho}^{\rm ng}, \hat{\chi})$, $\bar{\mathcal{H}}_\chi^{\rm ibm} = \bar{\mathcal{H}}(\hat{\rho}^{\rm ibm}, \hat{\chi})$ as the number of qubits n increases from 2 to 5. The diagonal elements of χ are the outcome probabilities of ibm_oslo. Fig. 4.5.12 (a) displays again the average values of $\bar{\mathcal{H}}_\chi^{\rm ng} = \bar{\mathcal{H}}(\hat{\rho}^{\rm ng}, \hat{\chi})$, $\bar{\mathcal{H}}_\chi^{\rm ibm} = \bar{\mathcal{H}}(\hat{\rho}^{\rm ibm}, \hat{\chi})$ up to 8 qubits, where the diagonal elements of χ come from ibmq_kolkata. In Fig. 4.5.12 (c) we compute again $\mathcal{H}_\chi^{\rm ng}$, $\mathcal{H}_\chi^{\rm ibm}$ to test the stability of ibmq_kolkata in different runs. Only for Fig. 4.5.12 (c) we have run a single simulation of 1000 samples, thus standard deviations are not present. We notice that for every n and device we get $\bar{\mathcal{H}}_\chi^{\rm ng} < \bar{\mathcal{H}}_\chi^{\rm ibm}$ and $\Delta\mathcal{H}_\chi^{\rm ng} < \Delta\mathcal{H}_\chi^{\rm ibm}$. The relative improvements, shown in green in Fig. 4.5.11 (b) and Figs. 4.5.12 (b), (d), changes significantly

between different devices and also for the same device but in different runs, namely with different noise parameters, meaning that the performances of such devices are not very stable. For example at $n = 3$, in panel (b) of Fig. 4.5.11 the relative improvement is $\sim 25\%$, in panel (b) of Fig. 4.5.12 it is $\sim 5\%$ and in panel (d) of Fig. 4.5.12 it is $\sim 25\%$. The highest relative improvement obtained with the runs on ibm_oslo is $\sim 30\%$ and for runs on ibmq_kolkata is $\sim 35\%$. As a final remark, we stress that we obtain better results with respect to Qiskit, despite the fact that we have chosen a rectangular pulse shape in the Hamiltonians (see Eqs. (4.15) and (4.16)), while gates on real hardware are realized using Gaussian pulses. We refer the reader to [30] for further analysis, including results for higher numbers of qubits and for the GHZ algorithm.

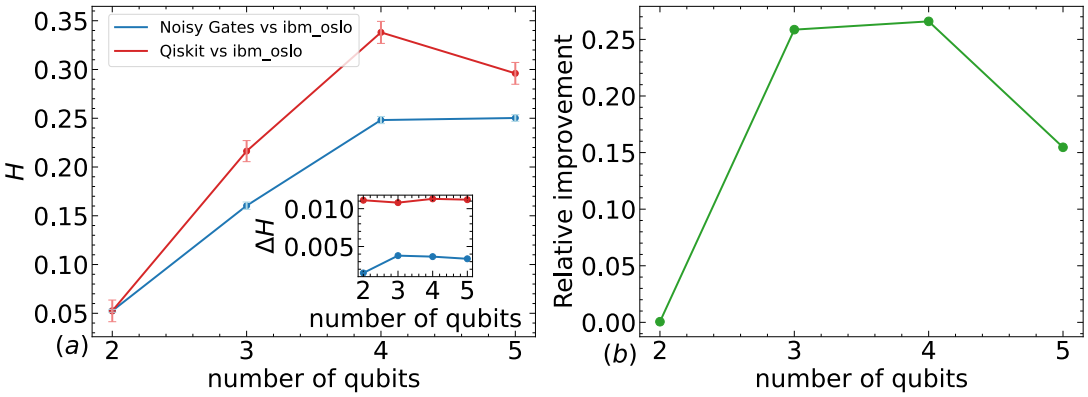

Figure 4.5.11: Quantum Fourier Transform. Panel (a) shows the Hellinger distances between the noisy gate approach and ibm_oslo, and between the Qiskit simulator and ibm_oslo, when executing the $\mathrm{QFT}^\dagger$ algorithm for $n = 2, \ldots, 5$ qubits. Each value is the mean of 100 independent simulations for the noisy gates, in blue, and for the Qiskit simulations, in red. The inset shows the standard deviations as functions of the number of qubits. Panel (b) shows the relative improvement, calculated as $|\bar{\mathcal{H}}_\chi^{\mathrm{ibm}} - \bar{\mathcal{H}}_\chi^{\mathrm{ng}}|/\bar{\mathcal{H}}_\chi^{\mathrm{ibm}}$.

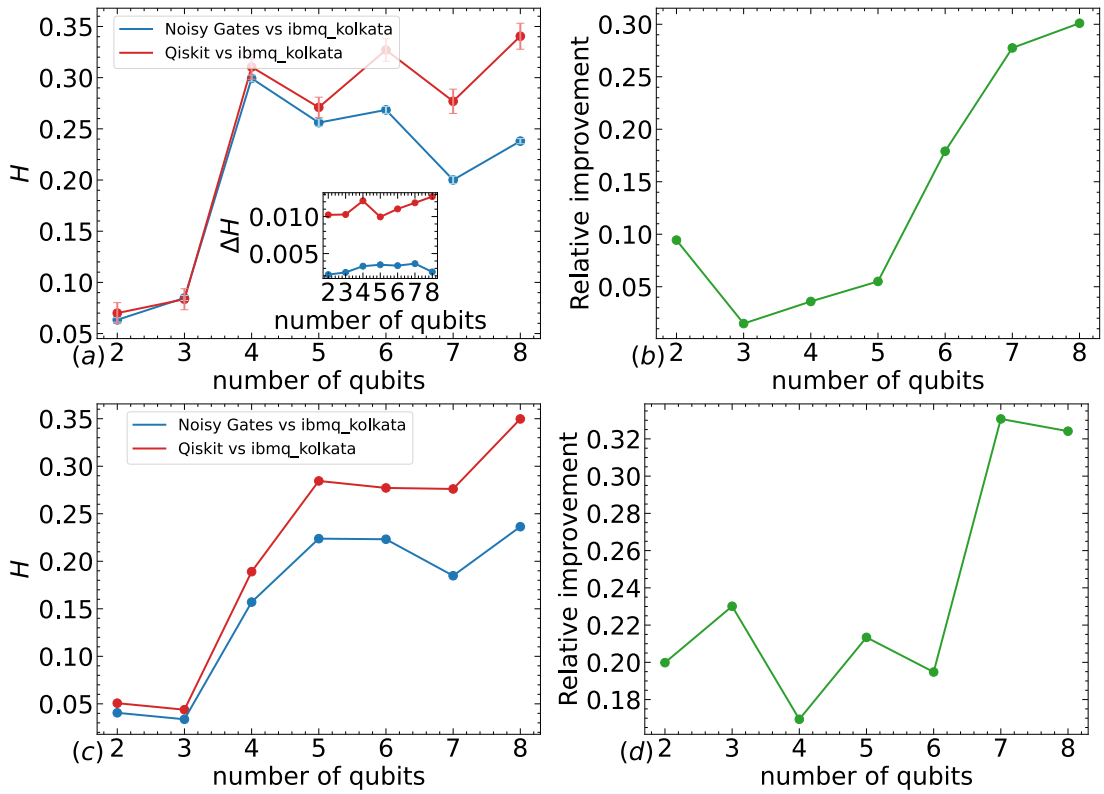

Figure 4.5.12: Quantum Fourier Transform. Panel (a) shows the Hellinger distances between the noisy gate approach and ibmq_kolkata, and between the Qiskit simulator and ibmq_kolkata, when executing the $\mathrm{QFT}^{\dagger}$ algorithm for $n = 2, \ldots, 8$ qubits. Each value is the mean of 100 independent simulations for the noisy gates, in blue, and for the Qiskit simulations, in red. The inset shows the standard deviations as functions of the number of qubits. Panel (b) shows the relative improvement, calculated as $|\bar{\mathcal{H}}_{\chi}^{\mathrm{ibm}} - \bar{\mathcal{H}}_{\chi}^{\mathrm{ng}}|/\bar{\mathcal{H}}_{\chi}^{\mathrm{ibm}}$. In panel (c) the comparison presented in (a) has been repeated a second time on ibmq_kolkata; in this case, only a single simulation of 1000 samples is considered. Panel (d) shows the relative improvement.

4.6 Conclusions

We have developed a novel approach, called noisy quantum gates, to improve classical simulations of NISQ computers: it is based on integrating the noise into the gates, rather than keeping gates and noise as two separate dynamics. We have shown that our approach is very successful in simulating the GKLS dynamics, with a relative improvement between 50% and 90% and more, compared with the standard gate-noise separation method.

When compared against real quantum devices, the improvement fluctuates between 10% and 30%; this is largely due to the fact that the underlying noise model is too simple to accurately represent the dynamics of the device, as discussed in connection to the simulation of the CNOT gate. This is not a weakness of the noisy gate approach here presented, but of the underlying noise model, which we used since it is rather standard in the literature.

There is a number of potential improvements that can be straightforwardly implemented; all of them require an update of the noise model, not of the simulation strategy, which is already very good. First of all, there are likely additional single-qubit errors which should be taken into account, for example those induced by the driving pulses. Secondly, in the present work we considered only non-correlated single-qubit errors, but the method can easily accommodate also correlated two-qubits errors [132, 136] by introducing proper correlated noises into the stochastic equations. Another possible extension of the approach is to add in the Hamiltonians small interactions between adjacent qubits in order to mimic cross talk errors [110, 133]. Last, the current version of the noisy gates approach relies on the GKLS equation that works in the Markovian limit; this is reflected in the fact that we used stochastic equations based on white noises. The approach can be generalized to non-Markovian dynamics by using colored noises, as already discussed in the literature in different contexts [9, 119–121].

Furthermore, our approach is also useful for other purposes that go beyond plane error analysis. For example, the shape of the pulse in the driving Hamiltonians, (see Eq. (4.15) and Eq. (4.22)), can affect the noise. In our work we chose for simplicity a rectangular shape,

but usually in real devices different shapes can be used, for example Gaussian ones. Consequentially, a natural application of our approach is error mitigation [137, 138], by optimizing the parameters of the pulse in order to minimize the effect of the noise [139–141]; the optimization can be performed for example by exploiting machine learning techniques, to find the best pulse parameters, which can be tested on real quantum hardware.
In this work we specified our approach to the native gate set and noise model of IBM devices; clearly the approach is general and can be used to describe in principle any NISQ platform.

Chapter 5

Simulating photonic devices with noisy optical elements

Photonic quantum devices are very promising potential candidates for achieving quantum advantage [142, 143]: integrated photonics benefits from low error rates and ease of manipulation, making it eligible for scalable quantum computation [144, 145]. However, like all quantum computing platforms, photonic devices in the NISQ era are affected by noise from various sources, such as photon losses and imperfect indistinguishability of single photons, that can negatively impact the performance of quantum algorithms [144, 146, 147]. Therefore, studying the noise effects on quantum algorithms and performing accurate classical simulations becomes crucial for their successful deployment [148–150]. This task can be achieved by employing efficient classical simulation methods based on reliable noise models.

Building on the results presented in Chapter 4, we develop the noisy gates approach for optical devices in the dual-rail encoding. The distinctive feature of this approach is that the noise is integrated in the dynamics defining the quantum gates—which turn into noisy gates—offering in this way a superior tool for simulating the behavior of a (unavoidably) noisy quantum device. Here we extend the formalism to second quantization for optical elements [151, 152], and we apply it to specific instances of dual-rail encoding, showing that it is a very flexible and efficient framework for simulating noisy optical computers [31].

We successfully formulate the noisy versions of linear optical elements as phase shifters and beam splitters; we also consider the

effects of imperfect single-photon sources, lossy optical guides and detectors as fictitious noisy optical elements that act on photons at the proper step of the circuit. The approach is first tested through simulations of both gate based and measurement based quantum circuits, whereby the algorithms are expressed in the dual-rail formalism. Then, the approach is applied to a specific variational algorithm solving an optimisation problem, through the study of noise effects on the optimization loop of a variational quantum algorithm.

5.1 Noises in dual-rail encoding optical circuits

This work focuses on discrete variable quantum optics [153, 154], in particular on the so called dual-rail encoding of linear optics quantum computing [155, 156], where the computational units are qubits. We consider optical circuits that are essentially made up of single photon sources, single-mode optical guides (also called spatial modes) in which photons propagate, linear optical elements that modify the photons state and single photon detectors. Thus, an optical circuit can be thought as a unitary transformation on N modes with symmetry group $SU(N)$, followed by the detection. Since a qubit has a $SU(2)$ symmetry, then two spatial optical modes (dual-rail) with a single photon is a natural implementation of a qubit.
The logical states of the qubit are encoded in the two modes Fock states $|0\rangle_L = |10\rangle$, $|1\rangle_L = |01\rangle$ (with this notation we indicate that one of the two modes is occupied by the photon). Thus to represent a system of M qubits one needs $2M$ modes plus a certain number of additional ancillary modes used to implement the correct unitary transformation.
Although it is believed that optical quantum computing is very promising because of the weak interaction of photons with their surrounding environment, optical quantum circuits are not immune to noise. We focus on two main sources of noise affecting optical devices: photon losses and non-perfect indistinguishability of single photons [144, 146].
Photon losses are particularly daunting in the dual rail encoding, since after a loss the photon state exits from the logical computational states of the single qubit. They can occur at any step of the

optical circuit, from the source to optical guides, optical elements and detectors. For each of these steps, one can associate a different loss probability $\mathrm{p} = 1 - e^{-\Delta t/T}$, where Δt is the time interval and T is a characteristic time. Indeed the state of a photonic mode traveling through a fiber can be expressed as [147, 157, 158]

$$\hat{\rho}(\Delta t) = \mathrm{p}\,|0\rangle\langle 0| + (1-\mathrm{p})\,|1\rangle\langle 1| \tag{5.1}$$

where $|0\rangle$ is the state of a single mode without photons and $|1\rangle$ is the state of a single mode occupied by the photon. In practice, the value of p depends specifically on the material used for the optical circuit as well as other experimental parameters. In the following, for the purposes of this work, we vary p from 10^{-4} to 10^{-2}.

Photons non-perfect indistinguishability occurs at the stage of photon/qubits generation. Single photons emitted for example by quantum dots [159] are indistinguishable if they have the same wavelength, polarization, temporal and spatial extent. A quantum dot sources indistinguishable photons if it is subject only to radiative decay. If there is any other decoherence process, then sourced photons will be not perfectly indistinguishable. For this reason we simulate indistinguishably using decoherence models. Typical decoherence processes in semiconductor platforms are depolarization or dephasing [160, 161] and for this reason somehow photons non-perfect indistinguishability is connected to depolarization/dephasing errors because photons are in turn coupled to an electronic spin state that is susceptible to such errors.

We notice that photon losses and non-perfect indistinguishability lead to incoherent evolution. Here we do not consider coherent errors caused by imperfect calibration of optical elements. The latter can be accounted for using already existing techniques [162]. Other sources of error, e.g. cross-talk effects, are beyond the scope of this work and can be added with further developments.

5.2 Noisy optical elements

We now apply the theory outlined in Chapter 4 to build the noisy version of linear optical elements. In particular we focus on phase shifters and beam splitters, showing how to write down their noisy version under the effect of photon loss errors.

5.2.1 Noiseless phase shifter and beam splitter

We briefly recap the noiseless expression of optical elements in order to set the main notation used in the following sections. A phase shifter is an optical element that acts on a single photon mode by changing the phase of the photon state. Its action can be described by the Hamiltonian [151, 152]

$$\hat{\mathrm{H}}_{\mathrm{P}} = -\hbar\omega\hat{\mathrm{P}}, \qquad \hat{\mathrm{P}} = \hat{a}^{\dagger}\hat{a}, \tag{5.2}$$

where $\hat{a}$ and $\hat{a^{\dagger}}$ are respectively the annihilation and creation operators of a photon in a single mode. By solving the Schrödinger equation one arrives at the unitary evolution operator $\hat{\mathrm{U}}_{\mathrm{P}} = e^{i\theta\hat{\mathrm{P}}}$, where $\theta = \omega\cdot(t-t_0) = \omega\cdot\Delta t$. Thus, the evolution of the annihilation and creation operators is given by

$$\hat{\mathrm{U}}_{\mathrm{P}}\hat{a}^{\dagger}\hat{\mathrm{U}}_{\mathrm{P}}^{\dagger} = e^{i\theta}\hat{a}^{\dagger}, \qquad \hat{\mathrm{U}}_{\mathrm{P}}\hat{a}\hat{\mathrm{U}}_{\mathrm{P}}^{\dagger} = e^{-i\theta}\hat{a}. \tag{5.3}$$

The beam splitter acts on two photon modes and can be defined through the Hamiltonian [151, 152]

$$\hat{\mathrm{H}}_{\mathrm{B}} = -\frac{\hbar\omega}{2}\hat{\mathrm{B}}(\phi), \quad \hat{\mathrm{B}}(\phi) = e^{-i\phi}\hat{a}_0\hat{a}_1^{\dagger} + e^{i\phi}\hat{a}_0^{\dagger}\hat{a}_1, \tag{5.4}$$

where the indices of the annihilation and creation operators refer to photon modes 0 and 1. The unitary evolution operator is $\hat{\mathrm{U}}_{\mathrm{B}} = e^{i\frac{\theta}{2}\hat{\mathrm{B}}(\phi)}$, with $\theta = \omega\Delta t$; the annihilation/creation operators evolve as follows:

$$\hat{\mathrm{U}}_{\mathrm{B}}\hat{a}_0^{\dagger}\hat{\mathrm{U}}_{\mathrm{B}}^{\dagger} = \cos(\theta/2)\hat{a}_0^{\dagger} + ie^{-i\phi}\sin(\theta/2)\hat{a}_1^{\dagger}, \tag{5.5}$$

$$\hat{\mathrm{U}}_{\mathrm{B}}\hat{a}_1^{\dagger}\hat{\mathrm{U}}_{\mathrm{B}}^{\dagger} = ie^{i\phi}\sin(\theta/2)\hat{a}_0^{\dagger} + \cos(\theta/2)\hat{a}_1^{\dagger}, \tag{5.6}$$

$$\hat{\mathrm{U}}_{\mathrm{B}}\hat{a}_0\hat{\mathrm{U}}_{\mathrm{B}}^{\dagger} = \cos(\theta/2)\hat{a}_0 - ie^{i\phi}\sin(\theta/2)\hat{a}_1, \tag{5.7}$$

$$\hat{\mathrm{U}}_{\mathrm{B}}\hat{a}_1\hat{\mathrm{U}}_{\mathrm{B}}^{\dagger} = -ie^{-i\phi}\sin(\theta/2)\hat{a}_0 + \cos(\theta/2)\hat{a}_1. \tag{5.8}$$

It is possible to express in a compact way these latter transformations by defining unitary matrices that act on vectors of creation operators $(\hat{a}_0^{\dagger}, \hat{a}_1^{\dagger})^T$ or annihilation operators $(\hat{a}_0, \hat{a}_1)^T$. The matrix for creation operators reads

$$\hat{\mathcal{U}}_{\mathrm{B}} = \begin{pmatrix} \cos(\theta/2) & ie^{-i\phi}\sin(\theta/2) \\ ie^{i\phi}\sin(\theta/2) & \cos(\theta/2) \end{pmatrix}, \tag{5.9}$$

while that for annihilation operators is $\hat{\mathcal{U}}_{\mathrm{B}}^{\dagger}$.

5.2.2 Noisy phase shifter

A natural way to describe the effects of photon losses on a given mode 0 in the noisy gates formalism is to consider the system in contact with an environment that absorbs photons. By following the protocol described in Chapter 4 we have to choose the operators in Eq. (1.19): the Hamiltonian operator is the phase shifter Hamiltonian in Eq. (5.2) on mode 0, i.e. $\hat{\mathrm{P}}_0 = \hat{a}_0^\dagger \hat{a}_0$, while we choose $\hat{a}_0$ as Lindblad operator $\hat{\mathrm{L}}$. By using Eq. (4.10), the corresponding expression for the noisy gate reads

$$\hat{\mathrm{N}}_0 = \hat{\mathrm{U}}_0 e^{-\frac{\epsilon_0^2}{2}\hat{\mathrm{D}}_0} e^{i\epsilon_0 \hat{\mathrm{S}}_0}, \tag{5.10}$$

where $\hat{\mathrm{U}}_0 = e^{i\theta\hat{\mathrm{P}}_0}$, $\hat{\mathrm{D}}_0 = \int_{t_0}^t \mathrm{ds}(\hat{a}_0^\dagger(s)\hat{a}_0(s) - \hat{a}_0^2(s))$ and
$\hat{\mathrm{S}}_0 = \int_{t_0}^t \mathrm{dW(s)}\hat{a}_0(s)$. The time dependent creation operator reads

$$\hat{a}_0^\dagger(s) = \hat{\mathrm{U}}_0^\dagger(s,t_0)\hat{a}_0^\dagger\hat{\mathrm{U}}_0(s,t_0) = e^{-i\theta(s,t_0)}\hat{a}_0^\dagger \tag{5.11}$$

similarly to Eq.(5.3). Thus we can write

$$\hat{\mathrm{D}}_0 = \Delta t \hat{a}_0^\dagger \hat{a}_0 + (\mathrm{D}_C - i\mathrm{D}_S)\hat{a}_0^2\,, \;\; \hat{\mathrm{S}}_0 = (\mathrm{I}_C - i\mathrm{I}_S)\hat{a}_0 \tag{5.12}$$

where $\mathrm{D}_C = \int_{t_0}^t \mathrm{ds}\cos 2\theta(s,t_0)$, $\mathrm{D}_S = \int_{t_0}^t \mathrm{ds}\sin 2\theta(s,t_0)$,
$\mathrm{I}_C = \int_{t_0}^t \mathrm{dW(s)}\cos\theta(s,t_0)$, $\mathrm{I}_S = \int_{t_0}^t \mathrm{dW(s)}\sin\theta(s,t_0)$. The latters are Gaussian stochastic processes with means $\mathbb{E}\big[\mathrm{I}_C\big] = \mathbb{E}\big[\mathrm{I}_S\big] = 0$, variances $\mathbb{V}\big[\mathrm{I}_C\big] = \int_{t_0}^t \mathrm{d}s\cos^2\theta(s,t_0)$, $\mathbb{V}\big[\mathrm{I}_S\big] = \int_{t_0}^t \mathrm{d}s\sin^2\theta(s,t_0)$ and covariance $\mathbb{E}\big[\mathrm{I}_C\mathrm{I}_S\big] = \int_{t_0}^t \mathrm{d}s\cos\theta(s,t_0)\sin\theta(s,t_0)$.
However, at this point a difficulty arises because $\hat{\mathrm{N}}_0\hat{a}_0^\dagger\hat{\mathrm{N}}_0^\dagger$ cannot be expressed explicitly as a unitary matrix acting on the creation operators, as in Eqs. (5.3) and (5.9).
In order to avoid such problem we consider a larger physical system consisting of two photon modes: mode 0 is the physical mode where the phase shifter acts, while mode 1 is a virtual mode that we exploit to model photon losses. The idea is to model the environment as a beam splitter between the two modes, and then trace out the virtual mode. In such a way, the effective action on the system is that the photon is absorbed with some probability. In this new configuration, we choose $\hat{\mathrm{B}}_{01} = \hat{a}_0\hat{a}_1^\dagger + \hat{a}_0^\dagger\hat{a}_1$ as Lindblad operator $\hat{\mathrm{L}}$; the latter can be obtained from the expression for $\hat{\mathrm{B}}(\phi)$ in Eq. (5.4)

by setting $\phi = 0$. This Lindblad operator acts as a virtual beam splitter that can shift photons from mode 0 to the virtual mode 1. The resulting noisy phase shifter is of the form in Eq. (4.10) without the deterministic term due to the fact that the Lindblad operator $\hat{\mathrm{B}}_{01}$ that we chose is Hermitian. Then we can write

$$\hat{\mathrm{N}}_{01} = \hat{\mathrm{U}}_0 e^{i\epsilon_0 \hat{\mathrm{S}}_{01}}, \tag{5.13}$$

where $\hat{\mathrm{U}}_0 = e^{i\theta \hat{\mathrm{P}}_0}$ and $\hat{\mathrm{S}}_{01} = \int_{t_0}^{t} \mathrm{dW(s)} \hat{\mathrm{B}}_{01}(s)$.
At this point we need to compute the form of the stochastic operator $\hat{\mathrm{S}}_{01}$. We notice that

$$\begin{aligned}
&\hat{\mathrm{B}}_{01}(s) = \hat{\mathrm{U}}_0^\dagger(s,t_0)\hat{\mathrm{B}}_{01}\hat{\mathrm{U}}_0(s,t_0) \\
&= e^{-i\theta(s,t_0)\hat{\mathrm{P}}_0}\hat{a}_0 e^{i\theta(s,t_0)\hat{\mathrm{P}}_0}\hat{a}_1^\dagger + e^{-i\theta(s,t_0)\hat{\mathrm{P}}_0}\hat{a}_0^\dagger e^{i\theta(s,t_0)\hat{\mathrm{P}}_0}\hat{a}_1 \\
&= e^{i\theta(s,t_0)}\hat{a}_0\hat{a}_1^\dagger + e^{-i\theta(s,t_0)}\hat{a}_0^\dagger\hat{a}_1 \\
&= \cos\theta(s,t_0)(\hat{a}_0\hat{a}_1^\dagger + \hat{a}_0^\dagger\hat{a}_1) + i\sin\theta(s,t_0)(\hat{a}_0\hat{a}_1^\dagger - \hat{a}_0^\dagger\hat{a}_1) \\
&= \cos\theta(s,t_0)\hat{\mathrm{B}}_{01} - \sin\theta(s,t_0)\hat{\mathrm{C}}_{01}
\end{aligned} \tag{5.14}$$

where in the third line we used Eq.(5.3) with the adjoint unitary evolution and we define $\hat{\mathrm{C}}_{01} = i(\hat{a}_0^\dagger\hat{a}_1 - \hat{a}_0\hat{a}_1^\dagger)$, which can be obtained from $\hat{\mathrm{B}}(\phi)$ in Eq.(5.4) by choosing $\phi = \pi/2$.
Then the stochastic operator reads

$$\hat{\mathrm{S}}_{01} = \mathrm{I}_C\hat{\mathrm{B}}_{01} - \mathrm{I}_S\hat{\mathrm{C}}_{01}, \tag{5.15}$$

where $\mathrm{I}_C = \int_{t_0}^{t} \mathrm{dW(s)} \cos\theta(s,t_0)$ and $\mathrm{I}_S = \int_{t_0}^{t} \mathrm{dW(s)} \sin\theta(s,t_0)$. The latters are the same stochastic integrals defined before.
Finally, by exploiting the fact that at second order in ϵ one has $e^{\epsilon(\hat{\mathrm{A}}+\hat{\mathrm{B}})} = e^{\epsilon\hat{\mathrm{A}}}e^{\epsilon\hat{\mathrm{B}}}$, from Eq. (5.13) we get

$$\hat{\mathrm{N}}_{01} = \hat{\mathrm{U}}_0 e^{i\epsilon_0 \mathrm{I}_C \hat{\mathrm{B}}_{01}} e^{-i\epsilon_0 \mathrm{I}_S \hat{\mathrm{C}}_{01}}. \tag{5.16}$$

Through Eq. (5.16) one can compute the evolution of creation and annihilation operators under the action of a noisy phase shifter. As seen before, we can express compactly these transformations with unitary matrices that act on vectors of creation operators. In the case of the noisy phase shifter we have

$$\begin{aligned}
\hat{\mathcal{N}}_{01} = &\begin{pmatrix} e^{i\theta} & 0 \\ 0 & 1 \end{pmatrix} \cdot \begin{pmatrix} \cos(\epsilon_0 \mathrm{I_C}) & i\sin(\epsilon_0 \mathrm{I_C}) \\ i\sin(\epsilon_0 \mathrm{I_C}) & \cos(\epsilon_0 \mathrm{I_C}) \end{pmatrix} \cdot \\
&\begin{pmatrix} \cos(\epsilon_0 \mathrm{I_S}) & -\sin(\epsilon_0 \mathrm{I_S}) \\ \sin(\epsilon_0 \mathrm{I_S}) & \cos(\epsilon_0 \mathrm{I_S}) \end{pmatrix},
\end{aligned} \tag{5.17}$$

whereas $\hat{\mathcal{N}}_{01}^{\dagger}$ acts on annihilation operators. In Eq. (5.17) the parameter ϵ_0 is connected to photon loss probability p_0 on mode 0 as $\epsilon_0 = \sqrt{-\log(1-2\mathrm{p}_0)/2}$ where $\mathrm{p}_0 = (1-e^{-2\Delta t/T})/2$ and $\epsilon_0^2 = \Delta t/T$, with T the characteristic time of photon losses. We choose such time dependence for p_0 because by taking the average over the processes I_C and I_S one has $\mathbb{E}[\sin^2(\epsilon \mathrm{I}_k)] = (1-e^{-2\epsilon_0^2})/2 = \mathrm{p}_0$ with $k = C, S$. Moreover, we are not interested in the regime in which there is more than 50% of loss probability.
By tracing out the virtual mode we get the expression for the noisy phase shifter

$$\hat{\mathcal{N}}_0 = e^{i\theta}\cos(\epsilon_0 \mathrm{I_C})\cos(\epsilon_0 \mathrm{I_S}) \tag{5.18}$$

5.2.3 Noisy beam splitter

For the beam splitter we consider modes 0 and 1 as physical modes and mode 2 as virtual mode. The Hamiltonian operator we choose is that in Eq. (5.2) with $\phi = 0$, ie $\hat{\mathrm{B}}_{01} = \hat{a}_0\hat{a}_1^{\dagger} + \hat{a}_0^{\dagger}\hat{a}_1$. As Lindblad operators we choose $\hat{\mathrm{B}}_{02} = \hat{a}_0\hat{a}_2^{\dagger} + \hat{a}_0^{\dagger}\hat{a}_2$ and $\hat{\mathrm{B}}_{12} = \hat{a}_1\hat{a}_2^{\dagger} + \hat{a}_1^{\dagger}\hat{a}_2$. The corresponding noisy beam splitter reads

$$\hat{\mathrm{N}}_{012} = \hat{\mathrm{U}}_{01} e^{i\epsilon_0 \hat{\mathrm{S}}_{02} + i\epsilon_1 \hat{\mathrm{S}}_{12}}, \tag{5.19}$$

where $\hat{\mathrm{U}}_{01} = e^{i\frac{\theta}{2}\hat{\mathrm{B}}_{01}}$ and $\hat{\mathrm{S}}_{j2} = \int_{t_0}^{t} \mathrm{dW_j(s)}\hat{\mathrm{B}}_{j2}(s)$ with $j = 0, 1$. In Eq. (5.19) the parameters ϵ_j are defined as $\epsilon_j = \sqrt{-\log(1-2\mathrm{p}_j)/2}$ analogously to the noisy phase shifter case. By performing a similar calculation to Eq.(5.14) where now one uses the beam splitter relations in Eqs. (5.5),(5.6),(5.7) and (5.8) with the adjoint unitary evolution, the expressions for $\hat{\mathrm{B}}_{j2}(s)$ are

$$\hat{\mathrm{B}}_{02}(s) = \cos\left(\frac{\theta(s,t_0)}{2}\right)\hat{\mathrm{B}}_{02} - \sin\left(\frac{\theta(s,t_0)}{2}\right)\hat{\mathrm{C}}_{12}, \tag{5.20}$$

$$\hat{\mathrm{B}}_{12}(s) = \cos\left(\frac{\theta(s,t_0)}{2}\right)\hat{\mathrm{B}}_{12} - \sin\left(\frac{\theta(s,t_0)}{2}\right)\hat{\mathrm{C}}_{02}, \tag{5.21}$$

where $\hat{\mathrm{C}}_{j2} = i(\hat{a}_j^{\dagger}\hat{a}_2 - \hat{a}_j\hat{a}_2^{\dagger})$. The stochastic operators are then:

$$\hat{\mathrm{S}}_{02} = \mathrm{I}_{C0}\hat{\mathrm{B}}_{02} - \mathrm{I}_{S0}\hat{\mathrm{C}}_{12}, \tag{5.22}$$

$$\hat{\mathrm{S}}_{12} = \mathrm{I}_{C1}\hat{\mathrm{B}}_{12} - \mathrm{I}_{S1}\hat{\mathrm{C}}_{02}, \tag{5.23}$$

where $\mathrm{I}_{Cj} = \int_{t_0}^{t} \mathrm{dW_j(s)} \cos\theta(s,t_0)$ and $\mathrm{I}_{Sj} = \int_{t_0}^{t} \mathrm{dW_j(s)} \sin\theta(s,t_0)$. The latter Gaussian processes have the same variances and covariances computed before for the case of phase shifter. Finally we can express Eq.(5.19) as

$$\hat{\mathrm{N}}_{012} = \hat{\mathrm{U}}_{01} e^{i\epsilon_0 \mathrm{I}_{C0} \hat{\mathrm{B}}_{02}} e^{-i\epsilon_0 \mathrm{I}_{S0} \hat{\mathrm{C}}_{12}} e^{i\epsilon_1 \mathrm{I}_{C1} \hat{\mathrm{B}}_{12}} e^{-i\epsilon_1 \mathrm{I}_{S1} \hat{\mathrm{C}}_{02}} , \tag{5.24}$$

and the corresponding action on creation operators is given by

$$\begin{aligned}
\hat{\mathcal{N}}_{012} = &\begin{pmatrix} \cos\theta/2 & i\sin\theta/2 & 0 \\ i\sin\theta/2 & \cos\theta/2 & 0 \\ 0 & 0 & 1 \end{pmatrix} \cdot \begin{pmatrix} \cos(\epsilon_0 \mathrm{I_{C0}}) & 0 & i\sin(\epsilon_0 \mathrm{I_{C0}}) \\ 0 & 1 & 0 \\ i\sin(\epsilon_0 \mathrm{I_{C0}}) & 0 & \cos(\epsilon_0 \mathrm{I_{C0}}) \end{pmatrix} \cdot \\
&\begin{pmatrix} 1 & 0 & 0 \\ 0 & \cos(\epsilon_0 \mathrm{I_{S0}}) & -\sin(\epsilon_0 \mathrm{I_{S0}}) \\ 0 & \sin(\epsilon_0 \mathrm{I_{S0}}) & \cos(\epsilon_0 \mathrm{I_{S0}}) \end{pmatrix} \cdot \begin{pmatrix} 1 & 0 & 0 \\ 0 & \cos(\epsilon_1 \mathrm{I_{C1}}) & i\sin(\epsilon_1 \mathrm{I_{C1}}) \\ 0 & i\sin(\epsilon_1 \mathrm{I_{C1}}) & \cos(\epsilon_1 \mathrm{I_{C1}}) \end{pmatrix} \cdot \\
&\begin{pmatrix} \cos(\epsilon_1 \mathrm{I_{S1}}) & 0 & -\sin(\epsilon_1 \mathrm{I_{S1}}) \\ 0 & 1 & 0 \\ \sin(\epsilon_1 \mathrm{I_{S1}}) & 0 & \cos(\epsilon_1 \mathrm{I_{S1}}) \end{pmatrix} .
\end{aligned} \tag{5.25}$$

By tracing out the virtual mode we get the expression for the noisy beam splitter

$$\begin{aligned}
\hat{\mathcal{N}}_{01} = &\begin{pmatrix} \cos\theta/2 & i\sin\theta/2 \\ i\sin\theta/2 & \cos\theta/2 \end{pmatrix} \cdot \begin{pmatrix} \cos(\epsilon_0 \mathrm{I_{C0}}) & 0 \\ 0 & 1 \end{pmatrix} \cdot \\
&\begin{pmatrix} 1 & 0 \\ 0 & \cos(\epsilon_0 \mathrm{I_{S0}}) \end{pmatrix} \cdot \begin{pmatrix} 1 & 0 \\ 0 & \cos(\epsilon_1 \mathrm{I_{C1}}) \end{pmatrix} \cdot \begin{pmatrix} \cos(\epsilon_1 \mathrm{I_{S1}}) & 0 \\ 0 & 1 \end{pmatrix} .
\end{aligned} \tag{5.26}$$

5.3 Imperfect single-photon sources, lossy optical guides and detection

As explained in section 5.1, photon generation, propagation of photons inside optical guides and detection are also affected by errors. We now describe how to account for such errors with our formalism.

5.3.1 Imperfect single-photon sources

A quantum dot undergoing decoherence processes generates non perfect indistinguishable photons. In the case of dual rail encoding, the only relevant property is the photon path, i.e. through

which optical guide the photon is traveling. Then, in this setup, the only way to understand whether two photons are distinguishable, if we consider only non-coherent errors, is when the associated qubit state is not completely pure. This can be described by considering depolarizing errors arising at the sources and inherited by the photons.

To model imperfect single-photon sources we apply at the beginning of the optical circuit a layer of fictitious optical elements to each mode that simulate the depolarizing errors. Such optical elements can be built by applying again the noisy gates formalism. Here we focus on single qubit depolarizing channel, but one could straightforwardly extend the approach to multi-qubit depolarizing channel.

Depolarizing for a single spin state can be described by the Lindblad operators $\hat{\mathrm{X}}$,$\hat{\mathrm{Y}}$ and $\hat{\mathrm{Z}}$. We can map such operators to operators defined in terms of creation and annihilation operators on the physical modes, thus acting on photons of the circuit. We notice for example that by solving the Schrödinger equation with the beam splitter Hamiltonian in Eq.(5.4) with $\phi = 0$ and $\theta = \pi$, one gets a unitary on the creation operators that acts as an $\hat{\mathrm{X}}$ gate on a qubit in the dual rail encoding (see Eq.(5.9)). Similarly a $\hat{\mathrm{Y}}$ is obtained with $\phi = \pi/2$ and $\theta = \pi$. The operator $\hat{\mathrm{Z}}$ is obtained by solving the Schrödinger equation with the phase shifter Hamiltonian in Eq.(5.2) with $\theta = \pi$ applied to mode 1. For these reasons, to describe depolarizing errors, we can use Eq.(7.9) without Hamiltonian operator and with the Lindblad operators $\hat{\mathrm{B}}_{01}$, $\hat{\mathrm{C}}_{01}$ and $\hat{\mathrm{P}}_1$. The resulting noisy gate is:

$$\hat{\mathrm{N}}_{01}^{(\mathrm{dep})} = e^{i\epsilon_d \hat{\mathrm{S}}_{01}^{(x)}} e^{i\epsilon_d \hat{\mathrm{S}}_{01}^{(y)}} e^{i\epsilon_d \hat{\mathrm{S}}_{01}^{(z)}}, \tag{5.27}$$

where $\hat{\mathrm{S}}_{01}^{(x)} = \hat{\mathrm{B}}_{01}\mathrm{W}_x(t,t_0)$, $\hat{\mathrm{S}}_{01}^{(y)} = \hat{\mathrm{C}}_{01}\mathrm{W}_y(t,t_0)$ and $\hat{\mathrm{S}}_{01}^{(z)} = \hat{\mathrm{P}}_1\mathrm{W}_z(t,t_0)$. The corresponding unitary on the creation and annihilation operators becomes:

$$\begin{aligned}\hat{\mathcal{N}}_{01}^{(\mathrm{dep})} = &\begin{pmatrix} \cos(\epsilon_d \mathrm{W}_x) & i\sin(\epsilon_d \mathrm{W}_x) \\ i\sin(\epsilon_d \mathrm{W}_x) & \cos(\epsilon_d \mathrm{W}_x) \end{pmatrix} \cdot \\ &\begin{pmatrix} \cos(\epsilon_d \mathrm{W}_y) & -\sin(\epsilon_d \mathrm{W}_y) \\ \sin(\epsilon_d \mathrm{W}_y) & \cos(\epsilon_d \mathrm{W}_y) \end{pmatrix} \cdot \begin{pmatrix} 1 & 0 \\ 0 & e^{i\epsilon_d \mathrm{W}_z} \end{pmatrix}.\end{aligned} \tag{5.28}$$

Here the parameter ϵ_d has the same definition of the loss parameter

but now it is related to depolarizing probability p_d. Moreover we stress that, despite the similarity with the noisy gate of lossy optical elements, the effects of Eqs. (5.27), (5.28) are different because modes 0 and 1 are both physical modes, there are not virtual modes.

5.3.2 Lossy optical guides and detection

In Sec. 5.2 we have dealt with optical elements affected by photon losses, however photons inside optical guides and detectors are also subject to this kind of noise. Then, as in the case of noisy phase shifter we can consider two photon modes 0, 1, respectively physical and virtual mode, with Lindblad operator $\hat{\mathrm{B}}_{01}$ but this time we use Eq. (7.9) without Hamiltonian operator. A straightforward calculation leads to:

$$\hat{\mathrm{N}}_{01}^{(\mathrm{loss})} = e^{i\epsilon\hat{\mathrm{S}}_{01}}, \tag{5.29}$$

where $\hat{\mathrm{S}}_{01} = \hat{\mathrm{B}}_{01}\mathrm{W}(t,t_0)$ and $\epsilon = \sqrt{-\log\left(1-2\mathrm{p}\right)/2}$ with p the loss probability inside the optical guide or the detector. Consequentially we have:

$$\hat{\mathcal{N}}_{01}^{(\mathrm{loss})} = \begin{pmatrix} \cos\left(\epsilon\mathrm{W}\right) & i\sin\left(\epsilon\mathrm{W}\right) \\ i\sin\left(\epsilon\mathrm{W}\right) & \cos\left(\epsilon\mathrm{W}\right) \end{pmatrix}. \tag{5.30}$$

By tracing out the virtual mode we obtain:

$$\hat{\mathcal{N}}_{0}^{(\mathrm{loss})} = \cos\left(\epsilon\mathrm{W}\right). \tag{5.31}$$

5.4 Comparison with other approaches

In the literature, there are two main approaches for simulating photon losses: fixed-loss model [163–165] and beam splitter loss model [165–168]. The former one was developed when the number of lost particles can be effectively controlled; indeed it is based on the assumption that initially there are n photons and exactly $n-l$ of them are lost. The loss is simulated by tracing out $n-l$ of the n photons $\hat{\rho}' = \mathrm{Tr}_{n-l}(\hat{\rho})$ and by using the fact that $\mathrm{Tr}_{n-l}(\hat{\mathrm{U}}^{\otimes n}\hat{\rho}\hat{\mathrm{U}}^{\dagger\otimes n}) = \hat{\mathrm{U}}^{\otimes n}\,\mathrm{Tr}_{n-l}(\hat{\rho})\hat{\mathrm{U}}^{\dagger\otimes n}$. Thus, it does not matter whether losses occurred before or after the implemented linear transformation. However, a simulation method that describes a fixed number of lost photons is limited since in real optical circuits this number is a random variable.

In the second approach, the beam splitter loss model is based on the idea of adding a virtual mode to the physical mode and applying a beam splitter (see Eq. (5.9) with $\phi = 0$) with a reflectance equal to the loss probability: $\mathrm{R} = \mathrm{p}$. Since the relation between reflectance and the angle θ of a beam splitter is $\cos(\theta/2) = \sqrt{1-\mathrm{R}}$ and $\sin(\theta/2) = \sqrt{\mathrm{R}}$, then one gets

$$\begin{pmatrix} \sqrt{1-\mathrm{p}} & i\sqrt{\mathrm{p}} \\ i\sqrt{\mathrm{p}} & \sqrt{1-\mathrm{p}} \end{pmatrix}, \tag{5.32}$$

where the probability of losing a photon is exactly $|{}_{\text{out}}\langle 01|10\rangle_{\text{in}}|^2 = \mathrm{p}$. This approach is very close to what we derived for lossy optical guides and detection in Sec. 5.3.2, because Eq. (5.30) is the stochastic version of Eq. (5.32). Indeed, in our case the probability of losing a photon is $|{}_{\text{out}}\langle 01|10\rangle_{\text{in}}|^2 = \sin^2(\epsilon \mathrm{W})$ and by taking the average over the Wiener process one has $\mathbb{E}[\sin^2(\epsilon \mathrm{W})] = (1 - e^{-2\epsilon^2})/2 = \mathrm{p}$.
This analogy is limited only to lossy optical guides and detectors. Indeed, the stochastic processes appearing in the expressions for noisy optical elements in Eq. (5.17) and (5.25) are not independent from the parameters of the corresponding optical elements. Therefore our approach is not reducible to the beam splitter loss model: as a result of including the noise into the gates, each noisy optical elements has its own lossy behaviour (even if the error probability is the same for all elements). Experimentally the dependence of photon losses on the parameters of optical elements is small and the usual assumption to perform simulations is that photon loss is independent from the angles of beam splitters and phase shifters [144]. However, we already proved in [30], for the case of superconducting devices, that relaxing this assumption, namely that of separating the noise and unitary evolution, provides a more accurate noise simulation tool.
Regarding the treatment of imperfect photon sources, different approaches exist in the literature. In [169], the authors considered a parametrized quantum dot able to simulate the creation of pairs of entangled photon in a mixed state. Another example is the modeling used in [170] where an imperfect quantum-dot based single-photon source is modeled by a statistical mixture of Fock states. In this work we deal with single-photon sources thus, following the latter approach, we implemented the stochastic unraveling of a single

qubit depolarizing Kraus map as shown in Eq. (5.28), that equivalently outputs a mixed Fock state of the qubits. In general one could use n qubits depolarizing channels to take into account multi photon distinguishability [146].

5.5 Testing the protocol

In the following section we test the performances of our noisy gates method. First, in subsection 5.5.1 we simulate the effects of imperfect photon sources and photon loss on the X gate and on the preparation of the Bell state in the gate based quantum computing (GBQC) framework. Then, in subsection 5.5.2 we perform the same simulation in the measurement based quantum computing (MBQC) framework [171, 172] reproducing the X gate. Finally in subsection 5.5.3 we build a noisy variational quantum algorithm (VQA) [60, 173] to solve the max 2-cut problem [174–176] and we study its performances in different noise scenarios.

All the optical circuits we implement are written in the standard triangular Reck decomposition [177], except for the VQA ansatz. As computational backend for the simulations we used the SLOS backend [178] in Perceval [170] and measurements in MBQC framework are handled with the MBQC module of Paddle Quantum [179]. Moreover, the transpilation required to obtain the optical circuits in subsections 5.5.1 and 5.5.2 are performed by using the Qiskit-Converter functionality of Perceval.

To simulate the effect of imperfect photon sources, we add to the optical circuit a layer of fictitious optical elements modeling depolarization, see Eq. (5.28), for each couple of modes. To simulate photon losses, each optical element of the original circuit is replaced with the corresponding noisy one, see Eqs. (5.18) and (5.26), and for losses at detection we add a layer of lossy channel for each mode as in Eq. (5.31). The corresponding noisy optical circuit is schematically depicted in Fig. 5.5.1.

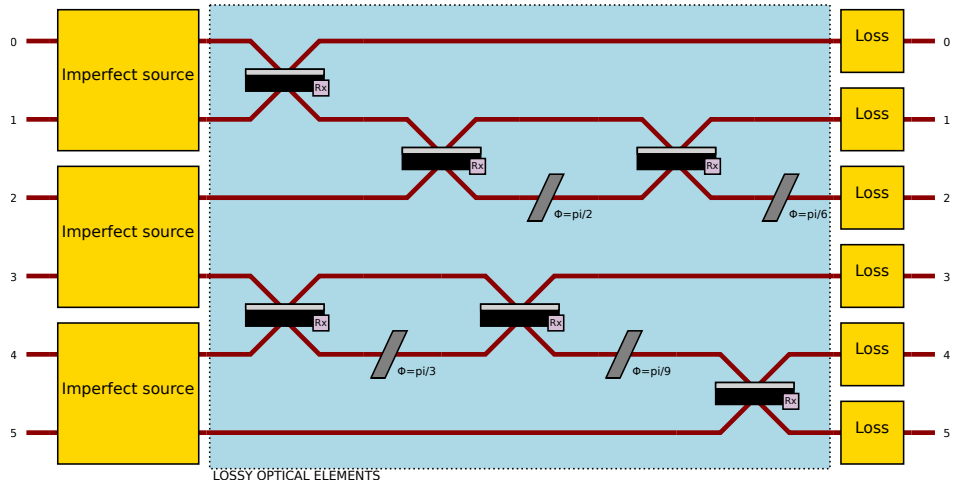

Figure 5.5.1: Schematic depiction of how we simulate a generic noisy optical circuit. On the left in yellow, a layer of fictitious optical elements models depolarization for each couple of modes. In the blue area, each optical element of the original circuit is replaced with the corresponding noisy one and for losses at detection we add a layer of lossy channel for each mode, shown here in yellow on the right.

5.5.1 X gate and Bell state in the gate based framework

We simulate the X gate and Bell state preparation with our approach, eventually obtaining the output density matrix $\hat{\rho}^{\text{ng}}$. If $\hat{\sigma}$ is the noiseless output density matrix, we compare these two states by computing the Hellinger distance $\mathcal{H}^{\text{ng}} = \mathcal{H}(\hat{\rho}^{\text{ng}}, \hat{\sigma})$ defined in Eq. (4.26). We repeat these simulations for diverse type of noise (depolarizing and photon loss) and different error probabilities.
The results of the simulations are shown in Figs. 5.5.2 and 5.5.3.

All results shown are normalized with respect to the postselection/heralding probability. In Fig. 5.5.2, panel (a) shows the effect of depolarization that is to bring the system to the completely mixed state, with $\rho_{00} = \rho_{11} = 1/2$. The effect of photon losses, shown in panel (b), is to decrease ρ_{11}, as expected: in this case the state is not normalized as the action of losses is non unitary, see also Eqs. (5.18), (5.26) and (5.31). The combined action of depolarization and photon losses is shown in panel (c): the effects of depolarization are lowered by the presence of photon losses. Panel (d) displays the Hellinger distances of the three simulations with respect to the ideal result. For the circuit preparing the Bell state in

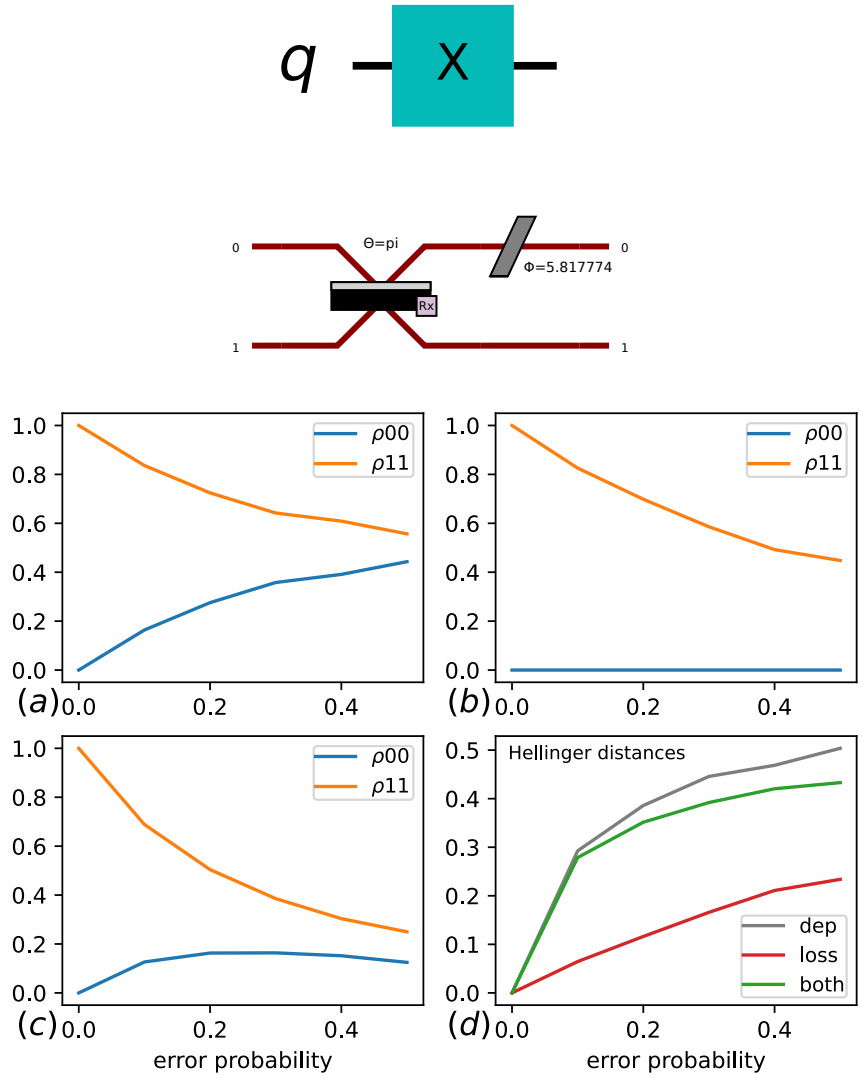

Figure 5.5.2: X gate in the gate based framework. Panels (a), (b), (c) show the values of the entries ρ_{00} (blue) and ρ_{11} (orange) of the density matrix for the X gate, as the error probabilities increase. Panel (a) takes into account only imperfect photon sources (modeled as depolarization), panel (b) photon loss errors and panel (c) the combination of the two. Panel (d) shows the Hellinger distances between the outcomes of the simulations in (a) (grey), (b) (green), (c) (red) and the ideal result of the X gate. On the top, the circuit for the X gate in GBQC and the corresponding optical circuit.

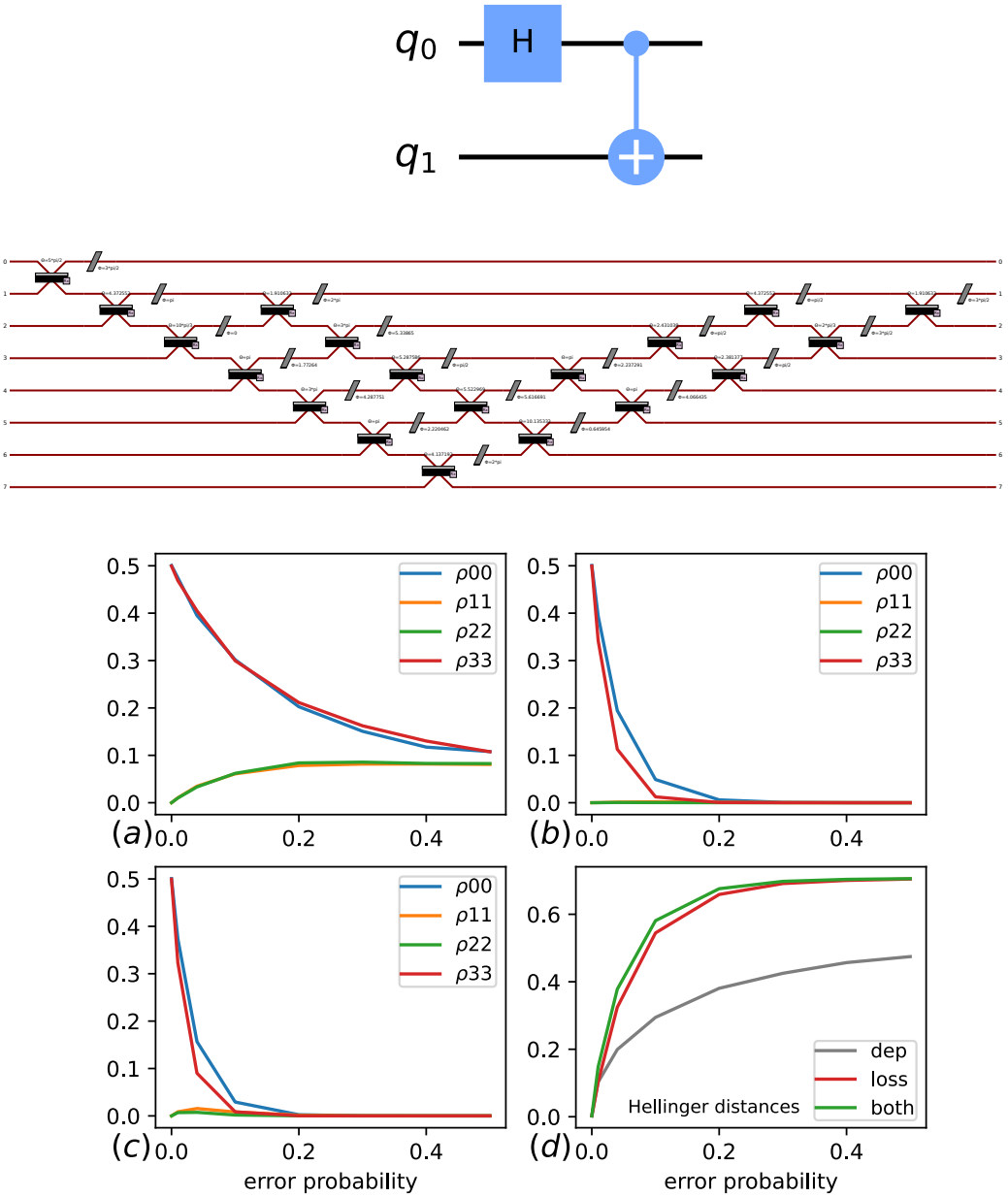

Figure 5.5.3: Bell state in the gate based framework. Panels (a), (b), (c) show the values of the entries of ρ_{00} (blue) and ρ_{11} (orange), ρ_{22} (green), ρ_{33} (red) of the density matrix for the Bell state. The order of the different noise sources considered is the same as for the X gate Fig.5.5.2. Panel (d) shows the Hellinger distances between the outcomes of the simulations and the ideal result of the Bell state, colors have the same meaning as for panel (d) of Fig.5.5.2. On the top the circuit for the Bell state in GBQC is shown, and on the bottom the corresponding optical circuit.

Fig. 5.5.3, the effect of depolarization, shown in panel (a), is again to bring the system to a mixed state. In general, for two qubits the equal probability of the maximally mixed state is 1/4, however in this case depolarization is applied not only on system qubits but also on ancillary qubits, necessary to implement the CX gate; this leads to a mixed state different from the maximally mixed state for two qubits.
The effect of photon losses in panel (b) is way larger than for the X gate; the reason is that the optical circuit to realize the Bell state has a significantly higher depth and a larger number of modes as can be seen by comparing the optical circuits in Figs. 5.5.2 and 5.5.3. Panel (c) shows that photon losses are dominant in this case, as the plot is very close to panel (b). Panel (d) displays the Hellinger distances of the three simulations with respect to the ideal result.

5.5.2 X gate in the measurement based framework

The framework of dual rail encoding of linear optics quantum computing is suitable to implement alternative scheme for quantum computation, in particular measurement based quantum computing (MBQC). Such a scheme involves the generation of particular entangled states called cluster states and appropriate single qubit measurement to drive the computation. These two stages involve photon generation, manipulation and detection thus, as for GBQC, MBQC is affected by photon losses and imperfect photon sourcing. To test the robustness of MBQC against such noises, we focus on the realization of X gate. The simplest implementation of the X gate is schematically depicted as

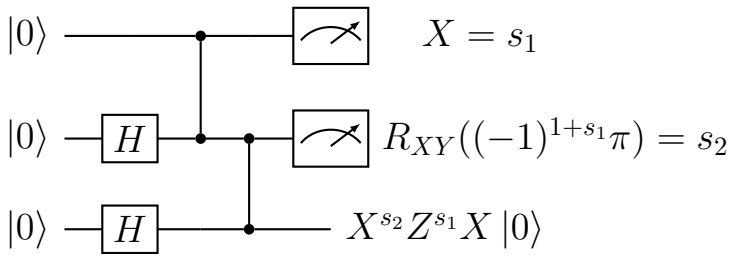

(5.33)

Qubit 1 is prepared in the state $|0\rangle$, while qubits 2,3 are both prepared into the $|+\rangle$ state. Qubit 1 is entangled with 2, and qubit 2 is entangled with 3 via CZ gates; The output state at this stage is

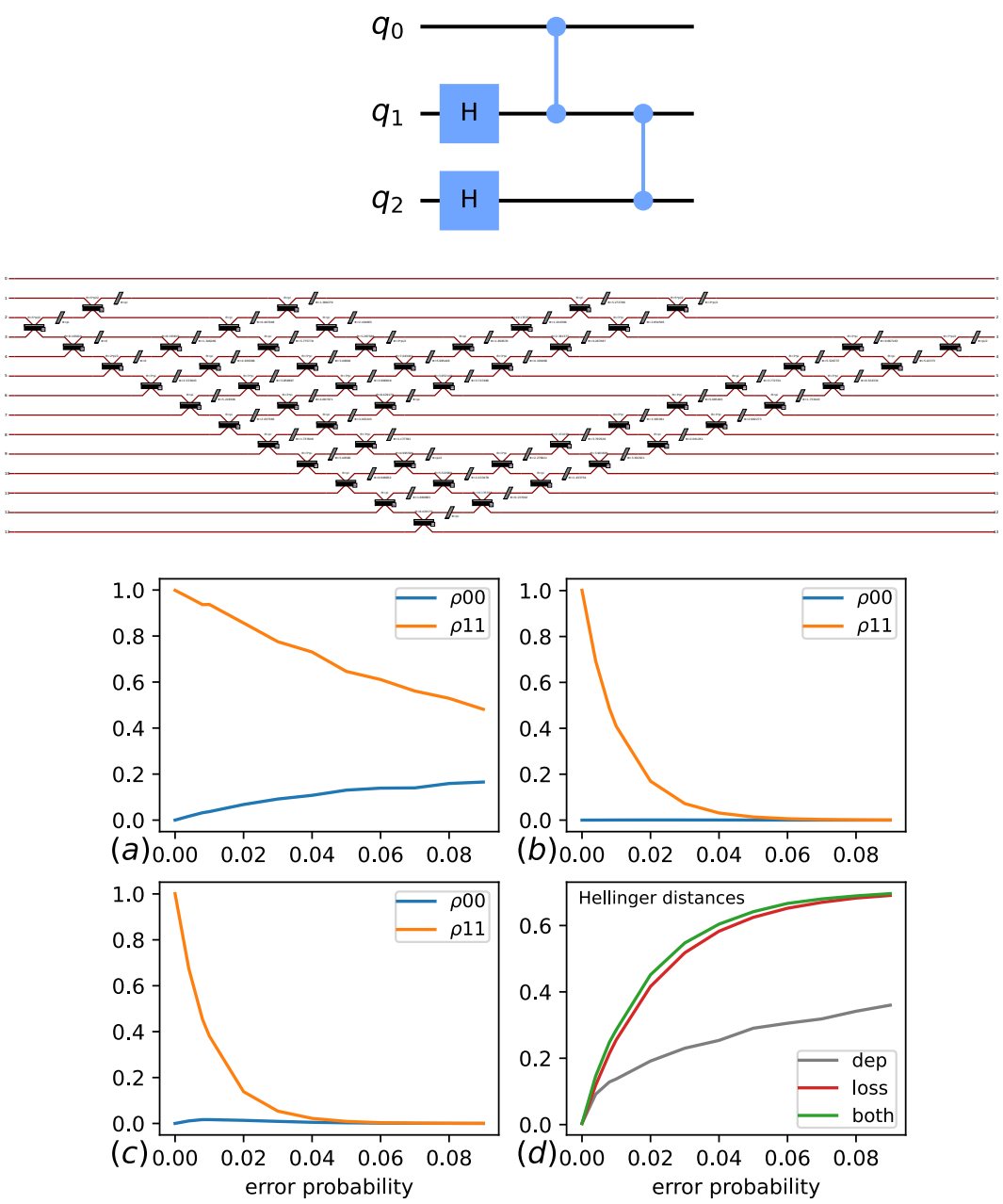

Figure 5.5.4: X gate in the measurement based framework. Panels (a), (b), (c) show the values of the entries ρ_{00} (blue) and ρ_{11} (orange) of the density matrix for the X gate in the MBQC framework as the error probabilities increase. Panel (a) takes into account only imperfect photon sources (modeled as depolarization), panel (b) photon loss errors and panel (c) the combination of the two. Panel (d) shows the Hellinger distances between the outcomes of the simulations in (a) (grey), (b) (green), (c) (red) and the ideal result of the X gate. On the top, the circuit required to prepare the cluster state for the X gate in MBQC is shown, and at the bottom the corresponding optical circuit is displayed. Measurements for the MBQC are not shown.

called cluster state. Then the first qubit is measured in the X basis and the measurement outcome s_1 is recorded. Qubit 2 is measured in the XY plane with an angle $\theta = (-1)^{1+s_1}\pi$ and the measurement outcome s_2 is recorded. After these two measurements, the state of qubit 3 is $\hat{\mathrm{X}}^{s_2}\hat{\mathrm{Z}}^{s_1}\hat{\mathrm{X}}\,|0\rangle = \hat{\mathrm{X}}^{s_2}\hat{\mathrm{Z}}^{s_1}\,|1\rangle$. Thus the initial $|0\rangle$ is flipped to $|1\rangle$ up to byproduct Pauli operators. We notice that a generic rotation around the X axis of angle α is realized by taking $\theta = (-1)^{1+s_1}\alpha$. The corresponding optical circuit that implements the cluster state for the X gate and the effect of noise are shown in Fig. 5.5.4.

As in the previous section, the effect of depolarization is to bring the system to the completely mixed state (panel (a)) and the effect of photon losses (panel (b)) is to decrease ρ_{11}; panel (c) reports the effect of both depolarization and photon losses. As one can notice by comparing the order of magnitude of the error probabilities of Figs. 5.5.2, 5.5.3 and Fig. 5.5.4, the impact of noise in the MBQC framework is way stronger due to the larger number of modes and optical elements in the MBQC optical circuit. For example, to perform the GBQC X gate, two modes and one beam splitter are enough, while for the MBQC X gate cluster state in the Reck decomposition one needs 14 modes and 116 optical elements.

We notice that all the CZ gates are implemented by adding four additional modes to herald the success of the gate. This extra ancillary cost is not always required, and most efficient layouts can be found but for the only purpose of testing our method, we did not further optimize the photonic circuits.

5.5.3 Variational quantum algorithm applied to the max 2-cut problem

We now focus on a VQA algorithm applied to the MAX 2-CUT problem. The MAX 2-CUT problem is a well known optimization problem that requires to find a cut dividing the vertices of a graph in two complementary subsets, such that the number of edges crossed by the cut is maximized. Given a graph $G = (V, E)$, with $V = \{1, \ldots, N\}$ and $E = \{\langle i, j\rangle\}$ the sets of vertices i and edges $\langle i, j\rangle$,

the goal is to maximize the following objective function

$$\hat{\mathrm{H}}_C = \sum_{\langle i,j \rangle} \frac{1}{2}(1 - \hat{\mathrm{Z}}_i \hat{\mathrm{Z}}_j). \tag{5.34}$$

We focus on a graph with $V = \{1, 2, 3, 4\}$ and
$E = \{\langle 1, 2\rangle \langle 2, 3\rangle \langle 3, 4\rangle \langle 4, 1\rangle\}$, thus a square graph with four nodes. The problem is equivalent to minimizing the cost Hamiltonian:

$$\hat{\mathrm{H}}_C = \sum_{\langle i,j \rangle} \hat{\mathrm{Z}}_i \hat{\mathrm{Z}}_j; \tag{5.35}$$

for this cost Hamiltonian, the optimal, or exact, energy is $E_0 = -4$, corresponding to the cut giving $V_1 = \{1, 3\}$ and $V_2 = \{2, 4\}$ as complementary subsets of V. This is the target energy of the optimization of the variational ansatz.
We choose a specific ansatz $\hat{\mathrm{U}}_{ansatz}(\theta)$ for the optimization shown in Fig. 5.5.5. The output of each simulations is a density matrix $\hat{\rho}$.

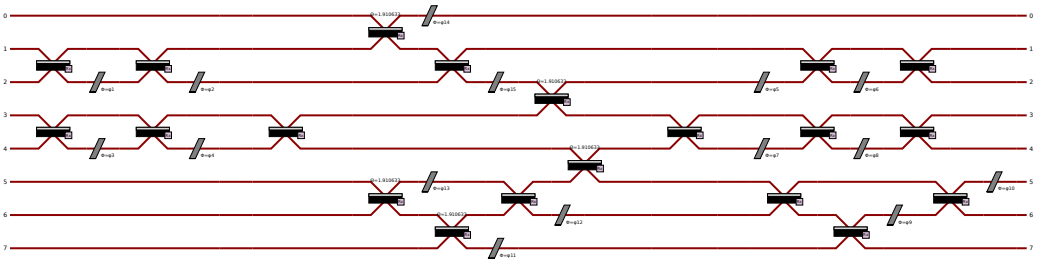

Figure 5.5.5: Optical circuit ansatz for the VQA solving the MAX 2-CUT on a square graph.

The cost function for the optimization is the energy calculated as $E = \mathrm{Tr}\left(\hat{\rho}(\theta)\hat{\mathrm{H}}_C\right)$, where $\hat{\rho}(\theta) = |\psi(\theta)\rangle \langle\psi(\theta)|$ and $|\psi(\theta)\rangle = \hat{\mathrm{U}}_{ansatz}(\theta) |0\rangle^{\otimes 4}$. We choose a number of samples $\mathrm{N}_{samples} = 500$ and initial parameters are chosen randomly. The classical optimizer method used to update the parameters is the gradient-free method COBYLA [180].
We study the convergence of the optimization in the noiseless case, in the presence of depolarization with $\mathrm{p} = 10^{-4}, 10^{-3}, 10^{-2}$, in the presence of loss with $\mathrm{p} = 10^{-4}, 10^{-3}, 10^{-2}$ and under the combined action of depolarization and loss with $\mathrm{p} = 10^{-4}, 10^{-3}, 10^{-2}$. We restrict the analysis to such orders of magnitude of the error probability, because for $\mathrm{p} < 10^{-4}$ the effects of noises on the ansatz circuit

are negligible and for $p > 10^{-2}$ results might not be reliable since our approach is perturbative, as shown in Chapter 4, as the error probability approaches 1.
The results are shown in Fig. 5.5.6.

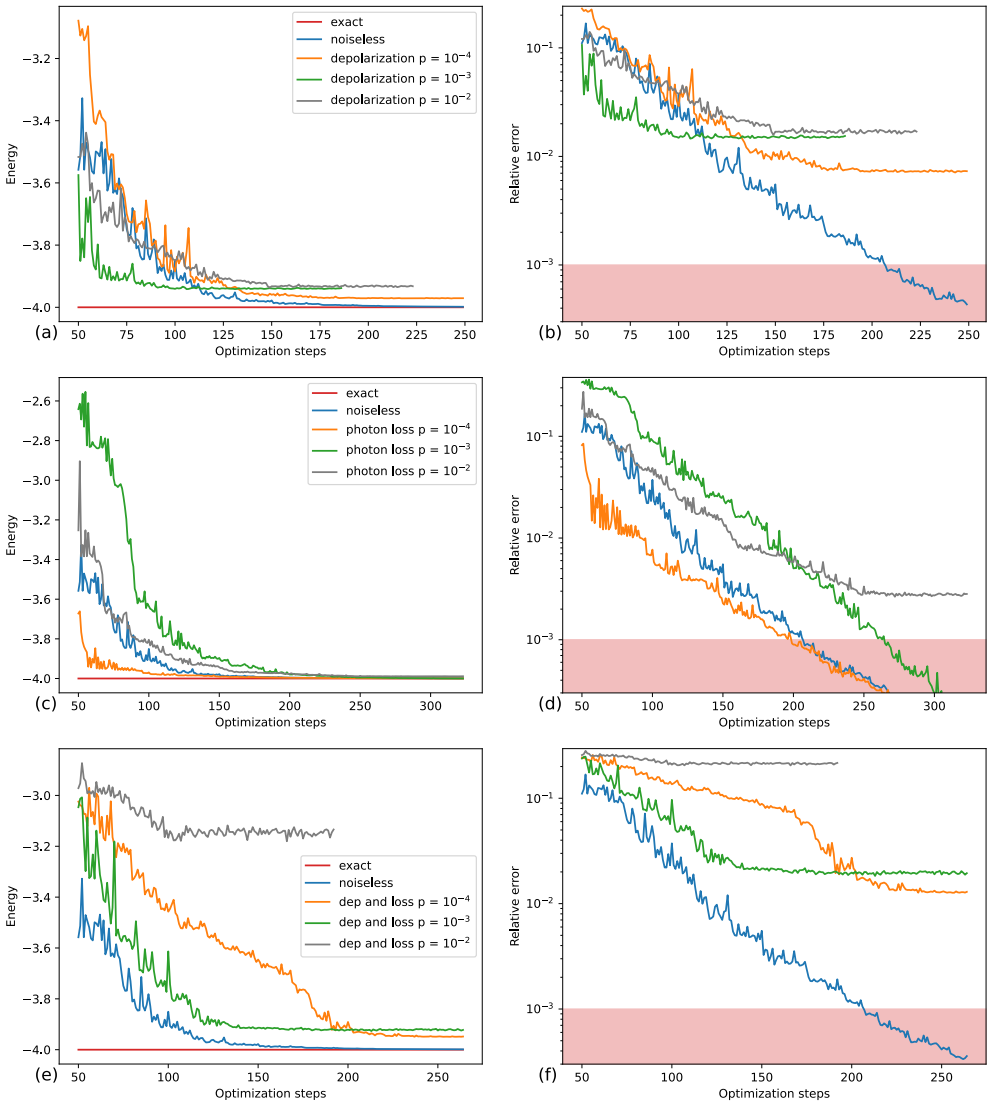

Figure 5.5.6: Panels (a), (c), and (e) show the optimization of the variational energy as a function of the number of optimization steps obtained with the simulations. Each curve is obtained by simulating the variational ansatz starting from random parameters. For visualization purposes, all panels start from the 50th optimization step. In each (a), (c) and (e) panels the red line is the exact energy $E_0 = -4$, the blue curve is the optimization in the noiseless case (which is the same curve in all plots), the orange, green and grey curves are obtained with an error probability of 10^{-4}, 10^{-3}, 10^{-2} respectively. Figures (b), (d), and (f) show the relative errors $|(E_0 - E)/E_0|$ as a function of the training steps. Colors of the curves have the same meaning of the upper panels. A 0.1% relative error threshold is here highlighted with a red shaded region for better visualization.

	$p = 10^{-4}$	$p = 10^{-3}$	$p = 10^{-2}$
Depolarization	0.9927	0.9846	0.9831
Photon Loss	0.999998	0.999985	0.997180
Dep and Loss	0.9875	0.9808	0.7835

Table 5.5.1: Values of the approximation ratio for different types of noises and for increasing order of magnitude of the error probability.

The noiseless optimization converges to the optimum value, showing that the ansatz works. Panels (a) and (b) show the simulations in the presence of depolarization: as expected, the higher the error probability, the higher the deviation from the exact energy. When $p = 10^{-4}$, the variational algorithm is still able to output an estimate E with a $\sim 1\%$ relative error. In case of photon losses, shown in panels (c) and (d), the ansatz seem to be more resilient: for $p = 10^{-4}$ and $p = 10^{-3}$ the relative error is below 0.1% and for $p = 10^{-2}$ the relative error is below 1%. The combined action of photon losses and depolarization, shown in panels (e) and (f), is to further decrease the accuracy of the optimization as all relative errors are above 1%. We report the approximation ratios, defined as $R = E_f/E_0$ where E_f is the final energy for different noises and different orders of magnitude of the error probability in Table 5.5.1. The best approximation ratios are obtained with the simulations considering photon losses only.

5.6 Conclusions

We have extended the noisy gates approach [30] to simulate noisy optical circuits, within the second quantization framework (see sections 5.2 and 5.3), which is the one commonly used in the dual rail encoding for linear optics quantum computing. The simulation method is applicable both to GBQC and MBQC, as shown in sections 5.5.1 and 5.5.2. In section 5.5.3 we have shown that the simulations are suitable to describe variational problems when noises are present.
When considering quantum computing on linear optics, the situation is not yet as mature as for other quantum platforms. Linear optical quantum computing, which utilizes photons for quantum in-

formation processing, faces unique challenges in designing efficient and expressive ansatz circuits. The absence of non-linear interactions in linear optics limits the complexity of quantum computations that can be performed. Consequently, creating ansatz designs that can effectively encode and manipulate quantum information in linear optics remains an ongoing research challenge. MBQC was proposed as a solution to these issues.
For this reason, the next natural target of this work is to understand the practical applicability of a noisy native MBQC algorithm, such as the Quantum Approximate Optimization Algorithm (QAOA) [181] formulated in the MBQC framework for the max K-cut problem in [176].
Another important goal is to compare our simulations with the output of optical devices available in the cloud, for example the one recently provided by Quandela [145]. These targets will be the subject of future research.

Chapter 6

Linear-friction many-body equation for dissipative spontaneous wave-function collapse

As mentioned in Section 1.4.2, an acknowledged challenge within collapse models is the energy divergence due to the collapse mechanism. Although the rate of energy increase is extremely small, e.g. for the CSL this is of the order of $10^{-15}\,\mathrm{K/yr}$ for a free nucleon with $\lambda = 10^{-16}\,\mathrm{s}^{-1}$ at $r_\mathrm{c} = 10^{-7}\,\mathrm{m}$ [8], and the interaction with the external noise field is expected to violate energy conservation solely for the system, one does not expect that the noise field will convey energy indefinitely to the system. To address this concern, dissipative extensions of collapse models were proposed as a solution [182, 183], implying the existence of a fundamental and universal damping mechanism which can be probed by mechanical systems with very low dissipation [184–186]. Here we construct and study the simplest universal dissipative GKLS master equation for many-body systems based on a different mechanism with respect to that previously proposed, namely the linear-friction of the current of the many-body system [187]. In the following we show that our choice of the Lindblad collapse operator, which is independent from the details of the considered system, leads to the dissipation of the current and of the mean energy.

6.1 Dissipative extension - an exercise

Before introducing our dissipative extension of the DP and the CSL models, it is instructive to understand the elementary Lindblad form of friction. We start by considering the master equation for a single free particle of Hamiltonian $\hat{H} = \hat{\mathbf{p}}^2/2m$ with a decoherence term of the form

$$\mathcal{D}\hat{\rho} = -\frac{D}{\hbar^2}[\hat{\mathbf{x}}, [\hat{\mathbf{x}}, \hat{\rho}]]. \tag{6.1}$$

This can be considered as a minimal model for the spontaneous measurement of $\hat{\mathbf{x}}$. It yields a spatial decoherence at rate $D/\hbar^2$. Equivalently, it implies a momentum diffusion with diffusion constant $D/2$, yielding a constant heating at power $P = 3D/m$. A way to include dissipation is to replace the Hermitian Lindblad generator $\hat{\mathbf{x}}$ with the non-Hermitian operator [5, 188]:

$$\hat{\mathbf{L}} = \hat{\mathbf{x}} + i\frac{\hbar\beta}{4m}\hat{\mathbf{p}}, \tag{6.2}$$

where β will turn out to be the inverse equilibrium temperature. Correspondingly, the Lindbladian term of the master equation takes the form

$$\mathcal{D}\hat{\rho} = \frac{2D}{\hbar^2}\Big(\hat{\mathbf{L}}\hat{\rho}\hat{\mathbf{L}}^\dagger - \tfrac{1}{2}\{\hat{\mathbf{L}}^\dagger\hat{\mathbf{L}}, \hat{\rho}\}\Big). \tag{6.3}$$

By expanding $\hat{\mathbf{L}}$, we find

$$\begin{aligned}\mathcal{D}\hat{\rho} = &\frac{i}{\hbar}\left[D\frac{\beta}{4m}\{\hat{\mathbf{x}}, \hat{\mathbf{p}}\}, \hat{\rho}\right] - \\ &- \frac{D}{\hbar^2}\left([\hat{\mathbf{x}}, [\hat{\mathbf{x}}, \hat{\rho}]] + i\frac{\hbar\beta}{2m}[\hat{\mathbf{x}}, \{\hat{\mathbf{p}}, \hat{\rho}\}] + \frac{\hbar^2\beta^2}{16m^2}[\hat{\mathbf{p}}, [\hat{\mathbf{p}}, \hat{\rho}]]\right),\end{aligned} \tag{6.4}$$

where we can cancel the first Hamiltonian term with a counterterm in $\hat{H}$. The first term of the second line generates the heating power P as before. The second term yields to the standard mechanical friction via the Heisenberg equation $\mathcal{D}^\dagger\hat{\mathbf{p}} = -\frac{2\beta D}{m}\hat{\mathbf{p}}$. The second term imposes a relaxation mechanism also for $\hat{\mathbf{p}}^2$. For the mean kinetic energy we get

$$\frac{\mathrm{d}}{\mathrm{d}t}\left\langle\hat{H}\right\rangle_t = \frac{3D}{m} - \frac{2\beta D}{m}\left\langle\hat{H}\right\rangle_t. \tag{6.5}$$

This is the balance expressed in Eq. (1.59) with power $P = 3D/m$ and positive dissipation rate $\Gamma = 2\beta D/m$. We get a finite equilibrium energy $\left\langle \hat{H} \right\rangle_\infty = \frac{3}{2}\beta^{-1}$. We conclude that the effective temperature is $T = 1/(k_B\beta)$. Fortunately, it is known that the equilibrium state of the master equation with the dissipator in Eq. (6.4) is the exact Gibbs state [5, 188]:

$$\hat{\rho}_\beta \propto e^{-\beta \hat{\mathbf{p}}^2/2m}, \tag{6.6}$$

hence $1/(k_B\beta)$ is not only an effective temperature but the true one.

6.2 The many-body master equation of linear friction

Now we introduce our model. In analogy with the single particle linear friction in the previous section, we replace the Hermitian Lindblad generator $\hat{\mu}(\hat{\mathbf{x}})$ in the dissipator of Eq. (1.46) with a non-Hermitian operator of the form

$$\hat{L}(\mathbf{x}) = \hat{\mu}(\mathbf{x}) - i\frac{\hbar\beta}{4}\nabla_{\mathbf{x}}\hat{\mathbf{J}}(\mathbf{x}), \tag{6.7}$$

whose Fourier representation is

$$\hat{L}_{\mathbf{k}} = \hat{\mu}_{\mathbf{k}} + \frac{\hbar\beta}{4}\mathbf{k}\hat{\mathbf{J}}_{\mathbf{k}}, \tag{6.8}$$

and where we introduced the current

$$\hat{\mathbf{J}}(\mathbf{x}) = -i\frac{\hbar}{2}\left(\hat{\psi}^\dagger(\mathbf{x})\nabla_{\mathbf{x}}\hat{\psi}(\mathbf{x}) - \nabla_{\mathbf{x}}\hat{\psi}^\dagger(\mathbf{x})\hat{\psi}(\mathbf{x})\right), \tag{6.9}$$

with $\hat{\psi}(\mathbf{x})$ being the (fermionic) annihilation field operator.
We note that the anti-Hermitian part of $\hat{L}(\mathbf{x})$ needs to be a scalar, like the Hermitian part $\hat{\mu}(\mathbf{x})$. Indeed, one cannot just take the current $\hat{\mathbf{J}}(\mathbf{x})$, but needs to take its divergence. With this choice for the Lindblad generator, the master equation becomes

$$\begin{aligned}\mathcal{D}\hat{\rho} &= \frac{1}{\hbar^2}\int \mathrm{d}^3x \int \mathrm{d}^3y\, D(\mathbf{x}-\mathbf{y})\left(\hat{L}(\mathbf{x})\hat{\rho}\hat{L}^\dagger(\mathbf{y}) - \frac{1}{2}\{\hat{L}^\dagger(\mathbf{x})\hat{L}(\mathbf{y}), \hat{\rho}\}\right) \\ &= \frac{1}{\hbar^2}\int \frac{\mathrm{d}^3k}{(2\pi)^3}\, D_{\mathbf{k}}\left(\hat{L}_{\mathbf{k}}\hat{\rho}\hat{L}_{\mathbf{k}}^\dagger - \frac{1}{2}\{\hat{L}_{\mathbf{k}}^\dagger\hat{L}_{\mathbf{k}}, \hat{\rho}\}\right).\end{aligned} \tag{6.10}$$

By merging the latter expression with the definition in Eq. (6.7), we get

$$\begin{aligned}\mathcal{D}\hat{\rho} = &-\frac{1}{2\hbar^2}\int d^3x \int d^3y\, D(\mathbf{x}-\mathbf{y})\Bigg(\frac{i}{\hbar}\Bigg[\frac{\hbar^2\beta}{4}\{\hat{\mu}(\mathbf{x}), \nabla_{\mathbf{y}}\hat{\mathbf{J}}(\mathbf{y})\}, \hat{\rho}\Bigg] \\ &+ [\hat{\mu}(\mathbf{x}), [\hat{\mu}(\mathbf{y}), \hat{\rho}]] - \frac{i\hbar\beta}{2}[\hat{\mu}(\mathbf{x}), \{\nabla_{\mathbf{y}}\hat{\mathbf{J}}(\mathbf{y}), \hat{\rho}\}] \\ &+ \frac{\hbar^2\beta^2}{16}[\nabla_{\mathbf{x}}\hat{\mathbf{J}}(\mathbf{x}), [\nabla_{\mathbf{y}}\hat{\mathbf{J}}(\mathbf{y}), \hat{\rho}]]\Bigg) \\ = &-\frac{1}{2\hbar^2}\int \frac{d^3k}{(2\pi)^3}\, D_{\mathbf{k}}\Bigg(\frac{i}{\hbar}\Bigg[\frac{\hbar^2\beta}{4}\{\hat{\mu}_{-\mathbf{k}}, \mathbf{k}\hat{\mathbf{J}}_{\mathbf{k}}(\mathbf{y})\}, \hat{\rho}\Bigg] \\ &+ [\hat{\mu}_{-\mathbf{k}}, [\hat{\mu}_{\mathbf{k}}, \hat{\rho}]] - \frac{i\hbar\beta}{2}[\hat{\mu}_{-\mathbf{k}}, \{\mathbf{k}\hat{\mathbf{J}}_{\mathbf{k}}, \hat{\rho}\}] \\ &+ \frac{\hbar^2\beta^2}{16}[\mathbf{k}\hat{\mathbf{J}}_{-\mathbf{k}}, [\mathbf{k}\hat{\mathbf{J}}_{\mathbf{k}}, \hat{\rho}]]\Bigg),\end{aligned} \tag{6.11}$$

where the three terms of $\mathcal{D}$ are respectively responsible for the decoherence in mass density $\hat{\mu}$, the damping of the current $\hat{\mathbf{J}}$ (dissipation), and the decoherence in the (divergence) of the current $\hat{\mathbf{J}}$, respectively. The corresponding Heisenberg equation of motion for an arbitrary observable $\hat{O}$ can be obtained from the adjoint of the master equation $\frac{\mathrm{d}}{\mathrm{d}t}\hat{O} = \frac{i}{\hbar}[\hat{H}, \hat{O}] + \mathcal{D}^\dagger\hat{O}$, where

$$\begin{aligned}\mathcal{D}^\dagger\hat{O} = &-\frac{1}{2\hbar^2}\int d^3x \int d^3y\, D(\mathbf{x}-\mathbf{y})\Bigg(\frac{i}{\hbar}\Bigg[\frac{\hbar^2\beta}{4}\{\hat{\mu}(\mathbf{x}), \nabla_{\mathbf{y}}\hat{\mathbf{J}}(\mathbf{y})\}, \hat{O}\Bigg] \\ &+ [\hat{\mu}(\mathbf{x}), [\hat{\mu}(\mathbf{y}), \hat{O}]] + \frac{i\hbar\beta}{2}\{\nabla_{\mathbf{y}}\hat{\mathbf{J}}(\mathbf{y}), [\hat{\mu}(\mathbf{x}), \hat{O}]\} \\ &+ \frac{\hbar^2\beta^2}{16}[\nabla_{\mathbf{x}}\hat{\mathbf{J}}(\mathbf{x}), [\nabla_{\mathbf{y}}\hat{\mathbf{J}}(\mathbf{y}), \hat{O}]]\Bigg) \\ = &-\frac{1}{2\hbar^2}\int \frac{d^3k}{(2\pi)^3}\, D_{\mathbf{k}}\Bigg(\frac{i}{\hbar}\Bigg[\frac{\hbar^2\beta}{4}\{\hat{\mu}_{-\mathbf{k}}, \mathbf{k}\hat{\mathbf{J}}_{\mathbf{k}}(\mathbf{y})\}, \hat{\rho}\Bigg] \\ &+ [\hat{\mu}_{-\mathbf{k}}, [\hat{\mu}_{\mathbf{k}}, \hat{O}]] + \frac{i\hbar\beta}{2}\{\mathbf{k}\hat{\mathbf{J}}_{\mathbf{k}}, [\hat{\mu}_{-\mathbf{k}}, \hat{O}]\} \\ &+ \frac{\hbar^2\beta^2}{16}[\mathbf{k}\hat{\mathbf{J}}_{-\mathbf{k}}, [\mathbf{k}\hat{\mathbf{J}}_{\mathbf{k}}, \hat{O}]]\Bigg).\end{aligned} \tag{6.12}$$

6.2.1 Damping of the current

It is central to this work to confirm that the second term in Eq. (6.12) is indeed a damping of the current. The corresponding contribution to the evolution of $\hat{\mathbf{J}}(\mathbf{x})$ is given by

$$\frac{\mathrm{d}}{\mathrm{d}t}\hat{\mathbf{J}}(\mathbf{x})|_2 = -\frac{i\beta}{4\hbar}\int \mathrm{d}^3y \int \mathrm{d}^3y'\, D(\mathbf{y}-\mathbf{y}')\{\nabla_{\mathbf{y}}\hat{\mathbf{J}}(\mathbf{y}), [\hat{\mu}(\mathbf{y}'), \hat{\mathbf{J}}(\mathbf{x})]\}. \quad (6.13)$$

We can calculate the commutator of the second quantized (fermionic) density and current:

$$[\hat{\mu}(\mathbf{y}'), \hat{\mathbf{J}}(\mathbf{x})] = -i\hbar\nabla_{\mathbf{y}'}\Big(\delta(\mathbf{y}'-\mathbf{x})\hat{\mu}(\mathbf{x})\Big). \quad (6.14)$$

Inserting it in Eq. (6.13) and integrating the latter by parts, we get

$$\frac{\mathrm{d}}{\mathrm{d}t}\hat{\mathbf{J}}(\mathbf{x})|_2 = -\frac{\beta}{4}\int \mathrm{d}^3y \nabla_{\mathbf{x}} \otimes \nabla_{\mathbf{y}} D(\mathbf{y}-\mathbf{x})\{\hat{\mathbf{J}}(\mathbf{y}), \hat{\mu}(\mathbf{x})\}, \quad (6.15)$$

where $\otimes$ indicates the tensor product. We expand the anti-commutator of the fermionic density and current:

$$\tfrac{1}{2}\{\hat{\mu}(\mathbf{x}), \hat{\mathbf{J}}(\mathbf{y})\} = m\delta(\mathbf{x}-\mathbf{y})\hat{\mathbf{J}}(\mathbf{x}) - \frac{i\hbar}{2}m\left(\hat{\psi}^\dagger(\mathbf{x})\nabla_{\mathbf{y}}\hat{\psi}^\dagger(\mathbf{y})\hat{\psi}(\mathbf{x})\hat{\psi}(\mathbf{y}) - \text{H.C.}\right) \quad (6.16)$$

and we find that

$$\frac{\mathrm{d}}{\mathrm{d}t}\hat{\mathbf{J}}(\mathbf{x})|_2 = -\zeta\,\hat{\mathbf{J}}(\mathbf{x}) + i\left(\hat{\mathbf{Y}}(\mathbf{x}) - \text{H.C.}\right), \quad (6.17)$$

where ζ is the friction rate and

$$\hat{\mathbf{Y}}(\mathbf{x}) = \frac{\beta\hbar m}{4}\int \mathrm{d}^3y \nabla_{\mathbf{x}} \otimes \nabla_{\mathbf{y}} D(\mathbf{y}-\mathbf{x})\hat{\psi}^\dagger(\mathbf{x})\nabla_{\mathbf{y}}\hat{\psi}^\dagger(\mathbf{y})\hat{\psi}(\mathbf{x})\hat{\psi}(\mathbf{y}). \quad (6.18)$$

The latter contributes only when multiple fermions are present, while it vanishes when applied to a single fermion state. As a first order approximation, we neglect $\hat{\mathbf{Y}}(\mathbf{x})$ contributions.
Then, the current effectively decays with a friction rate

$$\zeta = -\frac{\beta m}{2}D''(\mathbf{x})|_{\mathbf{x}=0}, \quad (6.19)$$

which depends crucially on the parameter σ that regularizes $D(\mathbf{x})$ at $\mathbf{x} = 0$, see expressions in Eq. (1.54). In Appendix D, we show

that, in the case of a single particle, Eq. (6.17) holds with no approximations.
Since the methods to infer exact analytic features of the dissipative master equation are limited, we turn to the special single particle case. In such a case the mechanism of dissipation is transparent, and exact analytic calculations are possible. Moreover, in the case of both the standard CSL and DP models, i.e. with no dissipation included, the heating rate is independent from the presence of interactions or external potentials. This has been well addressed in [189]. The inclusion of dissipative effects however raptures this simple feature in dense interactive fermionic matter. To include interaction and fermionic exchange one should employ perturbative methods such those used in [190], which can be applied independently of the Hamiltonian structure. However, this goes beyond the scope of the manuscript. Nonetheless, as long as our single fermion approximation is valid the thermodynamics remains trivial as in the non-dissipative case, while the rates and the equilibrium temperature are calculable exactly as for single fermions.

6.3 Single particle dissipative mechanism

In case of the single particle, it is most convenient to work in the Fourier representation of the mass density and the current:

$$\hat{\mu}_{\mathbf{k}} = m e^{i\mathbf{k}\hat{\mathbf{x}}}, \qquad \hat{\mathbf{J}}_{\mathbf{k}} = \tfrac{1}{2}\{\hat{\mathbf{p}}, e^{i\mathbf{k}\hat{\mathbf{x}}}\}. \tag{6.20}$$

Then, the Lindblad generator, leading to the many-body dissipator $\mathcal{D}$ shown in Eq. (6.11), reduces to simple alternative forms:

$$\begin{aligned} \hat{L}_{\mathbf{k}} &= \left(m - \frac{\hbar^2 k^2 \beta}{8} + \frac{\hbar \mathbf{k} \beta}{4}\hat{\mathbf{p}}\right) e^{i\mathbf{k}\hat{\mathbf{x}}}, \\ &= e^{i\mathbf{k}\hat{\mathbf{x}}} \left(m + \frac{\hbar^2 k^2 \beta}{8} + \frac{\hbar \mathbf{k} \beta}{4}\hat{\mathbf{p}}\right). \end{aligned} \tag{6.21}$$

Let us see how the kinetic equation of the momenta differs from that of the standard DP and CSL in Sec. 1.4.2. We use both forms in Eq. (6.21) of the Lindblad generator in the dissipator in Eq. (6.10),

to yield

$$\frac{\mathrm{d}\rho(\hat{\mathbf{p}})}{\mathrm{d}t} = \frac{1}{\hbar^2}\int \frac{\mathrm{d}^3k}{(2\pi)^3} D_{\mathbf{k}} \Bigg(\left(m - \frac{\beta\hbar^2k^2}{8} + \frac{\beta\hbar\mathbf{k}}{4}\hat{\mathbf{p}} \right)^2 \rho(\hat{\mathbf{p}} - \hbar\mathbf{k}) \\ - \left(m + \frac{\beta\hbar^2k^2}{8} + \frac{\beta\hbar\mathbf{k}}{4}\hat{\mathbf{p}} \right)^2 \rho(\hat{\mathbf{p}}) \Bigg). \tag{6.22}$$

This is equivalent with a classical kinetic equation, therefore $\mathbf{p}$ instead of $\hat{\mathbf{p}}$ can be written. According to this kinetic equation, the momentum jumps like $\mathbf{p} \to \mathbf{p} + \hbar\mathbf{k}$ at probability rate

$$\frac{m^2}{\hbar^2}\frac{\mathrm{d}^3k}{(2\pi)^3} D_{\mathbf{k}} \left(1 + \frac{\beta}{8m}[\mathbf{p}^2 - (\mathbf{p} - \hbar\mathbf{k})^2] \right)^2 . \tag{6.23}$$

This jump rate, unlike in standard DP and CSL, is not isotropic, and the anisotropy can generate the desired friction. Nevertheless, the above rate is subtle. Consider for simplicity a momentum transfer of $\hbar\mathbf{k} = \mp\kappa\mathbf{p}$ where $0 \leq \kappa \leq 1$, where upper and lower signs correspond to damping and heating respectively. The difference between damping and heating rates is proportional to the following expression:

$$\left(1 - \frac{\beta\hbar^2k^2}{8m} + \kappa\frac{\beta p^2}{4m} \right)^2 - \left(1 - \frac{\beta\hbar^2k^2}{8m} - \kappa\frac{\beta p^2}{4m} \right)^2 = \kappa\frac{\beta p^2}{m}\left(1 - \frac{\beta\hbar^2k^2}{8m} \right). \tag{6.24}$$

Damping dominates as long as $\beta(\hbar^2k^2/8m) < 1$ and heating takes over otherwise. Earlier, when we defined E_σ in Eq. (1.58), we noticed that the range of k is $1/\sigma$, hence $(\hbar^2k^2/4m) \sim E_\sigma$. Accordingly for damping, the largest value of $1/\beta$ is about $2E_\sigma$. The forthcoming analytic calculation shows that, indeed, there is an exact critical value of $1/\beta$ above which dissipation gives way to heating.

6.3.1 Derivation of the asymptotic effective temperature

In order to prove that the model exhibits the expected dissipative mechanism described in Eq. (1.59) for $\left\langle \hat{H} \right\rangle = \left\langle \hat{\mathbf{p}}^2 \right\rangle / 2m$, we derive the time-derivative of $\left\langle \hat{\mathbf{p}}^2 \right\rangle$. Since the dynamics of $\hat{\mathbf{p}}$ is semi-classical, we can derive the time-derivative of the equivalent semi-classical mean $\langle \mathbf{p}^2 \rangle$. According to the above discussion, the expression in

Eq. (6.23) is the rate of random jumps $\mathbf{p} \to \mathbf{p} + \hbar\mathbf{k}$, each of which leads to a change of $\hbar^2\mathbf{k}^2 + 2\hbar\mathbf{kp}$ for $\mathbf{p}^2$. Hence, we can write

$$\begin{aligned}\frac{\mathrm{d}}{\mathrm{d}t}\langle \mathbf{p}^2 \rangle = \frac{m^2}{\hbar^2}\int \frac{\mathrm{d}^3k}{(2\pi)^3}\int \mathrm{d}^3p D_{\mathbf{k}}\rho(\mathbf{p})\times \\ (\hbar^2\mathbf{k}^2 + 2\hbar\mathbf{pk})\left(1 + \frac{\beta}{8m}[\mathbf{p}^2 - (\mathbf{p}-\hbar\mathbf{k})^2]\right)^2.\end{aligned} \tag{6.25}$$

We temporarily set $\hbar = 1$ and introduce $a^2 = (\beta/4m)$. We then rewrite the following expression

$$\begin{aligned}&(\mathbf{k}^2 + 2\mathbf{pk})\left(1 - \tfrac{1}{2}a^2\mathbf{k}^2 - a^2\mathbf{kp}\right)^2 \\ &= k^2(1 - a^2k^2 + \tfrac{1}{4}a^4k^4) + a^2(3a^2k^2 - 4)(\mathbf{kp})^2 + ... \\ &\Rightarrow k^2(1 - a^2k^2 + \tfrac{1}{4}a^4k^4) + a^2k^2(a^2k^2 - \tfrac{4}{3})p^2,\end{aligned} \tag{6.26}$$

where the ellipsis stands for odd powers of $\mathbf{k}$ to be cancelled when integrating, and we replaced $(\mathbf{kp})^2$ by $\frac{1}{3}k^2p^2$ also because of the isotropy of $D_{\mathbf{k}}$ in the integral. We insert in Eq. (6.25) the bottom line of the above expansion and perform the integral in $\mathbf{p}$. We get the balance equation (1.59), where the power P and the dissipation Γ rates are respectively

$$\begin{aligned}P &= \frac{m}{2}\int \frac{\mathrm{d}^3k}{(2\pi)^3} D_{\mathbf{k}}k^2\left(1 - \frac{\beta\hbar^2}{4m}k^2 + \frac{\beta^2\hbar^4}{64m^2}k^4\right), \\ \Gamma &= \frac{\beta m}{3}\int \frac{\mathrm{d}^3k}{(2\pi)^3} D_{\mathbf{k}}k^2\left(1 - \frac{3\beta\hbar^2}{16m}k^2\right),\end{aligned} \tag{6.27}$$

where we have restored $\hbar$ and $a^2 = \beta/4m$. The obtained result shows that the energy of the system is dissipated, as expected, through the anisotropic process described by Eq. (6.23). Moreover, we show in Appendix D, that such a result is independent of the specific form of the state $\hat{\rho}$ and is valid beyond the assumption of having $\hat{\rho} = \rho(\hat{\mathbf{p}})$

The integrals in Eq. (6.27) can be calculated analytically for the two models. They respectively read

$$\begin{aligned}P^{\text{DP}} &= \frac{\hbar m G}{4\sqrt{\pi}\sigma^3}\left(1 - \frac{3}{4}x_\beta^2 + \frac{15}{64}x_\beta^4\right), \\ \Gamma^{\text{DP}} &= \beta\frac{\hbar m G}{6\sqrt{\pi}\sigma^3}\left(1 - \frac{9}{16}x_\beta^2\right).\end{aligned} \tag{6.28}$$

and

$$
\begin{aligned}
P^{\text{CSL}} &= \frac{3m\gamma\hbar^2}{32\pi^{3/2}\sigma^5}\left(1-\frac{5}{4}x_\beta^2+\frac{35}{64}x_\beta^4\right),\\
\Gamma^{\text{CSL}} &= \beta\frac{m\gamma\hbar^2}{16\pi^{3/2}\sigma^5}\left(1-\frac{15}{16}x_\beta^2\right),
\end{aligned}
\tag{6.29}
$$

where we defined the dimensionless parameter

$$
x_\beta^2 = 2\beta E_\sigma = \frac{\hbar^2\beta}{2m\sigma^2}, \tag{6.30}
$$

which is the ratio of the elementary energy transfer E_σ defined in Eq. (1.58) to $1/(2\beta)$, the latter being the equilibrium thermal kinetic energy at high temperatures. Note that, according to the mapping in Eq. (1.48), the relation $P^{\text{CSL}} = -(\hbar\gamma/4\pi G)\partial P^{\text{DP}}/\partial(\sigma^2)$ holds, and similarly between Γ^{CSL} and Γ^{DP}. The dissipative rates Γ become negative if x_β^2, which is proportional to the parameter β, is larger than a critical value, which is different for the two models.
It is in order now to interpret our results, shown in Eqs. (6.27)–(6.29), that exhibit the dissipation mechanism postulated by the balance Eq. (1.59). The equilibrium energy is obtained as $\left\langle \hat{H} \right\rangle_\infty = P/\Gamma$. Following the equipartition theorem, we define the effective temperature as $T = \frac{2}{3}\left\langle \hat{H} \right\rangle_\infty / k_{\text{B}}$ and we introduce the parameter $T_\beta = 1/\beta$ in place of β. Then, we have $x_\beta^2 = 2E_\sigma/T_\beta$, and we can express the effective temperatures of the two models as

$$
T^{\text{DP}} = T_\beta \frac{1-\frac{3}{2}(E_\sigma/k_{\text{B}}T_\beta)+\frac{15}{16}(E_\sigma/k_{\text{B}}T_\beta)^2}{1-\frac{9}{8}(E_\sigma/k_{\text{B}}T_\beta)}, \tag{6.31}
$$

and

$$
T^{\text{CSL}} = T_\beta \frac{1-\frac{5}{2}(E_\sigma/k_{\text{B}}T_\beta)+\frac{35}{16}(E_\sigma/k_{\text{B}}T_\beta)^2}{1-\frac{15}{8}(E_\sigma/k_{\text{B}}T_\beta)}. \tag{6.32}
$$

In the regime $k_{\text{B}}T_\beta \gg E_\sigma$, the effective temperature T asymptotically coincides with the parameter T_β, which justifies our choice of parametrizing the dissipator in Eq. (6.11) by $\beta = 1/T_\beta$. When lowering the parameter temperature T_β, the effective temperature T is also lowering. But the dissipation rate Γ is also decreasing and at a point the effective T is no longer lowering together with T_β, but it is growing again and becomes infinite when the dissipation rate reduces to zero, i.e. at $k_{\text{B}}T_\beta = (9/8)E_\sigma$ in the DP model

and at $k_B T_\beta = (15/8)E_\sigma$ in the CSL model. Below these critical temperatures, the negative dissipative rate Γ is contributing to a higher heating power P rather than balancing it. This effect follows from what we noticed about the subtlety of momentum jump rate in Eq. (6.23). The standard DP and CSL models correspond to $T = T_\beta = \infty$, where dissipative rates Γ vanish, the powers P reduce to the expressions in Eq. (1.55). The kinetic energy $\left\langle \hat{H} \right\rangle_t$ goes to infinity and, from a theoretical viewpont, this looks unphysical.

6.3.2 Environmental effects

In practice, however, we face a different situation. The predicted powers in Eq. (1.55) are extremely small and are typically masked by the environmental effects (see experimental investigations summarised in [47]). Clearly, studying experimentally a system under the action of a collapse mechanism, but otherwise isolated, is impossible. Indeed, there will be always a coupling of the system with its surrounding environment. This might be the residual gas in the vacuum chamber, the blackbody radiation or the noises (e.g., seismic or electronic) that shake, and thus heat, the experiment (see for instance [191, 192]). As a matter of fact, current laboratory efforts of isolation are not yet able to exclude the values $T = T_\beta = \infty$ neither for the DP or the CSL model, however unphysical they would theoretically be.

For this reason, we now consider the case of a system undergoing simultaneously to the dissipative collapse mechanism and the interaction of an external thermal environment. Let T_{E} be the temperature of the environment, and let us define the power P_{E} and the dissipative rate Γ_{E} model the environmental effect on our particle, where $\frac{3}{2} k_{\text{B}} T_{\text{E}} = P_{\text{E}} / \Gamma_{\text{E}}$ is satisfied. One can straightforwardly derive the evolution of the mean energy of the system, which reads:

$$\frac{\mathrm{d}}{\mathrm{d}t} \langle H \rangle_t = P + P_{\text{E}} - (\Gamma + \Gamma_E) \langle H \rangle_t \,, \tag{6.33}$$

According to the equipartition theorem, the asymptotic (equilibrium) temperature of our particle is $T_{\text{eff}} = \frac{2}{3} k_{\text{B}}^{-1} \left\langle \hat{H} \right\rangle_\infty$, i.e.:

$$T_{\text{eff}} = \frac{\Gamma T + \Gamma_{\text{E}} T_{\text{E}}}{\Gamma + \Gamma_{\text{E}}}, \tag{6.34}$$

where $T = \frac{2}{3}k_{\text{B}}^{-1}P/\Gamma$ is the effective temperature obtained in Eqs. (6.31)–(6.32) of the collapse noise and $T_{\text{E}} = \frac{2}{3}k_{\text{B}}^{-1}P_{\text{E}}/\Gamma_{\text{E}}$ is that of the thermal environment. The relation in Eq. (6.34) is fundamental when it comes to experiments. Indeed, it provides the experimental requirement to be reached in terms of Γ_{E} and T_{E} to be able to measure the temperature T of the collapse noise.

6.4 Conclusions

We introduced a simple and universal dissipative extension of the DP and the CSL models. Contrary to previous attempts [182, 183], our model modifies the collapse operator by adding (instead of a multiplying) a new term leading to dissipative effects. A similar method has been considered for a different gravity-related model in [193]. Such a term is proportional to the divergence of the current and is parametrized by the constant β [cf. Eq. (6.7)]. We demonstrate that the model dissipates the current and leads to the thermalisation of the system's energy to the asymptotic value of $\left\langle \hat{H} \right\rangle_{\infty} = \frac{3}{2}k_{\text{B}}T$, where the expression for T is given in Eq. (6.31) for the DP model and in Eq. (6.32) for the CSL model.
We find a threshold temperature T_0, which is defined as

$$T_0 = \frac{\hbar^2}{m k_{\text{B}} \sigma^2}, \tag{6.35}$$

and is determined by the cutoff-length σ of the DP and the CSL models. For k_{B}/β much higher than T_0, the system's mean energy asymptotically converges to $1/(2\beta)$, which suggests that β can be interpreted as the inverse temperature of the collapse noise. Nevertheless, for generic values of β, the latter enters non-trivially in $\left\langle \hat{H} \right\rangle_{\infty}$. The noise temperature T becomes different from k_{B}/β when the latter approaches T_0 from above. At a certain point, the noise temperature T inverts its trend with respect to k_{B}/β and increases to infinity at T_0. It is thus impossible to draw a clear one to one connection between the temperature T of the collapse noise and the parameter β. In general, the temperature of the collapse noise does not coincide with β^{-1}/k_{B}, and the latter plays the role of a parameter in the master equation that is detached from its familiar statistical mechanical interpretation.

Chapter 7

Experimental bounds on linear-friction dissipative collapse models from levitated optomechanics

In Chapter 6 we presented a new approach to the introduction of dissipation in collapse model. Such an approach has not been tested yet. Thus in the following chapter we derive the first experimental bounds on linear-friction dissipative DP (dDP) and CSL (dCSL) models from levitated optomechanics [194] characterised by ultralow damping [185, 186, 195]. In particular, for the dDP model, values of the temperature T_β of the collapse field lower than $10^{-13}\,\mathrm{K}$ and $6 \times 10^{-12}\,\mathrm{K}$ are excluded respectively for values of the localisation length smaller than $10^{-6}\,\mathrm{m}$ and $10^{-8}\,\mathrm{m}$. On the other hand, for the dCSL model, the entire parameter space is excluded for T_β lower than $6\times10^{-9}\,\mathrm{K}$. Finally, we compare the approach recently proposed in [187] with those previously suggested in [182, 183], and conclude that they can be in principle experimentally distinguished.

7.1 Dissipative dynamics of the center of mass of a N-particle system

We compute the dynamics of the center of mass of a rigid system made of N particles. For convenience, we work in the Fourier representation showed in Eq. (6.10) where the Lindblad operators are those in Eq. (6.8). The Fourier representation of the mass density

and of the current for a N-particle system is

$$\hat{\mu}_{\mathbf{k}} = m \sum_{j=1}^{N} e^{i\mathbf{k}\hat{\mathbf{x}}_j}, \quad \hat{\mathbf{J}}_{\mathbf{k}} = \frac{1}{2} \sum_{j=1}^{N} \left\{ \hat{\mathbf{p}}_j, e^{i\mathbf{k}\hat{\mathbf{x}}_j} \right\}. \tag{7.1}$$

In general the position and momentum operators in Eq. (7.1) can be written as

$$\hat{\mathbf{x}}_j = \hat{\mathbf{x}} + \mathbf{x}_j^{(0)} + \Delta\hat{\mathbf{x}}_j, \quad \hat{\mathbf{p}}_j = \frac{m}{M}\hat{\mathbf{p}} + \mathbf{p}_j^{(0)} + \Delta\hat{\mathbf{p}}_j, \tag{7.2}$$

where $\hat{\mathbf{x}}$ and $\hat{\mathbf{p}}$ are the position and momentum operators of the center of mass, $\mathbf{x}_j^{(0)}$ and $\mathbf{p}_j^{(0)}$ are the classical equilibrium position and momentum of the j-th particle with respect to the center of mass, and $\Delta\hat{\mathbf{x}}_j$ and $\Delta\hat{\mathbf{p}}_j$ are the relative fluctuations, and M is the total mass of the system. Under the assumption of a rigid body, the relative fluctuations are negligible, namely $\Delta\hat{\mathbf{x}}_j = \Delta\hat{\mathbf{p}}_j = 0$. By substituting Eq. (7.2) into Eq. (7.1) and by assuming that the spread of the wavefunction of the center of mass is much smaller than σ, we can Taylor expand the mass density and the current for small fluctuations of $\hat{\mathbf{x}}$, finding

$$\hat{\mu}_{\mathbf{k}} \simeq \mu_{\mathbf{k}} + i\mathbf{k}\mu_{\mathbf{k}}\hat{\mathbf{x}}, \tag{7.3a}$$

$$\hat{\mathbf{J}}_{\mathbf{k}} \simeq \mathbf{J}_{\mathbf{k}} + \frac{\mu_{\mathbf{k}}}{M}\hat{\mathbf{p}} + i\mathbf{k}\mathbf{J}_{\mathbf{k}}\hat{\mathbf{x}} + \frac{i\mathbf{k}}{2M}\mu_{\mathbf{k}}\{\hat{\mathbf{p}}, \hat{\mathbf{x}}\}, \tag{7.3b}$$

where $\mu_{\mathbf{k}} = m\sum_{j=0}^{N} e^{i\mathbf{k}\mathbf{x}_j^{(0)}}$ and $\mathbf{J}_{\mathbf{k}} = \sum_{j=0}^{N} \mathbf{p}_j^{(0)} e^{i\mathbf{k}\mathbf{x}_j^{(0)}}$ are respectively the classical mass density and current of the system in the Fourier representation. We notice that for a rigid body $\mathbf{p}_j^{(0)} = 0$ thus $\mathbf{J}_{\mathbf{k}} = 0$.

7.1.1 Linearized master equation

For the sake of simplicity, we reduce the problem in one dimension, namely $\hat{\mathbf{x}} = (\hat{x}, 0, 0)$ and $\hat{\mathbf{p}} = (\hat{p}, 0, 0)$. Moreover, by assuming small $\mathbf{k}$ (i.e., $|\mathbf{k}| \ll 1/\sigma$) we neglect all the terms of order higher than $O(\mathbf{k}^2)$ and substitute the latter expressions for the mass density and the current in Eq. (6.10). In such a way, we obtain the following master equation for the motion of the center of mass in the linear limit

$$\frac{\mathrm{d}}{\mathrm{d}t}\hat{\rho}_{cm} = -\frac{i}{\hbar}[\hat{H}, \hat{\rho}_{cm}] + \eta\left(\hat{L}\hat{\rho}_{cm}\hat{L}^\dagger - \frac{1}{2}\{\hat{L}^\dagger\hat{L}, \hat{\rho}_{cm}\}\right), \tag{7.4}$$

where $\hat{L} = \hat{x} + i\alpha\hat{p}$ with $\alpha = \Gamma_c/2\eta\hbar$ and where

$$\Gamma_c = \frac{\hbar^2 \beta \eta}{2M}, \quad \eta = \frac{1}{\hbar^2} \int \frac{\mathrm{d}^3 k}{(2\pi)^3} k_x^2 D_{\mathbf{k}} |\mu_{\mathbf{k}}|^2, \tag{7.5}$$

are respectively the dissipation and the diffusion rates with $\mathbf{k} = (k_x, k_y, k_z)$. For the purpose of this work, we can consider the case of a system being a continuous and homogeneous sphere of radius r. For such a case, we have

$$\mu(\mathbf{x}) = \frac{3M}{4\pi r^3} \theta(r - |\mathbf{x}|), \tag{7.6}$$

where θ is the Heaviside function. Then, η takes the following form

$$\eta_{\mathrm{DP}} = \frac{GM^2 R_0}{\hbar \sqrt{\pi} r^6} \left[-3r^2 + 2R_0^2 + e^{-(r^2/R_0^2)}(r^2 - 2R_0^2) + \sqrt{\pi} r^3 \operatorname{erf}(r/R_0) \right], \tag{7.7}$$

for the dDP model and

$$\eta_{\mathrm{CSL}} = \lambda \frac{3 e^{-(r^2/r_{\mathrm{C}}^2)} M^2 r_{\mathrm{C}}^2}{m_0^2 r^6} \left[r^2 + 2r_{\mathrm{C}}^2 + e^{r^2/r_{\mathrm{C}}^2}(r^2 - 2r_{\mathrm{C}}^2) \right], \tag{7.8}$$

for the dCSL model.

7.2 Application to Langevin equations of a mechanical oscillator

In the present section, we explore the dissipative dynamics of the center of mass of a one-dimensional mechanical oscillator in order to set experimental bounds on dDP and dCSL free parameters. To include the effects of dissipation in the Langevin equations for the mechanical oscillator [196], we use the unitary stochastic unravelling (see Section 1.2.3) [14, 184] of Eq. (7.4)

$$\mathrm{d}|\psi_t\rangle = \left[-\frac{i}{\hbar} \hat{H} \mathrm{d}t + \hat{L} \mathrm{d}\hat{B}_t^\dagger - \hat{L}^\dagger \mathrm{d}\hat{B}_t - \frac{\eta}{2} \hat{L}^\dagger \hat{L} \mathrm{d}t \right] |\psi_t\rangle, \tag{7.9}$$

where $\hat{B}_t$ is equipped with the following statistical features: $\mathbb{E}[\mathrm{d}\hat{B}_t] = 0$, $\mathbb{E}[\mathrm{d}\hat{B}_t \mathrm{d}\hat{B}_t^\dagger] = \eta \mathrm{d}t$ and $\mathbb{E}[\mathrm{d}\hat{B}_t^\dagger \mathrm{d}\hat{B}_t^\dagger] = \mathbb{E}[\mathrm{d}\hat{B}_t \mathrm{d}\hat{B}_t] = \mathbb{E}[\mathrm{d}\hat{B}_t^\dagger \mathrm{d}\hat{B}_t] = 0$. From Eq. (7.9), one can build the Langevin equation for a generic operator $\hat{O}$ via

$$\frac{\mathrm{d}}{\mathrm{d}t} \hat{O} = \frac{i}{\hbar} [\hat{H}, \hat{O}] + \eta \left(\hat{L}^\dagger \hat{O} \hat{L} - \frac{1}{2} \{ \hat{L}^\dagger \hat{L}, \hat{O} \} \right) + \hat{b}_t^\dagger [\hat{O}, \hat{L}] + \hat{b}_t [\hat{L}^\dagger, \hat{O}], \tag{7.10}$$

where $\hat{b}_t = \mathrm{d}\hat{\mathrm{B}}_t / \mathrm{d}t$.

7.2.1 Langevin equations of one-dimensional mechanical oscillator

Finally, by using Eq. (7.10) with $\hat{O} = \hat{x}, \hat{p}$ and $\hat{H} = \hat{p}^2/2M + M\omega_0^2\hat{x}^2/2$, we find the following modified Langevin equations for a one-dimensional mechanical oscillator of mass M and frequency ω_0

$$\frac{\mathrm{d}\hat{x}}{\mathrm{d}t} = \frac{\hat{p}}{M} - \frac{\Gamma_c}{2}\hat{x} - \hbar\alpha\hat{w}_x, \tag{7.11a}$$

$$\frac{\mathrm{d}\hat{p}}{\mathrm{d}t} = -M\omega_0^2\hat{x} - \Big(\frac{\Gamma_c}{2} + \gamma_m\Big)\hat{p} + \xi - \hbar\hat{w}_p, \tag{7.11b}$$

where $\hat{x}$ is the position operator for the center of mass of the oscillator, $\hat{p}$ is the corresponding momentum. The parameter γ_m is the dissipation rate due to the environment and ξ his stochastic effect. We define the noises $\hat{w}_x = \hat{b}_t^\dagger + \hat{b}_t$ and $\hat{w}_p = i(\hat{b}_t^\dagger - \hat{b}_t)$. We notice that the addition of a collapse-induced dissipative mechanism has changed both the equation for the position and for the momentum. Notably, this raptures the proportionality between the velocity $\mathrm{d}\hat{x}/\mathrm{d}t$ and the momentum $\hat{p}$. However, from the experimental perspective, the relevant quantity to consider is the second derivative of the position operator, which reads

$$\frac{\mathrm{d}^2\hat{x}}{\mathrm{d}t^2} = -\Omega_0^2\hat{x} - (\Gamma_c + \gamma_m)\frac{\mathrm{d}\hat{x}}{\mathrm{d}t} + \hat{\mathcal{N}}, \tag{7.12}$$

where $\Omega_0^2 = \omega_0^2 + \frac{\Gamma_c}{2}(\frac{\Gamma_c}{2} + \gamma_m)$ and $\hat{\mathcal{N}} = -(\frac{\Gamma_c}{2} + \gamma_m)\hbar\alpha\hat{w}_x + \frac{\xi}{M} - \frac{\hbar\hat{w}_p}{M} - \hbar\alpha\frac{\mathrm{d}\hat{w}_x}{\mathrm{d}t}$. Thus, we have that $\Gamma_c + \gamma_m$ is the total dissipation rate of the center of mass. This means that the effect of the inclusion of collapse-induced dissipation is to change the total dissipation rate of the mechanical oscillator by a quantity Γ_c.

7.2.2 Steady-state density noise spectrum

Following the same procedure as that presented in [184], one can derive the corresponding steady-state density noise spectrum [14, 197]. By starting from Eq. (7.12), one obtains

$$S(\omega) = \frac{\frac{\hbar\omega\gamma_m}{M}\coth\Big(\frac{\hbar\omega}{2k_\mathrm{B}T}\Big) + \eta\left[\frac{\Gamma_c^2(2\gamma_m+\Gamma_c)^2}{16\eta^2} + \frac{\Gamma_c^2\omega^2}{4\eta^2} + \frac{\hbar^2}{M^2}\right]}{\Big(\omega_0^2 + \frac{\Gamma_c}{2}\Big(\frac{\Gamma_c}{2} + \gamma_m\Big) - \omega^2\Big)^2 + \omega^2(\Gamma_c + \gamma_m)^2}, \tag{7.13}$$

where the first term quantifies for the environmental effects, while the second accounts for the collapse-induced ones. Fundamentally, the Lorentzian profile of $S(\omega)$ has a width half-height being equal to $\Gamma_c + \gamma_m$.

7.3 Experimental bounds

Now we are able to set experimental bounds on dDP and dCSL free parameters. We focus on levitated optomechanics, which provides promising platforms for testing fundamental physics and quantum mechanics [198–200]. In particular, experiments with low dissipation are of our interest. We notice that it is challenging to establish bounds on the parameter Γ_c from Eq. (7.13) since it appears in different contributions to $S(\omega)$. In contrast, the task becomes straightforward when examining Eq. (7.12). Indeed, owning the fact that the total dissipation rate in Eq. (7.12) is $\Gamma_c + \gamma_m$, we know that experimentally measured dissipative rate $\gamma_{\rm exp}$ will provide an estimation of the upper bound for Γ_c. Such an estimation is conservative since the value of γ_m is fully neglected. Then, by using the expression for Γ_c in Eq. (7.5) and defining $T_\beta = 1/k_{\rm B}\beta$ as the temperature of the collapse field, we find

$$\gamma_{\rm exp} \geq \Gamma_c = \frac{\hbar^2 \eta}{2M} \frac{1}{k_{\rm B} T_\beta}, \tag{7.14}$$

where $k_{\rm B}$ is the Boltzmann constant. Since for the dDP model, $\eta_{\rm DP}$ in Eq. (7.7) is a function of R_0 only, we can bound the possible values of T_β as a function of R_0. Conversely, for the dCSL model $\eta_{\rm CSL}$ in Eq. (7.8) is a function of two free parameters (λ and $r_{\rm c}$). Thus, we study how the bounds on λ with respect to $r_{\rm c}$ change when varying the values of T_β. Specifically, one has

$$T_\beta \geq \frac{\hbar^2 \eta_{\rm DP}}{2M k_{\rm B} \gamma_{\rm exp}}, \quad \lambda \leq \frac{2M k_{\rm B} T_\beta \gamma_{\rm exp}}{\hbar^2 \bar{\eta}_{\rm CSL}}, \tag{7.15}$$

where $\bar{\eta}_{\rm CSL} = \eta_{\rm CSL}/\lambda$. To be quantitative, we use the experimental data from three recent experiments in levitated optomechanics, which are those of Pontin *et al.* [185], Vinante *et al.* [201] and Dania *et al.* [195]. The first and last experiment use linear Paul traps to

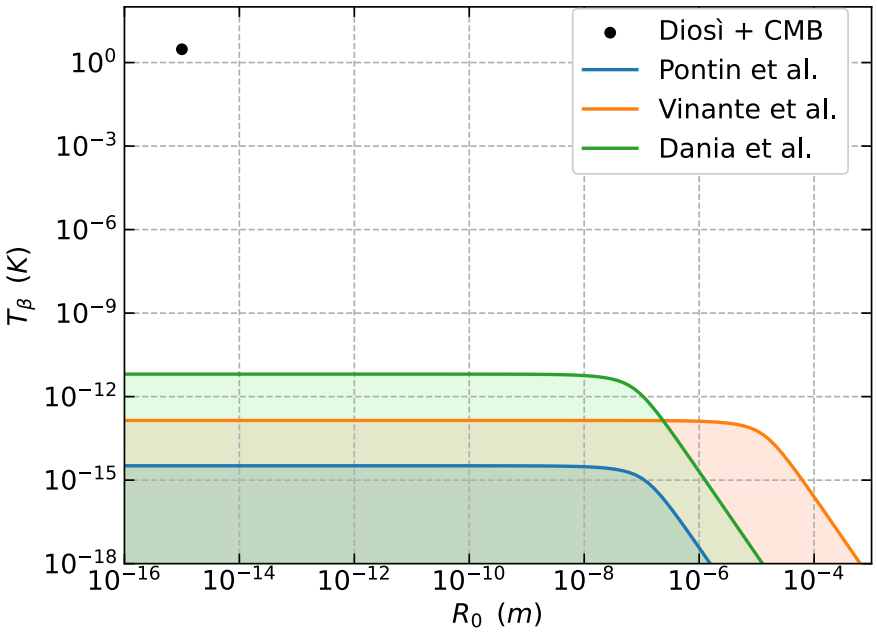

Figure 7.3.1: Experimental bounds for the dDP model. Blue, orange and green shaded areas represent the excluded values of the collapse parameters, respectively, from the experiments of Pontin *et al.*, Vinante *et al.* and Dania *et al.*. The black point represents the proposal by Diósi of $R_0 = 10^{-15}\,\mathrm{m}$ and $T_\beta \sim 3\,\mathrm{K}$ being the CMB temperature.

levitate a silica nanoparticles of mass and linewidth respectively being $M = 9.6 \times 10^{-17}\,\mathrm{kg}$, $\gamma_{\mathrm{exp}} = 2\pi \times 48\,\mu\mathrm{Hz}$ and $M = 4.3 \times 10^{-17}\,\mathrm{kg}$, $\gamma_{\mathrm{exp}} = 2\pi \times 80\,\mathrm{nHz}$. Conversely, Vinante uses a lavitated micromagnet of mass $M = 6.1 \times 10^{-10}\,\mathrm{kg}$ from which one infers a linewidth $\gamma_{\mathrm{exp}} = 2\pi \times 9\,\mu\mathrm{Hz}$ at zero pressure. The experiments of Pontin and Vinante were already used to set bounds on an earlier dissipative version of the DP and CSL model, while that of Dania has not yet been exploited for collapse model testing. We show the experimental bounds on the dDP and dCSL respectively in Fig. 7.3.1 and Fig. 7.3.2. Here, the blue, orange and green shaded areas correspond to the excluded values of the collapse parameters by the experiments of Pontin *et al.*, Vinante *et al.* and Dania *et al.*

In Fig. 7.3.1 we show the excluded values of T_β for the dDP model when varying R_0. For comparison, we also report (black dot) the values of Diósi proposal of $R_0 = 10^{-15}\,\mathrm{m}$ matched with $T_\beta \sim 3\,\mathrm{K}$ being the temperature of the cosmic microwave background (CMB). This choice is based on the hypothesis of a cosmological origin of the collapse mechanism, and thus one would expect a value of T_β

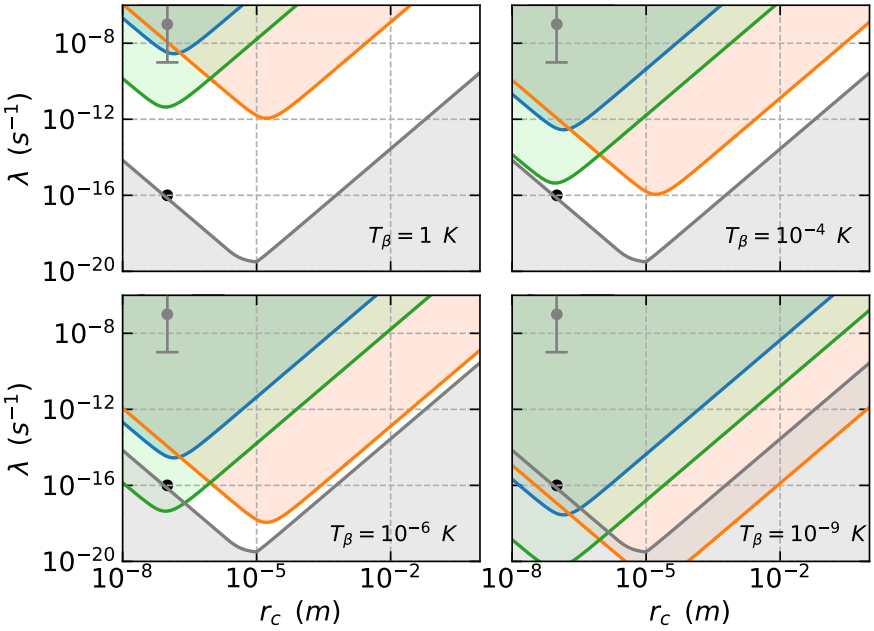

Figure 7.3.2: Experimental bounds for the dCSL model. Blue, orange and green shaded areas represent the excluded values of the collapse parameters, respectively, from the experiments of Pontin *et al.*, Vinante *et al.* and Dania *et al.*. Each panel considers different values of T_β, left-to-right, top-to-bottom, these are 1 K, 10^{-4} K, 10^{-6} K and 10^{-9} K. The grey area is excluded for theoretical reasons [202]. The grey bar is the Adler proposal of the CSL parameters [203] and the black point is the GRW proposal [204].

of this order of magnitude. We notice that below $T_\beta \sim 10^{-13}$ K and $T_\beta \sim 6 \times 10^{-12}$ K all the values of R_0 respectively smaller than 10^{-6} m and 10^{-8} m are excluded, this includes the mesoscopic regime where one would expect a collapse.
In Fig. 7.3.2 we show the bounds on the dCSL parameters λ and r_c for four values of $T_\beta = 1$ K, 10^{-3} K, 10^{-5} K and 10^{-7} K. The gray region is excluded theoretically as it would not guarantee an effective collapse of macroscopic quantum superpositions [202]. The grey bar, which is the Adler proposal [203] for the CSL parameters, is excluded for each value of T_β reported, while the GRW proposal [204] is excluded for $T_\beta = 10^{-5}$ K and below. We notice that all the parameter space is excluded for temperatures lower than 6×10^{-9} K.

7.4 Comparison with the previous dissipative model

Here we compare the linear friction (LF) dissipative model, introduced in Ref. [187] and shown in Chapter 6, with the previously

proposed dissipative collapse models [182, 183]. The latter have a mathematical structure similar to the collisional dynamics of a test particle interacting with a low-density gas in the weak coupling regime [205]. Thus, for simplicity, we refer to these as collisional dynamics (CD) models. For such a comparison, we compute the asymptotic temperature of the center of mass of the mechanical oscillator, which in both frameworks can be derived from their respective master equations. Indeed, given an arbitrary operator $\hat{O}$, one can compute the evolution of its expectation value as $\frac{\mathrm{d}}{\mathrm{d}t}\left\langle \hat{O} \right\rangle_t = \mathrm{Tr}\left(\hat{O}\frac{\mathrm{d}}{\mathrm{d}t}\hat{\rho}_{cm}\right)$. The equation with $\hat{O} = \hat{H}$ is not in a closed form, however we can write the system of three differential equations for $\hat{O} = \hat{V}$, $\hat{K}$ and $\{\hat{x}, \hat{p}\}$, where $\hat{K} = \hat{p}^2/2M$ and $\hat{V} = M\omega_0^2\hat{x}^2/2$. Under the assumption of a reaching a stable condition at the thermal equilibrium, we can set all the derivatives to zero and find the asymptotic values of $\left\langle \hat{K} \right\rangle_\infty$ and $\left\langle \hat{V} \right\rangle_\infty$, from which we obtain $\left\langle \hat{H} \right\rangle_\infty = \left\langle \hat{K} \right\rangle_\infty + \left\langle \hat{V} \right\rangle_\infty$. Then, we define the temperature of the system by exploiting the equipartition theorem for single harmonic oscillator $\left\langle \hat{H} \right\rangle_\infty = k_{\text{B}} T$.
In the LF framework, we have

$$\begin{aligned}
\frac{\mathrm{d}}{\mathrm{d}t}\left\langle \hat{V} \right\rangle_t &= -\Gamma_c \left\langle \hat{V} \right\rangle_t + \frac{\omega_0^2}{2}\left\langle \{\hat{x}, \hat{p}\} | \{\hat{x}, \hat{p}\} \right\rangle_t + \frac{\Gamma_c^2 M \omega_0^2}{8\eta}, \\
\frac{\mathrm{d}}{\mathrm{d}t}\left\langle \hat{K} \right\rangle_t &= -\Gamma_c \left\langle \hat{K} \right\rangle_t - \frac{\omega_0^2}{2}\left\langle \{\hat{x}, \hat{p}\} \right\rangle_t + \frac{\hbar^2 \eta}{2M}, \\
\frac{\mathrm{d}}{\mathrm{d}t}\left\langle \{\hat{x}, \hat{p}\} \right\rangle_t &= -\Gamma_c \left\langle \{\hat{x}, \hat{p}\} \right\rangle_t + 4\left\langle \hat{K} \right\rangle_t - 4\left\langle \hat{V} \right\rangle_t,
\end{aligned} \tag{7.16}$$

which correspond to

$$T = T_\beta + \frac{\hbar^2 \omega_0^2}{16 k_{\text{B}}^2 T_\beta}, \tag{7.17}$$

both for the dDP and the dCSL model. We notice that Eq. (7.17) does not depend on the free parameters of the model except for the dissipation parameter $\beta = (k_{\text{B}} T_\beta)^{-1}$. When T_β is high, the asymptotic temperature T coincides with the collapse temperature T_β. Indeed, in the limit of $T_\beta \to \infty$ ($\beta \to 0$, i.e. $\Gamma_c \to 0$), the last term of the first expression in Eq. (7.16) can be neglected and the only important collapse term is the last one in the second expression.

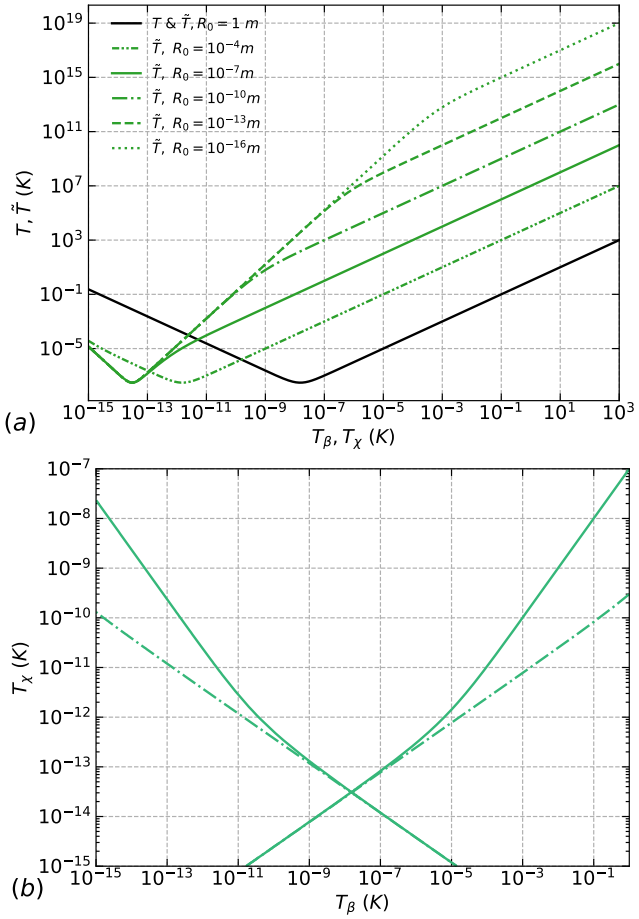

Figure 7.4.3: Comparison between the linear friction dDP and the collisional dynamics dDP models. In panel (a) the solid black curve represents the asymptotic temperature T of the LF-dDP model as a function of the dissipation parameter T_β, while the green curves show the asymptotic temperature $\tilde{T}$ of the CD-dDP model as a function of the dissipation parameter T_χ for different values of R_0. For $R_0 = 1$ m, T and $\tilde{T}$ coincide in the black curve. Panel (b) shows the contour plot of the function $T(T_\beta) - \tilde{T}(T_\chi) = 0$ where the solid green line is for $R_0 = 10^{-7}$ m and the dash dotted green line is for $R_0 = 10^{-10}$ m.

In such a way one recovers the predictions of the standard collapse model without dissipation, for which one has $T = \infty$. Also in the limit of $T_\beta \to 0$, the asymptotic temperature T goes to infinity. Indeed, in such a limit, is the last term in the second expression of Eq. (7.16) that can be neglected, and the last term in the first expression becomes the relevant one. The latter leads to an infinite increase to the mean potential energy, and thus to $\left\langle \hat{H} \right\rangle_\infty = \infty$.

In the CD framework, one has

$$\begin{aligned}
\frac{\mathrm{d}}{\mathrm{d}t}\left\langle \hat{V}\right\rangle_t &= \frac{\omega_0^2}{2}\left\langle\{\hat{x},\hat{p}\}\right\rangle_t + \frac{\tilde{\Gamma}_c^2 M\omega_0^2}{8\tilde{\eta}},\\
\frac{\mathrm{d}}{\mathrm{d}t}\left\langle \hat{K}\right\rangle_t &= -2\tilde{\Gamma}_c\left\langle \hat{K}\right\rangle_t - \frac{\omega_0^2}{2}\left\langle\{\hat{x},\hat{p}\}\right\rangle_t + \frac{\hbar^2\tilde{\eta}}{2M},\\
\frac{\mathrm{d}}{\mathrm{d}t}\left\langle\{\hat{x},\hat{p}\}\right\rangle_t &= -\tilde{\Gamma}_c\left\langle\{\hat{x},\hat{p}\}\right\rangle_t + 4\left\langle \hat{K}\right\rangle_t - 4\left\langle \hat{V}\right\rangle_t,
\end{aligned} \tag{7.18}$$

whose corresponding asymptotic temperature reads

$$\tilde{T} = \frac{\tilde{\Gamma}_c M\omega_0^2}{8\tilde{\eta}k_{\mathrm{B}}} + \frac{\hbar^2\tilde{\eta}}{2M\tilde{\Gamma}_c k_{\mathrm{B}}} + \frac{\tilde{\Gamma}_c^3 M}{16\tilde{\eta}k_{\mathrm{B}}}. \tag{7.19}$$

The latter depends on two parameters $\tilde{\eta}$ and $\tilde{\Gamma}_c$ that play the role, respectively, of η and Γ_c in the LF framework [184]. To be specific, we have $\tilde{\Gamma}_c = 4\tilde{\eta}\sigma^2\chi(1+\chi)m_0/M$ with $\sigma = R_0$ or r_{C} and where $\chi = \hbar^2/8m_0\sigma^2 k_{\mathrm{B}}T_\chi$ is the dissipation parameter of the CD model and T_χ is the associated temperature of the collapse field (analogous to T_β in the LF framework). The coefficient $\tilde{\eta}$ takes the following form

$$\tilde{\eta}_{\mathrm{DP}} = \sqrt{\pi}\,\mathrm{erf}\left(\frac{r}{\tilde{R}_0}\right) + \frac{GM^2R_0}{\sqrt{\pi}r^3}\left[\frac{R_1}{r}\left(e^{-\frac{r^2}{R_1^2}} - 3\right) + 2\frac{R_1^3}{r^3}\left(1 - e^{-\frac{r^2}{R_1^2}}\right)\right], \tag{7.20}$$

for the CD-dDP model with $R_1 = R_0(1+\chi)$, and

$$\tilde{\eta}_{\mathrm{CSL}} = \frac{3\lambda M^2 r_{\mathrm{C}}^3}{R_{\mathrm{C}}m_0^2r^4}\left[1 - 2\left(\frac{R_{\mathrm{C}}}{r}\right)^2 + e^{-\frac{r^2}{R_{\mathrm{C}}^2}}\left(1 + 2\frac{R_{\mathrm{C}}^2}{r^2}\right)\right], \tag{7.21}$$

for the CD-dCSL model with $R_{\mathrm{C}} = r_{\mathrm{C}}(1+\chi)$. Notably, in the CD framework, $\tilde{T}$ depends on all the free parameters of the CD model. In the limit $T_\chi \to \infty$ ($\chi \to 0$), one recovers the standard collapse model with $\tilde{T} = \infty$. In the opposite limit, for $T_\chi \to 0$ (i.e. $\tilde{\Gamma}_c \to \infty$), the last term of the first expression of Eq. (7.18) is the relevant one, while the last of the second expression can be neglected. Then, following the same reasoning as in the LF framework, one has $\tilde{T} = \infty$. Table 7.4.1 presents a direct comparison between the parameters of the two models.

In Fig. 7.4.3 we compare LF-dDP and CD-dDP models, where the experimental values considered are the mass and the radius of the

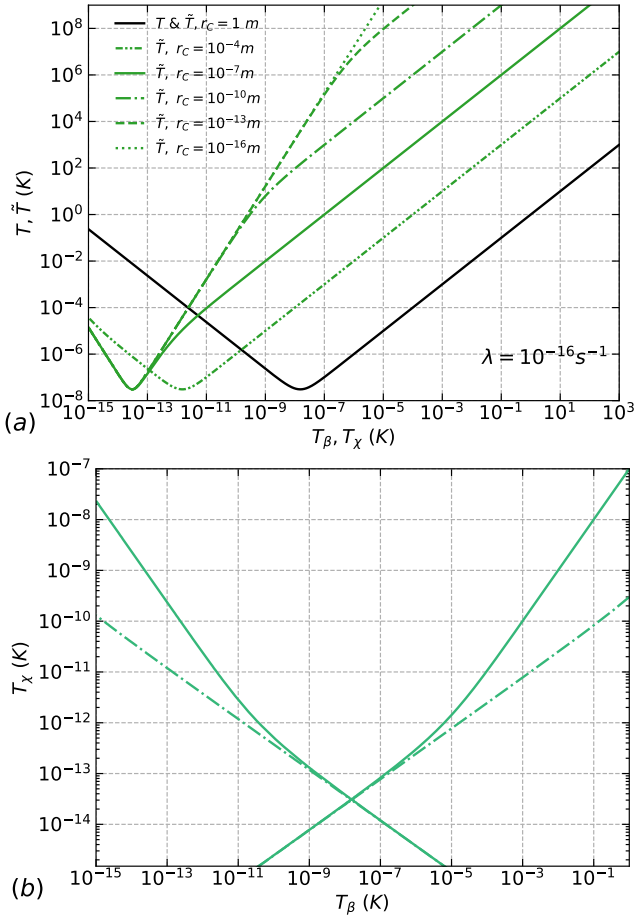

Figure 7.4.4: Comparison between the linear friction dCSL and the collisional dynamics dCSL models. In panel (a) the solid black curve represents the asymptotic temperature T of the LF-dCSL model as a function of the dissipation parameter T_β, while the green curves show the asymptotic temperature $\tilde{T}$ of the CD-dCSL model as a function of the dissipation parameter T_χ for different values of r_C. For $r_C = 1$ m, T and $\tilde{T}$ coincide in the black curve. Panel (b) shows the contour plot of the function $T(T_\beta) - \tilde{T}(T_\chi) = 0$ where the solid green line is for $r_C = 10^{-7}$ m and the dash dotted green line is for $r_C = 10^{-10}$ m. We fix $\lambda = 10^{-16}\,\mathrm{s}^{-1}$.

nano-particle from Dania *et al.* [195]. In panel (a) we show in black the plot of T as a function of T_β and in green the plots of $\tilde{T}$ as a function of T_χ for various values of R_0. We notice that T and $\tilde{T}$ coincide for $R_0 = 1\,\mathrm{m}$. As R_0 decreases, the difference between T and $\tilde{T}$ increases.

More interestingly if we assume that both the models reach the same asymptotic temperature, namely $T = \tilde{T}$, then we can link the two dissipation parameters T_β and T_χ and display how they are related. Thus, in panel (b) of Fig. 7.4.3 we show the plot of the function $T(T_\beta) - \tilde{T}(T_\chi) = 0$. The solid green line is for $R_0 = 10^{-7}\,\mathrm{m}$

and the dash dotted one for $R_0 = 10^{-10}\,\mathrm{m}$. In general the relation between T_β and T_χ is non-linear and it does not lead to a one-to-one relation. However, in some regimes, we have a linear behaviour and we can compare the two collapse temperatures T_β and T_χ directly. For example $T_\beta = 1\,\mathrm{K}$ corresponds to $T_\chi = 10^{-7}\,\mathrm{K}$ for $R_0 = 10^{-7}\,\mathrm{m}$ (solid line) and to $T_\chi \sim 10^{-10}\,\mathrm{K}$ for $R_0 = 10^{-10}\,\mathrm{m}$ (dashed line).
We show the same analysis for LF-dCSL and CD-dCSL models in Fig. 7.4.4 where we used the same colouring and dashing as in Fig. 7.4.3, and where we set $\lambda = 10^{-16}\,\mathrm{s}^{-1}$ corresponding to the GRW point at $r_\mathrm{c} = 10^{-7}\,\mathrm{m}$. We notice that the LF-dCSL and CD-dCSL models lead two different predictions. This is exemplified by the GRW point, which in the CD-dCSL model is excluded for collapse temperatures T_χ below $10^{-9}\,\mathrm{K}$ (see Ref. [201]. On the other hand, focusing on the top right branch of the solid line in Fig. 7.4.4b, the value of $T_\chi = 10^{-9}\,\mathrm{K}$ corresponds to $T_\beta = 10^{-2}\,\mathrm{K}$ for which the GRW point is not excluded [cf. Fig. 7.3.2]. This means that the two frameworks, LF and CD, can be in principle discriminates experimentally. A similar example can be showcased in the comparison of the LF-dDP and CD-dDP models. Notably, the relation between T_χ and T_β for the dDP and dCSL models show the same behaviour [cf. Fig. 7.4.3b and Fig. 7.4.4b].

Linear Friction (LF) model	Collisional Dynamics (CD) model
$\hat{L}_{\mathbf{k}} = \hat{\mu}_{\mathbf{k}} + \frac{\hbar\beta}{4}\mathbf{k}.\hat{\mathbf{J}}_{\mathbf{k}}$	$\hat{\tilde{L}}_{\mathbf{k}} = m\sum_{j=1}^{N} e^{i\mathbf{k}\hat{\mathbf{x}}_j} e^{-2\sigma^2[(1+\chi)\mathbf{k}\hat{\mathbf{p}}_j + 2k^2\hat{\mathbf{p}}_j^2]}$
$D_{\mathbf{k}} = \exp(-\sigma^2 k^2) \times \begin{cases} \hbar^2\gamma & \text{(CSL)} \\ 4\pi\hbar G/k^2 & \text{(DP)} \end{cases}$	$\tilde{D}_{\mathbf{k}} = \exp\!\left(-\sigma^2 k^2 (1+\chi)^2\right) \times \begin{cases} \hbar^2\gamma & \text{(CSL)} \\ 4\pi\hbar G/k^2 & \text{(DP)} \end{cases}$
$\Gamma = \frac{\hbar^2\eta}{2Mk_{\mathrm{B}}T_\beta}$	$\tilde{\Gamma} = \frac{\hbar^2\tilde{\eta}}{2Mk_{\mathrm{B}}T_\chi}\left(1 + \frac{\hbar^2}{8m_0\sigma^2 k_{\mathrm{B}}T_\chi}\right)$
$\eta = \frac{1}{\hbar^2}\int \frac{\mathrm{d}^3k}{(2\pi)^3} k_x^2 D_{\mathbf{k}} \lvert\mu_{\mathbf{k}}\rvert^2$	$\tilde{\eta} = \frac{1}{\hbar^2}\int \frac{\mathrm{d}^3k}{(2\pi)^3} k_x^2 \tilde{D}_{\mathbf{k}} \lvert\mu_{\mathbf{k}}\rvert^2$
$T = T_\beta + \frac{\hbar^2\omega_0^2}{16k_{\mathrm{B}}^2 T_\beta}$	$\tilde{T} = \frac{T_\chi}{1+\frac{\hbar^2}{8m_0\sigma^2 k_{\mathrm{B}}T_\chi}} + \frac{\hbar^2\omega_0^2}{16k_{\mathrm{B}}^2 T_\chi}\left(1 + \frac{\hbar^2}{8m_0\sigma^2 k_{\mathrm{B}}T_\chi}\right) + \frac{\hbar^6\tilde{\eta}^2}{128M^2k_{\mathrm{B}}^4T_\chi^3}\left(1 + \frac{\hbar^2}{8m_0\sigma^2 k_{\mathrm{B}}T_\chi}\right)^3$

Table 7.4.1: Comparison between the parameters of the Linear Friction and Collisional Dynamics dissipative models. Here $\sigma = R_0$, r_{C} for DP and CSL respectively, $\gamma = (\sqrt{4\pi}\sigma)^3\lambda/m_0^2$ and $\chi = \hbar^2/8m_0\sigma^2 k_{\mathrm{B}}T_\chi$. $\hat{\mu}_{\mathbf{k}}$ and $\hat{\mathbf{J}}_{\mathbf{k}}$ are defined in Eq. (7.1).

7.5 Conclusions

Our mechanism to introduce dissipation in collapse models, conversely to a previously proposed one (indicated as Collisional Dynamics (CD) dissipative model), is based on the linear-friction of the current being linear in the current of the many-body system (thus, named as Linear Friction (LF) dissipative model). LF is easier to investigate, as evidenced in Table 7.4.1, which enables a comparison of the parameters of the two models. LF model has not yet been tested, opens a promising avenue for new investigations in the collapse models framework. We focus on establishing the first experimental bounds for linear-friction dissipative DP (dDP) and CSL (dCSL) models, using data from levitated optomechanical experiments. The results reveal significant exclusions of the parameter space, with collapse temperatures below $T_\beta \sim 10^{-13}\,\mathrm{K}$ and $T_\beta \sim 6 \times 10^{-12}\,\mathrm{K}$ for dDP model and all parameter space for dCSL model is excluded for temperatures below $T_\beta \sim 6 \times 10^{-9}\,\mathrm{K}$. Finally, we compare the two models. We find the relations between the respective collapse temperature under the assumption that the collapse process leads the system to thermalisation. We conclude that they can in principle be discriminated experimentally.

Conclusions and outlook

This thesis has investigated various aspects of quantum system dynamics, from the simulation of open quantum systems and noisy quantum devices to the theoretical extension of spontaneous wavefunction collapse models. These efforts, spanning computational and theoretical approaches, aimed to address challenges at the intersection of quantum information science and fundamental quantum mechanics.

The first part of the work focused on a novel quantum algorithm for simulating the Gorini-Kossakowski-Lindblad-Sudarshan (GKLS) master equation. By employing a single ancilla qubit to represent the environment, the proposed approach demonstrated significant efficiency in resource management, making it particularly suitable for near-term quantum computing platforms. For future research the next step is to implement the algorithm on real quantum computers, coupled with error mitigation techniques to counteract the impact of noise. Further, one could explore the inclusion of non-Markovian effects, for example by relaxing the assumption of resetting the bath qubit after each time step.

The thesis also explored the impact of noise on variational quantum eigensolvers (VQEs) applied to the J1–J2 Heisenberg model. By designing an equivariant quantum circuit that respects these symmetries, the study demonstrated how noise affects the variational state, breaking the desired symmetry properties. However, through noise mitigation techniques as Zero Noise Extrapolation (ZNE), it was possible to restore these symmetries and recover accurate results. This opens promising avenues for future studies for example generalizing the approach to more complex systems, including those with long-range interactions or two-dimensional structures, where phase transitions remain an active area of research.

The second part of the work addressed the critical issue of noise in

quantum computers, introducing the "Noisy Gates" method. This approach, rooted in the framework of stochastic differential equations, provided a more detailed and realistic simulation of quantum circuits by considering the interplay between noise and gate operations. Its application to both superconducting and optical systems highlighted its versatility and potential to improve classical simulations of noisy quantum devices. Further developments of the Noisy Gates approach are possible by refining the noise model and extending it to account for correlated errors and cross-talk in order achieve even more accurate simulations. The method also holds potential for improving error mitigation techniques, particularly in optimizing pulse parameters to minimize noise impact, which could be tested on current quantum hardware.

In the final part, we explored extensions of spontaneous wave function collapse models, focusing on a dissipative mechanism characterized by linear friction. The model was also tested through comparisons with experimental data in levitated optomechanics offering meaningful constraints on the free parameters of collapse models. Future work will focus on refining these models and exploring their applicability to various experimental settings, potentially leading to more precise experimental tests of quantum collapse models.

To conclude while we are aware of the challenges that surround the investigations presented in this thesis, we are excited about the potential insights and developments these research directions could reveal, setting the stage for new advances in the field of quantum mechanics.

Appendix A

Appendix of chapter 2

A.1 Perturbative solution of the QSDE

To derive the approximate solution of the QSDE in the main text we use a perturbative method known as *small noise expansion* [11]. The following derivation is performed by using the generic expression for $\mathrm{d}\hat{B}_t$ and $\mathrm{d}\hat{B}_t^\dagger$, but the same results apply when substituting their finite expression and the prescriptions introduced in the main text. For simplicity, let us consider the QSDE with one single Lindblad operator,

$$\mathrm{d}|\Psi_t\rangle = \left[-\frac{i}{\hbar}\hat{H}\mathrm{d}t + \epsilon\big(\hat{L}\mathrm{d}\hat{B}_t^\dagger - \hat{L}^\dagger \mathrm{d}\hat{B}_t\big) - \frac{\epsilon^2}{2}\hat{L}^\dagger\hat{L}\mathrm{d}t \right] |\Psi_t\rangle\,, \tag{A.1}$$

where $\epsilon = \sqrt{\gamma}$. The generalization to $2^{2n}-1$ Lindblad operators again being straightforward, and let us set the following perturbative expansion:

$$|\Psi_s\rangle = \left|\Psi_s^0\right\rangle + \epsilon\left|\Psi_s^1\right\rangle + \epsilon^2\left|\Psi_s^2\right\rangle + \dots \tag{A.2}$$

Substituting the latter into Eq.(A.1) and equating terms with the same power of ϵ, up to second order we have the following system of QSDEs:

$$\begin{aligned}
\mathrm{d}\left|\Psi_t^0\right\rangle &= -\frac{i}{\hbar}\hat{H}\left|\Psi_t^0\right\rangle \mathrm{d}t \\
\mathrm{d}\left|\Psi_t^1\right\rangle &= -\frac{i}{\hbar}\hat{H}\left|\Psi_t^1\right\rangle \mathrm{d}t + \left(\hat{L}\mathrm{d}\hat{B}_t^\dagger - \hat{L}^\dagger\mathrm{d}\hat{B}_t\right)\left|\Psi_t^0\right\rangle \\
\mathrm{d}\left|\Psi_t^2\right\rangle &= -\frac{i}{\hbar}\hat{H}\left|\Psi_t^2\right\rangle \mathrm{d}t + \left(\hat{L}\mathrm{d}\hat{B}_t^\dagger - \hat{L}^\dagger\mathrm{d}\hat{B}_t\right)\left|\Psi_t^1\right\rangle - \frac{1}{2}\hat{L}^\dagger\hat{L}\left|\Psi_t^0\right\rangle \mathrm{d}s,
\end{aligned}$$

which has to be solved with the initial conditions $|\Psi_0^0\rangle = |\Psi_0\rangle$ and $\left|\Psi_0^j\right\rangle = 0$ for $j > 0$. The zero-th order differential equation is the

deterministic equation given by the Hamiltonian evolution alone, hence its solution is simply $|\Psi_t^0\rangle = \hat{U}_t |\Psi_0\rangle$. The solution of the first order QSDE is:

$$\left|\Psi_t^1\right\rangle = \hat{U}_t \hat{S}_t |\Psi_0\rangle , \tag{A.3}$$

where we introduced $\hat{S}_t := \int_0^t (\hat{L}_s \mathrm{d}\hat{B}_s^\dagger - \hat{L}_s^\dagger \mathrm{d}\hat{B}_s)$ with $\hat{L}_s = \hat{U}_s^\dagger \hat{L} \hat{U}_s$. Last, the solution to the second order QSDE is

$$\left|\Psi_t^2\right\rangle = -\hat{U}_t \int_0^t \left[\frac{1}{2}\hat{L}_s^\dagger \hat{L}_s \mathrm{d}s - (\hat{L}_s \mathrm{d}\hat{B}_s^\dagger - \hat{L}_s^\dagger \mathrm{d}\hat{B}_s)\hat{S}_s \right] |\Psi_0\rangle . \tag{A.4}$$

Then, the solution at order ϵ^2 is given by $|\Psi_t\rangle = \hat{N} |\Psi_0\rangle + \mathcal{O}(\epsilon^3)$, where the evolution operator is $\hat{N} = \hat{U}\hat{N}'$, with

$$\hat{N}' = \hat{\mathbb{I}} + \epsilon \hat{S}_t - \frac{\epsilon^2}{2} \int_0^t \hat{L}_s^\dagger \hat{L}_s \mathrm{d}s + \epsilon^2 \int_0^t \big(\hat{L}_s \mathrm{d}\hat{B}_s^\dagger - \hat{L}_s^\dagger \mathrm{d}\hat{B}_s\big)\hat{S}_s. \tag{A.5}$$

In order to express the solution in the form given in the main text, we make use of the following equality obtained by using the Itô rule [11, 14]

$$\int_0^t \big(\hat{L}_s \mathrm{d}\hat{B}_s^\dagger - \hat{L}_s^\dagger \mathrm{d}\hat{B}_s\big)\hat{S}_s = \frac{1}{2}\left[\hat{S}_t^2 + \int_0^t \mathrm{d}s \hat{L}_s^\dagger \hat{L}_s - \hat{C}_t\right], \tag{A.6}$$

where $\hat{C}_t = \frac{1}{2}\int_0^t \big[\hat{S}_s, \hat{L}_s \mathrm{d}\hat{B}_s^\dagger - \hat{L}_s^\dagger \mathrm{d}\hat{B}_s\big]$. By substituting this expression into Eq.(A.5), we have to second order:

$$\hat{N}' = \hat{\mathbb{I}} + \epsilon \hat{S}_t + \frac{\epsilon^2}{2}\hat{S}_t^2 - \epsilon^2 \hat{C}_t = e^{\epsilon \hat{S}_t - \epsilon^2 \hat{C}_t} + \mathcal{O}(\epsilon^3). \tag{A.7}$$

We can neglect the term $\epsilon^2 \hat{C}_t$ which in principle contributes to order ϵ^2; this is legitimate because it is a nested Itô integral of non anticipating functions [11, 14], and hence its stochastic average is 0. In this way we obtain the same expression in Eq. (2.2).

A.2 Approximation error due to the perturbative expansion

We derive an estimate of the upper bound on the approximation error due to the perturbative expansion used in the main text. To estimate the bound we adopt the superoperator norm $\|\mathcal{E}\|_{1\to 1} \equiv$

$\sup_{\|\hat{O}\|_1=1} \left\|\mathcal{E}(\hat{O})\right\|_1$ [34, 57] where $\left\|\hat{O}\right\|_1 \equiv \mathrm{Tr}\left(\sqrt{\hat{O}^\dagger \hat{O}}\right)$ and $\mathcal{E}(\,\cdot\,)$ is a generic superoperator. Moreover we use the fact that a formal solution of the GKLS equation in interaction picture can be written as $\hat{\rho}_S(t+\Delta t) = \hat{U}(\Delta t)\mathrm{T}\left[e^{\int_t^{t+\Delta t} \mathrm{d}s \mathcal{D}(s)}\right]\hat{\rho}_S(t)\hat{U}^\dagger(\Delta t)$, where $\mathrm{T}[\,\cdot\,]$ is the time ordering operator.

The approximation error is quantified by assuming a m-locality condition, namely by considering the decomposition of $\mathcal{D}(s)$ into $\mathcal{D}(s) = \sum_j^K \mathcal{D}_j(s)$ where each $\mathcal{D}_j(s)$ acts non trivially on a subset of $m < n$ qubits. Each of $\mathcal{D}_j(s)$ has a maximum of $2^{2m} - 1$ Lindblad operators. For simplicity we assume that all the parameters γ_k have the same order of magnitude $\gamma_k = \gamma$. We define the unitary superoperator $\mathcal{U}(\Delta t)(\hat{\rho}_S) = \hat{U}(\Delta t)\hat{\rho}_S\hat{U}^\dagger(\Delta t)$. Given the the approximate expression of the density matrix we found in the main text the upper bound on the approximation error can be computed as

$$
\begin{aligned}
\varepsilon_p &= \left\| \hat{U}(\Delta t)\mathrm{T}\left[e^{\int_t^{t+\Delta t} \mathrm{d}s \mathcal{D}(s)}\right]\hat{U}^\dagger(\Delta t) - \hat{U}(\Delta t)\Big(\hat{\mathbb{I}} + \int_t^{t+\Delta t} \mathrm{d}s \mathcal{D}(s)\Big)\hat{U}^\dagger(\Delta t)\right\|_{1\to 1} \\
&\leq \|\mathcal{U}(\Delta t)\|_{1\to 1} \cdot \left\| \mathrm{T}\left[e^{\int_t^{t+\Delta t} \mathrm{d}s \mathcal{D}(s)}\right] - \Big(\hat{\mathbb{I}} + \int_t^{t+\Delta t} \mathrm{d}s \mathcal{D}(s)\Big)\right\|_{1\to 1} \\
&= \left\| \mathrm{T}\left[e^{\int_t^{t+\Delta t} \mathrm{d}s \mathcal{D}(s)}\right] - \Big(\hat{\mathbb{I}} + \int_t^{t+\Delta t} \mathrm{d}s \mathcal{D}(s)\Big)\right\|_{1\to 1} \\
&= \left\| \sum_{k=2}^{\infty} \frac{1}{k!} \int_t^{t+\Delta t} \cdots \int_t^{t+\Delta t} \mathrm{d}t_1 \ldots \mathrm{d}t_k \mathrm{T}\Big[\mathcal{D}(t_1)\ldots\mathcal{D}(t_k)\Big]\right\|_{1\to 1} \\
&\leq \sum_{k=2}^{\infty} \frac{1}{k!} \left\| \int_t^{t+\Delta t} \cdots \int_t^{t+\Delta t} \mathrm{d}t_1 \ldots \mathrm{d}t_k \mathrm{T}\Big[\mathcal{D}(t_1)\ldots\mathcal{D}(t_k)\Big]\right\|_{1\to 1} \\
&= \sum_{k=2}^{\infty} \frac{1}{k!} \left\| \mathrm{T}\left[\Big(\int_t^{t+\Delta t} \mathrm{d}s \mathcal{D}(s)\Big)^k\right]\right\|_{1\to 1} \\
&\leq \sum_{k=2}^{\infty} \frac{1}{k!} \Big(\int_t^{t+\Delta t} \mathrm{d}s \|\mathcal{D}(s)\|_{1\to 1}\Big)^k \leq \frac{1}{2}\Big(\int_t^{t+\Delta t} \mathrm{d}s \|\mathcal{D}(s)\|_{1\to 1}\Big)^2 \sum_{k=0}^{\infty} \frac{1}{k!}\Big(\int_t^{t+\Delta t} \mathrm{d}s \|\mathcal{D}(s)\|_{1\to 1}\Big)^k \\
&= \frac{1}{2}\Big(\int_t^{t+\Delta t} \mathrm{d}s \|\mathcal{D}(s)\|_{1\to 1}\Big)^2 e^{\int_t^{t+\Delta t} \mathrm{d}s \|\mathcal{D}(s)\|_{1\to 1}} \leq \frac{e}{2}\Big(\int_t^{t+\Delta t} \mathrm{d}s \|\mathcal{D}(s)\|_{1\to 1}\Big)^2,
\end{aligned}
\tag{A.8}
$$

where we use the fact that $\gamma \Delta t \ll 1$, thus $\sup_{s\in[t,t+\Delta t]} \|D(s)\|_{1\to 1}\Delta t \leq 1$ and the inequalities $\|\mathcal{E}_1 + \mathcal{E}_2\|_{1\to 1} \leq \|\mathcal{E}_1\|_{1\to 1} + \|\mathcal{E}_2\|_{1\to 1}$, $\|\mathcal{E}_1\mathcal{E}_2\|_{1\to 1} \leq \|\mathcal{E}_1\|_{1\to 1}\|\mathcal{E}_2\|_{1\to 1}$.

Now by considering the m-locality condition on $\mathcal{D}(s)$ described above, one can write $\|\mathcal{D}(s)\|_{1\to 1} \leq K \max_j \|\mathcal{D}_j(s)\|_{1\to 1}$.

Thus, $\|\mathcal{D}_j(s)\|_{1\to 1}$ can be expressed as

$$\begin{aligned}
\|\mathcal{D}_j(s)\|_{1\to 1} &= \sup_{\|\hat{O}\|_1=1} \Big\| \sum_{k=1}^{2^{2m}-1} \gamma\Big((\hat{L}_{k,j}(s)\hat{O}\hat{L}_{k,j}^\dagger(s) - \frac{1}{2}\{\hat{L}_{k,j}^\dagger(s)\hat{L}_{k,j}(s), \hat{O}\}\Big) \Big\|_1 \\
&\leq \gamma \sum_{k=1}^{2^{2m}-1} \Big(\sup_{\|\hat{O}\|_1=1} \big\|\hat{L}_{k,j}(s)\hat{O}\hat{L}_{k,j}^\dagger(s)\big\|_1 + \frac{1}{2} \sup_{\|\hat{O}\|_1=1} \big\|\{\hat{L}_{k,j}^\dagger(s)\hat{L}_{k,j}(s), \hat{O}\}\big\|_1 \Big) \\
&\leq 2\gamma \sum_{k=1}^{2^{2m}-1} \sup_{\|\hat{O}\|_1=1} \big\|\hat{O}\big\|_1 \big\|\hat{L}_{k,j}^\dagger(s)\big\|_\infty \big\|\hat{L}_{k,j}(s)\big\|_\infty \\
&\leq 2\gamma \sum_{k=1}^{2^{2m}-1} \big\|\hat{L}_{k,j}^\dagger(s)\big\|_\infty \big\|\hat{L}_{k,j}(s)\big\|_\infty \\
&= 2\gamma \sum_{k=1}^{2^{2m}-1} \big\|\hat{L}_{k,j}(s)\big\|_\infty^2 \leq 2\gamma(2^{2m}-1)\max_k\Big(\big\|\hat{L}_{k,j}(s)\big\|_\infty^2\Big) \\
&= 2\gamma(2^{2m}-1)\max_k\Big(\big\|\hat{L}_{k,j}\big\|_\infty^2\Big),
\end{aligned} \tag{A.9}$$

where we use the inequalities $\big\|\hat{A}\hat{B}\big\|_1 \leq \big\|\hat{A}\big\|_1\big\|\hat{B}\big\|_\infty$, $\big\|\hat{A}\hat{B}\big\|_1 \leq \big\|\hat{A}\big\|_\infty\big\|\hat{B}\big\|_1$ and $\big\|\hat{A}\big\|_\infty = \sup_{\||\psi\rangle\|=1}\big\|\hat{A}\,|\psi\rangle\big\| = \sup_{\||\psi\rangle\|=1}\sqrt{\langle\psi|\,\hat{A}^\dagger\hat{A}\,|\psi\rangle}$. Moreover we exploit the fact that
$\big\|\hat{L}_{k,j}(s)\big\|_\infty^2 = \sup_{\||\psi\rangle\|=1}\langle\psi|\,\hat{U}^\dagger(s,t)\hat{L}_{k,j}^\dagger\hat{L}_{k,j}\hat{U}(s,t)\,|\psi\rangle =$
$\sup_{\||\psi'\rangle\|=1}\langle\psi'|\,\hat{L}_{k,j}^\dagger\hat{L}_{k,j}\,|\psi'\rangle = \big\|\hat{L}_{k,j}\big\|_\infty^2$. Finally by inserting Eq. (A.9) in Eq. (A.8) one finds

$$\varepsilon_a \leq 2e\Big(K(2^{2m}-1)\max_k\big\|\hat{L}_{k,j}\big\|_\infty^2\gamma\Delta t\Big)^2. \tag{A.10}$$

K that in general takes the value $n!/m!(n-m)!$ scales polinomially as the system size n goes to infinity and read

$$K \sim \frac{n^m}{m!e^m} \sim \mathcal{O}(n^m), \tag{A.11}$$

where we use the Stirling formula.

A.3 Derivation of the master equation of the system assuming the finite representation of bath operators

We show how to recover the GKLS equation for the system density matrix $\hat{\rho}_S$ in the case of finite representation of the bath operators.

We substite the finite representation of the bath operators in the main text inside Eq.(1.31) to get

$$\begin{aligned}\mathrm{d}\hat{\rho}_S =&\mathbb{E}_C\Bigg[-\frac{i}{\hbar}[\hat{H}_\mathrm{S},\hat{\rho}_S]\mathrm{d}t-\frac{\gamma}{2}\{\hat{L}^\dagger\hat{L},\hat{\rho}_S\}\mathrm{d}t+\sqrt{\gamma}\hat{L}\mathrm{d}W\,\mathrm{Tr}_\mathrm{E}\big(\hat{\sigma}_E^+\left|\Psi\right\rangle\left\langle\Psi\right|\big)\\&-\sqrt{\gamma}\hat{L}^\dagger\mathrm{d}W\,\mathrm{Tr}_\mathrm{E}\big(\hat{\sigma}_E^-\left|\Psi\right\rangle\left\langle\Psi\right|\big)+\sqrt{\gamma}\,\mathrm{Tr}_\mathrm{E}\big(\left|\Psi\right\rangle\left\langle\Psi\right|\hat{\sigma}_E^-\big)\hat{L}^\dagger\mathrm{d}W\\&-\sqrt{\gamma}\,\mathrm{Tr}_\mathrm{E}\big(\left|\Psi\right\rangle\left\langle\Psi\right|\hat{\sigma}_E^+\big)\hat{L}\mathrm{d}W+\gamma\hat{L}\,\mathrm{Tr}_\mathrm{E}\big(\left|\Psi\right\rangle\left\langle\Psi\right|\hat{\sigma}_E^-\hat{\sigma}_E^+\big)\hat{L}^\dagger\mathrm{d}t\\&-\gamma\hat{L}\,\mathrm{Tr}_\mathrm{E}\big(\left|\Psi\right\rangle\left\langle\Psi\right|\hat{\sigma}_E^+\hat{\sigma}_E^+\big)\hat{L}\mathrm{d}t-\gamma\hat{L}^\dagger\,\mathrm{Tr}_\mathrm{E}\big(\left|\Psi\right\rangle\left\langle\Psi\right|\hat{\sigma}_E^-\hat{\sigma}_E^-\big)\hat{L}^\dagger\mathrm{d}t\\&+\gamma\hat{L}^\dagger\,\mathrm{Tr}_\mathrm{E}\big(\left|\Psi\right\rangle\left\langle\Psi\right|\hat{\sigma}_E^+\hat{\sigma}_E^-\big)\hat{L}\mathrm{d}t\Bigg].\end{aligned}\tag{A.12}$$

By using the fact that $(\hat{\sigma}_E^\pm)^2=0$, $\hat{P}_0=\left|0\right\rangle_E\left\langle 0\right|_E=\hat{\sigma}_E^-\hat{\sigma}_E^+$ and $\hat{P}_1=\left|1\right\rangle_E\left\langle 1\right|_E=\hat{\sigma}_E^+\hat{\sigma}_E^-$ and that $\mathbb{E}_C[dW]=0$, Eq. (A.12) becomes

$$\begin{aligned}\mathrm{d}\hat{\rho}_S=&-\frac{i}{\hbar}[\hat{H}_\mathrm{S},\hat{\rho}_S]\mathrm{d}t-\frac{\gamma}{2}\{\hat{L}^\dagger\hat{L},\hat{\rho}_S\}\mathrm{d}t+\gamma\hat{L}\,\mathrm{Tr}_\mathrm{E}\big(\left|\Psi\right\rangle\left\langle\Psi\right|\hat{P}_0\big)\hat{L}^\dagger\mathrm{d}t\\&+\gamma\hat{L}^\dagger\,\mathrm{Tr}_\mathrm{E}\big(\left|\Psi\right\rangle\left\langle\Psi\right|\hat{P}_1\big)\hat{L}\mathrm{d}t.\end{aligned}\tag{A.13}$$

The GKLS master equation is recovered by using the prescriptions in Section 2.2. Since $\left|\Psi\right\rangle=\left|\psi\right\rangle_S\left|0\right\rangle_\mathrm{E}$ the $\hat{P}_1$ term give a zero contribution and $\mathrm{Tr}_\mathrm{E}\big(\left|\Psi\right\rangle\left\langle\Psi\right|\hat{P}_0\big)=\left|\psi\right\rangle_S\left\langle\psi\right|_S\left\langle 0\right|_E\hat{P}_0\left|0\right\rangle_E=\left|\psi\right\rangle_S\left\langle\psi\right|_S$.

A.4 Total approximation error of a single time step

Given the implementation of the algorithm in Sec. 2.3 in this appendix we compute the total approximation error ε for a single time step Δt. Here we define $\hat{U}_1(s-t)=\prod_{\alpha=1}^K e^{-\frac{i}{\hbar}\hat{H}_\alpha(s-t)}$ the first order Trotter-Suzuki product formula [59] and $\mathcal{D}_1(s)=\hat{U}_1^\dagger(s-t)\mathcal{D}\hat{U}_1(s-t)$. In the following we use the Zassenhaus formula

$\hat{U}(s-t) = \hat{U}_1(s-t)e^{-\frac{1}{2}\sum_{\alpha<\beta}^{K}[\hat{H}_\alpha,\hat{H}_\beta](s-t)^2} + o((s-t)^3)$ [206].

$$
\begin{aligned}
\varepsilon &= \left\| \hat{U}(\Delta t)\mathrm{T}\left[e^{\int_t^{t+\Delta t}\mathcal{D}(s)\,ds}\right]\hat{U}^\dagger(\Delta t) - \hat{U}_1(\Delta t)\Big(\hat{\mathbb{I}} + \int_t^{t+\Delta t}\mathcal{D}_1(s)\,ds\Big)\hat{U}_1^\dagger(\Delta t)\right\|_{1\to 1} \\
&= \Bigg\| \hat{U}(\Delta t)\mathrm{T}\left[e^{\int_t^{t+\Delta t}\mathcal{D}(s)\,ds}\right]\hat{U}^\dagger(\Delta t) - \hat{U}(\Delta t)\Big(\hat{\mathbb{I}} + \int_t^{t+\Delta t}\mathcal{D}(s)\,ds\Big)\hat{U}^\dagger(\Delta t) \\
&\quad + \hat{U}(\Delta t)\Big(\hat{\mathbb{I}} + \int_t^{t+\Delta t}\mathcal{D}(s)\,ds\Big)\hat{U}^\dagger(\Delta t) - \hat{U}_1(\Delta t)\Big(\hat{\mathbb{I}} + \int_t^{t+\Delta t}\mathcal{D}_1(s)\,ds\Big)\hat{U}_1^\dagger(\Delta t)\Bigg\|_{1\to 1} \\
&\leq \left\| \hat{U}(\Delta t)\mathrm{T}\left[e^{\int_t^{t+\Delta t}\mathcal{D}(s)\,ds}\right]\hat{U}^\dagger(\Delta t) - \hat{U}(\Delta t)\Big(\hat{\mathbb{I}} + \int_t^{t+\Delta t}\mathcal{D}(s)\,ds\Big)\hat{U}^\dagger(\Delta t)\right\|_{1\to 1} \\
&\quad + \left\| \hat{U}(\Delta t)\Big(\hat{\mathbb{I}} + \int_t^{t+\Delta t}\mathcal{D}(s)\,ds\Big)\hat{U}^\dagger(\Delta t) - \hat{U}_1(\Delta t)\Big(\hat{\mathbb{I}} + \int_t^{t+\Delta t}\mathcal{D}_1(s)\,ds\Big)\hat{U}_1^\dagger(\Delta t)\right\|_{1\to 1} \\
&\leq \varepsilon_p + \left\| \hat{U}(\Delta t)\Big(\hat{\mathbb{I}} + \int_t^{t+\Delta t}\mathcal{D}(s)\,ds\Big)\hat{U}^\dagger(\Delta t) - \hat{U}_1(\Delta t)\Big(\hat{\mathbb{I}} + \int_t^{t+\Delta t}\mathcal{D}_1(s)\,ds\Big)\hat{U}_1^\dagger(\Delta t)\right\|_{1\to 1}.
\end{aligned}
\tag{A.14}
$$

At this point we exploit the Zassenhaus formula truncated at second order $\hat{U}(s-t) \simeq \hat{U}_1(s-t)\hat{R}(s-t)$, where $\hat{R}(s-t) = e^{-\frac{1}{2}\sum_{\alpha<\beta}^{K}[\hat{H}_\alpha,\hat{H}_\beta](s-t)^2} \simeq \hat{\mathbb{I}} - \frac{1}{2}\sum_{\alpha<\beta}^{K}[\hat{H}_\alpha,\hat{H}_\beta](s-t)^2 = \hat{\mathbb{I}} - \frac{\omega^2}{2}\sum_{\alpha<\beta}^{K}\sum_{j,j'=1}^{J}[\hat{h}_{\alpha,j},\hat{h}_{\beta,j'}](s-t)^2$. In the latter we defined $\hat{H}_\alpha = \omega\sum_{j=1}^{J},\hat{h}_{\alpha,j}$ where J is a constant whose value depends on the system Hamiltonian under study, $\hat{h}_{\alpha,j}$ are generic m-local operators and for simplicity we choose the same frequency ω for each $\hat{H}_\alpha$. By defining the superoperator $\mathcal{U}_1(\Delta t)(\hat{\rho}_S) = \hat{U}_1(\Delta t)\hat{\rho}_S\hat{U}_1^\dagger(\Delta t)$ and by plugging the above expressions in Eq. (A.14) we can further bound ε as

$$
\begin{aligned}
\varepsilon &\leq \varepsilon_p + \|\mathcal{U}_1(\Delta t)\|_{1\to 1}\cdot\Big\|\hat{R}(\Delta t)\Big(\mathbb{I} + \int_t^{t+\Delta t}\mathrm{d}s\hat{R}^\dagger(s-t)\mathcal{D}_1(s)\hat{R}(s-t)\Big)\hat{R}^\dagger(\Delta t) \\
&\quad - \Big(\hat{\mathbb{I}} + \int_t^{t+\Delta t}\mathrm{d}s\mathcal{D}_1(s)\Big)\Big\|_{1\to 1} \\
&\leq \varepsilon_p + K^2J^2\max_{\alpha,\beta,j,j'}\Big\|[\hat{h}_{\alpha,j},\hat{h}_{\beta,j'}]\Big\|_\infty(\omega\Delta t)^2 + o(\gamma\omega^2(\Delta t)^3) \\
&\leq \varepsilon_p + \Big(KJ\max_{\alpha,j}\Big\|\hat{h}_{\alpha,j}\Big\|_\infty\omega\Delta t\Big)^2 + o(\gamma\omega^2(\Delta t)^3) = \varepsilon_p + \varepsilon_T + o(\gamma\omega^2(\Delta t)^3)
\end{aligned}
\tag{A.15}
$$

A.5 Sampling error analysis

As it is known in the literature [207–209], the estimate of the expectation value of an observable $\hat{O}$ with finite number of realization of the stochastic processes have a sampling error of the form

$$
\eta = |\langle\hat{O}\rangle - \langle\hat{O}\rangle_{\mathcal{N}_r}| = \frac{\Delta\hat{O}(\gamma,\Delta t)}{\sqrt{\mathcal{N}_r}} \tag{A.16}
$$

where $\langle \hat{O} \rangle = \mathrm{Tr}\Big(\hat{O}\hat{\rho}_S(t+\Delta t)\Big)$ is the expected value in the limit of infinite samples, where
$\hat{\rho}_S(t+\Delta t) = \mathbb{E}_C\big[\mathrm{Tr}_E(\hat{N}(\Delta t)\,|\Psi(t)\rangle\,\langle\Psi(t)|\,\hat{N}^\dagger(\Delta t))\big]$ and $\langle \hat{O} \rangle_{\mathcal{N}_r} = \mathrm{Tr}\Big(\hat{O}\hat{\rho}_{\mathcal{N}_r}(t+\Delta t)\Big)$ is the estimate with $\mathcal{N}_r$ total number of samples of the classical stochastic processes where
$\hat{\rho}_{\mathcal{N}_r}(t+\Delta t) = \frac{1}{\mathcal{N}_r}\sum_k^{\mathcal{N}_r} \mathrm{Tr}_E(\hat{N}_k(\Delta t)\,|\Psi(t)\rangle\,\langle\Psi(t)|\,\hat{N}_k^\dagger(\Delta t))$. The value $\Delta\hat{O}(\gamma,\Delta t)$ is the square root of the sample variance $\Delta\hat{O}^2(\gamma,\Delta t) = \frac{1}{\mathcal{N}_r}\sum_k^{\mathcal{N}_r} \mathrm{Tr}^2(\hat{O}\,\mathrm{Tr}_E(\hat{N}_k(\Delta t)\,|\Psi(t)\rangle\,\langle\Psi(t)|\,\hat{N}_k^\dagger(\Delta t))) - \langle\hat{O}\rangle^2_{\mathcal{N}_r}$ which is upper bounded by (see [207])

$$\Delta\hat{O}^2(\gamma,\Delta t) \leq \langle\hat{O}^2\rangle_{\mathcal{N}_r} - \langle\hat{O}\rangle^2_{\mathcal{N}_r} \simeq \langle\hat{O}^2\rangle - \langle\hat{O}\rangle^2. \tag{A.17}$$

It can be shown [207] that for global operators $\hat{O}$ the following relation holds

$$\sqrt{\langle\hat{O}^2\rangle - \langle\hat{O}\rangle^2} \sim \langle\hat{O}\rangle, \tag{A.18}$$

thus by using Eqs. (A.16) and (A.17) we get

$$\langle\hat{O}\rangle \pm \eta \leq \langle\hat{O}\rangle\left(1 \pm 1/\sqrt{\mathcal{N}_r}\right), \tag{A.19}$$

showing that the numbers of samples needed to reach a target accuracy does not depend on the dimension of the system.

Appendix B

Appendix of chapter 3

B.1 Initial states

B.1.1 Singlet state $|\phi_0\rangle$

The initial state representing factorized singlet pairs, as given in Eq. (3.6), is easily prepared on a quantum computer. Simultaneously for each singlet pair $2r-1, 2r$, we prepare the state $|1,+\rangle$ using Pauli X and Hadamard H gates, followed by a CNOT gate (refer to Fig. B.1.1). In general, we dub $\hat{U}_s$ the unitary transformation responsible for generating the product of singlet state on N qubits.

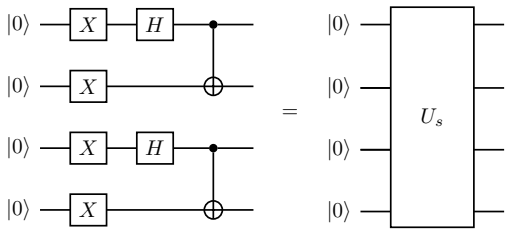

Figure B.1.1: Circuit $\hat{U}_s$ for preparing the $|\phi_0\rangle$ state on 4 qubits.

B.1.2 Triplet state $|\phi_1\rangle$

The triplet states in Eq. (3.7) are not two-site transalation invariant. To get the invariant state $|\phi_1\rangle$ in Eq. (3.8) we use a particular class of entangled states called W states [210]. The W state for n qubits is the superposition of all the possible n-qubit states with just a single qubit in the state $|1\rangle$

$$\left|W^{(n)}\right\rangle = \frac{1}{\sqrt{n}}\big(\,|10\ldots0\rangle + |01\ldots0\rangle + \cdots + |00\ldots1\rangle\,\big). \qquad \text{(B.1)}$$

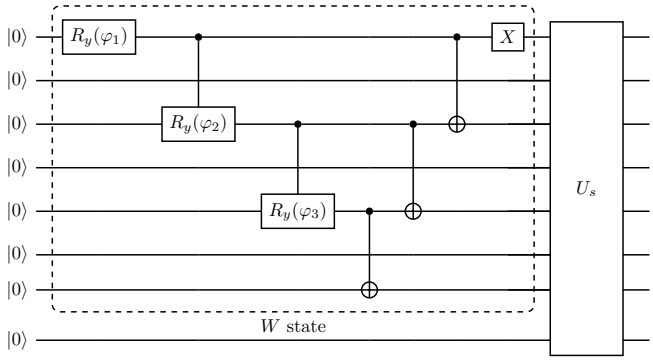

Figure B.1.2: Circuit for preparing the $|\phi_1\rangle$ state on 8 qubits.

As an example for the preparation of $|\phi_1\rangle$, we consider the case of $N = 4$ qubits. We set qubits 2 and 4 in the state $|00\rangle$ and qubits 1 and 3 in the W state, that reads

$$\left|W^{(2)}\right\rangle_{13} = \frac{1}{\sqrt{2}}\big(\,|10\rangle_{13} + |01\rangle_{13}\,\big). \tag{B.2}$$

Then, the total state is expressed as

$$\left|W^{(2)}\right\rangle_{13}|00\rangle_{24} = \frac{1}{\sqrt{2}}\big(\,|1000\rangle + |0010\rangle\,\big)\ , \tag{B.3}$$

where in the right-hand side of Eq. (B.3) the states of single qubits are indexed in ascending order. By applying the unitary $\hat{U}_s$ to the state in Eq. (B.3) we get

$$\frac{1}{\sqrt{2}}\big(|t\rangle_{12}\,|s\rangle_{34} + |s\rangle_{12}\,|t\rangle_{34}\big) = \frac{1}{\sqrt{2}}\Big(\big|\tilde{\phi}_1^1\big\rangle + \big|\tilde{\phi}_1^2\big\rangle\Big), \tag{B.4}$$

where the right-hand side of Eq. (B.4) is $|\phi_1\rangle$ for $N = 4$ qubits. Thus in general, to get $|\phi_1\rangle$ all odd indexed qubits are prepared in the W state and this transformation is followed by the singlet preparation $\hat{U}_s$ on all qubits. An example of the resulting circuit for eight qubits is shown in Fig. B.1.2, where the preparation of the W state is performed efficiently with the techniques described in Ref. [211]. The angles φ_i in Fig. B.1.2 are defined as $\varphi_i = 2\arccos\big(1/\sqrt{n-i+1}\big)$ where i is the index of the qubit.

B.2 Kraus maps

We report the Kraus maps used for the noisy simulations in Chapter 3.

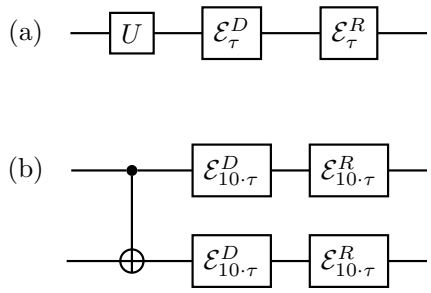

Figure B.2.3: Schematic depiction of the noise model. In panel (a) we show quantum channels associated to a generic single-qubit gate U and in panel (b) those associated to CNOT gates.

The Kraus map of single-qubit depolarization is in Eq. (1.34) [42, 43]. We assume a behaviour in time of the form $p_\tau = (1 - e^{-\gamma_d \tau})$ for a characteristic time $T_d = 1/\gamma_d$ [212]. The Kraus map of the single-qubit relaxation is in Eq. (1.37) [42, 43]. Here, $p_\tau^{(1)} = (1 - e^{-\tau/T_1})$ is the probability of reset to $|0\rangle$ and T_1 the relaxation time. Additionally, we introduce $p_\tau^{(z)} = (1 - p_\tau^{(1)}) \cdot p_\tau^{(pd)}$, where $p_\tau^{(pd)} = (1 - e^{-\tau/T_{pd}})$ is the probability of pure dephasing with $T_{pd} = T_1 T_2/(2T_1 - T_2)$ and T_2 the decoherence time. The time scales T_1 and T_2 are related as $T_2 \leq 2T_1$ [212].
The circuits used in our simulations are transpiled into the native gate set of IBM devices, i.e., $\{RZ(\alpha), X, \sqrt{X}, \text{CNOT}\}$, where $\alpha \in [-\pi, \pi]$ is a rotation angle. Typically the duration of the execution of CNOT gate is 10 times larger with respect to the single-qubit gate time. We set the noise time scales as $T_1 = T_2 = T_d \approx 10^{-4}$ s, compatible with the average values of current IBM devices [44] (see Fig. B.2.3).

Appendix C

Appendix of chapter 4

C.1 Small noise expansion

In this appendix, we show how the approximate solution in Eq. (4.10) can be rigorously derived to order $\mathcal{O}(\epsilon^2)$. We use of a perturbative method known as small noise expansion or asymptotic perturbative expansion [11]. For simplicity, let us consider the SSE in Eq. (1.19) with one single Lindblad operator and $\epsilon = \sqrt{\gamma}$,

$$d\left|\psi_s\right\rangle = \left(-\frac{i}{\hbar}\hat{H}_s \mathrm{d}s + i\epsilon\hat{L}\mathrm{d}W_s - \frac{\epsilon^2}{2}\hat{L}^\dagger\hat{L}\mathrm{d}s \right)\left|\psi_s\right\rangle, \tag{C.1}$$

the generalization to d^2-1 Lindblad operators with $d = 2^n$ being straightforward, and let us set the following ansatz:

$$\left|\psi_s\right\rangle = \left|\psi_s^0\right\rangle + \epsilon\left|\psi_s^1\right\rangle + \epsilon^2\left|\psi_s^2\right\rangle + \dots \tag{C.2}$$

Substituting this ansatz into Eq.(C.1) and equating terms with the same power of ϵ, up to second order we get a system of SDEs:

$$\begin{aligned}
\mathrm{d}\left|\psi_s^0\right\rangle &= -\frac{i}{\hbar}\hat{H}_s\left|\psi_s^0\right\rangle \mathrm{d}s \\
\mathrm{d}\left|\psi_s^1\right\rangle &= -\frac{i}{\hbar}\hat{H}_s\left|\psi_s^1\right\rangle \mathrm{d}s + i\hat{L}\left|\psi_s^0\right\rangle \mathrm{d}W_s \\
\mathrm{d}\left|\psi_s^2\right\rangle &= -\frac{i}{\hbar}\hat{H}_s\left|\psi_s^2\right\rangle \mathrm{d}s + i\hat{L}\left|\psi_s^1\right\rangle \mathrm{d}W_s - \frac{1}{2}\hat{L}^\dagger\hat{L}\left|\psi_s^0\right\rangle \mathrm{d}s,
\end{aligned} \tag{C.3}$$

which must be solved with the initial conditions $\left|\psi_0^0\right\rangle = \left|\psi_0\right\rangle$. The zero-th order differential equation is the deterministic one given by the Hamiltonian evolution alone, hence its solution is simply $\left|\psi_s^0\right\rangle = \hat{U}_s\left|\psi_0\right\rangle$. The first order SDE is an example of a time-dependent

Ornstein-Uhlenbeck process [11]: the solution is

$$\left|\psi_s^1\right\rangle = i\hat{U}_s\hat{S}_s\left|\psi_0\right\rangle, \tag{C.4}$$

where we defined $\hat{S}_s = \int_0^s \mathrm{d}W_\tau \hat{L}_\tau$. Finally, the solution to the second order SDE is

$$\left|\psi_s^2\right\rangle = -\hat{U}_s\int_0^s \left(\frac{1}{2}\hat{L}_s^\dagger\hat{L}_s\mathrm{d}s + \hat{L}_s\hat{S}_s\mathrm{d}W_s\right)\left|\psi_0\right\rangle, \tag{C.5}$$

where $\hat{L}_s = \hat{U}_s^\dagger\hat{L}\hat{U}_s$. Then, the solution at order ϵ^2 is given by $|\psi_1\rangle = \hat{N}\left|\psi_0\right\rangle + \mathcal{O}(\epsilon^3)$, where the evolution operator is $\hat{N} = \hat{U}_g\hat{N}'$, with

$$\hat{N}' = \left[\hat{\mathbb{I}} + \epsilon\hat{S}_1 - \epsilon^2\int_0^1 \left(\frac{1}{2}\hat{L}_s^\dagger\hat{L}_s\mathrm{d}s + \hat{L}_s\hat{S}_s\mathrm{d}W_s\right)\right]. \tag{C.6}$$

In order to evaluate the solution in the form given in the main text, we make use of the following equality:

$$\int_0^\tau \mathrm{d}W_s\hat{L}_s\hat{S}_s = \frac{1}{2}\left(\hat{S}_s^2 + \int_0^\tau \mathrm{d}W_s[\hat{L}_s,\hat{S}_s] - \int_0^\tau \mathrm{d}s\hat{L}_s^2\right) \tag{C.7}$$

obtained by using the Itô rule [11] for each entry of the stochastic matrices. Substituting this expression into Eq.(A.5), we get to second order:

$$\begin{aligned}\hat{N}' &= \hat{\mathbb{I}} + i\epsilon\hat{S}_1 - \frac{\epsilon^2}{2}\left(\hat{S}_1^2 + \int_0^1 \mathrm{d}s\left(\hat{L}_s^\dagger - \hat{L}_s\right)\hat{L}_s + \mathcal{C}\right) = \\ &= e^{\hat{D}_g}e^{\hat{S}_g} + \mathcal{O}(\epsilon^3),\end{aligned}$$

where $\hat{D}_g$, $\hat{S}_g$ and $\hat{\mathcal{C}} = \int_0^1 \mathrm{d}W_s\left[\hat{L}_s,\hat{S}_s\right]$ are the same quantities defined in Section 4.2.

C.2 Comparison of the approximations

Here we focus on the main differences between the approximation made in the standard approach (see Section 1.3.2) versus the one considered in the noisy gates approach in Section 4.2.
Given the following Lindblad master equation

$$\frac{\mathrm{d}}{\mathrm{d}t}\hat{\rho}_t = -\frac{i}{\hbar}[\hat{H}_t,\hat{\rho}_t] + \gamma\mathfrak{L}\hat{\rho}_t, \tag{C.8}$$

where $\mathfrak{L}\hat{\rho}_t = \hat{L}\hat{\rho}_t\hat{L}^\dagger - \frac{1}{2}\{\hat{L}^\dagger\hat{L}, \hat{\rho}_t\}$, let's move to the interaction picture by defining $\hat{\chi}_t = \hat{U}^\dagger_{t,t_0}\hat{\rho}_t\hat{U}_{t,t_0}$ and $\hat{\chi}_{t_0} = \hat{\rho}_{t_0}$. Then

$$\frac{\mathrm{d}}{\mathrm{d}t}\hat{\chi}_t = \gamma\mathfrak{L}(t)\hat{\chi}_t, \tag{C.9}$$

where $\mathfrak{L}(t)\hat{\chi}_t = \hat{U}^\dagger_{t,t_0}\mathfrak{L}\hat{\rho}_t\hat{U}_{t,t_0}$.

The formal solution of Eq. (C.9) is

$$\hat{\chi}_t = \mathrm{T}\left[e^{\gamma\int_{t_0}^{t}\mathrm{d}s\mathfrak{L}(s)}\right]\hat{\chi}_{t_0}, \tag{C.10}$$

where $\mathrm{T}[\cdot]$ is the time ordering. Thus in the Schrödinger picture we can write the formal solution of Eq. (C.8) as

$$\hat{\rho}_t = \hat{U}_{t,t_0}\mathrm{T}\left[e^{\gamma\int_{t_0}^{t}\mathrm{d}s\mathfrak{L}(s)}\right]\hat{\rho}_{t_0}\hat{U}^\dagger_{t,t_0}. \tag{C.11}$$

- *Standard approximation* - The main approximation that can be found in the literature is to separate the Hamiltonian dynamics from the noise one [42, 43]. This choice is based on the observation that in general in quantum devices $\omega >> \gamma$, where ω is the pulse frequency of the Hamiltonian. Thus, the noise dynamics can be seen as frozen with respect to the faster Hamiltonian one. It means that in Eq. (C.11) one assumes

$$\mathfrak{L}(t) \simeq \mathfrak{L} \tag{C.12}$$

getting

$$\hat{\rho}_t \simeq \hat{U}_{t,t_0}e^{\gamma\mathfrak{L}\cdot(t-t_0)}\hat{\rho}_{t_0}\hat{U}^\dagger_{t,t_0}. \tag{C.13}$$

We notice that indeed in Eq. (C.13) the two dynamics are independent.

- *Noisy gates approximation* - Also in this case the approximation is based on $\omega >> \gamma$, but we assume that γ is not small enough to completely separate the dynamics. An example of this can be seen in the devices of IBM where the noise evolution can be influenced in a non-negligible manner by the pulse of the drive Hamiltonian

[213, 214]. Thus we make a first order approximation over γ in Eq. (C.11)

$$\mathrm{T}\left[e^{\gamma\int_{t_0}^{t}\mathrm{d}s\mathfrak{L}(s)}\right] \simeq \hat{\mathbb{I}} + \gamma\int_{t_0}^{t}\mathrm{d}s\mathfrak{L}(s), \tag{C.14}$$

and we get

$$\hat{\rho}_t \simeq \hat{U}_{t,t_0}\left(\hat{\mathbb{I}} + \gamma\int_{t_0}^{t}\mathrm{d}s\mathfrak{L}(s)\right)\hat{\rho}_{t_0}\hat{U}_{t,t_0}^{\dagger}. \tag{C.15}$$

In Eq. (C.15) the noise depends on the Hamiltonian dynamics through $\mathfrak{L}(s)$. We stress that the perturbative solution of the SDE in the noisy gates approach reproduce density matrices of the form of Eq. (C.15).

C.3 Noise gates for Spam and Relaxation on idle qubits

In this section we address SPAM and relaxation noises on idle qubits, where the corresponding noise gates can be derived exactly [7, 12, 215]. We do not consider depolarization error on idle qubits, because this channel is used to model incoherent gate infidelities.

C.3.1 Noise gate for SPAM

The Kraus map of SPAM is in Eq.(1.33). Assuming a behaviour in time of the form $p = (1-e^{-2t/T})/2$ for a characteristic time $T = \gamma^{-1}$, one gets the corresponding Lindblad master equation

$$\frac{\mathrm{d}}{\mathrm{d}t}\hat{\rho}_t = \gamma(\hat{X}\hat{\rho}_t\hat{X} - \hat{\rho}_t). \tag{C.16}$$

The associated stochastic differential equation is

$$\mathrm{d}|\psi_t\rangle = \left[i\sqrt{\gamma}\hat{X}\mathrm{d}W_t - \frac{\gamma}{2}\mathrm{d}t\right]|\psi_t\rangle\,. \tag{C.17}$$

This equation is analytically solvable with standard methods [11,12], and thus we can exactly evaluate the corresponding noise gate as

$$\hat{N}^{\mathrm{SPAM}}(t,t_0) = e^{i\sqrt{\gamma}\hat{X}W(t,t_0)}, \tag{C.18}$$

where $W(t,t_0) := \int_{t_0}^{t}\mathrm{d}W_s$. In this case, the noise gate happens to be unitary, thus we can interpret it as a stochastic Schrödinger

evolution due to the presence of the Wiener process $W(t,t_0)$. In the simulations we can directly sample $W(t,t_0)$ from a Gaussian distribution with mean $\mathbb{E}[W(t,t_0)]=0$ and variance $\mathbb{E}[W^2(t,t_0)]=t-t_0$.

C.3.2 Noise gate for relaxation

The Kraus map of relaxation is in Eq.(1.34). Defining $\gamma_1=1/T_1$, $\gamma_{pd}=1/T_{pd}$, the corresponding GKLS equation is

$$\frac{\mathrm{d}}{\mathrm{d}t}\hat{\rho}_t=\gamma_1\hat{\sigma}^+\rho_t\hat{\sigma}^- -\frac{\gamma_1}{2}\{\hat{P}_1,\rho_t\}+\frac{\gamma_{pd}}{4}(\hat{Z}\hat{\rho}_t\hat{Z}-\hat{\rho}_t), \tag{C.19}$$

and the relative Itô equation reads:

$$\mathrm{d}|\psi_t\rangle = \mathrm{d}\hat{\mathcal{W}}\,|\psi_t\rangle\,, \tag{C.20}$$

where

$$\mathrm{d}\hat{\mathcal{W}}=i\sqrt{\gamma}_1\hat{\sigma}^+\mathrm{d}W_{t,1}-\frac{\gamma_1}{2}\hat{P}_1\mathrm{d}t+i\sqrt{\frac{\gamma_{pd}}{4}}\hat{Z}\mathrm{d}W_{t,2}-\frac{\gamma_{pd}}{8}\mathrm{d}t. \tag{C.21}$$

With this stochastic term the Itô equation is analytically solvable [10] and we get the following non-unitary noisy gate

$$\hat{N}^{\text{relax}}(t,t_0)=\begin{pmatrix} e^{i\alpha\bar{W}_2(t,t_0)} & iS(t,t_0)e^{i\alpha W_2(t,t_0)} \\ 0 & e^{-\frac{\gamma_1}{2}(t-t_0)}e^{-i\alpha W_2(t,t_0)} \end{pmatrix}, \tag{C.22}$$

where we defined for simplicity $\alpha:=\sqrt{\gamma_{pd}/4}$, and

$$S(t,t_0)=\sqrt{\gamma_1}\int_{t_0}^{t}e^{-\frac{\gamma_1}{2}(s-t_0)}e^{-2i\alpha W_2(s,t_0)}\mathrm{d}W_{s,1} \tag{C.23}$$

is a complex stochastic Itô process. In principle, such a term is problematic in view of a simulation, since it is not easy to sample. To understand this, look for instance at the real part,

$$S_R(t,t_0)=\sqrt{\gamma_1}\int_{t_0}^{t}e^{-\frac{\gamma_1}{2}(s-t_0)}\cos\Big(2\alpha W_2(s,t_0)\Big)\mathrm{d}W_{s,1}; \tag{C.24}$$

this is an Itô integral of a stochastic function, and it is not easy to derive its probability distribution; thus, sampling $S(t,t_0)$ may be

problematic. We can avoid such a difficulty by adequately substituting $\hat{N}^{\text{relax}}(t,t_0)$ with some modified noisy gate, which is equivalent to the former once the average is carried out, in the sense that Eq. (1.37) still holds even if the new noisy gate is not a solution of the unraveling (C.21) anymore. For instance, it is straightforward to verify that this holds for the following choice:

$$\tilde{\hat{N}}^{\text{relax}}(t,t_0) = \begin{pmatrix} e^{i\alpha W_2(t,t_0)} & i\tilde{S}(t,t_0)e^{-i\alpha W_2(t,t_0)} \\ 0 & e^{-\frac{\gamma_1}{2}(t-t_0)}e^{-i\alpha W_2(t,t_0)} \end{pmatrix}, \tag{C.25}$$

with the definition

$$\tilde{S}(t,t_0) = \sqrt{\gamma_1}\int_{t_0}^{t} e^{-\frac{\gamma_1}{2}(s-t_0)}\mathrm{d}W_{s,1}; \tag{C.26}$$

i.e., one always has that

$$\mathbb{E}\big[\hat{N}^{\text{relax}}\left|\psi\right\rangle\left\langle\psi\right|\hat{N}^{\text{relax}\dagger}\big] = \mathbb{E}\big[\tilde{\hat{N}}^{\text{relax}}\left|\psi\right\rangle\left\langle\psi\right|\tilde{\hat{N}}^{\text{relax}\dagger}\big]. \tag{C.27}$$

The difference is that now the process $\tilde{S}(t,t_0)$ is just the Itô integral of a deterministic function, hence we know that it must have a Gaussian statistics [11], which makes it more convenient for a simulation.

Appendix D

Appendix of chapter 6

D.1 Single particle dissipative mechanism in the Heisenberg picture

We re-derive here the results appearing in Sections 6.2 and 6.3 in Heisenberg picture for a generic state $\hat{\rho}$. In particular, we show that the second term of $\mathcal{D}$ in Eq. (6.11) leads to the dissipation of the current, and that the energy follows the balance equation displayed in Eq. (1.59). For the sake of simplicity, we focus on the case of a single particle. In such a case, the explicit forms of the Fourier transform of the mass density $\hat{\mu}_{\mathbf{k}}$ and the current $\hat{\mathbf{J}}_{\mathbf{k}}$, are

$$\hat{\mu}_{\mathbf{k}} = m e^{i\mathbf{k}\hat{\mathbf{x}}}, \qquad \hat{\mathbf{J}}_{\mathbf{k}} = \frac{1}{2}\{\hat{\mathbf{p}}, e^{i\mathbf{k}\hat{\mathbf{x}}}\}. \tag{D.1}$$

From these and from Eq. (1.53), one can compute their commutator and anticommutator, which respectively read

$$\begin{aligned} [\hat{\mu}_{\mathbf{q}}, \hat{\mathbf{J}}_{\mathbf{k}}] &= -m\hbar\mathbf{q} e^{i(\mathbf{k}+\mathbf{q})\hat{\mathbf{x}}} = -\hbar\mathbf{q}\hat{\mu}_{\mathbf{k}+\mathbf{q}} \\ \{\hat{\mu}_{\mathbf{q}}, \hat{\mathbf{J}}_{\mathbf{k}}\} &= m e^{i(\mathbf{k}+\mathbf{q})\hat{\mathbf{x}}}\big(2\hat{\mathbf{p}} + \hbar(\mathbf{k}+\mathbf{q})\big) = 2m\hat{\mathbf{J}}_{\mathbf{k}+\mathbf{q}}. \end{aligned} \tag{D.2}$$

The dynamics of the current due to the second term in Eq. (6.11) is given, equivalently, by the following two expressions

$$\frac{\mathrm{d}}{\mathrm{d}t}\hat{\mathbf{J}}(\mathbf{x})|_2 = -\frac{i\beta}{4\hbar}\int \mathrm{d}^3y \int \mathrm{d}^3y'\, D(\mathbf{y}-\mathbf{y}')\{\nabla_{\mathbf{y}}\hat{\mathbf{J}}(\mathbf{y}), [\hat{\mu}(\mathbf{y}'), \hat{\mathbf{J}}(\mathbf{x})]\} \tag{D.3}$$

$$= -\frac{\beta}{4\hbar}\int \frac{\mathrm{d}^3k'}{(2\pi)^3} e^{-i\mathbf{k}'\mathbf{x}} \int \frac{\mathrm{d}^3k}{(2\pi)^3} D_{\mathbf{k}}\{\mathbf{k}\hat{\mathbf{J}}_{\mathbf{k}}, [\hat{\mu}_{-\mathbf{k}}, \hat{\mathbf{J}}_{\mathbf{k}'}]\}. \tag{D.4}$$

By employing the second of these expressions, and merging it with Eq. (D.2), one straightforwardly finds

$$\frac{\mathrm{d}}{\mathrm{d}t}\hat{\mathbf{J}}(\mathbf{x})|_2 = -\zeta\,\hat{\mathbf{J}}(\mathbf{x}), \tag{D.5}$$

where

$$\zeta = \frac{\beta m}{2} \int \frac{\mathrm{d}^3 k}{(2\pi)^3} D_{\mathbf{k}} k^2, \tag{D.6}$$

and shows explicitly that the contributions due $\hat{\mathbf{Y}}(\mathbf{x})$ in Eq. (6.17) vanishes exactly in the single fermion case. Similarly, one computes the following commutators of $\hat{\mu}_{\mathbf{k}}$ and $\hat{\mathbf{J}}_{\mathbf{k}}$ with $\hat{H} = \frac{\hat{\mathbf{p}}^2}{2m}$:

$$[\hat{\mu}_{\mathbf{k}}, \hat{H}] = -\frac{e^{i\mathbf{k}\hat{\mathbf{x}}}}{2}(\hbar^2 k^2 + 2\hbar \mathbf{k}\hat{\mathbf{p}}) \quad \text{and} \quad \left[\mathbf{k}\hat{\mathbf{J}}_{\mathbf{k}}, \hat{H}\right] = -\frac{\hbar e^{i\mathbf{k}\hat{\mathbf{x}}}}{4m}(\hbar k^2 + 2\mathbf{k}\hat{\mathbf{p}})^2, \tag{D.7}$$

from which one obtains

$$[\hat{\mu}_{-\mathbf{k}}, [\hat{\mu}_{\mathbf{k}}, \hat{H}]] = -m\hbar^2 k^2, \tag{D.8}$$

$$\{\mathbf{k}\hat{\mathbf{J}}_{\mathbf{k}}, [\hat{\mu}_{-\mathbf{k}}, \hat{H}]\} = 2\hbar(\mathbf{k}\hat{\mathbf{p}})^2 + \frac{\hbar^3 k^4}{2}, \tag{D.9}$$

$$\left[\mathbf{k}\hat{\mathbf{J}}_{-\mathbf{k}}, \left[\mathbf{k}\hat{\mathbf{J}}_{\mathbf{k}}, \hat{H}\right]\right] = -\frac{3\hbar^2 k^2 (\mathbf{k}\hat{\mathbf{p}})^2}{m} - \frac{\hbar^4 k^6}{4m}. \tag{D.10}$$

Owning that, for any spherically symmetric kernel $D_{\mathbf{k}} = D_k$, the following holds

$$\int \mathrm{d}\mathbf{k} D_k (\mathbf{k}\hat{\mathbf{p}})^2 = \int \mathrm{d}\mathbf{k} D_k (k\hat{p}\cos\theta)^2 = \hat{p}^2 \frac{4\pi}{3} \int \mathrm{d}k D_k k^4 = \int \mathrm{d}\mathbf{k} D_k \left(\frac{k^2 \hat{p}^2}{3}\right), \tag{D.11}$$

we can substitute $(\mathbf{k}\hat{\mathbf{p}})^2$ with $(k^2\hat{p}^2)/3$ [this has been used also in Eq. (6.26)]. Then, from Eq. (6.12) we obtain the dynamics for the Hamiltonian:

$$\mathcal{D}^\dagger \hat{H} = P - \Gamma \hat{H}, \tag{D.12}$$

where the explicit form of P and Γ is given in Eq. (6.27). We underline that such an equation is state independent, thus it can be straightforwardly used to evaluate the expectation value of the energy for any state, also beyond the assumption of $\hat{\rho} = \rho(\hat{\mathbf{p}})$, which has been considered in the main text.

Bibliography

[1] Vittorio Gorini, Andrzej Kossakowski, and Ennackal Chandy George Sudarshan. Completely positive dynamical semigroups of n-level systems. *Journal of Mathematical Physics*, 17(5):821–825, 1976. doi:10.1063/1.522979.

[2] Goran Lindblad. On the generators of quantum dynamical semigroups. *Communications in Mathematical Physics*, 48(2):119–130, 1976. doi:10.1007/BF01608499.

[3] Maximilian Schlosshauer. Decoherence and the quantum-to-classical transition. *The Frontiers Collection (Springer-Verlag, 2007)*, 2007. doi:10.1007/978-3-540-35775-9.

[4] Karl Kraus. *States, Effects, and Operations: Lectures in Mathematical Physics at the University of Texas at Austin*. Springer, 1983. doi:10.1007/3-540-12732-1.

[5] Heinz-Peter Breuer, Francesco Petruccione, et al. *The theory of open quantum systems*. Oxford University Press on Demand, 2002. doi:10.1093/acprof:oso/9780199213900.001.0001.

[6] Kurt Jacobs. *Quantum measurement theory and its applications*. Cambridge University Press, 2014. doi:10.1017/CBO9781139179027.

[7] Kurt Jacobs and Peter L Knight. Linear quantum trajectories: Applications to continuous projection measurements. *Physical review A*, 57(4):2301, 1998. doi:10.1103/PhysRevA.57.2301.

[8] Angelo Bassi and GianCarlo Ghirardi. Dynamical reduction models. *Physics Reports*, 379(5-6):257–426, 2003. doi:10.1016/s0370-1573(03)00103-0.

[9] Angelo Bassi. Stochastic schrödinger equations with general complex gaussian noises. *Physical Review A*, 67(6), 2003. doi:10.1103/physreva.67.062101.

[10] Ludwig Arnold. Stochastic differential equations. *New York*, 1974. doi:10.1002/zamm.19770570413.

[11] Crispin W Gardiner et al. *Handbook of stochastic methods*, volume 3. springer Berlin, 1985. doi:10.1007/978-3-662-02452-2.

[12] Kurt Jacobs. *Stochastic processes for physicists: understanding noisy systems*. Cambridge University Press, 2010. doi:10.1017/CBO9780511815980.

[13] Howard M Wiseman and Gerard J Milburn. *Quantum measurement and control*. Cambridge university press, 2009. doi:10.1017/CBO9780511813948.

[14] CW Gardiner and P Zoller. *Quantum Noise*. Springer-Verlag Berlin, 2004. URL: https://link.springer.com/book/9783540223016?wt_mc=GoogleBooks.GoogleBooks.3.EN&token=gbgen.

[15] Peter Zoller and C. W. Gardiner. Quantum noise in quantum optics: the stochastic schrödinger equation, 1997. arXiv:quant-ph/9702030.

[16] RP Feynman. A computer-algebraic approach to the simulation of multi-qubit systems. *Int. J. Theoret. Phys*, 21:467, 1982. doi:10.1007/BF02650179.

[17] Adam Smith, MS Kim, Frank Pollmann, and Johannes Knolle. Simulating quantum many-body dynamics on a current digital quantum computer. *npj Quantum Information*, 5(1):106, 2019. doi:10.1038/s41534-019-0217-0.

[18] Iulia M Georgescu, Sahel Ashhab, and Franco Nori. Quantum simulation. *Reviews of Modern Physics*, 86(1):153, 2014. doi:10.1103/RevModPhys.86.153.

[19] Ehud Altman, Kenneth R Brown, Giuseppe Carleo, Lincoln D Carr, Eugene Demler, Cheng Chin, Brian DeMarco, Sophia E Economou, Mark A Eriksson, Kai-Mei C Fu, et al. Quantum simulators: Architectures and opportunities. *PRX Quantum*, 2(1):017003, 2021. doi:10.1103/PRXQuantum.2.017003.

[20] Stephen P Jordan, Keith SM Lee, and John Preskill. Quantum algorithms for quantum field theories. *Science*, 336(6085):1130–1133, 2012. doi:10.1126/science.1217069.

[21] Benjamin Nachman, Davide Provasoli, Wibe A De Jong, and Christian W Bauer. Quantum algorithm for high energy physics simulations. *Physical review letters*, 126(6):062001, 2021. doi:10.1103/PhysRevLett.126.062001.

[22] Bela Bauer, Sergey Bravyi, Mario Motta, and Garnet Kin-Lic Chan. Quantum algorithms for quantum chemistry and quantum materials science. *Chemical Reviews*, 120(22):12685–12717, 2020. doi:0.1021/acs.chemrev.9b00829.

[23] Youngseok Kim, Andrew Eddins, Sajant Anand, Ken Xuan Wei, Ewout Van Den Berg, Sami Rosenblatt, Hasan Nayfeh, Yantao Wu, Michael Zaletel, Kristan Temme, et al. Evidence for the utility of quantum computing before fault tolerance. *Nature*, 618(7965):500–505, 2023. doi:10.1038/s41586-023-06096-3.

[24] Jiehang Zhang, Guido Pagano, Paul W Hess, Antonis Kyprianidis, Patrick Becker, Harvey Kaplan, Alexey V Gorshkov, Z-X Gong, and Christopher Monroe. Observation of a many-body dynamical phase transition with a 53-qubit quantum simulator. *Nature*, 551(7682):601–604, 2017. doi:10.1038/nature24654.

[25] Thomas E O'Brien, G Anselmetti, Fotios Gkritsis, VE Elfving, Stefano Polla, William J Huggins, Oumarou Oumarou, Kostyantyn Kechedzhi, Dmitry Abanin, Rajeev Acharya, et al. Purification-based quantum error mitigation of pair-correlated electron simulations. *Nat. Phys. 19, 1787–1792*, 2023. doi:10.1038/s41567-023-02240-y.

[26] José D. Guimarães, James Lim, Mikhail I. Vasilevskiy, Susana F. Huelga, and Martin B. Plenio. Noise-assisted digital quantum simulation of open systems using partial probabilistic error cancellation. *PRX Quantum*, 4:040329, Nov 2023. doi:10.1103/PRXQuantum.4.040329.

[27] Juha Leppäkangas, Nicolas Vogt, Keith R. Fratus, Kirsten Bark, Jesse A. Vaitkus, Pascal Stadler, Jan-Michael Reiner, Sebastian Zanker, and Michael Marthaler. Quantum algorithm for solving open-system dynamics on quantum computers using noise. *Phys. Rev. A*, 108:062424, Dec 2023. doi:10.1103/PhysRevA.108.062424.

[28] Shin Sun, Li-Chai Shih, and Yuan-Chung Cheng. Efficient quantum simulation of open quantum system dynamics on noisy quantum computers. *Physica Scripta*, 99(3):035101, feb 2024. doi:10.1088/1402-4896/ad1c27.

[29] Konstantinos Georgopoulos, Clive Emary, and Paolo Zuliani. Modeling and simulating the noisy behavior of near-term quantum computers. *Phys. Rev. A*, 104:062432, Dec 2021. doi:10.1103/PhysRevA.104.062432.

[30] Giovanni Di Bartolomeo, Michele Vischi, Francesco Cesa, Roman Wixinger, Michele Grossi, Sandro Donadi, and Angelo Bassi. Noisy gates for simulating quantum computers. *Phys. Rev. Res.*, 5:043210, Dec 2023. doi:10.1103/PhysRevResearch.5.043210.

[31] Michele Vischi, Giovanni Di Bartolomeo, Massimiliano Proietti, Seid Koudia, Filippo Cerocchi, Massimiliano Dispenza, and Angelo Bassi. Simulating photonic devices with noisy optical elements. *Physical Review Research*, 6(3), September 2024. doi:10.1103/physrevresearch.6.033337.

[32] Andreas Ketterer and Thomas Wellens. Characterizing crosstalk of superconducting transmon processors. *Phys. Rev. Appl.*, 20:034065, Sep 2023. doi:10.1103/PhysRevApplied.20.034065.

[33] Stefano Martina, Lorenzo Buffoni, Stefano Gherardini, and Filippo Caruso. Learning the noise fingerprint of quantum devices. *Quantum Machine Intelligence*, 4(1), April 2022. doi:10.1007/s42484-022-00066-0.

[34] Ryan Sweke, Ilya Sinayskiy, Denis Bernard, and Francesco Petruccione. Universal simulation of markovian open quantum systems. *Phys. Rev. A*, 91:062308, Jun 2015. doi:10.1103/PhysRevA.91.062308.

[35] Wibe A. de Jong, Mekena Metcalf, James Mulligan, Mateusz Płoskoń, Felix Ringer, and Xiaojun Yao. Quantum simulation of open quantum systems in heavy-ion collisions. *Phys. Rev. D*, 104:L051501, Sep 2021. doi:10.1103/PhysRevD.104.L051501.

[36] Marco Cattaneo, Gabriele De Chiara, Sabrina Maniscalco, Roberta Zambrini, and Gian Luca Giorgi. Collision models can efficiently simulate any multipartite markovian quantum dynamics. *Phys. Rev. Lett.*, 126:130403, Apr 2021. doi:10.1103/PhysRevLett.126.130403.

[37] Marco Cattaneo, Matteo A.C. Rossi, Guillermo García-Pérez, Roberta Zambrini, and Sabrina Maniscalco. Quantum simulation of dissipative collective effects on noisy quantum computers. *PRX Quantum*, 4:010324, Mar 2023. doi:10.1103/PRXQuantum.4.010324.

[38] Richard Cleve and Chunhao Wang. Efficient quantum algorithms for simulating lindblad evolution, 2019. arXiv:1612.09512.

[39] Hirsh Kamakari, Shi-Ning Sun, Mario Motta, and Austin J. Minnich. Digital quantum simulation of open quantum systems using quantum imaginary–time evolution. *PRX Quantum*, 3:010320, Feb 2022. doi:10.1103/PRXQuantum.3.010320.

[40] Kishor Bharti, Alba Cervera-Lierta, Thi Ha Kyaw, Tobias Haug, Sumner Alperin-Lea, Abhinav Anand, Matthias Degroote, Hermanni Heimonen, Jakob S. Kottmann, Tim Menke,

Wai-Keong Mok, Sukin Sim, Leong-Chuan Kwek, and Alán Aspuru-Guzik. Noisy intermediate-scale quantum algorithms. *Reviews of Modern Physics*, 94(1), February 2022. doi:10.1103/revmodphys.94.015004.

[41] John Preskill. Quantum computing in the nisq era and beyond. *Quantum*, 2:79, 2018. doi:10.22331/q-2018-08-06-79.

[42] Michael A Nielsen and Isaac L Chuang. *Quantum computing and quantum information*. Cambridge University Press, Cambridge, 2000. doi:10.1017/CBO9780511976667.

[43] Giuliano Benenti, Giulio Casati, Davide Rossini, and Giuliano Strini. *Principles of Quantum Computation and Information: A Comprehensive Textbook*. World Scientific, 2019. doi:10.1142/10909.

[44] Ibm quantum compute resources, 2022. URL: https://quantum-computing.ibm.com/services/resources.

[45] Yvan Castin, Jean Dalibard, and Klaus Molmer. A wave function approach to dissipative processes, 2008. arXiv:0805.4002.

[46] Angelo Bassi, Kinjalk Lochan, Seema Satin, Tejinder P Singh, and Hendrik Ulbricht. Models of wave-function collapse, underlying theories, and experimental tests. *Reviews of Modern Physics*, 85(2):471, 2013. doi:10.1103/RevModPhys.85.471.

[47] Matteo Carlesso, Sandro Donadi, Luca Ferialdi, Mauro Paternostro, Hendrik Ulbricht, and Angelo Bassi. Present status and future challenges of non-interferometric tests of collapse models. *Nature Physics*, 18(3):243–250, 2022. doi:10.1038/s41567-021-01489-5.

[48] Lajos Diosi. A universal master equation for the gravitational violation of quantum mechanics. *Physics Letters A*, 120(8):377–381, 1987. doi:10.1016/0375-9601(87)90681-5.

[49] Roger Penrose. On gravity's role in quantum state reduction. *General relativity and gravitation*, 28(5):581–600, 1996. doi:10.1007/BF02105068.

[50] Philip Pearle. Combining stochastic dynamical state-vector reduction with spontaneous localization. *Physical Review A*, 39(5):2277–2289, 1989. doi:10.1103/PhysRevA.39.2277.

[51] Gian Carlo Ghirardi, Philip Pearle, and Alberto Rimini. Markov processes in hilbert space and continuous spontaneous localization of systems of identical particles. *Physical Review A*, 42(1):78, 1990. doi:10.1103/PhysRevA.42.78.

[52] Sandro Donadi, Kristian Piscicchia, Catalina Curceanu, Lajos Diósi, Matthias Laubenstein, and Angelo Bassi. Underground test of gravity-related wave function collapse. *Nature Physics*, 17(1):74–78, 2021. doi:10.1038/s41567-020-1008-4.

[53] D. Salart, A. Baas, J. A. W. van Houwelingen, N. Gisin, and H. Zbinden. Spacelike separation in a bell test assuming gravitationally induced collapses. *Phys. Rev. Lett.*, 100:220404, Jun 2008. doi:10.1103/PhysRevLett.100.220404.

[54] Giulio Gasbarri, Alessio Belenchia, Matteo Carlesso, Sandro Donadi, Angelo Bassi, Rainer Kaltenbaek, Mauro Paternostro, and Hendrik Ulbricht. Testing the foundation of quantum physics in space via interferometric and non-interferometric experiments with mesoscopic nanoparticles. *Communications Physics*, 4(1), July 2021. doi:10.1038/s42005-021-00656-7.

[55] Stephen L Adler, Angelo Bassi, and Matteo Carlesso. The continuous spontaneous localization layering effect from a lattice perspective. *Journal of Physics A: Mathematical and Theoretical*, 54(8):085303, February 2021. doi:10.1088/1751-8121/abdbc8.

[56] Giovanni Di Bartolomeo, Michele Vischi, Tommaso Feri, Angelo Bassi, and Sandro Donadi. Efficient quantum algorithm to simulate open systems through the quantum noise formalism, 2023. URL: https://journals.aps.org/prresearch/

accepted/d307dYffY8b1f68055a66d066d385f162e35c0d6c, arXiv:2311.10009.

[57] M. Kliesch, T. Barthel, C. Gogolin, M. Kastoryano, and J. Eisert. Dissipative quantum church-turing theorem. *Phys. Rev. Lett.*, 107:120501, Sep 2011. doi:10.1103/PhysRevLett.107.120501.

[58] Matthew Pocrnic, Dvira Segal, and Nathan Wiebe. Quantum simulation of lindbladian dynamics via repeated interactions, 2024. arXiv:2312.05371.

[59] Masuo Suzuki. Decomposition formulas of exponential operators and lie exponentials with some applications to quantum mechanics and statistical physics. *Journal of mathematical physics*, 26(4):601–612, 1985. doi:10.1063/1.526596.

[60] Marco Cerezo, Andrew Arrasmith, Ryan Babbush, Simon C Benjamin, Suguru Endo, Keisuke Fujii, Jarrod R McClean, Kosuke Mitarai, Xiao Yuan, Lukasz Cincio, et al. Variational quantum algorithms. *Nature Reviews Physics*, 3(9):625–644, 2021. doi:10.1038/s42254-021-00348-9.

[61] Giulio Crognaletti, Giovanni Di Bartolomeo, Michele Vischi, and Luciano Loris Viteritti. Equivariant variational quantum eigensolver to detect phase transitions through energy level crossings. *Quantum Science and Technology*, 10(1):015048, December 2024. doi:10.1088/2058-9565/ad9be3.

[62] Subir Sachdev. Quantum phase transitions. *Physics World*, 12(4):33, apr 1999. doi:10.1088/2058-7058/12/4/23.

[63] S. Eggert. Numerical evidence for multiplicative logarithmic corrections from marginal operators. *Phys. Rev. B*, 54:R9612–R9615, Oct 1996. doi:10.1103/PhysRevB.54.R9612.

[64] A.W. Sandvik. Computational studies of quantum spin systems. *AIP Conference Proceedings*, 1297(1):135–338, 2010. doi:10.1063/1.3518900.

[65] K Nomura. Correlation functions of the 2d sine-gordon model. *Journal of Physics A: Mathematical and General*, 28(19):5451, oct 1995. doi:10.1088/0305-4470/28/19/003.

[66] Masaaki Nakamura. Mechanism of cdw-sdw transition in one dimension. *Journal of the Physical Society of Japan*, 68(10):3123–3126, October 1999. doi:10.1143/jpsj.68.3123.

[67] Masaaki Nakamura. Tricritical behavior in the extended hubbard chains. *Phys. Rev. B*, 61:16377–16392, Jun 2000. doi:10.1103/PhysRevB.61.16377.

[68] Anders W. Sandvik, Leon Balents, and David K. Campbell. Ground state phases of the half-filled one-dimensional extended hubbard model. *Phys. Rev. Lett.*, 92:236401, Jun 2004. doi:10.1103/PhysRevLett.92.236401.

[69] Anders W. Sandvik. Ground states of a frustrated quantum spin chain with long-range interactions. *Phys. Rev. Lett.*, 104:137204, Mar 2010. doi:10.1103/PhysRevLett.104.137204.

[70] Ling Wang and Anders W. Sandvik. Critical level crossings and gapless spin liquid in the square-lattice spin-1/2 $J_1 - J_2$ heisenberg antiferromagnet. *Phys. Rev. Lett.*, 121:107202, Sep 2018. doi:10.1103/PhysRevLett.121.107202.

[71] Francesco Ferrari and Federico Becca. Gapless spin liquid and valence-bond solid in the J_1-J_2 heisenberg model on the square lattice: Insights from singlet and triplet excitations. *Phys. Rev. B*, 102:014417, Jul 2020. doi:10.1103/PhysRevB.102.014417.

[72] Yusuke Nomura and Masatoshi Imada. Dirac-type nodal spin liquid revealed by refined quantum many-body solver using neural-network wave function, correlation ratio, and level spectroscopy. *Phys. Rev. X*, 11:031034, Aug 2021. doi:10.1103/PhysRevX.11.031034.

[73] Fabio Franchini. *An Introduction to Integrable Techniques for One-Dimensional Quantum Systems*. Springer International Publishing, 2017. doi:10.1007/978-3-319-48487-7.

[74] S.R. White and I. Affleck. Dimerization and incommensurate spiral spin correlations in the zigzag spin chain: Analogies to the kondo lattice. *Phys. Rev. B*, 54:9862–9869, Oct 1996. doi:10.1103/PhysRevB.54.9862.

[75] Claudine Lacroix, Philippe Mendels, and Frederic Mila. *Introduction to Frustrated Magnetism: Materials, Experiments, Theory*. Springer, 01 2011. doi:10.1007/978-3-642-10589-0.

[76] Luciano Loris Viteritti, Francesco Ferrari, and Federico Becca. Accuracy of restricted Boltzmann machines for the one-dimensional $J_1 - J_2$ Heisenberg model. *SciPost Phys.*, 12:166, 2022. doi:10.21468/SciPostPhys.12.5.166.

[77] Luciano Loris Viteritti, Riccardo Rende, and Federico Becca. Transformer variational wave functions for frustrated quantum spin systems. *Physical Review Letters*, 130(23), June 2023. doi:10.1103/physrevlett.130.236401.

[78] Jianwei Yang, Anders W. Sandvik, and Ling Wang. Quantum criticality and spin liquid phase in the shastry-sutherland model. *Phys. Rev. B*, 105:L060409, Feb 2022. doi:10.1103/PhysRevB.105.L060409.

[79] Shou-Shu Gong, Wei Zhu, D. N. Sheng, Olexei I. Motrunich, and Matthew P. A. Fisher. Plaquette ordered phase and quantum phase diagram in the spin-$\frac{1}{2}$ J_1-J_2 square heisenberg model. *Phys. Rev. Lett.*, 113:027201, Jul 2014. doi:10.1103/PhysRevLett.113.027201.

[80] Tom Vieijra, Corneel Casert, Jannes Nys, Wesley De Neve, Jutho Haegeman, Jan Ryckebusch, and Frank Verstraete. Restricted boltzmann machines for quantum states with non-abelian or anyonic symmetries. *Phys. Rev. Lett.*, 124:097201, Mar 2020. doi:10.1103/PhysRevLett.124.097201.

[81] Tom Vieijra and Jannes Nys. Many-body quantum states with exact conservation of non-abelian and lattice symmetries through variational monte carlo. *Phys. Rev. B*, 104:045123, Jul 2021. doi:10.1103/PhysRevB.104.045123.

[82] Giuseppe Carleo and Matthias Troyer. Solving the quantum many-body problem with artificial neural networks. *Science*, 355(6325):602–606, February 2017. doi:10.1126/science.aag2302.

[83] Yusuke Nomura. Helping restricted boltzmann machines with quantum-state representation by restoring symmetry. *Journal of Physics: Condensed Matter*, 33(17):174003, April 2021. doi:10.1088/1361-648x/abe268.

[84] Christopher Roth and Allan H. MacDonald. Group convolutional neural networks improve quantum state accuracy, 2021. arXiv:2104.05085.

[85] Christopher Roth, Attila Szabó, and Allan H. MacDonald. High-accuracy variational monte carlo for frustrated magnets with deep neural networks. *Phys. Rev. B*, 108:054410, Aug 2023. doi:10.1103/PhysRevB.108.054410.

[86] Luciano Loris Viteritti, Riccardo Rende, Alberto Parola, Sebastian Goldt, and Federico Becca. Transformer wave function for the shastry-sutherland model: emergence of a spin-liquid phase, 2024. arXiv:2311.16889.

[87] Riccardo Rende, Luciano Loris Viteritti, Lorenzo Bardone, Federico Becca, and Sebastian Goldt. A simple linear algebra identity to optimize large-scale neural network quantum states, 2023. arXiv:2310.05715.

[88] Mohamed Hibat-Allah, Martin Ganahl, Lauren E. Hayward, Roger G. Melko, and Juan Carrasquilla. Recurrent neural network wave functions. *Phys. Rev. Res.*, 2:023358, Jun 2020. doi:10.1103/PhysRevResearch.2.023358.

[89] Kazuhiro Seki, Tomonori Shirakawa, and Seiji Yunoki. Symmetry-adapted variational quantum eigensolver. *Phys.*

Rev. A, 101:052340, May 2020. doi:10.1103/PhysRevA.101.052340.

[90] Johannes Jakob Meyer, Marian Mularski, Elies Gil-Fuster, Antonio Anna Mele, Francesco Arzani, Alissa Wilms, and Jens Eisert. Exploiting symmetry in variational quantum machine learning. *PRX Quantum*, 4(1), March 2023. doi:10.1103/prxquantum.4.010328.

[91] Su Yeon Chang, Michele Grossi, Bertrand Le Saux, and Sofia Vallecorsa. Approximately equivariant quantum neural network for $p4m$ group symmetries in images, 2023. arXiv:2310.02323.

[92] Isabel Nha Minh Le, Oriel Kiss, Julian Schuhmacher, Ivano Tavernelli, and Francesco Tacchino. Symmetry-invariant quantum machine learning force fields, 2023. arXiv:2311.11362.

[93] Joris Kattemölle and Jasper van Wezel. Variational quantum eigensolver for the heisenberg antiferromagnet on the kagome lattice. *Phys. Rev. B*, 106:214429, Dec 2022. doi:10.1103/PhysRevB.106.214429.

[94] Takahiro Mizusaki and Masatoshi Imada. Quantum-number projection in the path-integral renormalization group method. *Phys. Rev. B*, 69:125110, Mar 2004. doi:10.1103/PhysRevB.69.125110.

[95] Cenk Tüysüz, Su Yeon Chang, Maria Demidik, Karl Jansen, Sofia Vallecorsa, and Michele Grossi. Symmetry breaking in geometric quantum machine learning in the presence of noise, 2024. arXiv:2401.10293.

[96] Kristan Temme, Sergey Bravyi, and Jay M. Gambetta. Error mitigation for short-depth quantum circuits. *Phys. Rev. Lett.*, 119:180509, Nov 2017. doi:10.1103/PhysRevLett.119.180509.

[97] Dave Wecker, Matthew B Hastings, and Matthias Troyer. Progress towards practical quantum variational algorithms. *Physical Review A*, 92(4):042303,

2015. doi:https://journals.aps.org/pra/pdf/10.1103/PhysRevA.92.042303.

[98] Roeland Wiersema, Cunlu Zhou, Yvette de Sereville, Juan Felipe Carrasquilla, Yong Baek Kim, and Henry Yuen. Exploring entanglement and optimization within the hamiltonian variational ansatz. *PRX Quantum*, 1(2), December 2020. doi:10.1103/prxquantum.1.020319.

[99] Antonio A. Mele, Glen B. Mbeng, Giuseppe E. Santoro, Mario Collura, and Pietro Torta. Avoiding barren plateaus via transferability of smooth solutions in a hamiltonian variational ansatz. *Physical Review A*, 106(6), December 2022. doi:10.1103/physreva.106.l060401.

[100] Baptiste Anselme Martin, Pascal Simon, and Marko J. Rančić. Simulating strongly interacting hubbard chains with the variational hamiltonian ansatz on a quantum computer. *Physical Review Research*, 4(2), June 2022. doi:10.1103/physrevresearch.4.023190.

[101] David Wierichs, Christian Gogolin, and Michael Kastoryano. Avoiding local minima in variational quantum eigensolvers with the natural gradient optimizer. *Physical Review Research*, 2(4), November 2020. doi:10.1103/physrevresearch.2.043246.

[102] Wen Wei Ho and Timothy H. Hsieh. Efficient variational simulation of non-trivial quantum states. *SciPost Physics*, 6(3), March 2019. doi:10.21468/scipostphys.6.3.029.

[103] Verena Feulner and Michael J. Hartmann. Variational quantum eigensolver ansatz for the J_1-J_2-model. *Phys. Rev. B*, 106:144426, Oct 2022. doi:10.1103/PhysRevB.106.144426.

[104] Farrokh Vatan and Colin Williams. Optimal quantum circuits for general two-qubit gates. *Phys. Rev. A*, 69:032315, Mar 2004. doi:10.1103/PhysRevA.69.032315.

[105] Chufan Lyu, Xusheng Xu, Man-Hong Yung, and Abolfazl Bayat. Symmetry enhanced variational quantum spin eigen-

solver. *Quantum*, 7:899, January 2023. doi:10.22331/q-2023-01-19-899.

[106] Andrew M. Childs and Nathan Wiebe. Hamiltonian simulation using linear combinations of unitary operations. *Quantum Information and Computation*, 12(11 and 12), 11 2012. doi:10.26421/qic12.11-12.

[107] Almudena Carrera Vazquez, Daniel J. Egger, David Ochsner, and Stefan Woerner. Well-conditioned multi-product formulas for hardware-friendly hamiltonian simulation. *Quantum*, 7:1067, July 2023. doi:10.22331/q-2023-07-25-1067.

[108] Shantanav Chakraborty. Implementing any linear combination of unitaries on intermediate-term quantum computers, 2023. arXiv:2302.13555.

[109] Philip Krantz, Morten Kjaergaard, Fei Yan, Terry P Orlando, Simon Gustavsson, and William D Oliver. A quantum engineer's guide to superconducting qubits. *Applied Physics Reviews*, 6(2):021318, 2019. doi:10.1063/1.5089550.

[110] Mohan Sarovar, Timothy Proctor, Kenneth Rudinger, Kevin Young, Erik Nielsen, and Robin Blume-Kohout. Detecting crosstalk errors in quantum information processors. *Quantum*, 4:321, 2020. doi:10.22331/q-2020-09-11-321.

[111] Mahdi Naghiloo. Introduction to experimental quantum measurement with superconducting qubits, 2019. arXiv:1904.09291.

[112] Ewout Van Den Berg, Zlatko K Minev, and Kristan Temme. Model-free readout-error mitigation for quantum expectation values. *Physical Review A*, 105(3):032620, 2022. doi:10.1103/PhysRevA.105.032620.

[113] Ying Li and Simon C. Benjamin. Efficient variational quantum simulator incorporating active error minimization. *Phys. Rev. X*, 7:021050, Jun 2017. doi:10.1103/PhysRevX.7.021050.

[114] Tudor Giurgica-Tiron, Yousef Hindy, Ryan LaRose, Andrea Mari, and William J. Zeng. Digital zero noise extrapolation

for quantum error mitigation. In *2020 IEEE International Conference on Quantum Computing and Engineering (QCE)*. IEEE, October 2020. doi:10.1109/qce49297.2020.00045.

[115] Ville Bergholm, Josh Izaac, Maria Schuld, Christian Gogolin, Shahnawaz Ahmed, and Vishnu Ajith et al. Pennylane: Automatic differentiation of hybrid quantum-classical computations, 2022. arXiv:1811.04968.

[116] Cornelius Lanczos. An iterative method for the solution of the eigenvalue problem of linear differential and integral operators. *J. Res. Nat. Bur. Standards*, 45:225–280, 1950. doi:10.6028/jres.045.026.

[117] Nikita Astrakhantsev, Guglielmo Mazzola, Ivano Tavernelli, and Giuseppe Carleo. Phenomenological theory of variational quantum ground-state preparation. *Phys. Rev. Res.*, 5:033225, Sep 2023. doi:10.1103/PhysRevResearch.5.033225.

[118] Stephen L Adler and Angelo Bassi. Collapse models with non-white noises. *Journal of Physics A: Mathematical and Theoretical*, 40(50):15083, 2007. doi:10.1088/1751-8113/40/50/012.

[119] Sabrina Maniscalco and Francesco Petruccione. Non-markovian dynamics of a qubit. *Physical Review A*, 73(1):012111, 2006. doi:10.1103/PhysRevA.73.012111.

[120] Walter T Strunz, Lajos Diósi, Nicolas Gisin, and Ting Yu. Quantum trajectories for brownian motion. *Physical Review Letters*, 83(24):4909, 1999. doi:10.1103/PhysRevLett.83.4909].

[121] Jay Gambetta and HM Wiseman. The non-markovian stochastic schrödinger equation for the position unravelling. *Journal of Optics B: Quantum and Semiclassical Optics*, 6(8):S821, 2004. doi:10.1103/PhysRevA.66.012108.

[122] pyQuill, 2022. URL: https://pyquil-docs.rigetti.com/en/v3.3.2/noise.html.

[123] Qiskit notebook, 2022. URL: https://github.com/qiskit-community/qiskit-presentations/blob/master/2019-02-26_QiskitCamp/QiskitCamp_Simulation.ipynb.

[124] Ewout van den Berg, Zlatko K Minev, Abhinav Kandala, and Kristan Temme. Probabilistic error cancellation with sparse pauli-lindblad models on noisy quantum processors. *arXiv e-prints*, pages arXiv–2201, 2022. doi:10.1038/s41567-023-02042-2.

[125] Shuaining Zhang, Yao Lu, Kuan Zhang, Wentao Chen, Ying Li, Jing-Ning Zhang, and Kihwan Kim. Error-mitigated quantum gates exceeding physical fidelities in a trapped-ion system. *Nature communications*, 11(1):587, 2020. doi:10.1038/s41467-020-14376-z.

[126] Abdullah Ash-Saki, Mahabubul Alam, and Swaroop Ghosh. Analysis of crosstalk in nisq devices and security implications in multi-programming regime. In *Proceedings of the ACM/IEEE International Symposium on Low Power Electronics and Design*, pages 25–30, 2020. doi:10.1145/3370748.3406570+.

[127] Matteo Caiaffa, Andrea Smirne, and Angelo Bassi. Stochastic unraveling of positive quantum dynamics. *Physical Review A*, 95(6):062101, 2017. doi:10.1103/PhysRevA.95.062101.

[128] Ibm qiskit, 2022. URL: https://qiskit.org/.

[129] David C McKay, Christopher J Wood, Sarah Sheldon, Jerry M Chow, and Jay M Gambetta. Efficient z gates for quantum computing. *Physical Review A*, 96(2):022330, 2017. doi:10.1103/PhysRevA.96.022330.

[130] Chad Rigetti and Michel Devoret. Fully microwave-tunable universal gates in superconducting qubits with linear couplings and fixed transition frequencies. *Physical Review B*, 81(13):134507, 2010. doi:10.1103/PhysRevB.81.134507.

[131] Wolfram Research, Inc. Mathematica, Version 13.1. Champaign, IL, 2022. URL: https://www.wolfram.com/mathematica.

[132] Christopher D Wilen, S Abdullah, NA Kurinsky, C Stanford, L Cardani, G d'Imperio, C Tomei, L Faoro, LB Ioffe, CH Liu, et al. Correlated charge noise and relaxation errors in superconducting qubits. *Nature*, 594(7863):369–373, 2021. doi:10.1038/s41586-021-03557-5.

[133] Peng Zhao, Kehuan Linghu, Zhiyuan Li, Peng Xu, Ruixia Wang, Guangming Xue, Yirong Jin, and Haifeng Yu. Quantum crosstalk analysis for simultaneous gate operations on superconducting qubits. *PRX Quantum*, 3(2):020301, 2022. doi:10.1038/s41586-021-03557-5.

[134] Peter W Shor. Algorithms for quantum computation: discrete logarithms and factoring. In *Proceedings 35th annual symposium on foundations of computer science*, pages 124–134. Ieee, 1994. doi:10.1109/SFCS.1994.365700.

[135] Lidia Ruiz-Perez and Juan Carlos Garcia-Escartin. Quantum arithmetic with the quantum fourier transform. *Quantum Information Processing*, 16(6):1–14, 2017. doi:10.1007/s11128-017-1603-1.

[136] John Preskill. Sufficient condition on noise correlations for scalable quantum computing, 2012. arXiv:1207.6131.

[137] Zhenyu Cai, Ryan Babbush, Simon C. Benjamin, Suguru Endo, William J. Huggins, Ying Li, Jarrod R. McClean, and Thomas E. O'Brien. Quantum error mitigation. *Reviews of Modern Physics*, 95(4), December 2023. doi:10.1103/revmodphys.95.045005.

[138] Suguru Endo, Simon C Benjamin, and Ying Li. Practical quantum error mitigation for near-future applications. *Physical Review X*, 8(3):031027, 2018. doi:10.1103/PhysRevX.8.031027.

[139] Zhiding Liang, Hanrui Wang, Jinglei Cheng, Yongshan Ding, Hang Ren, Zhengqi Gao, Zhirui Hu, Duane S Boning, Xuehai Qian, Song Han, et al. Variational quantum pulse learning. In *2022 IEEE International Conference on Quantum Computing*

and Engineering (QCE), pages 556–565. IEEE, 2022. doi:10.1109/QCE53715.2022.00078].

[140] Mohannad M. Ibrahim, Hamed Mohammadbagherpoor, Cynthia Rios, Nicholas T. Bronn, and Gregory T. Byrd. Evaluation of parameterized quantum circuits with cross-resonance pulse-driven entanglers. *IEEE Transactions on Quantum Engineering*, 3:1–13, 2022. doi:10.1109/tqe.2022.3231124.

[141] Sean Greenaway, Francesco Petiziol, Zhao Hongzheng, and Florian Mintert. Variational quantum gate optimization at the pulse level. *SciPost Physics*, 16(3), March 2024. doi:10.21468/scipostphys.16.3.082.

[142] Lars S Madsen, Fabian Laudenbach, Mohsen Falamarzi Askarani, Fabien Rortais, Trevor Vincent, Jacob FF Bulmer, Filippo M Miatto, Leonhard Neuhaus, Lukas G Helt, Matthew J Collins, et al. Quantum computational advantage with a programmable photonic processor. *Nature*, 606(7912):75–81, 2022. doi:10.1038/s41586-022-04725-x+.

[143] Han-Sen Zhong, Hui Wang, Yu-Hao Deng, Ming-Cheng Chen, Li-Chao Peng, Yi-Han Luo, Jian Qin, Dian Wu, Xing Ding, Yi Hu, et al. Quantum computational advantage using photons. *Science*, 370(6523):1460–1463, 2020. doi:10.1126/science.abe8770.

[144] Rawad Mezher and Shane Mansfield. Assessing the quality of near-term photonic quantum devices, 2022. arXiv:2202.04735.

[145] Nicolas Maring, Andreas Fyrillas, Mathias Pont, Edouard Ivanov, Petr Stepanov, Nico Margaria, William Hease, Anton Pishchagin, Thi Huong Au, Sébastien Boissier, Eric Bertasi, Aurélien Baert, Mario Valdivia, Marie Billard, Ozan Acar, Alexandre Brieussel, Rawad Mezher, Stephen C. Wein, Alexia Salavrakos, Patrick Sinnott, Dario A. Fioretto, Pierre-Emmanuel Emeriau, Nadia Belabas, Shane Mansfield, Pascale

Senellart, Jean Senellart, and Niccolo Somaschi. A general-purpose single-photon-based quantum computing platform, 2023. arXiv:2306.00874.

[146] Mathias Pont, Riccardo Albiero, Sarah E Thomas, Nicolò Spagnolo, Francesco Ceccarelli, Giacomo Corrielli, Alexandre Brieussel, Niccolo Somaschi, Hêlio Huet, Abdelmounaim Harouri, et al. Quantifying n-photon indistinguishability with a cyclic integrated interferometer. *Physical Review X*, 12(3):031033, 2022. doi:10.1103/PhysRevX.12.031033.

[147] Artur Czerwinski and Katarzyna Czerwinska. Statistical analysis of the photon loss in fiber-optic communication. In *Photonics*, volume 9, page 568. MDPI, 2022. doi:10.3390/photonics9080568+.

[148] Marcel Niedermeier, Jose L. Lado, and Christian Flindt. Simulating the quantum fourier transform, grover's algorithm, and the quantum counting algorithm with limited entanglement using tensor networks. *Physical Review Research*, 6(3), September 2024. doi:10.1103/physrevresearch.6.033325.

[149] Jerimiah Wright, Meenambika Gowrishankar, Daniel Claudino, Phillip C. Lotshaw, Thien Nguyen, Alexander J. McCaskey, and Travis S. Humble. Numerical simulations of noisy quantum circuits for computational chemistry, 2022. arXiv:2112.15540.

[150] Song Cheng, Chenfeng Cao, Chao Zhang, Yongxiang Liu, Shi-Yao Hou, Pengxiang Xu, and Bei Zeng. Simulating noisy quantum circuits with matrix product density operators. *Physical Review Research*, 3(2):023005, 2021. doi:10.1103/PhysRevResearch.3.023005+.

[151] Pieter Kok, W. J. Munro, Kae Nemoto, T. C. Ralph, Jonathan P. Dowling, and G. J. Milburn. Linear optical quantum computing with photonic qubits. *Reviews of Modern Physics*, 79(1):135–174, January 2007. doi:10.1103/revmodphys.79.135.

[152] E. Knill, R. Laflamme, and G. Milburn. Efficient linear optics quantum computation, 2000. arXiv:quant-ph/0006088.

[153] Marlan O Scully and M Suhail Zubairy. Quantum optics, 1999. doi:10.1017/CBO9780511813993.

[154] Werner Vogel and Dirk-Gunnar Welsch. *Quantum optics*. John Wiley & Sons, 2006. doi:10.1002/3527608524.

[155] Daniel Klaus Burgarth and Vittorio Giovannetti. Dual- and multi-rail encoding. In *Quantum State Transfer and Network Engineering*, pages 87–122. 2013. doi:10.1007/978-3-642-39937-4.

[156] Daniel Burgarth and Sougato Bose. Conclusive and arbitrarily perfect quantum-state transfer using parallel spin-chain channels. *Physical Review A*, 71(5):052315, 2005. doi:10.1103/physreva.71.052315.

[157] Artur Czerwinski and Jakub Szlachetka. Efficiency of photonic state tomography affected by fiber attenuation. *Physical Review A*, 105(6):062437, 2022. doi:10.1103/PhysRevA.105.062437+.

[158] Jakub Mielczarek. Quantum gravity on a quantum chip, 2018. arXiv:1803.10592.

[159] Lucjan Jacak, Pawel Hawrylak, and Arkadiusz Wojs. *Quantum dots*. Springer Science & Business Media, 2013. doi:10.1007/978-3-642-72002-4].

[160] Dan Cogan, Oded Kenneth, Netanel H Lindner, Giora Peniakov, Caspar Hopfmann, Dan Dalacu, Philip J Poole, Pawel Hawrylak, and David Gershoni. Depolarization of electronic spin qubits confined in semiconductor quantum dots. *Physical Review X*, 8(4):041050, 2018. doi:10.1103/PhysRevX.8.041050.

[161] H. C. Schneider, W. W. Chow, and S. W. Koch. Excitation-induced dephasing in semiconductor quantum dots. *Phys. Rev. B*, 70:235308, Dec 2004. doi:10.1103/PhysRevB.70.235308.

[162] Sunil Pai, Ben Bartlett, Olav Solgaard, and David AB Miller. Matrix optimization on universal unitary photonic devices. *Physical Review Applied*, 11(6):064044, 2019. doi:10.1103/PhysRevApplied.11.064044.

[163] Scott Aaronson and Daniel J Brod. Bosonsampling with lost photons. *Physical Review A*, 93(1):012335, 2016. doi:10.1103/PhysRevA.93.012335].

[164] Michal Oszmaniec, Remigiusz Augusiak, Christian Gogolin, Jan Kołodyński, Antonio Acin, and Maciej Lewenstein. Random bosonic states for robust quantum metrology. *Physical Review X*, 6(4):041044, 2016. doi:10.1103/PhysRevX.6.041044.

[165] Michał Oszmaniec and Daniel J Brod. Classical simulation of photonic linear optics with lost particles. *New Journal of Physics*, 20(9):092002, 2018. doi:10.1088/1367-2630/aadfa8.

[166] Daniel Jost Brod and Michał Oszmaniec. Classical simulation of linear optics subject to nonuniform losses. *Quantum*, 4:267, 2020. doi:10.22331/q-2020-05-14-267.

[167] Nicolas Heurtel, Andreas Fyrillas, Grégoire de Gliniasty, Raphaël Le Bihan, Sébastien Malherbe, Marceau Pailhas, Eric Bertasi, Boris Bourdoncle, Pierre-Emmanuel Emeriau, Rawad Mezher, Luka Music, Nadia Belabas, Benoît Valiron, Pascale Senellart, Shane Mansfield, and Jean Senellart. Perceval: A Software Platform for Discrete Variable Photonic Quantum Computing. *Quantum*, 7:931, February 2023. doi:10.22331/q-2023-02-21-931.

[168] Nathan Killoran, Josh Izaac, Nicolás Quesada, Ville Bergholm, Matthew Amy, and Christian Weedbrook. Strawberry fields: A software platform for photonic quantum computing. *Quantum*, 3:129, 2019. doi:10.22331/q-2019-03-11-129.

[169] Javier Osca and Jiri Vala. Implementation of photon partial distinguishability in a quantum optical circuit simula-

tion. *Computer Physics Communications*, 289:108773, 2023. doi:10.1016/j.cpc.2023.108773.

[170] Perceval, 2022. URL: https://perceval.quandela.net/docs/.

[171] Robert Raussendorf and Hans J Briegel. A one-way quantum computer. *Physical review letters*, 86(22):5188, 2001. doi:10.1103/PhysRevLett.86.5188.

[172] Hans J Briegel, David E Browne, Wolfgang Dür, Robert Raussendorf, and Maarten Van den Nest. Measurement-based quantum computation. *Nature Physics*, 5(1):19–26, 2009. doi:10.1038/nphys1157.

[173] Alberto Peruzzo, Jarrod McClean, Peter Shadbolt, Man-Hong Yung, Xiao-Qi Zhou, Peter J Love, Alán Aspuru-Guzik, and Jeremy L O'brien. A variational eigenvalue solver on a photonic quantum processor. *Nature communications*, 5(1):4213, 2014. doi:10.1038/ncomms5213.

[174] Johan Håstad. Some optimal inapproximability results. *Journal of the ACM (JACM)*, 48(4):798–859, 2001. doi:10.1145/502090.502098].

[175] Piotr Berman and Marek Karpinski. On some tighter inapproximability results. In *Automata, Languages and Programming: 26th International Colloquium, ICALP'99 Prague, Czech Republic, July 11–15, 1999 Proceedings 26*, pages 200–209. Springer, 1999. doi:10.1007/3-540-45465-9.

[176] Massimiliano Proietti, Filippo Cerocchi, and Massimiliano Dispenza. Native measurement-based quantum approximate optimization algorithm applied to the max k-cut problem. *Physical Review A*, 106(2):022437, 2022. doi:10.1103/PhysRevA.106.022437.

[177] Michael Reck, Anton Zeilinger, Herbert J Bernstein, and Philip Bertani. Experimental realization of any discrete unitary operator. *Physical review letters*, 73(1):58, 1994. doi:10.1103/PhysRevLett.73.58.

[178] Nicolas Heurtel, Shane Mansfield, Jean Senellart, and Benoît Valiron. Strong simulation of linear optical processes. *Computer Physics Communications*, page 108848, 2023. doi:10.1016/j.cpc.2023.108848.

[179] Paddle Quantum, 2020. URL: https://github.com/PaddlePaddle/Quantum.

[180] scipy COBYLA documentation, 2023. URL: https://docs.scipy.org/doc/scipy/reference/optimize.minimize-cobyla.html.

[181] Edward Farhi, Jeffrey Goldstone, and Sam Gutmann. A quantum approximate optimization algorithm, 2014. arXiv:1411.4028.

[182] Andrea Smirne and Angelo Bassi. Dissipative continuous spontaneous localization (csl) model. *Scientific reports*, 5(1):1–9, 2015. doi:10.1038/srep12518+.

[183] M. Bahrami, A. Smirne, and A. Bassi. Role of gravity in the collapse of a wave function: A probe into the diósi-penrose model. *Phys. Rev. A*, 90:062105, Dec 2014. doi:10.1103/PhysRevA.90.062105.

[184] Jahangir Nobakht, Matteo Carlesso, Sandro Donadi, Mauro Paternostro, and Angelo Bassi. Unitary unraveling for the dissipative continuous spontaneous localization model: Application to optomechanical experiments. *Physical Review A*, 98(4):042109, 2018. doi:10.1103/PhysRevA.98.042109.

[185] A. Pontin, N. P. Bullier, M. Toroš, and P. F. Barker. Ultranarrow-linewidth levitated nano-oscillator for testing dissipative wave-function collapse. *Phys. Rev. Res.*, 2:023349, Jun 2020. doi:10.1103/PhysRevResearch.2.023349.

[186] A Vinante, A Pontin, M Rashid, M Toroš, PF Barker, and H Ulbricht. Testing collapse models with levitated nanoparticles: Detection challenge. *Physical Review A*, 100(1):012119, 2019. doi:10.1103/PhysRevA.100.012119.

[187] Giovanni Di Bartolomeo, Matteo Carlesso, Kristian Piscicchia, Catalina Curceanu, Maaneli Derakhshani, and Lajos Diósi. Linear-friction many-body equation for dissipative spontaneous wave-function collapse. *Phys. Rev. A*, 108:012202, Jul 2023. doi:10.1103/physreva.108.012202.

[188] L Diósi. Quantum master equation of a particle in a gas environment. *Europhysics Letters (EPL)*, 30(2):63–68, April 1995. doi:10.1209/0295-5075/30/2/001.

[189] Antoine Tilloy and Thomas M Stace. Neutron star heating constraints on wave-function collapse models. *Physical review letters*, 123(8):080402, 2019. doi:10.1103/PhysRevLett.123.080402.

[190] Stephen L. Adler, Angelo Bassi, Matteo Carlesso, and Andrea Vinante. Testing continuous spontaneous localization with fermi liquids. *Phys. Rev. D*, 99:103001, May 2019. doi:10.1103/PhysRevD.99.103001.

[191] Andrea Vinante, Renato Mezzena, Paolo Falferi, Matteo Carlesso, and Angelo Bassi. Improved noninterferometric test of collapse models using ultracold cantilevers. *Physical review letters*, 119(11):110401, 2017. doi:10.1103/PhysRevLett.119.110401.

[192] A. Vinante, M. Carlesso, A. Bassi, A. Chiasera, S. Varas, P. Falferi, B. Margesin, R. Mezzena, and H. Ulbricht. Narrowing the parameter space of collapse models with ultracold layered force sensors. *Phys. Rev. Lett.*, 125:100404, Sep 2020. doi:10.1103/PhysRevLett.125.100404.

[193] Giovanni Di Bartolomeo, Matteo Carlesso, and Angelo Bassi. Gravity as a classical channel and its dissipative generalization. *Phys. Rev. D*, 104:104027, Nov 2021. doi:10.1103/PhysRevD.104.104027.

[194] Giovanni Di Bartolomeo and Matteo Carlesso. Experimental bounds on linear-friction dissipative collapse models from levitated optomechanics. *New Journal of Physics*, 26(4):043006, April 2024. doi:10.1088/1367-2630/ad3842.

[195] Lorenzo Dania, Dmitry S Bykov, Florian Goschin, Markus Teller, and Tracy E Northup. Ultra-high quality factor of a levitated nanomechanical oscillator. *arXiv preprint arXiv:2304.02408*, 2023. doi:10.1103/PhysRevLett.132.133602.

[196] Stefano Mancini and Paolo Tombesi. Quantum noise reduction by radiation pressure. *Physical Review A*, 49(5):4055, 1994. doi:10.1103/PhysRevA.49.4055.

[197] Mauro Paternostro, Sylvain Gigan, Myung Shik Kim, Florian Blaser, HR Böhm, and Markus Aspelmeyer. Reconstructing the dynamics of a movable mirror in a detuned optical cavity. *New Journal of Physics*, 8(6):107, 2006. doi:10.1088/1367-2630/8/6/107.

[198] James Millen, Tania S Monteiro, Robert Pettit, and A Nick Vamivakas. Optomechanics with levitated particles. *Reports on Progress in Physics*, 83(2):026401, 2020. doi:10.1088/1361-6633/ab6100.

[199] Carlos Gonzalez-Ballestero, Markus Aspelmeyer, Lukas Novotny, Romain Quidant, and Oriol Romero-Isart. Levitodynamics: Levitation and control of microscopic objects in vacuum. *Science*, 374(6564):eabg3027, 2021. doi:10.1126/science.abg3027.

[200] David C Moore and Andrew A Geraci. Searching for new physics using optically levitated sensors. *Quantum Science and Technology*, 6(1):014008, 2021. doi:10.1088/2058-9565/abcf8a.

[201] Andrea Vinante, Giulio Gasbarri, Christopher Timberlake, M Toroš, and Hendrik Ulbricht. Testing dissipative collapse models with a levitated micromagnet. *Physical Review Research*, 2(4):043229, 2020. doi:10.1103/PhysRevResearch.2.043229].

[202] Marko Toroš, Giulio Gasbarri, and Angelo Bassi. Colored and dissipative continuous spontaneous localization model and bounds from matter-wave interferometry. *Physics Letters A*,

381(47):3921–3927, 2017. doi:10.1016/j.physleta.2017.10.002.

[203] Stephen L Adler. Lower and upper bounds on csl parameters from latent image formation and igm heating. *Journal of Physics A: Mathematical and Theoretical*, 40(12):2935, 2007. doi:doi:10.1088/1751-8113/40/12/S03.

[204] Gian Carlo Ghirardi, Alberto Rimini, and Tullio Weber. Unified dynamics for microscopic and macroscopic systems. *Physical review D*, 34(2):470, 1986. doi:10.1103/PhysRevD.34.470.

[205] Bassano Vacchini. Completely positive quantum dissipation. *Physical Review Letters*, 84(7):1374, 2000. doi:10.1103/PhysRevLett.84.1374.

[206] Masuo Suzuki. On the convergence of exponential operators—the zassenhaus formula, bch formula and systematic approximants. *Communications in Mathematical Physics*, 57(3):193–200, 1977. doi:10.1007/BF01614161.

[207] Klaus Mølmer, Yvan Castin, and Jean Dalibard. Monte carlo wave-function method in quantum optics. *J. Opt. Soc. Am. B*, 10(3):524–538, Mar 1993. doi:10.1364/JOSAB.10.000524.

[208] Andrew J Daley. Quantum trajectories and open many-body quantum systems. *Advances in Physics*, 63(2):77–149, 2014. doi:10.1080/00018732.2014.933502.

[209] Lars Bonnes and Andreas M. Läuchli. Superoperators vs. trajectories for matrix product state simulations of open quantum system: A case study, 2014. arXiv:1411.4831.

[210] W. Dür, G. Vidal, and J. I. Cirac. Three qubits can be entangled in two inequivalent ways. *Phys. Rev. A*, 62:062314, Nov 2000. doi:10.1103/PhysRevA.62.062314.

[211] James McClung. Constructions and applications of w-states. *Worcester Polytechnic Institute*, 2020. doi:https://digital.wpi.edu/downloads/mw22v793n?locale=en.

[212] Daniel Manzano. A short introduction to the lindblad master equation. *Aip Advances*, 10(2), 2020. doi:10.1063/1.5115323.

[213] Andre RR Carvalho, Harrison Ball, Michael J Biercuk, Michael R Hush, and Felix Thomsen. Error-robust quantum logic optimization using a cloud quantum computer interface. *Physical Review Applied*, 15(6):064054, 2021. doi:10.1103/PhysRevApplied.15.064054.

[214] Thomas Alexander, Naoki Kanazawa, Daniel J Egger, Lauren Capelluto, Christopher J Wood, Ali Javadi-Abhari, and David C McKay. Qiskit pulse: Programming quantum computers through the cloud with pulses. *Quantum Science and Technology*, 5(4):044006, 2020. doi:10.1088/2058-9565/aba404.

[215] Angelo Bassi and Dirk-André Deckert. Noise gates for decoherent quantum circuits. *Physical Review A*, 77(3):032323, 2008. doi:10.1103/PhysRevA.77.032323.